Hochauflösende elektronische Spektroskopie von heteroaromatischen Verbindungen

Dissertation

von

Thi Bao Chau Vu

aus Hanoi/Vietnam

Düsseldorf, September 2011

Hochauflösende elektronische Spektroskopie von heteroaromatischen Verbindungen

von

Thi Bao Chau Vu

Dissertation in Chemie

angefertigt am
Institut für Physikalische Chemie und Elektrochemie I
Lehrstuhl für Molekülspektroskopie und Nanosysteme

vorgelegt der
Mathematisch-Naturwissenschaftlichen Fakultät der
Heinrich-Heine-Universität Düsseldorf

Beginn der Arbeit:	April 2006
Abgabe der Arbeit:	September 2011
Referent:	PD. Dr. Michael Schmitt
Koreferent:	Prof. Dr. Karl Kleinermanns

Erklärung

Die hier vorgelegte Dissertation habe ich eigenständig und ohne unerlaubte Hilfe angefertigt. Die Dissertation wurde in der vorgelegten oder in ähnlicher Form noch bei keiner anderen Institution eingereicht. Ich habe bisher keine erfolglosen Promotionsversuche unternommen.

Düsseldorf, den 30.09.2011   _____

                                                    Chau Vu

Für meine Eltern

Inhaltsverzeichnis

II

Kapitel 1

Einleitung

Zur Untersuchung der Atom- und Molekülstrukturen steht uns eine große Bandbreite an spektroskopischen Methoden zur Verfügung, die aufgrund der Wechselwirkung der diskreten Übergänge im Molekül mit der elektromagnetischen Strahlung beruhen. Dabei kann man unbekannte Moleküle identifizieren, die Molekularstruktur bestimmen und die Wechselwirkung der Moleküle mit der Umgebung untersuchen.

Bei der chemischen Reaktion wird den Molekülen Energie zugeführt, sodass diese sich neu ordnen und einen Übergangzustand bilden. Um die chemischen Prozesse zu verstehen ist die Ermittlung der Strukturen der beteiligten Komponenten unabdingbar.

Die Struktur für den Grundzustand liefern zahlreiche Methoden, wie zum Beispiel die NMR-Spektroskopie, die Röntgenanalyse, die IR-Spektroskopie und die Mikrowellenspektroskopie. Für isolierte Systeme eignen sich insbesondere die rotationsaufgelösten Spektroskopien für die Strukturbestimmung.

Die Mikrowellenspektroskopie ermittelt für isolierte Moleküle mit permanentem Dipolmoment die Rotationskonstanten im elektronischen Grundzustand S_0. Die Trägheitsmomente, die sich aus den Rotationskonstanten ergeben, sind von der Massenverteilung, den Bindungslängen und -winkeln abhängig. Die Kenntnisse über die drei Rotationskonstanten erlauben bestenfalls die

Bestimmung von drei Strukturiparametern (Bindungslänge, Bindungswinkel und Diederwinkel). Um mehr über die Struktur des Systems zu erfahren, führt man Messungen an Isotopologen durch und berechnet mit Hilfe der Kraitchman-Gleichungen die Atompositionen.

Für Systeme mit schwingungsinduziertem Dipolmoment liefert die IR-Spektroskopie die benötigten Rotationskonstanten.

Durch die Kenntnis über die Ladungsverschiebung des Moleküls bei der elektronischen Anregung vereinfacht sich die Interpretation von der Reaktivität und der Funktionalität, daher sollte man der Struktur im angeregten Zustand besondere Aufmerksamkeit schenken. Durch die hochauflösende, laserinduzierte Fluoreszenzspektroskopie (HRLIF- High Resolution Laser Induced Fluorescence) lässt sich die Änderung der elektronischen Struktur, die durch die elektronische Anregung entsteht, bestimmen. Die HRLIF ermöglicht die Strukturbestimmung sowohl für den Grundzustand S_0 als auch für den elektronisch angeregten Zustand S_1. Das Verhältnis der Linienintensitäten für die verschiedenen Übergangstypen ist ein Maß für die Übergangsdipolmomente. Die Linienbreite der Bande ermöglicht zudem die Berechnung der Lebensdauer.

Kapitel 2

Theoretische Grundlagen

In diesem Kapitel werden die mathematischen Grundlagen, die für das Verständnis der rotationsaufgelösten Spektren erforderlich sind, dargestellt. Dabei wird zunächst auf die Herleitung des Hamiltonoperators eingegangen. Im Anschluss daran werden die mathematischen Beschreibungen der verschiedenen starren Kreiseltypen behandelt. Auf den anormeren Effekt, ein elektronischer Effekt, als Grund für die Veränderung der Strukturen im manchen Molekülen wird anschließend eingegangen. Im folgenden Kapitel wird auf den nicht starren Kreisel erweitert und die Zentrifugalverzerrung analysiert. Als nächstes wird gezeigt, wie man mit Hilfe der Kraitchman-Gleichungen die Strukturparameter der Moleküle aus den Rotationskonstanten ermittelt. Auf die Übergangwahrscheinlichkeit und verschiedenen Parameter, welche die Ursache der Linienintensität sind, wird anschließend eingegangen. Abschließend interessieren uns die Ursachen der Linienverbreiterung und die verschiedenen Verbreiterungsprofilen.

Die Referenzen [15] [61] [84] [92] [151] dienen zur Darstellung und zur Ableitung der theoretischen Grundlage in dieser Arbeit.

2.1   Die Herleitung der Hamiltonoperatoren

Das quantenmechanische Verständnis zur Beschreibung der Rotation verlangt einen geeigneten Hamiltonoperator. In der praktischen Anwendung wird der vollständige Hamiltonoperator mit Hilfe der Born-Oppenheimer-Näherung vereinfacht. Durch das Korrespondenzprinzip können quantenmechanische Ausdrücke aus der klassischen Beschreibung gewonnen werden. Aus diesem Grund wird im Anschluss der Ausdruck für kinetische Energie ermittelt, aus dem die quantenmechanischen Größen aufbauen.

2.1.1   Die Born-Oppenheimer Näherung

Die Terme der Elektronen- und Kernbewegung können unter Verwendung der *Born-Oppenheimer-Näherung* separiert betrachtet werden [siehe Anhang A]. Für einen festen Kernabstand bestimmen wir die elektronische Schrödingergleichung. Dadurch erhalten wir die Energie für diese Kernkonfiguration:

$$\widehat{H}\,\mathbf{\Psi} = \mathbf{E}\,\mathbf{\Psi}. \tag{2.1}$$

$\widehat{H}$ ist hierbei der Hamiltonoperator, E die Gesamtenergie und $\mathbf{\Psi}$ die Gesamtwellenfunktion. Die Gesamtwellenfunktion $\mathbf{\Psi}$ errechnet sich aus dem Produkt der Elektronwellenfunktion bei einem fixen Kernabstand $\psi^{el}(\vec{\mathbf{q_e}}\vec{\mathbf{q_n}})$ und der Kernwellenfunktion $\psi^n(\vec{\mathbf{q_n}})$:

$$\Psi(\vec{q_e}\,\vec{q_n}) = \psi^{el}(\vec{q_e}\,\vec{q_n})\psi^n\,\vec{q_n}. \tag{2.2}$$

$\vec{q_e}$ beschreibt hierbei den Positionsvektor der Elektronen und $\vec{q_n}$ den der Kernen. Die Gesamtenergie ergibt sich infolgedessen aus der Summe der elektronischen Energie und der kinetischen Energie der Kerne:

$$E = E_e + E_{kin}. \tag{2.3}$$

2.1.2 Die Definition der Eulerschen Winkel

Zur Beschreibung der Rotation sind zwei Koordinatensysteme notwendig: ein
molekülfestes Koordinatensystem, das seinen Ursprung im Schwerpunkt des
Moleküls hat und ein raumfestes Koordinatensystem (Laborkoordinaten) mit
dem Positionsvektor $\vec{q_n}$:

$$\vec{q_n} = \vec{R} + \mathbf{\Phi^{-1}}(\vec{g_n} + \vec{d_n}). \tag{2.4}$$

Dabei steht $\vec{g_n}$ für die Koordinaten einer Gleichgewichtstruktur und $\vec{d_n}$ für die
zeitabhängige Abweichung dieser Gleichgewichtstruktur in dem molekülfes-
ten Koordinatensystem x,y,z. $\vec{R}$ stellt den Vektor des Molekülschwerpunkts,
den Ursprung des molekülfesten Systems, im raumfesten Koordinatensystem
dar. $\mathbf{\Phi^{-1}}$ ist eine 3x3 Rotationsmatrix, welche die molekülfesten Koordina-
ten (x, y, z) in ein System parallel zu dem raumfesten System (X, Y, Z)
umwandelt:

$$\begin{pmatrix} x \\ y \\ z \end{pmatrix} = \Phi \begin{pmatrix} X \\ Y \\ Z \end{pmatrix} = \begin{pmatrix} \Phi_{xX} & \Phi_{xY} & \Phi_{xZ} \\ \Phi_{yX} & \Phi_{yY} & \Phi_{yZ} \\ \Phi_{zX} & \Phi_{zY} & \Phi_{zZ} \end{pmatrix}. \tag{2.5}$$

Durch drei aufeinander folgende Drehungen um die drei Eulerschen Winkel
φ, θ, χ (Abbildung 2.1) erhält man die sogenannte Richtungskosinusmatrix
$\mathbf{\Phi}$.

1. Drehung um den Winkel φ gegen den Uhrzeigersinn um die z-Achse:
   neues Koordinatensystem x', y', z.

2. Drehung um den Winkel θ gegen den Uhrzeigersinn um die y'-Achse :
   neues Koordinatensystem x'' y' z'.

3. Drehung um den Winkel χ gegen den Uhrzeigersinn um die z'-Achse:
   neues Koordinatensystem x''', y'', z'.

Der Richtungskosinusmatrix $\mathbf{\Phi}$ berechnet sich folgendermaßen:

$$\mathbf{\Phi} = \begin{pmatrix} \cos\chi & \sin\chi & 0 \\ -\sin\chi & \cos\chi & 0 \\ 0 & 0 & 1 \end{pmatrix} \begin{pmatrix} \cos\theta & 0 & -\sin\theta \\ 0 & 1 & 0 \\ \cos\theta & 0 & \cos\theta \end{pmatrix} \begin{pmatrix} \cos\varphi & \sin\varphi & 0 \\ -\sin\varphi & \cos\varphi & 0 \\ 0 & 0 & 1 \end{pmatrix}$$

$$= \tag{2.6}$$

$$\begin{pmatrix} \cos\chi\cos\theta\cos\varphi - \sin\chi\sin\varphi & \cos\chi\cos\theta\sin\varphi + \sin\chi\cos\varphi & \cos\chi\sin\theta \\ -\sin\chi\cos\theta\cos\varphi - \sin\chi\cos\theta & -\sin\chi\cos\theta\sin\varphi + \cos\chi\cos\theta & \sin\chi\sin\theta \\ \sin\theta\cos\varphi & \sin\theta\sin\varphi & \cos\theta \end{pmatrix}$$

Die Drehung um die molekülfesten Achsensysteme gegen den Uhrzeigersinn führt zu einer Rotation der Atomkoordinaten im Uhrzeigersinn. Man benötigt zur Beschreibung der Molekülkoordinaten im raumfesten System daher die transponierte Matrix $\mathbf{\Phi}'$, die mit der inversen Matrix $\mathbf{\Phi}^{-1}$ äquivalent ist.
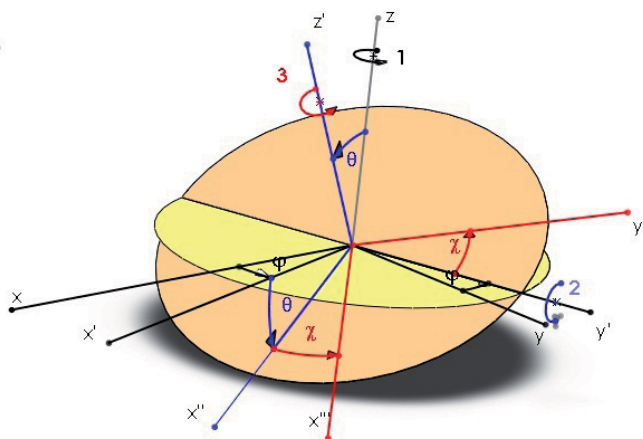
Abbildung 2.1: Definition der Eulerschen Winkel im rechtsdrehenden Koordinatensystem

2.1.3 Die Kinetische Energie des Moleküls

Die klassische Physik definiert die kinetische Energie eines N-atomigen Moleküls:

$$T = \frac{1}{2} \sum m_n \, \dot{\vec{q}}_n \, \dot{\vec{q}}_n, \tag{2.7}$$

wobei m_n die Masse des n-ten Atoms wiedergibt.

Die Ableitung der Ortskoordinaten $\vec{q}_n$ der Gleichung 2.4 ergibt:

$$\dot{\vec{q}}_n = \dot{\vec{R}} + \dot{\boldsymbol{\Phi}}^{-1}(\vec{g}_n + \vec{d}_n) + \dot{\boldsymbol{\Phi}}^{-1}\dot{\vec{d}}_n. \tag{2.8}$$

Durch das Einsetzen der Gleichung 2.8 in Gleichung 2.7 entstehen neun Terme, die wie folgt zusammengefasst werden:

$$T = \frac{1}{2} \sum m_n \left[\dot{\vec{R}} + \dot{\vec{\boldsymbol{\Phi}}}^{-1}(\vec{g}_n + \vec{d}_n) + \vec{\boldsymbol{\Phi}}^{-1}\dot{\vec{d}}_n \right] \left[\dot{\vec{R}} + \dot{\vec{\boldsymbol{\Phi}}}^{-1}(\vec{g}_n + \vec{d}_n) + \vec{\boldsymbol{\Phi}}^{-1}\dot{\vec{d}}_n \right]$$

$$= \frac{1}{2} \sum m_n \begin{bmatrix} \dot{\vec{R}}\dot{\vec{R}} + 2(\dot{\vec{R}}\dot{\vec{\boldsymbol{\Phi}}}^{-1}(\vec{g}_n + \vec{d}_n)) + 2(\dot{\vec{R}}\vec{\boldsymbol{\Phi}}^{-1}\dot{\vec{d}}_n) \\ +(\vec{\boldsymbol{\Phi}}^{-1}\dot{\vec{d}}_n)(\vec{\boldsymbol{\Phi}}^{-1}\dot{\vec{d}}_n) + 2(\dot{\vec{\boldsymbol{\Phi}}}^{-1}(\vec{g}_n + \vec{d}_n))(\vec{\boldsymbol{\Phi}}^{-1}\dot{\vec{d}}_n) \\ +(\dot{\vec{\boldsymbol{\Phi}}}^{-1}(\vec{g}_n + \vec{d}_n))(\dot{\vec{\boldsymbol{\Phi}}}^{-1}(\vec{g}_n + \vec{d}_n)) \end{bmatrix} \tag{2.9}$$

Die ersten drei Summanden der Gleichung 2.9 beschreiben die Translation und werden in einem homogenen Potenzialfeld vernachlässigt.Das Skalarprodukt zweier Vektoren ist von der Achsenrotation unabhängig. Der vierte Term der Gleichung 2.9 ist deshalb auch nicht relevant.Die nachfolgenden Gleichungen berechnen die kinetische Energie im raumfesten Koordinatensystem, werden aber durch die molekülfesten Koordinaten beschrieben:

$$T = T_{vib} + T_{vibrot} + T_{rot} \tag{2.10}$$

mit

$$T_{vib} = \frac{1}{2} \sum m_n \vec{\Phi}^{-1}(\dot{\vec{d}}_n)(\dot{\vec{d}}_n) \tag{2.11}$$

$$
\begin{aligned}
T_{vibrot} &= \sum m_n \left(\dot{\vec{\boldsymbol{\Phi}}}^{-1}(\vec{g}_n + \vec{d}_n) \right) \left(\vec{\boldsymbol{\Phi}}^{-1} \dot{\vec{d}}_n \right) \\
&= \sum m_n (\dot{\vec{\boldsymbol{\Phi}}}^{-1} \vec{\boldsymbol{\Phi}}^{-1})((\vec{g}_n + \vec{d}_n)\dot{\vec{d}}_n)
\end{aligned}
\tag{2.12}
$$

$$
T_{rot} = \frac{1}{2} \sum m_n \left(\dot{\vec{\boldsymbol{\Phi}}}^{-1}(\vec{g}_n + \vec{d}_n)(\dot{\vec{\boldsymbol{\Phi}}}^{-1}(\vec{g}_n + \vec{d}_n)) \right)
\tag{2.13}
$$

Die Gleichung 2.11 definiert die kinetische Energie der reinen Vibration, die nur von der Abweichung um den Gleichgewichtzustand abhängt.

Die Winkelgeschwindigkeiten $\omega_x, \omega_y, \omega_z$, ergeben sich durch die erste Ableitung der Winkelkoordinaten:

$$
\omega_\alpha = (\dot{\chi})_\alpha + (\dot{\theta})_\alpha + (\dot{\varphi})_\alpha \qquad \text{mit } (\alpha = x, y, z)
\tag{2.14}
$$

Die drei Winkelgeschwindigkeiten sind wie folgt von den drei Eulerschen Winkeln (Abbildung 2.1 S. 6) abhängig:

$$
\omega_x = \dot{\theta} \sin\chi + \dot{\varphi} \cos\chi \sin\theta
\tag{2.15}
$$

$$
\omega_y = \dot{\theta} \cos\chi + \dot{\varphi} \sin\chi \sin\theta
\tag{2.16}
$$

$$
\omega_z = \dot{\chi} + \dot{\varphi} \cos\theta
\tag{2.17}
$$

Somit vereinfacht sich der Ausdruck $(\dot{\vec{\boldsymbol{\Phi}}}^{-1} \vec{\boldsymbol{\Phi}}^{-1})$ der Gleichung 2.12:

$$
(\dot{\vec{\boldsymbol{\Phi}}}^{-1} \vec{\boldsymbol{\Phi}}^{-1}) = \begin{pmatrix} 0 & -\omega_z & \omega_y \\ \omega_z & 0 & -\omega_x \\ -\omega_y & \omega_x & 0 \end{pmatrix}
\tag{2.18}
$$

Durch Einsetzen der Permutation erhält man zyklische und antizyklische Permutationen:

$$
\dot{\vec{\boldsymbol{\Phi}}}^{-1} \vec{\boldsymbol{\Phi}}^{-1} = -e_{\alpha\beta\gamma}\omega_\alpha \qquad \text{mit } (\alpha\beta\gamma = x, y, z)
\tag{2.19}
$$

$$
\begin{aligned}
\text{Zyklische Permutationen} \qquad & e_{x,y,z} = e_{y,z,x} = e_{z,x,y} \\
\text{Antizyklische Permutationen} \qquad & e_{x,z,y} = e_{y,x,z} = e_{z,y,x} \\
\text{Bei mindestens zwei gleichen Indizes} \qquad & e_{\alpha\beta\gamma} = 0
\end{aligned}
\tag{2.20}
$$

Nun betrachten wir den restlichen Teil der Gleichung 2.12: $\sum m_n(\vec{g}_n + \vec{d}_n)\dot{\vec{d}}_n$

Mit Hilfe der zwei Eckart'schen Bedingungen vereinfachen sich die Gleichungen für die Coriolis- und die Vibration-Rotation Wechselwirkungen:

$$\sum_n m_n \vec{d}_n = 0 \tag{2.21}$$

und

$$\sum_n m_n \vec{g}_n \times \vec{d}_n = 0 \tag{2.22}$$

Damit ergibt sich für die Gleichung 2.12 den vereinfachten Ausdruck:

$$T_{vibrot} = \sum_n m_n \omega_\alpha e_{\alpha\beta\gamma} d_{n\beta} \dot{d}_{n\gamma} \tag{2.23}$$

Analog erhält man für den reinen Rotationsterm (Gleichung 2.13):

$$T_{rot} = \sum_n m_n e_{\epsilon\alpha\gamma} e_{\epsilon\beta\gamma} \omega_\alpha \omega_\beta g_{n\gamma} g_{n\delta} \qquad \text{mit}(\alpha, \beta, \gamma, \delta, \epsilon = x, y, z) \tag{2.24}$$

Das Modell des starren Rotators, der den reinen Rotationsterm (Gleichung 2.24) darstellt, wird im Folgenden beschrieben.

2.2 Der starre Rotator

Der Ausdruck *starr* beruht auf der Annahme, dass durch die Rotation die Struktur des Moleküls unverändert bleibt, d.h. man vernachlässigt alle Geometrieverzerrungen sowie die Kopplung zwischen der Rotation mit der Schwingung bzw. der Torsion.

2.2.1 Der klassische starre Rotator

Die Rotationsenergie des starren Rotators berechnet sich wie folgt:

$$T_{rot} \;=\; \frac{1}{2}\sum_i^n m_n(\omega \times r_n)^2 \tag{2.25}$$

$$=\; \frac{1}{2}\sum_i^n m_n(\omega \times r_i)_x^2 + \frac{1}{2}\sum m_n(\omega \times r_i)_y^2 + \frac{1}{2}\sum m_n(\omega \times r_i)_z^2$$

$$=\; \frac{1}{2}\sum_i^n m_i[\omega_x^2(z_i^2 + y_i^2) + \omega_y^2(x_i^2 + z_i^2) + \omega_z^2(x_i^2 + y_i^2)$$

$$+\; \omega_x\omega_y x_i y_i - \omega_x\omega_z x_i z_i - \omega_y\omega_z y_i z_i]$$

$$T_{rot} = \frac{1}{2} \begin{pmatrix} \omega_x & \omega_y & \omega_z \end{pmatrix} \begin{pmatrix} I_{xx} & I_{xy} & I_{xz} \\ I_{yx} & I_{yy} & I_{yz} \\ I_{zx} & I_{zy} & I_{zz} \end{pmatrix} \begin{pmatrix} \omega_x \\ \omega_y \\ \omega_z \end{pmatrix} = \frac{1}{2}\omega\tilde{\mathbf{I}}\omega. \tag{2.26}$$

Hierbei ist der Trägheitstensor definiert als:

$$\tilde{\mathbf{I}} = \begin{pmatrix} I_{xx} & I_{xy} & I_{xz} \\ I_{yx} & I_{yy} & I_{yz} \\ I_{zx} & I_{zy} & I_{zz} \end{pmatrix}. \tag{2.27}$$

Die Diagonalelemente des Trägheitstensors heißen Trägheitsmomente, die anderen Trägheitsprodukte:

$$I_{xx} = \sum_i^n m_i(z_i^2 + y_i^2) \qquad\qquad I_{xy} = I_{yx} = -\sum_i^n m_i x_i y_i$$

$$I_{yy} = \sum_i^n m_i(x_i^2 + z_i^2) \qquad\qquad I_{xz} = I_{yx} = -\sum_i^n m_i x_i z_i \tag{2.28}$$

$$I_{zz} = \sum_i^n m_i(x_i^2 + y_i^2) \qquad\qquad I_{xy} = I_{yz} = -\sum_i^n m_i y_i z_i.$$

Indem man das molekülfeste System so anlegt, dass seine Achsen genau in den drei Richtungen der Hauptträgheitsachse liegen, wird der Tensor I diagonal, d.h. die Trägheitsprodukte verschwinden. Die Hauptträgheitsachsen trans-

formation wird durch die folgende Gleichung vollzogen:

$$\begin{vmatrix} I_{xx} - I & I_{xy} & I_{xz} \\ I_{yx} & I_{yy} - I & I_{yz} \\ I_{zx} & I_{zy} & I_{zz} - I \end{vmatrix} = 0. \tag{2.29}$$

Als Lösung dieser Gleichung erhält man drei Trägheitsmomente, die den drei Hauptträgheitsachsen I_a, I_b, I_c entsprechen:

$$I_a \leq I_b \leq I_c \tag{2.30}$$

Somit ergeben sich 3!=6 verschiedene mögliche Zuordnungen (Tabelle 2.1).

	I_r	I_l	II_r	II_l	III_r	III_l
x	b	c	c	a	a	b
y	c	b	a	c	b	a
z	a	a	b	b	c	c

Tabelle 2.1: Zuordnungen der Hauptträgheitsachsen zu den molekülfesten Koordinatenachsen

Der Berechnungsaufwand unterscheidet sich erheblich zwischen den Darstellungen I, II, III, während die links- und rechtshändigen Repräsentationen lediglich die Vorzeichen der Außendiagonalelemente der Hamiltonmatrix tauschen.

Je nach verschiedenen Verhältnissen der Trägheitsmomente unterscheidet man verschiedene Kreiseltypen, die in der Tabelle 2.2 wiedergegeben werden.

Kreiseltyp	Trägheitsmerkmal	Symmetrieoperation	Beispiele
Linear	$I_a = 0; I_b = I_c$	C_∞	HCl, CO_2
Sphärisch	$I_a = I_b = I_c$	mehrere $C_n, n \geq 3$	SF_6, CH_4
Oblat symmetrisch	$I_a = I_b < I_c$	eine $C_n, n \geq 3$	NH_3, C_6H_6
Prolat symmetrisch	$I_a < I_b = I_c$	eine $C_n, n \geq 3$	CH_3Br, PCl_5
Assymetrisch	$I_a < I_b < I_c$	keine $C_n, n \geq 2$ und keine S_4	H_2O

Tabelle 2.2: Kreiseltypen

Die kinetische Energie der Gleichung 2.26 vereinfacht sich zu:

$$T_{rot} = \frac{1}{2}(I_a\omega_a^2 + I_b\omega_b^2 + I_c\omega_c^2). \tag{2.31}$$

Man ersetzt die Winkelgeschwindigkeit durch den Drehimpuls durch folgende Beziehung:

$$J = \sum r_i \times p_i = \sum m_i(r_i \times (\omega_i \times r_1)) = \tilde{\mathbf{I}}\omega \tag{2.32}$$

Für das Hauptachsensystem ergibt sich entsprechend für den Drehimpuls:

$$J = \{I_x\omega_x; I_y\omega_y; I_z\omega_z\} \tag{2.33}$$

wobei die Trägheitsmomente $I_x, I_y; I_z$ je nach ihren Größen den drei Hauptträgheitsmomenten $I_a, I_b; I_c$ zugeordnet werden.
Die kinetische Energie berechnet sich somit:

$$T_{rot} = \frac{1}{2}\left(\frac{\mathbf{J}_a^2}{I_a} + \frac{\mathbf{J}_b^2}{I_b} + \frac{\mathbf{J}_c^2}{I_c}\right). \tag{2.34}$$

2.2.2   Die quantenmechanische Analyse der Rotation

2.2.2.1   Der Hamilton Operator

Das Korrespondenzprinzip ermöglicht die Darstellung der klassischen Größen in der Quantenmechanik durch ihre Operatoren.
Die Gleichung 2.34 für die kinetische Energie lässt sich umformen in:

$$\hat{H} = \frac{1}{2}\left(\frac{\hat{J}_a^2}{I_a} + \frac{\hat{J}_b^2}{I_b} + \frac{\hat{J}_c^2}{I_c}\right) = A\hat{J}_a^2 + B\hat{J}_b^2 + C\hat{J}_c^2. \tag{2.35}$$

$\hat{J}$ ist der Operator des Drehimpulses, auf dem im nächsten Abschnitt 2.2.2.2 detailliert eingegangen wird. A, B und C sind Rotationskonstanten, die indirekt mit den Trägheitsmomenten proportional sind:

$$A = \frac{1}{2I_a} \qquad B = \frac{1}{2I_b} \qquad C = \frac{1}{2I_c}. \tag{2.36}$$

Um eine bessere Vorstellung über die aus dem Experiment ermittelten Werte zu haben, drückt man häufig den Hamiltonoperator und die Rotationskonstante in der gleichen Einheit aus. Am meisten benutzt werden die Einheiten Joule, Hertz, und cm^{-1}:

$$A = \frac{\hbar^2}{2I_a} \qquad B = \frac{\hbar^2}{2I_b} \qquad C = \frac{\hbar^2}{2I_c} \qquad [J] \tag{2.37}$$

$$A = \frac{h}{8\pi^2 I_a} \qquad B = \frac{h}{8\pi^2 I_b} \qquad C = \frac{h}{8\pi^2 I_c} \qquad [Hz] \tag{2.38}$$

$$A = \frac{h}{8\pi^2 c I_a} \qquad B = \frac{h}{8\pi^2 c I_b} \qquad C = \frac{h}{8\pi^2 c I_c} \qquad [cm^{-1}] \tag{2.39}$$

2.2.2.2   Der Drehimpuls

Die klassischen Größen werden in der Quantenmechanik durch ihre Operatoren ersetzt. Für den Impuls p und den Abstand r sehen die Operatoren wie folgt

aus:

$$p \rightarrow \hat{p} = \left(\frac{\hbar}{i} \right) \nabla \qquad\qquad r \rightarrow \hat{r} = r. \tag{2.40}$$

Darin ist i die imaginäre Einheit, $\hbar$ die reduzierte Plancksche Konstante und ∇ ein Vektor mit den Komponenten $\frac{\partial}{\partial x_i}$.

Aus der klassischen Definition für den Drehimpuls $J = \sum r_i \times p_i$ folgt:

$$\hat{J} = \frac{\hbar}{i} \sum r_i \times p_i. \tag{2.41}$$

Für die Komponenten des Drehimpulses ergeben sich folgende Abhängigkeiten von den Winkelkoordinaten θ, φ, χ

$$
\begin{aligned}
\hat{J}_x &= \frac{\hbar}{i} \left(Y \frac{\partial}{\partial Z} - Z \frac{\partial}{\partial Y} \right) \\
&= -\frac{\hbar}{i} \left[\frac{-\cos\chi}{\sin\theta} \frac{\partial}{\partial\varphi} + \frac{\cos\chi \cos\theta}{\sin\theta} \frac{\partial}{\partial\chi} + \sin\chi \frac{\partial}{\partial\varphi} \right]
\end{aligned} \tag{2.42}
$$

$$
\begin{aligned}
\hat{J}_y &= \frac{\hbar}{i} \left(Z \frac{\partial}{\partial X} - X \frac{\partial}{\partial Z} \right) \\
&= -\frac{\hbar}{i} \left[\frac{-\sin\chi}{\sin\theta} \frac{\partial}{\partial\varphi} + \frac{\sin\chi \cos\theta}{\sin\theta} \frac{\partial}{\partial\chi} + \cos\chi \frac{\partial}{\partial\varphi} \right]
\end{aligned} \tag{2.43}
$$

$$\hat{J}_z = \frac{\hbar}{i} \left(X \frac{\partial}{\partial Y} - Y \frac{\partial}{\partial X} \right) = \frac{\hbar}{i} \frac{\partial}{\partial\chi} \tag{2.44}$$

Die Umrechnung von $\hat{J}_x, \hat{J}_y, \hat{J}_z$ in das sphärische Polarkoordinatensystem (Abbildung 2.2), ergibt:

$$\hat{J}_x = \frac{\hbar}{i} \left[-\sin\phi \frac{\partial}{\partial\theta} - \cot\theta \cos\phi \frac{\partial}{\partial\phi} \right] \tag{2.45}$$

$$\hat{J}_y = \frac{\hbar}{i} \left[-\cos\phi \frac{\partial}{\partial\theta} - \cot\theta \cos\phi \frac{\partial}{\partial\phi} \right] \tag{2.46}$$

$$\hat{J}_z = \frac{\hbar}{i} \frac{\partial}{\partial\phi} \tag{2.47}$$
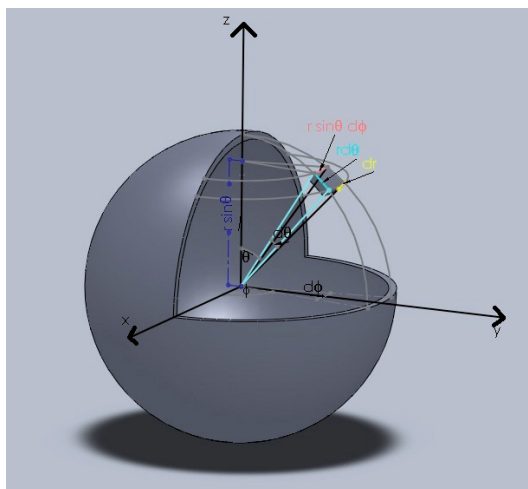
Abbildung 2.2: Definition der Polarkoordinaten Polarwinkel θ, $0 \leq \theta \leq \pi$, und den Azimutwinkel ϕ mit $0 \leq \phi \leq 2\pi$

θ ist hierbei der Polarwinkel, der von 0 bis π geht, und ϕ der Azimutwinkel mit $0 \leq \phi \leq 2\pi$.

Das Quadrat des Drehimpulses ermittelt man aufgrund der Beziehung $J^2 = J_x^2 + J_y^2 + J_z^2$ zu:

$$\hat{J}^2 = -\hbar^2 \left[-\frac{1}{\sin\theta} \frac{\partial}{\partial\theta} \left(\sin\theta \frac{\partial}{\partial\theta} \right) + \frac{1}{\sin^2\theta} \frac{\partial^2}{\partial\phi^2} \right]. \tag{2.48}$$

Dabei gelten folgende Vertauschungsoperationen:

$$[\hat{J}^2, \hat{J}_i] = 0 \qquad \text{mit } i = X, Y, Z \tag{2.49}$$

$$[\hat{J}^2, \hat{J}_\alpha] = 0 \qquad \text{mit } \alpha = x, y, z \tag{2.50}$$

$$[\hat{J}_\alpha, \hat{J}_i] = 0 \tag{2.51}$$

$$[\hat{J}_i, \hat{J}_j] = ie_{fgh}\hbar\hat{J}_j \qquad \text{mit } f, g, h = X, Y, Z \tag{2.52}$$

$$[\hat{J}_\alpha, \hat{J}_\beta] = ie_{\alpha,\beta,\gamma}\hbar\hat{J}_j \qquad \text{mit } \alpha, \beta, \gamma = x, y, z \tag{2.53}$$

$$[\hat{H}_{rr}, \hat{J}^2] = 0 \qquad \text{führt zu } J \tag{2.54}$$

$$[\hat{H}_{rr}, \hat{J}_z] = 0 \qquad\qquad \text{führt zu } M \qquad\qquad (2.55)$$

$$[\hat{H}_{rr}, \hat{J}_Z] = i\hbar \left(\frac{1}{2I_x} - \frac{1}{2I_y} \right) \left(\hat{J}_x \hat{J}_y - \hat{J}_y \hat{J}_x \right) \qquad \text{führt zu } M \qquad (2.56)$$

Aus den Gleichungen 2.49 bis 2.56 folgt, dass der Betrag des Drehimpulses und seine Projektion auf einer Achse sowohl im Molekülkoordinatensystem als auch im Laborkoordinatensystem kommutieren. Daher besitzen die Operatoren $\hat{J}^2$, $\hat{J}_z$, $\hat{J}_Z$ einen gemeinsamen Satz von Eigenfunktionen $\Psi_{(JKM)}$. J ist hierbei die Rotationsquantenzahl. Die Quantenzahl M beschreibt die Projektion von J auf der raumfesten Z-Achse, und die Quantenzahl K ist die Projektion von J auf der molekülfesten z-Achse.

2.2.2.3   Die Eigenwerte von $\hat{J}^2$

Man legt jeweils zwei neue Operatoren, die sogenannten *Leiteroperationen*, für das raumfeste bzw. molekülfeste System fest. Diese sind mit $\hat{J}_X$ und $\hat{J}_Y$ sowie $\hat{J}_x$ und $\hat{J}_y$ verbunden:

Raumfeste Koordinaten: $\qquad\qquad \hat{J}_+ = \hat{J}_X + i\hat{J}_Y \qquad\qquad \hat{J}_- = \hat{J}_X - i\hat{J}_Y$

Molekülfeste Koordinaten: $\qquad\qquad \hat{J}_+ = \hat{J}_x + i\hat{J}_y \qquad\qquad \hat{J}_- = \hat{J}_x - i\hat{J}_y$

Im Folgenden werden die Abhängigkeit des Drehimpulses und seine Komponente auf der raumfesten Z-Achse abgeleitet:
Für $\hat{J}^2$ gilt:

$$\hat{J}^2 = \hat{J}_X^2 + \hat{J}_Y^2 + \hat{J}_Z^2 = \hat{J}_- \hat{J}_+ + \hat{J}_Z^2 + \hbar^2 \hat{J}_Z = \hat{J}_+ \hat{J}_- + \hat{J}_Z^2 - \hbar^2 \hat{J}_Z. \quad (2.57)$$

Außerdem gelten folgende Vertauschungsrelationen:

$$\left[\hat{J}^2, J_\pm \right] = 0 \qquad\qquad (2.58)$$

$$\left[\hat{J}_Z, J_\pm \right] = \hbar J_\pm \qquad\qquad (2.59)$$

$$\left[\hat{J}_+, J_-\right] = 2\hbar J_z. \tag{2.60}$$

Gleichung 2.49 zeigt wie schon erwähnt eine Kommutation zwischen $\hat{J}^2$ und $\hat{J}_Z$ d.h. sie haben die gleichen Eigenfunktionen:

$$\hat{J}^2\Psi = \hbar^2 A\Psi \tag{2.61}$$

$$\hat{J}_Z\Psi = \hbar M\Psi. \tag{2.62}$$

Die Untersuchung von der Wirkung der Leiteroperation auf die Wellenfunktion ergibt somit:

$$\hat{J}_Z\hat{J}_\pm\Psi = \hat{J}_\pm\hat{J}_Z + [\hat{J}, \hat{J}_\pm]\Psi. \tag{2.63}$$

Aus $\hat{J}_\pm\hat{J}_Z\Psi = (\hat{J}_Z\hat{J}_\pm - \hbar\hat{J}_\pm)\Psi = \hbar\hat{J}_\pm M\Psi$ und der Gleichung 2.59 resultiert:

$$\hat{J}_Z\hat{J}_\pm\Psi = \hbar\hat{J}_\pm(M \pm 1)\Psi. \tag{2.64}$$

Aus der Gleichung 2.64 wird ersichtlich, dass durch die Anwendung der Leiteroperator auf eine Eigenfunktion von $\hat{J}_Z$ zu den Eigenwerten $\hbar(M + 1)$ bzw. $\hbar(M - 1)$ führt. Den Leiteroperator $\hat{J}_+$ nennt man *Erhöhungsoperator* und den Leiteroperator $\hat{J}_-$ *Erniedrigungsoperator*.

Das Quadrat der Leiteroperationen berechnet sich folgendermaßen:

$$\|J_+\Psi\|^2 = (J_+\Psi, J_-\Psi) = (\Psi, J_-J_+\Psi) = \Psi, (\hat{J}^2 - \hat{J}_Z^2 + \hbar^2 J_z)\Psi \tag{2.65}$$

$$= \hbar^2(A - M^2 + M)$$

$$\|J_-\Psi\|^2 = \hbar(A - M^2 - M). \tag{2.66}$$

Die Gleichungen 2.65 und 2.66 verbieten negative Zahlen, d.h.:

$$A - M^2 + M \geq 0 \Rightarrow A \geq M(M - 1) \tag{2.67}$$

und

$$A - M^2 - M \geq 0 \Rightarrow A \geq M(M + 1) \tag{2.68}$$

Aus der Lösung der Gleichung 2.61 ergibt sich für $A = \hbar J(J+1)$. Im Anschluss berechnet sich daraus die Quantenzahl M:

$$M = J, J-1, J-2, \ldots, -J-2, -J-1, -J. \tag{2.69}$$

J ist hierbei ganz- oder halbzahlig. Für jede Rotationskonstante J existieren $2J+1$ mögliche Projektionen davon auf der raumfesten Z- Achse.
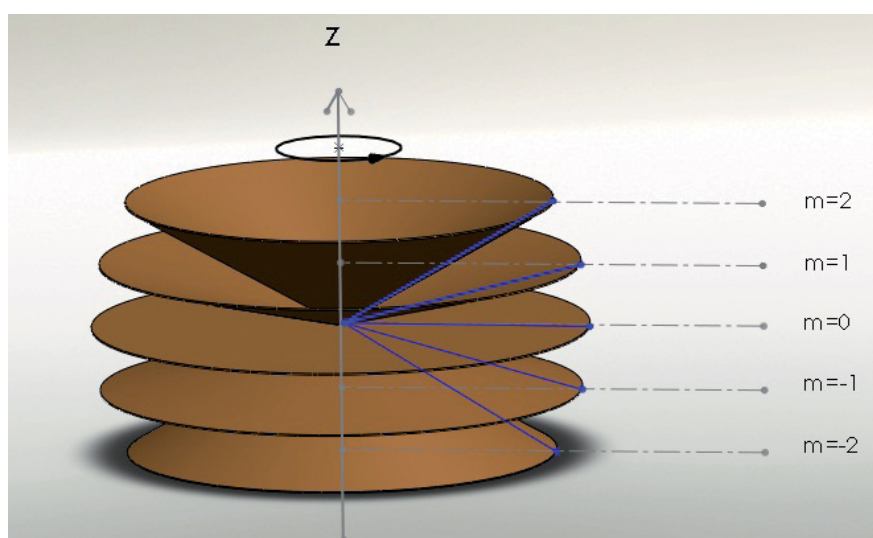
Abbildung 2.3: Projektion des Drehimpulses auf der raumfesten Koordinate Z-Achse

In Abbildung 2.3 wird der Zusammenhang zwischen J und M für $J = 2$ verdeutlicht, wobei die Z-Achse in der Einheit $\hbar$ dargestellt wird.
Für die Projektion auf der molekülfesten Koordinate ergibt sich analog zu der raumfesten Koordinate auch $2J+1$ mögliche Orientierungen. Für jedes $K > 0$ ist der Betrag von $|K|$ zweifach in M entartet. Dabei ergeben sich für jede Rotationsquantenzahl J $2(2J+1)$ mögliche Orientierungen.
Für die Eigenfunktionen der Drehimpulsoperatoren gelten:

$$\hat{J}^2\Psi_{JKM} = \hbar^2 J(J+1)\Psi_{JKM} \tag{2.70}$$

$$\hat{J}_Z\Psi_{JKM} = \hbar M\Psi_{JKM} \tag{2.71}$$

$$\hat{J}_z \Psi_{JKM} = \hbar K \Psi_{JKM} \tag{2.72}$$

$$(\hat{J}_X \pm i\hat{J}_Y)\Psi_{JKM} = \hat{J} \pm \Psi_{JKM} = \sqrt{(J \mp M)(J \pm M + 1)}\Psi_{JKM} \tag{2.73}$$

$$(\hat{J}_x \pm i\hat{J}_y)\Psi_{JKM} = \hat{J} \mp \Psi_{JKM} = \sqrt{(J \mp K)(J \pm K + 1)}\Psi_{JKM} \tag{2.74}$$

2.2.2.4 Die Wellenfunktion

Aus der Gleichung 2.48 (Seite 15) der Darstellung von $\hat{J}^2$ hängt der erste Summand nur von dem Polarwinkel θ und der zweite Summand nur von dem Azimutwinkel φ ab. Die Gesamtwellenfunktion wird daher als Produkt zweier Wellenfunktionen dargestellt:

$$\Psi = \Theta_{JM}(\theta)\Phi_M(\varphi) \equiv |JM\rangle. \tag{2.75}$$

Die Kommutation von $\hat{J}^2$ und $\hat{J}_Z$ (Gleichung 2.49) fordert Ψ als Lösungsfunktion sowohl für $\hat{J}^2$ als auch für $\hat{J}_Z$.

Als Lösung erhält man die Kugelflächenfunktionen:

$$|JM\rangle = (-1)^{\frac{M+|M|}{2}} N_{JM}\Theta_{JM}(\cos\theta)e^{iM\varphi} \tag{2.76}$$

Aus der Richtungskosinusmatrix geht hervor, dass durch die Drehung um die Winkel θ und φ, die die molekülfeste Koorfinaten im raumfesten Koordinaten ungewandelt. Bei einem Molekül mit mehreren Massenpunkten sollte man auch die Drehung um den Winkel χ berücksichtigen. Die Eigenfunktion nimmt folgende Form an:

$$\Psi = \Theta_{JM}(\theta)\Phi_M(\varphi)X_K(\chi) \equiv |JKM\rangle. \tag{2.77}$$

$X_K(\chi)$ berechnet sich:

$$X_K(\chi) = -\frac{1}{2\pi}e^{iK\chi}. \tag{2.78}$$

$$|JKM\rangle = (-1)^\beta N_{JM}\Theta_{JM}(\cos\theta)e^{iM\varphi}e^{iK\chi}. \tag{2.79}$$

Daraus ergibt sich für die Gesamtwellenfunktion in Abhängigkeit von θ, φ, χ: Die Werte von K und M werden miteinander verglichen. Dabei nimmt β immer den größeren Wert an. N_{JM} ist der Normierungsfaktor.

2.2.3   Der lineare Rotator

2.2.3.1   Die Eigenwerte

Wie aus Tabelle 2.2 zu erkennen ist, gilt für den linearen Rotator: $I_a = 0, I_b = I_c$. Die Gleichung 2.35 (S. 13) vereinfacht sich deshalb zu:

$$\hat{H}_{rr} = B\hat{J}_b^2 + \hat{C}_c^2 = B\hat{J}^2. \tag{2.80}$$

Damit ist der lineare Rotator unabhängig von K.
Die Energieeigenwerte berechnen sich aus der Gleichung 2.70 (S. 18):

$$E(J) = J(J+1)\hbar^2. \tag{2.81}$$

2.2.3.2   Die Wellenfunktion

Die Wellenfunktion für den starren linearen Rotator hängt von dem Beitrag des Drehimpulsoperators $\hat{J}$ und beim Anlegen eines äußeren Feldes auch von der Projektion des Drehimpulses auf der raumfesten Z-Achse ab. Die Wellenfunktion ist in Gleichung 2.76 (S 19) angegeben:

$$|JM\rangle = (-1)^{\frac{M+|M|}{2}} N_{JM}\Theta_{JM}(\cos\theta)e^{iM\varphi}. \tag{2.82}$$

2.2.3.3   Die Auswahlregeln

Unter der Bedingung, dass das Übergangsdipolmoment (Gleichung 2.83) nicht verschwindet:

$$M = \int \Psi_n^* \vec{\mu}\Psi_m \neq 0 \tag{2.83}$$

ergibt sich für die Auswahlregel für die Drehimpulsquantenzahl:

$$\Delta J = \pm 1, \tag{2.84}$$

und beim Anlegen eines äußeren Feldes:

$$\Delta M = \pm 1. \tag{2.85}$$

2.2.4 Der sphärische Rotator

2.2.4.1 Die Eigenwerte

Beim Einsetzen der Bedingung $I_a = I_b = I_c$ in die Gleichung 2.35 (S. 13):

$$\hat{H}_{rr} = B\hat{J}^2. \tag{2.86}$$

ergibt sich die Eigenwerte von Gleichung 2.70 (S. 18)zu:

$$E(J) = J(J+1)\hbar^2. \tag{2.87}$$

2.2.4.2 Die Wellenfunktion

Wie beim linearen Kreisel ist auch die Wellenfunktion des sphärischen Rotator von der Projektion des Drehimpulses $\hat{J}_z$ auf der molekülfesten z-Achse unabhängig. Die Wellenfunktionen lassen sich entsprechend der Gleichung 2.76 (S. 19) darstellen:

$$|JM\rangle = (-1)^{\frac{M+|M|}{2}} N_{JM} \Theta_{JM}(\cos\theta) e^{iM\varphi}. \tag{2.88}$$

2.2.4.3 Die Auswahlregeln

Das Übergangsdipolmoment darf für einen erlaubten Übergang nicht verschwinden. Der sphärische Rotator enthält kein Dipolmoment, d.h. reine Ro-

tationsübergänge sind verboten. Durch Zentrifugalverzerrung können allerdings Übergängen beobachtet werden.

2.2.5   Der symmetrische Rotator

2.2.5.1   Die Eigenwerte

Betrachtet man zuerst den prolaten, symmetrischen Kreisel mit $I_a < I_b = I_c$ ergibt sich für den Hamiltonoperator gemäß der Gleichung 2.35 (S. 13):

$$\hat{H}_{rr} = BJ^2 + (A - B)\hat{J}_a^2. \tag{2.89}$$

Aus dieser Gleichung 2.89 erkennt man, dass der Hamiltonian $\hat{H}_{rr}$ mit dem Betrag des Drehimpulses J und seiner Projektion $\hat{J}_a$ auf einer der molekülfesten Achsen kommutiert. Aus den Gleichungen 2.70 und 2.72 (S. 18) ergeben sich für die Energieeigenwerte:

$$E(J, K) = [BJ(J + 1) + (A - B)K^2]. \tag{2.90}$$

Analog berechnet sich die Energieeigenwerte für den oblaten Kreisel:

$$E(J, K) = [BJ(J + 1) + (C - B)K^2]. \tag{2.91}$$

2.2.5.2   Die Wellenfunktion

Die Hamiltonian $\hat{H}_{rr}$ für die symmetrischen Kreiseln ist von den Betrag des Drehimpulses $\hat{J}$ und seine Projektion auf einer Achse $\hat{J}_\alpha$ abhängig. Die Wellenfunktionen lassen sich entsprechend der Gleichung 2.79 darstellen:

$$|JKM\rangle = (-1)^\beta N_{JM} \Theta_{JM}(\cos\theta) e^{iM\varphi} e^{iK\chi}. \tag{2.92}$$

2.2.5.3 Die Auswahlregel

Damit der Übergansdipolmoment nicht verschwindet, gilt:

$$\Delta J = \pm 1 \tag{2.93}$$

und:

$$\Delta K = 0. \tag{2.94}$$

2.2.6 Der asymmetrische Rotator

2.2.6.1 Die Eigenwerte

Die Hauptträgheitsachsen unterscheiden sich bei den asymmetrischen Kreiseln $(I_a < I_b < I_c)$, sodass sich der Hamiltonoperator nicht mehr wie bei den symmetrischen Fällen durch $\hat{J}$ und $\hat{J}_z$ ausdrücken lässt. Der Hamiltonoperator sieht wie folgt aus:

$$\hat{H}_{rr} = A\hat{J}_x^2 + B\hat{J}_y^2 + C\hat{J}_z^2. \tag{2.95}$$

Die Information über die Eigenfunktionen und Eigenwerte von $\hat{J}_x^2$ und $\hat{J}_y^2$ sind essentiell für die Bestimmung von $\hat{H}_{rr}$.
Für $\hat{J}^2$ und $\hat{J}_z$ existieren nur die Diagonalelemente, da die Eigenfunktionen des symmetrischen Kreisels auch die Eigenfunktionen von $\hat{J}^2$ und $\hat{J}_z$ sind. Diese Funktionen sind keine Eigenfunktionen bezüglich $\hat{J}_x$ und $\hat{J}_y$, d.h. in dieser Basis ist der Hamiltonoperator nicht diagonal. Die Energie des asymmetrischen Kreisels ergibt keine geschlossene Lösung. Die Einführung eines Asymmetrie-Parameters κ nach Ray[114], ermöglicht eine schnelle Konvergenzentwicklung der Wellenfunktionen:

$$\kappa = \frac{2B - A - C}{A - C}. \tag{2.96}$$

Dabei beschreibt κ die Abweichung von den symmetrischen Kreiseln und kann die Werte von -1 bis +1 annehmen. Im Falle eines prolaten Kreisels (B=C) nimmt κ den Wert von -1 an, bei einem oblaten Kreisel (A=B) den Wert von (+1). $\kappa=0$ beschreibt den Kreisel mit der höchsten Asymmetrie. Man formuliert die Gleichung 2.96 nach B um, und setzt es in die Gleichung 2.95 ein:

$$
\begin{aligned}
\hat{H}_{rr} &= \frac{1}{2}(A+C)J(J+1) + \frac{1}{2}(A-C)[\langle J_x^2 \rangle - \langle J_y^2 \rangle + \kappa \langle J_z^2 \rangle] \quad (2.97) \\
&= \frac{1}{2}(A+C)J(J+1) + \frac{1}{2}(A-C)F_\tau(\kappa).
\end{aligned}
$$

Mit $\tau = K_a - K_c$. K_a kennzeichnet die Projektion von J auf der molekülfesten Achse den prolaten Grenzfall ($\kappa = -1$) und K_c die Projektion von J auf der molekülfesten Achse den oblaten Grenzfall ($\kappa = -1$).

Die Funktion $F_\tau(\kappa) = [\langle J_x^2 \rangle - \langle J_y^2 \rangle + \kappa \langle J_z^2 \rangle]$ resultiert aus den Eigenwerten von $\langle J_x^2 \rangle$, $\langle J_y^2 \rangle$, $\langle J_z^2 \rangle$, die durch die Entwicklung des asymmetrischen Kreisels nach dem symmetrischen Kreisel berechnet werden.

2.2.6.2   Die Wellenfunktion

Die unbekannte Eigenfunktion des asymmetrischen Kreisels wird durch die Linearkombination der Eigenfunktionen der bekannten symmetrischen Kreisel ausgedrückt:

$$
\Psi = \sum_n c_n \Psi_n(J, K, M). \tag{2.98}
$$

Aus dieser Gleichung 2.98 werden die Energieeigenwerte für die Matrixelemente des Operators bestimmt:

$$
\langle m | \hat{H}_{rr} | n \rangle = \Psi_m^*(J, K, M) \hat{H}_{rr} \Psi_n(J, K, M). \tag{2.99}
$$

Gemäß den Definitionen für die Leiteroperatoren (Kapitel 2.2.2.3, (S. 16))
erhalten wir folgenden Ausdruck für $\hat{J}_x$ und $\hat{J}_y$:

$$\hat{J}_+ + \hat{J}_- = \hat{J}_x + i\hat{J}_y \qquad\qquad \hat{J}_- = \hat{J}_x - i\hat{J}_y \qquad (2.100)$$

$$\hat{J}_+ + \hat{J}_- = \hat{J}_x + i\hat{J}_y + \hat{J}_x - i\hat{J}_y \qquad \Leftrightarrow \qquad \hat{J}_x = \frac{1}{2}(\hat{J}_+ + \hat{J}_-) \quad (2.101)$$

$$\text{und}$$

$$\hat{J}_+ - \hat{J}_- = \hat{J}_x + i\hat{J}_y - \hat{J}_x + i\hat{J}_y \qquad \Leftrightarrow \qquad \hat{J}_y = \frac{1}{2i}(\hat{J}_+ - \hat{J}_-). \quad (2.102)$$

Unter der Anwendung der Produktregel für die Matrizenmultiplikation:

$$\langle J, K, M|J_i^2|J', K', M'\rangle$$
$$= \sum_{J'', K'', M''} \langle J, K, M|J_i|J'', K'', M''\rangle\langle J'', K'', M''|J_i|J', K', M'\rangle \quad (2.103)$$

berechnen sich die Diagonalelemente:

$$\langle J, K, M|J_x^2|J, K, M\rangle = \langle J, K, M|J_y^2|J, K, M\rangle = \frac{i\hbar}{2}\left(J(J+1) - K^2\right) \quad (2.104)$$

und die Nichtdiagonalelemente:

$$\langle J, K, M|J_x^2|J, K \pm 2, M\rangle = \langle J, K, M|J_y^2|J, K \pm 2, M\rangle$$
$$= \frac{\hbar^2}{4}\sqrt{J(J+1) - K(K \pm 1)}\sqrt{J(J+1) - (K \pm 1)(K \pm 2)}. \quad (2.105)$$

Für die nicht verschwindenden Hamiltonmatrixelemente ergeben sich:

$$\langle J, K|J|J, K\rangle = \frac{\hbar^2}{2}\left[J(J+1)\left(\frac{1}{I_x} + \frac{1}{I_y}\right) + K^2\left(\frac{2}{I_z} - \frac{1}{I_x} - \frac{1}{I_y}\right)\right] \quad (2.106)$$

$$\langle J, K|J|J, K \pm 2\rangle =$$
$$\left[\sqrt{J(J+1) - K(K \pm 1)}\sqrt{J(J+1) - (K \pm 1)(K \pm 2)}\right] \qquad (2.107)$$

Gemäß Tabelle 2.1(S. 11) gibt es 3!=6 verschiedene Zuordnungsmöglichkei-
ten der Hauptträgheitsachsen a, b, c zu den molekülfesten Achsen x, y, z und
damit sechs verschiedene Darstellung des Hamiltonmatrix.
Durch Diagonalisierung der Hamiltonmatrix erhält man aus den Diagonal-
elementen die Eigenwerte von $\hat{H}_{rr}$. Nach der Ähnlichkeitstransformation mit

der Wangmatrix:

$$U_J = U_J^{-1} = \frac{1}{\sqrt{2}} \begin{vmatrix} \cdot & & & & & & \cdot \\ & \cdot & & & & \cdot & \\ & & -1 & 0 & 0 & 0 & -1 \\ & & 0 & -1 & 0 & 1 & 0 \\ & & 0 & 0 & \sqrt{2} & 0 & 0 \\ & & 0 & 1 & 0 & 1 & 0 \\ & & 1 & 0 & 0 & 0 & 1 \\ & \cdot & & & & \cdot & \\ \cdot & & & & & & \cdot \end{vmatrix} \tag{2.108}$$

erhält man die jeweilige Basis:

$$|J, K, M +\rangle \qquad\qquad \text{für } K = 0, \tag{2.109}$$

und:

$$|J, K, M \pm\rangle = \frac{1}{\sqrt{2}} JKM\rangle \pm |J - KM\rangle \qquad \text{für } K > 0. \tag{2.110}$$

Die Wangmatrix diagonalisiert die gesuchte Hamiltonmatrix nach dem Prinzip [91]:

$$U_J H_{rr} U_J = H_{rr}^{Wang}. \tag{2.111}$$

Da keine Verbindung zwischen geraden und ungeraden Paritäten von K bestehen, kann durch die Wangtransformation die Hamiltonmatrix in vier unabhängige Untermatrizen faktorisiert werden.

$$H_{rr}^{Wang} = E^+ + E^- + O^+ + O^-. \tag{2.112}$$

E und O stehen für die Parität von K, gerade oder ungerade. Die Zeichen $+$ und $-$ charakterisieren die in der Gleichung 2.110 entsprechenden Linearkombinationen.

Für eine Zuordnung zu den Symmetrien: $E^+ + E^- + O^+ + O^-$ müssen zuerst die Symmetrieelemente des Hamiltonoperators bestimmt werden. Gemäß der Gleichung 2.95 (S. 23) ist $\hat{H}_{rr}$ von dem Quadrat der Drehmomentkomponenten bezüglich der drei Hauptträgheitsachsen abhängig.

Diese Aufspaltung der Wangmatrix in Submatrizen (Gleichung 2.112) ist nur möglich, wenn die Hamiltonmatrix D_2-Symmetrie besitzt. Die Charaktertafel der Gruppe D_2 wird in der Tabelle 2.3 wiedergegeben:

	E	$C_2(x)$	$C_2(y)$	$C_2(z)$
A	1	1	1	1
B_x	1	1	-1	-1
B_y	1	-1	1	-1
B_z	1	-1	-1	1

Tabelle 2.3: Charaktertafel der Gruppe D_2

Bei der Einführung eines neuen Parameters γ wandelt sich die Wangfunktion (Gleichung 2.110) um in:

$$|J, K, M\pm\rangle = \frac{1}{\sqrt{2}} \left\{ JKM\rangle (-1)^\gamma |J - KM\rangle \right\} \tag{2.113}$$

γ repräsentiert entweder eine gerade oder ungerade Linearkombination der Funktionen. Die resultierende Klassifizierung der Symmetrie nach der Wang-Submatrix ist in Tabelle 2.4 angegeben.

Aus Tabelle 2.4 erkennt man, dass jede benachbarten Rotationszustände den unterschiedlichen irreduziblen Darstellungen zugeordnet werden, d.h. die Rotationszustände gehören unterschiedlichen Submatrizen an.

Zudem verringert sich durch die Aufteilung in Submatrizen der Rechenaufwand für die Diagonalisierung des Hamiltonoperators erheblich.

Submatrix	(x,y,z)	
	J_{even}	J_{odd}
E^+	A	B_z
E^-	B_z	A
O^+	B_y	B_x
O^-	B_x	$B_y.$

Tabelle 2.4: Symmetrieklassifizierung der Wang-Submatrizen

King, Hainer und Cross [88] führen neue Symbole für die Symmetrieeigenschaften der Rotation bezüglich der $C_2(a)$-Operation und der $C_2(c)$-Operation ein. Dabei steht e für das symmetrische Verhalten der Rotationswellenfunktion bezüglich der C_2 Drehung und o für das asymmetrische Verhalten.

Bei der Notation nach Denninson bezieht sich das erste Zeichen auf die $C_2(a)$-Operation und das zweite auf die $C_2(c)$-Operation. Für die symmetrischen Rotationwellenfunktion bezüglich der jeweiligen Operatoren stehen $(+)$ und $(-)$ für die asymmetrische Fälle. Tabelle 2.5 fasst diese Bezeichnungen zusammen.

Mulliken	King et al.	Dennison
A	ee	$++$
B_a	eo	$-+$
B_b	oo	$--$
B_c	oe	$+-$

Tabelle 2.5: Nomenklatur nach Mulliken, King.et al. und Dennison

2.2.6.3   Die Auswahlregel

Zu jeder Rotationsquantenzahl J existieren $(2J+1)$ unterschiedliche Energieniveaus. Der Hamiltonoperator beim asymmetrischen Rotator ist aber nicht in K diagonal und stellt damit keine gute Quantenzahl dar. Man führt einen

Index $\tau = K_a - K_c$ ein und bezeichnet das Rotationsniveau J_τ oder $J_{K_a K_c}$. K_a, K_c können Werte von 0 bis J angenommen werden, jedoch gilt jenach Parität des Niveaus $K_a + K_c = J$, oder $K_a + K_c = J + 1$.

Das Übergangdipolmoment kann bei einem asymmetrischen Kreisel jede beliebige Orientierung haben. Liegt es in Richtung der a-Achse, so haben wir a-Typ Übergänge. Dem endsprechend gibt es je nach Lage des Übergangsdipolmoments Übergänge von Typ a, b, c, ab, bc und abc-Typen.

Mit der Anwendung der Gruppentheorie lässt sich die Auswahlregel für K_a und K_c herleiten. Denn für einen möglichen Übergang muss das Produkt der Anfangswellenfunktion, der Endwellenfunktion und des Dipolmomentoperators die totalsymmetrische Darstellung enthalten:

$$\Gamma(\Psi') \times \Gamma(\Psi'') \supseteq A. \tag{2.114}$$

Ψ ist dabei die Gesamtwellenfunktion, die nach der Born-Oppenheimer-Näherung aus Produkten von drei unabhängigen Bewegungen gebildet wird:

$$\Psi = \psi_e \psi_{vib} \psi_{rot}. \tag{2.115}$$

In der Regel sind die elektronischen und die vibronischen Wellenfunktionen totalsymmetrisch, sodass man die Auswahlregel für K_a und K_c aus Tabelle 2.6 entnehmen kann.

$a - Typ$	$\mu_a \neq 0$	$A \longleftrightarrow B_a$	$B_b \longleftrightarrow B_c$	$\Delta K_a = 0, \pm 2, \pm 4...$
		$ee \longleftrightarrow eo$	$oo \longleftrightarrow oe$	$\Delta K_c = \pm 1, \pm 3, \pm 5...$
$b - Typ$	$\mu_b \neq 0$	$A \longleftrightarrow B_b$	$B_a \longleftrightarrow B_c$	$\Delta K_a = \pm 1, \pm 3, \pm 5...$
		$ee \longleftrightarrow oo$	$eo \longleftrightarrow oe$	$\Delta K_c = \pm 1, \pm 3, \pm 5...$
$c - Typ$	$\mu_c \neq 0$	$A \longleftrightarrow B_c$	$B_a \longleftrightarrow B_b$	$\Delta K_a = \pm 1, \pm 3, \pm 5...$
		$ee \longleftrightarrow oe$	$eo \longleftrightarrow oo$	$\Delta K_c = 0, \pm 2, \pm 4...$

Tabelle 2.6: Auswahlregel für die einzelnen Übergangstypen

2.2.7   Die Kernspinstatistik und ihre Auswirkung auf die Spektren

Bei der Durchführung einer Symmetrieoperation können eine oder mehrere identische Kerne vertauscht werden. Die Anzahl der Vertauschungen hängt von der Symmetrie des Moleküls und von der Symmetrie der Wellenfunktion ab. Da diese Kerne einen Spin besitzen, muss dieser in der Betrachtung der Gesamtwellenfunktion mit einbezogen werden. Die Gesamtwellenfunktion setzt sich entsprechend aus dem Produkt der elektronischen Wellenfunktion, der Vibration-, der Rotation- und der Kernspinwellenfunktion zusammen:

$$\Psi = \psi_e \psi_{vib} \psi_{rot} \psi_{KS} \tag{2.116}$$

$$\Gamma\Psi = \Gamma\psi_e \times \Gamma\psi_{vib} \times \Gamma\psi_{rot} \times \Gamma\psi_{KS} \tag{2.117}$$

Gleichzeitig können bei einer Symmetrieoperation des asymmetrischen Kreisels nur zwei Kerne ausgetauscht werden, da Moleküle mit mehr als zwei identisch vertauschbaren Kernen nicht mehr asymmetrisch sind. Das Austauschen mehrerer identischen Kernpaare ist jedoch möglich. Bei mehreren identischen Kernen muss als Symmetrieelement eine C_n- Symmetrieachse vorhandeln sein. Wir betrachten das Verhalten der Rotationswellenfunktion bezüglich der C_2-Operatoren und fassen es in Tabelle 2.7 zusammen.

	$C_2(a)$	$C_2(b)$	$C_2(c)$
A	$+$	$+$	$+$
B_a	$+$	$-$	$-$
B_b	$-$	$+$	$-$
B_c	$-$	$-$	$+$

Tabelle 2.7: Verhalten der Rotationswellenfunktion bezüglich der C_2-Operatoren

Das Pauli-Prinzip kennzeichnet eine symmetrische Gesamtwellenfunktion für Bosonen (Kernspin ganzzahlig) und eine antisymmetrische Gesamtwellen-

funktion für Fermionen (Kernspin halbzahlig.)

Für die statischen Gewichte eines Überganges benötigt man neben der Entartung der jeweiligen Rotationsenergie noch den Anteil der symmetrischen und asymmetrischen Kernspinwellenfunktionen.

Beim Kernspin $I > 1/2$ existieren mehrere Kernwellenfunktionen. Die Projektion des Kernspins auf der raumfesten Achse ergibt $2I + 1$ mögliche Orientierungen. Zwei identische Kernen ergebe somit $(2I + 1)^2$ mögliche Kombinationen der Kernspinwellenfunktionen. Die Anzahl der symmetrischen Kernspinwellenfunktionen lässt sich wie folgt berechnen [139]:

$$n_{sym} = \frac{1}{2} \left[\prod_{i=1}^{n} (2I_i + 1) \right] \left[\prod_{i=1}^{n} (2I_i + 1) + 1 \right], \tag{2.118}$$

und für den asymmetrischen Fall:

$$n_{asym} = \frac{1}{2} \left[\prod_{i=1}^{n} (2I_i + 1) \right] \left[\prod_{i=1}^{n} (2I_i + 1) - 1 \right]. \tag{2.119}$$

Bei Vertauschung von einem Paar identischer Kerne sieht das Verhältnis der symmetrischen und asymmetrischen Anteile folgendermaßen aus:

$$\frac{n_{sym}}{n_{asym}} = \frac{I + 1}{I}. \tag{2.120}$$

2.3 Die interne Rotation

Die Drehung eines Molekülteils um eine fest verankerte Achse im Molekülrest nennt man die interne Rotation. Die potentielle Energie wird hierbei in einer periodischen Kosinusfunktion mit den Tiefpunkte am: $\frac{2\pi}{n}; n \in N$ ausgedrückt:

$$V(\tau) = \sum_{i} \frac{V_{in}}{2} (1 - \cos(in\tau)), \tag{2.121}$$

τ gibt den Torsions- beziehungsweise Rotationswinkel um diese verankerte Achse wieder. Die Principal Axis Method (PAM) nutzt zur Lösung der internen Rotation ein Koordinatensystem, das dem Hauptträgheitsachsensystem entspricht. Dadurch lassen sich die Eigenfunktionen in Abhängigkeit der relativen Orientierung der beiden Koordinaten darstellen. Der Torsion-Rotation-Halmiltonian wird wie folgt berechnet:

$$\hat{H} = \hat{H}_{rot}^{(sep)} + \hat{H}_{tor} + \hat{H}_{rt}, \tag{2.122}$$

mit

$$\hat{H}_{rot}^{(sep)} = A\hat{J}_a^2 + B\hat{J}_b^2 + C\hat{J}_c^2 + \mathbf{F}(p_g\hat{J})^2 \tag{2.123}$$

$$\hat{H}_{tor} = F\hat{J}_{tor}^2 + V_{tor} \tag{2.124}$$

$$\hat{H}_{rt} = -2Fp_g\hat{J}\hat{J}_{tor}. \tag{2.125}$$

$\hat{H}_{rot}^{(sep)}$ gibt den effektiven Rotationshamiltonian und $\hat{H}_{tor}$ den effektiven Torsionshamiltonian wieder. $\hat{H}_{rt}$ repräsentiert die Kopplung zwischen den Rotations- und der Torsionseigenfunktionen. Wenn die Barriere der internen Rotation groß ist, entkoppeln sich die Rotation und die Torsion und die Gleichung 2.122 reduziert zu:

$$\hat{H} = \hat{H}_{rot}^{(sep)} + \hat{H}_{tor}. \tag{2.126}$$

p_g aus der Gleichung 2.123 und der Gleichung 2.125 gibt die Abhängigkeit zwischen dem internen Koordinatensystem und dem Trägheitsachsensystem an:

$$p_\alpha = \frac{\cos(\eta_\alpha)I_{tor}}{I_\alpha}. \tag{2.127}$$

η_α stellt den Winkel zwischen den internen Rotationsachen mit der Hauptträgheitsachsen I_α ($\alpha = a, b, c$) dar. I_{tor} beschreibt das Trägheitsmoment der reinen Torsion, aus der die reduzierten Rotationskonstanten F_{tor} bestimmt

werden. F_{tor} hängt wie folgt von F (Gleichungen 2.123, 2.124, 2.125) ab:

$$F = \frac{F_{tor}}{1 - I_{tor}} \sum_g \cos^2 \eta_\alpha / I_\alpha. \tag{2.128}$$

Im Rahmen dieser Arbeit wurde die dreifache interne Rotation ($n = 3$) untersucht. Die potentielle Energie der Torsion berechnet sich nach der Abbruch des 2. Glied:

$$V_{tor} = \frac{V_3}{2}(1 - \cos 3\tau) + \frac{V_6}{2}(1 - \cos 6\tau). \tag{2.129}$$

Diese interne Rotation weist eine C_3-Symmetrie auf, deren irreduzible Darstellung in der Tabelle 2.8 wiedergegeben wird:

C_3	E	C_3	C_3^2
A	1	1	1
E_1	1	ϵ	ϵ^*
E_2	1	ϵ^*	ϵ

Tabelle 2.8: Charaktertafel der Gruppe C_3; $\epsilon = e^{\frac{i2\pi}{3}}$; $\epsilon^* = e^{\frac{-i2\pi}{3}}$

Das Übergangsdipolmoment hängt von dem internen Rotationswinkel τ ab. Wie aus der Tabelle 2.8 ersichtlich, unterscheidet sich der Charakter des einfach entarteten A-Niveaus und des zweifach entarteten E-Niveaus bezüglich dieser Winkel τ. Aus diesem Grund findet keine Kopplung zwischen den beiden Niveaus statt und wir erhalten für das Problem der dreifach internen Rotation 2 getrennten Spektren. Die Rotation der Wellenfunktion des A-Niveaus ist periodisch in $\frac{2\pi}{3}$ und des E-Niveaus periodisch in 2π. Das Erste entspricht der Schwingung innerhalb der Potentialwälle und das Letzte der Rotation [61].

2.4 Der Trägheitsdefekt

Der Trägheitsdefekt wird definiert als:

$$\Delta I = I_c - I_a - I_b. \tag{2.130}$$

Für den schwingungslosen Zustand eines planaren Moleküls, bei dem die Beiträge der zur Molekülebene senkrechte Achse c null sind, gilt:

$$\Delta I = I_c - I_a - I_b = \sum_i m_i(a^2 + b^2) - \sum_i m_i a^2 - \sum_i m_i b^2 = 0. \tag{2.131}$$

Bei der Betrachtung der Nullpunktschwingungen erhält man aufgrund der unterschiedlichen achsenbezogenen Beträge einen endlichen Wert für den Trägheitsdefekt:

$$\Delta I = I_c - I_a - I_b \neq 0. \tag{2.132}$$

Als planare Moleküle bezeichnet man alle Moleküle mit dem Trägheitsdefekt bis etwa $\pm 0,2 u \mathring{A}^2$.

Schwingungen, elektronische Effekte und die Zentrifugalverzerrung sind Gründe für einen von Null verschiedenen Trägheitsdefekt, wobei der Schwingungsbeitrag den größten Anteil liefert. Man unterscheidet bei dem Schwingungsanteil *in-plane-* und *out-of-plane-*Schwingungen. Erstere tragen zu einem positiven, letztere zu einem negativen Beitrag zum Trägheitsdefekt bei. Für das Charakteristikum der Planarität ist sowohl die Größe als auch das Vorzeichen des Trägheitsdefektes maßgebend.

Bei gleichen Substituenten ist der Betrag des Trägheitsmomentes größer, je weiter diese Atome sich von der planaren Ebene befinden. Bei den Untersuchungen von Dioxan-Derivate wurde eine Erhöhung des Betrags im Trägheitseffekt in den angeregten Zustand im Gegensatz zu diesem im Grundzustand gefunden. Eine mögliche Begründung hierfür ist der anormere Effekt, auf dem im Kapitel 2.5 detailliert eingegangen wird.

Die Zentrifugalverzerrung wird im Kapitel 2.6 ausführlich behandelt.
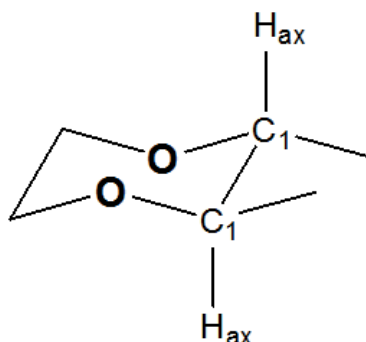
Abbildung 2.4: Definition der axiale Wasserstoff am 1-4 Dioxan-Ring [83]

2.5 Der anormere Effekt

Die Beschreibung des anormeren Effekts in der vorliegenden Arbeit ist im Wesentlichen an das Buch "The Anomeric Effect" von Juaristi et al. [84] angelehnt.

Die außergewöhnliche Bevorzugung einer sterisch ungünstigen synklinalen (*sc, gauche*) Position vor der antiperiplanen Position in einem Segment R-X-Y-R' (Abbildung 2.5) nennt man den anormeren Effekt.
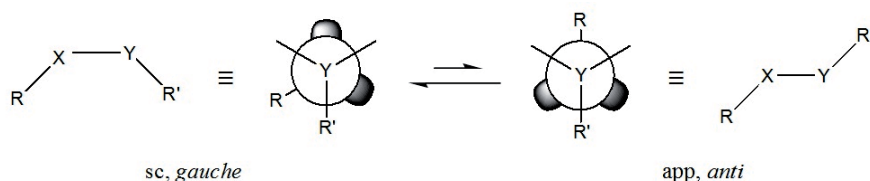
Abbildung 2.5: Definition der synklinalen und antiperiplanaren Positionen nach [86]

Hierbei steht R für Wasserstoff (H) oder eine Alkylgruppe. X besitzt mindesten ein ungebundenes Elektronenpaar. In der Abbildung 2.5 hat X zwei ungebundende Elektronenpaare. Y symbolisiert ein Element mit einer mittleren Elektronegativität wie Kohlenstoff (C), Schwefel (S). R' gibt ein Element mit einer höheren Elektronegativität als A wie Sauerstoff(O), Halogen und

Stickstoff(N) an.

2.5.1   Die Zerlegung der Gesamtenergie

Das Konformer mit dem größten Betrag der Gesamtenergie ist das stabilste Konformer. Um die Natur dieser Bevorzugung manches Konformer gegenüber anderem zu verstehen, ist eine Zerlegung der Gesamtenergie in einzelnen Komponenten notwendig. Bei Pople et al. [83][115] setzt sich die Gesamtenergie aus drei einzelnen Beträge zusammen(Gleichung 2.133).

$$E_{ges} = V_1 + V_2 + V_3 \qquad\qquad (2.133)$$

Dabei gibt V_1 die elektrostatische Energie wieder, die bei z.B. der Edward's Dipol-Dipol-Wechselwirkung entsteht. Im Abschnitt 2.5.2 wird auf diese Energie näher eingegangen.
V_2 beschreibt die stereoelektrische Energie, die unter anderem die Altorna's Zwei Elektronen- Zwei-Orbitale Stabilisierung beinhalten, auf der das Kapitel 2.5.3 gewidmet ist.
V_3 steht für die sterische Energie.

2.5.2   Das elektrostatische Model des anormeren Effekts

Die ungebundenen Elektronenpaare des Heteroatoms im Ring verursachen einen Ringdipol. Dieses steht mit der polaren Bindung am C(1) Atom in einer Wechselwirkung. Aus der Konformerenanalyse ist bekannt, dass dieses mit dem höheren Dipolmoment eine höhere elektrostatische Energie besitzt und dementsprechend instabile ist. Abbildung 2.6 ist zu entntnehmen, dass das Konformer mit X in axialer Stellung ein kleineres Dipolmoment vorweist und somit das stabilere Rotamer darstellt.
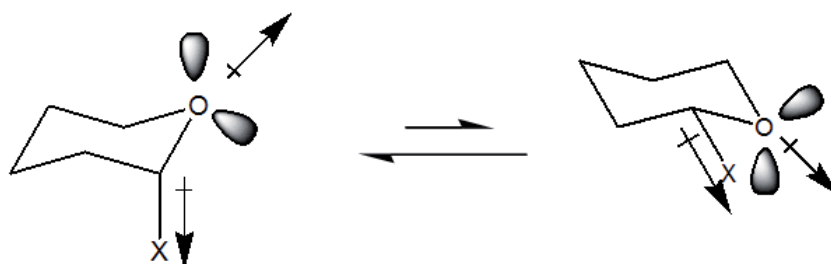
Abbildung 2.6: Dipol-Dipol-Wechselwirkung zur Erklärung des anormeren Effektes

2.5.3 Die stereoelektrische Interpretation des anormeren Effekts

Die bevorzugte *gauche* als die sterisch günstige Stellung bei der RX-CH-YR' (Abbildung 2.5), wenn X und Y elektronegative Gruppen darstellen, bezeichnet man auch als den *Gauche*-Effekt. Als Beispiel ist in der Abbildung 2.7 Wasserstoffperoxid aufgezeichnet:
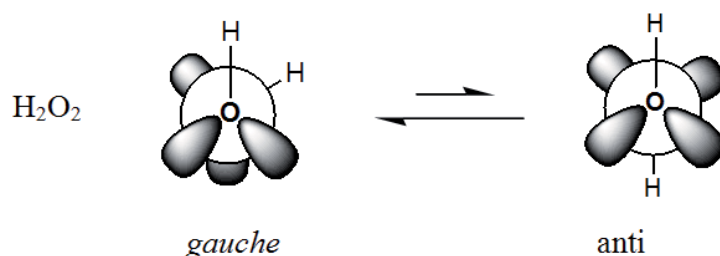
Abbildung 2.7: Wasserstoffperoxid zur Erklärung der *gauche*- und *anti*-Stellungen

Wolfe [155] [156] schlussfolgert, dass das Konformer mit einer maximalen Anzahl an *Gauche*-Wechselwirkungen am energiegünstigsten ist, wenn mindesten ein ungebundenes Elektronenpaar bzw. ein polarer Substituent am einem pyramidalen Atom hängt.

Die Ursache für die Bevorzugung einer sterisch ungünstigen Form beruht auf $\sigma \rightarrow \sigma^*$ bzw. auf $n \rightarrow \sigma^*$ Wechselwirkungen zwischen dem einem anti-

periplanaren Atom und einem Bindungsakzeptor bzw. einem ungebundenen
Elektronenpaar (Abbildung 2.8).
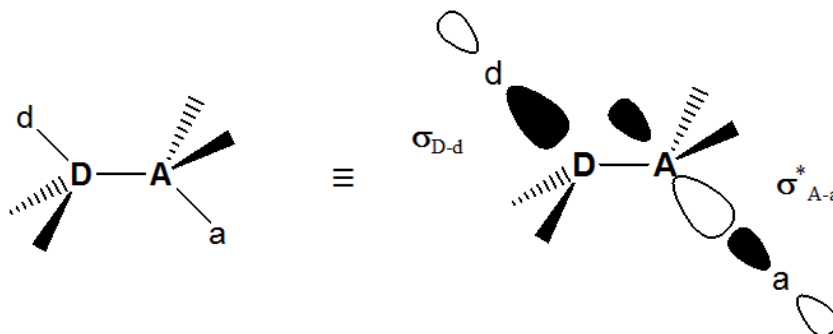
Abbildung 2.8: $\sigma \to \sigma^*$ Wechselwirkungen

Der Energiegewinn geschieht durch eine Zwei-Elektronen-Zwei-Orbitale Wech-
selwirkung (Abbildung 2.9)
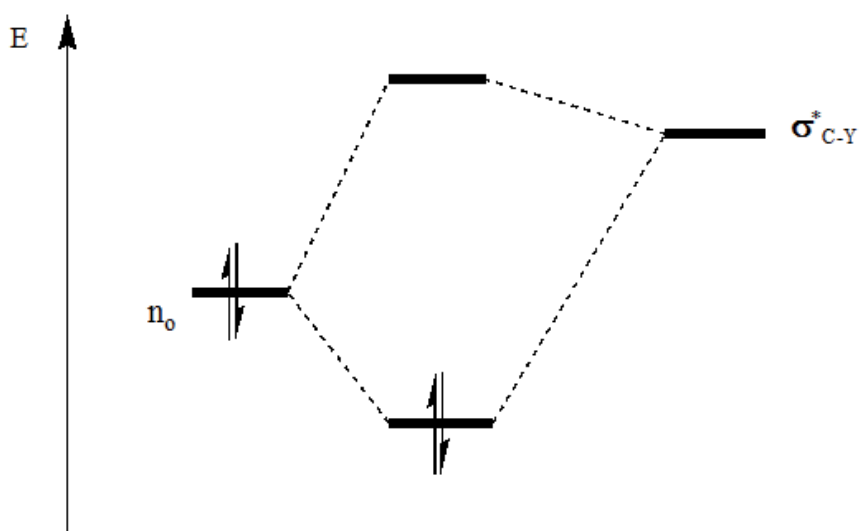
Abbildung 2.9: Stabilisierung durch die $n \to \sigma^*$ Wechselwirkungen

Je kleiner die Energiedifferenz zwischen den beiden Orbitalen ist, desto besser ist
die Überlappung und desto stärker ist die Auswirkung auf die Unterschiede
der Bindungslängen zwischen der axialen und equatorialen Stellung des Y-Atoms.

Am besten eignet sich das Carbanion-Ion daher als Elektronendonor, gefolgt von dem ungebundenen Elektronenpaar des Heteroatoms am Ring und der Sigma-Bindung [41]:

$$n_{C^-} > n_O > \sigma_{C-H} > \sigma_{C-C} > \sigma_{C-O}. \tag{2.134}$$

Die Reihe der Elektronenakzeptoren sieht daher wie folgt aus:

$$\sigma^*_{C-Cl} > \sigma^*_{C-O} > \sigma^*_{C-C} > \sigma^*_{C-H}. \tag{2.135}$$

Darüber hinaus findet man bei den Untersuchungen von 1,4-Dioxan-, Dithian-, Thioxanderivate eine verkürzte C-X Bindung in der axialen Stellung und eine verlängerte C-Y Bindung im Vergleich zu der in der equatorialen Stellung. In Abbildung 2.10 sind diese Abstände für *trans*-2,3-Dichloro-1,4- Dioxan abgebildet [121].
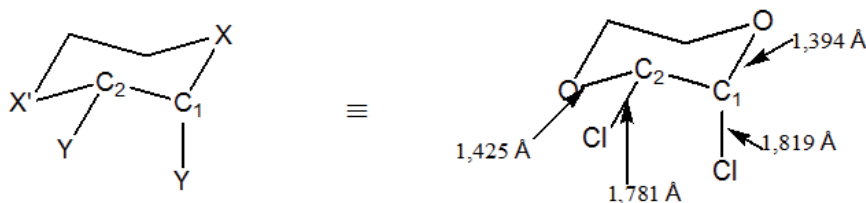
Abbildung 2.10: Die Bindungslängen am 2,3-Dichloro-1,4-Dioxan

Die Erklärung hierfür liefert die Valenzstruktur-Theorie, die das stabilste Konformer mit dem meisten Resonanzstrukturen besschreibt.
Bei einem elektronegativen Substituent findet bei einer axialen Stellung am C_1-Atom eine negative Hyperkonjugation statt (Abbildung 2.11).
 Die Verschiebung der Elektronen zu dem antibindenden Orbital im $C_1 - X$ verursacht eine Dehnung dieser C_1-X Bindung und die Verkürzung der C_1-O Bindung resultiert aus der Zunahme eines Doppelbindungscharakters im Ring.
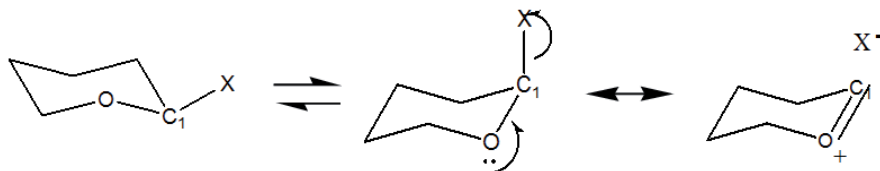
Abbildung 2.11: Valenzstruktur-Theorie zur Erklärung der unterschiedlichen Bindungslängen

2.6   Die Zentrifugalverzerrung

2.6.1   Allgemein

Auf ein rotierendes System wirkt aufgrund des Drehimpulses J immer eine Zentrifugalkraft, die zu einer Veränderung der Drehbindungen und der Drehwinkel führen. Die höheren Rotationszustände, die bei einer höheren 'Rotationstemperatur' besetzt werden, verursachen somit eine größere Veränderung der Gleichgewichtstruktur des nichtrotierenden Systems. Das Arbeiten im niedrigen Rotationstemperaturbereich unterdrückt die Besetzung der höheren Rotationszustände, die dadurch ein geringeres Ausmaß der Zentrifugalkräfte bewirkt.

Im Folgenden wird die Zentrifugalverzerrung, angelehnt an die Beschreibung nach Gordy/Cook [61] und Watson [145], als Störung wiedergegeben.

Bei einem nicht linearen N - atomigen Molekül sind $3N - 6$ Auslenkungskoordinaten möglich, die Änderungen der Bindungslänge r_x bzw. der Bindungswinkel r_α von einem Gleichgewichtzustand beschreiben.

$$R_i = r_x - r_x^e \vee R_i = r_\alpha - r_\alpha^e. \tag{2.136}$$

r_x^e oder r_α^e geben die Gleichgewichtskoordinaten des i-Atoms wieder.

Die Zentrifugalkräfte bewirken eine Veränderung der Gleichgewichtskoordinaten. Dies ruft eine elektrostatische Rückstellkraft hervor, die bei kleiner Auslenkung in guter Näherung als harmonisch angesehen wird. Aus der klassischen Mechanik berechnet sich die potenzielle Energie aus den Verschie-

bungskoordinaten:

$$V = \frac{1}{2} \sum_{ij} f_{ij} R_i R_j. \tag{2.137}$$

f_{ij} stellt die harmonischen Kraftkonstanten dar.

Die klassische Hamiltonfunktion berechnet sich wie folgt:

$$H = \frac{1}{2} \sum_{\alpha,\beta} \mu_{\alpha,\beta} J_\alpha J_\beta + V \qquad \alpha, \beta = x, y, z. \tag{2.138}$$

Der erste Term der Gleichung 2.138 beschreibt hierbei die kinetische Rotationsenergie. $\mu_{\alpha\beta} = \widetilde{I}^{-1}$ gibt die Komponenten des inversen Trägheitstensors wieder, die bei der Zentrifugalverzerrung von den Auslenkungskoordinaten abhängen. Der zweite Term gibt die potenzielle Energie wieder.

Insgesamt wirken auf das rotierende System keine Kräfte, d.h.:

$$-\frac{\partial H}{\partial R_i} = 0. \tag{2.139}$$

Die Gleichung 2.138 wandelt sich dementsprechend in Gleichung 2.140 um:

$$\frac{\partial H}{\partial R_i} = \frac{1}{2} \sum_{\alpha,\beta} \frac{\partial \mu_{\alpha\beta}}{\partial R_i} J_a J_b + \frac{\partial V}{\partial R_i} = 0. \tag{2.140}$$

Unter der Annahme einer kleineren Auslenkung werden $\partial \mu_{\alpha\beta}$, die man in einer Reihe um den Gleichgewichtwert entwickelt, nach dem ersten linearen Glied abgebrochen:

$$\mu_{\alpha\beta} = \mu_{\alpha\beta}^e + \sum_i \mu_{\alpha\beta}^i R_i + \ldots\ldots \tag{2.141}$$

mit

$$\mu_{\alpha\beta}^i = \frac{\partial \mu_{\alpha\beta}}{\partial R_i}. \tag{2.142}$$

Setzt man diese Entwicklung der Gleichung 2.141 und die Gleichung 2.137 für V in die Gleichung 2.140 ein, so erhält man:

$$\frac{1}{2} \sum_{\alpha\beta} \mu^i_{\alpha\beta} J_a J_b + \frac{1}{2} \sum_i f_{ij} R_j = 0 \qquad i = 1, 2, 3, \ldots, N - 6 \quad (2.143)$$

mit:

$$R_j = -\frac{1}{2} \sum_{i,\alpha,\beta} (f^{-1})_{ij} \mu^i_{\alpha\beta} J_\alpha J_\beta. \tag{2.144}$$

$(f^{-1})_{ij}$ sind hierbei die Elemente der inversen Kraftkonstantenmatrix. Die Gleichung 2.141, die die Reihenentwicklung für die Komponenten des Drehimpuls darstellt, lässt sich wiedergeben als:

$$\mu_{\alpha\beta} = \mu^e_{\alpha\beta} - \frac{1}{2} \sum_{i,\gamma,\delta} \mu^i_{\alpha\beta} (f^{-1})_{ij} \mu^i_{\gamma\delta} J_\gamma J_\delta. \tag{2.145}$$

Die potenzielle Energie der Gleichung 2.137 berechnet sich wie folgt:

$$V = \frac{1}{8} \sum_{i,j,\alpha,\beta,\gamma,\delta} \mu^i_{\alpha\beta} (f^{-1})_{ji} \mu_{\gamma\delta} J_\alpha J_\beta J_\gamma J_\delta. \tag{2.146}$$

Unter der Anwendung des Korrespondenzprinzips setzt sich der Hamiltonoperator zusammen aus einem Term $\hat{H}_{rr}$, der die reine Rotation beschreibt, und aus einem Term $\hat{H}_c$.für die Zentrifugalverzerrung.

$$\hat{H}_{rot} = \hat{H}_{rr} + \hat{H}_c \tag{2.147}$$

$$\hat{H}_{rr} = B_x \hat{J}_x^2 + B_y \hat{J}_y^2 + B_z \hat{J}_z^2 \tag{2.148}$$

$$\hat{H}_c = \frac{\hbar^4}{4} \sum_{i,j,\alpha,\beta,\gamma,\delta} \tau_{\alpha,\beta,\gamma,\delta} \hat{J}_\alpha \hat{J}_\beta \hat{J}_\gamma \widehat{J}_\delta \tag{2.149}$$

mit

$$\tau_{\alpha,\beta,\gamma,\delta} = \sum_{i,j} \mu^i_{\alpha\beta} (f^{-1})_{ji} \mu_{\gamma\delta} \qquad \alpha, \beta, \gamma, \delta = x, y, z. \tag{2.150}$$

Die Gleichung 2.148 behandelt die reine Rotation, in der der Hamilton-Operator nur von den drei Rotationskonstanten des Hauptträgheitsachsensystems abhängt. $\hat{H}_c$ aus der Gleichung 2.149 gibt die Energie der Zentrifugalverzerrung als Störung zu dem ungestörten System des 'starren Rotators' an und wird zu diesem addiert. Sie ist sowohl von den Verzerrungskonstanten $\tau_{\alpha,\beta,\gamma,\delta}$ als auch von den Drehimpulsoperatoren $\hat{J}_g$ abhängig. Die Störungsenergie erster Ordnung für ein bestimmtes Niveau J_τ berechnet sich nach:

$$E_d = \langle H_c \rangle = (J, \tau | H_c | J_\tau). \tag{2.151}$$

Da die Drehimpulskomponenten $\hat{J}_x$, $\hat{J}_y$, $\hat{J}_z$ nicht miteinander kommutieren, existieren für die Gleichung 2.149 $3^4 = 81$ Terme. Die Rotationswellenfunktionen des starren asymmetrischen Kreisels gehören der Vierergruppe D_2 an (Tabelle 2.3). Danach transformieren sich J_a nach B_a, J_b nach B_b und J_c nach B_c. Damit das Intergral der Gleichung 2.149 nicht verschwindet, müssen die Produkte der Drehimpulskomponenten der totalsymmetrischen Darstellung entsprechen, d.h. alle Termen mit ungerader Anzahl von Drehimpulskomponenten in der Näherung erster Ordnung verschwinden.

Von den verbleibenden 21 Termen sind viele gleich, sodass nur 9 verschiedene quadratische Verzerrungskonstanten übrig bleiben und in Tabelle 2.9 wiedergegeben werden.

Unter Anwendung der Vertauschungsregeln der Gleichungen 2.49 - 2.56 (S. 15) ergibt sich:

$$(\hat{J}_\alpha \hat{J}_\beta + \hat{J}_\beta \hat{J}_\alpha)^2 = 2(\hat{J}_\alpha^2 \hat{J}_\beta^2 + \hat{J}_\beta^2 \hat{J}_\alpha^2) + 3\hat{J}_\gamma^2 - 2\hat{J}_\alpha^2 - 2\hat{J}_\beta^2 \qquad \alpha \neq \beta \neq \gamma. \tag{2.152}$$

Für α, β, γ müssen zyklische Anordnungen gewählt werden. Dadurch kann man die letzten drei Verzerrungskonstanten der Tabelle 2.9 eliminieren und erhält die in der Tabelle 2.10 angegebenen 6 Verzerrungskonstanten.

1	τ_{xxxx}
2	τ_{yyyy}
3	τ_{zzzz}
4	$\tau_{yyzz} = \tau_{zzyy}$
5	$\tau_{zzxx} = \tau_{xxzz}$
6	$\tau_{xxyy} = \tau_{yyxx}$
7	$\tau_{yzyz} = \tau_{zyzy} = \tau_{yzzy} = \tau_{zyyz}$
8	$\tau_{xzxz} = \tau_{xzxz} = \tau_{xzzx} = \tau_{zxxz}$
9	$\tau_{xyxy} = \tau_{yxyx} = \tau_{xyyx} = \tau_{yxxy}$

Tabelle 2.9: Die 9 verschiedene Verzerrungskonstanten

1	$\tau'_{xxxx} = \tau_{xxxx}$
2	$\tau'_{yyyy} = \tau_{yyyy}$
3	$\tau'_{zzzz} = \tau_{zzzz}$
4	$\tau'_{xxzz} = \tau_{xxzz} + 2\tau_{xzxz}$
5	$\tau'_{xxyy} = \tau_{xxyy} + 2\tau_{xyxy}$
6	$\tau'_{yyzz} = \tau_{yyzz} + 2\tau_{yzyz}$

Tabelle 2.10: Die Reduzierung von 9 auf 6 verschiedene Verzerrungskonstanten durch die zyklische Anordnung

Die beobachteten Rotationskonstanten B'_x hängen von den Rotationskonstanten B_x des starren Gerüsts sowie von den Verzerrungskonstanten ab:

$$B'_x = B_x + \frac{\hbar^4}{4}(3\tau_{xyxy} - 2\tau_{xzxz} - 2\tau_{yzyz}) \qquad (2.153)$$

$$B'_y = B_y + \frac{\hbar^4}{4}(3\tau_{yzyz} - 2\tau_{xyxy} - 2\tau_{xzxz}) \qquad (2.154)$$

$$B'_z = B_z + \frac{\hbar^4}{4}(3\tau_{xzxz} - 2\tau_{xyxy} - 2\tau_{yzyz}) \qquad (2.155)$$

Für den Hamiltonian der Gleichung 2.147 erhalten wir:

$$\hat{H}_{rot} = \hat{H}_{rr} + \hat{H}_c = B'_x \hat{J}_x^2 + B'_y \hat{J}_y^2 + B'_z \hat{J}_z^2 + \frac{\hbar^4}{4} \sum_{\alpha,\beta} \tau_{\alpha\alpha\beta\beta} \hat{J}_\alpha^2 \hat{J}_\beta^2. \qquad (2.156)$$

Kivelson und Wilson [90] führten die Zentrifugalverzerrungskoeffizienten als Linearkombination der Verzerrungskonstanten ein, die in der Tabelle 2.11 wiedergegeben werden.

$$D_J = -\frac{1}{32}(3\tau_{xxxx} + 3\tau_{yyyy} + 2(\tau_{xxyy} + 2\tau_{xyxy}))$$

$$D_K = D_J - \frac{1}{4}\left(\tau_{zzzz} - (\tau_{xxzz} + 2\tau_{xzxz}) - (\tau_{yyzz} + 2\tau_{yzyz})\right)$$

$$D_{JK} = -D_J - D_K - 1/4\tau_{zzzz}$$

$$R_5 = -\frac{1}{32}(\tau_{xxxx} - \tau_{yyyy} - 2(\tau_{xxzz} + 2\tau_{xzxz}) + 2(\tau_{yyzz} + 2\tau_{yzyz}))$$

$$R_6 = \frac{1}{64}(\tau_{xxxx} + \tau_{yyyy} - 2(\tau_{xxyy} + 2\tau_{xyxy}))$$

$$\delta_J = -\frac{1}{16}(\tau_{xxxx} - \tau_{yyyy})$$

Tabelle 2.11: Verzerrungskonstanten nach Watson und Kivelson/Wilson [90]

Für den Hamiltonian der ersten Ordnung ergibt sich dann:

$$\begin{aligned}
\hat{H}_{rr} &= (B_x - 4R_6)\hat{J}_x^2 + (B_y - 4R_6)\hat{J}_y^2 + (B_z - 4R_6)\hat{J}_z^2 \\
&\quad - D_J\hat{J}^4 - D_{KJ}\hat{J}^2\hat{J}_z^2 - D_K\hat{J}_z^4 - \delta_J\left[(\hat{J}^+)^2 + (\hat{J}^-)^2\right] \qquad (2.157) \\
&\quad + R_5\left\{\hat{J}_z^2\left[(\hat{J}^+)^2 + (\hat{J}^-)^2\right] + \left[(\hat{J}^+)^2 + (\hat{J}^-)^2\right]\hat{J}_z^2\right\} \\
&\quad + R_6\left[(\hat{J}^+)^4 + (\hat{J}^-)^4\right]
\end{aligned}$$

2.6.2 Der reduzierte Hamiltonoperator

Die Standardform des Rotationshamiltonoperators nach Watson [147] wird wie folgt berechnet:

$$\hat{H}_{st} = \sum_{p,q,r=0}^{\infty} h_{pqr} \hat{J}_x^p \hat{J}_y^q \hat{J}_z^r + \hat{J}_z^p \hat{J}_y^q \hat{J}_x^r. \tag{2.158}$$

Die Hamiltonoperator muss unter der Operation der hermetischen Konjugation sowie der Zeitumkehr invariant sein:

$$\hat{H}_{st} = \hat{H}_{st}^\dagger = \widetilde{T}\hat{H}_{st}\widetilde{T}^{-1} = \left(\widetilde{T}\hat{H}_{st}\widetilde{T}^{-1}\right)^\dagger. \tag{2.159}$$

Somit müssen h_{pqr} reel und $p + q + r$ in der Gleichung 2.141 gerade Werte annehmen.

Experimentell lassen von den 6 Verzerrungskonstanten nur 5 unabhängig voneinander bestimmen lassen [61]. Um die experimentellen Daten besser anzupassen, und die unzugänglichen Parameter aus dem Hamiltonian zu entfernen, führt man den sogenannten reduzierten Hamiltonoperator (H_{rr}^{red}) ein. Durch eine Kontakttransformation werden die experimentellen Koeffizienten aus dem reduzierten Hamiltonoperator (H_{rr}^{red}) mit den Konstanten des 'originellen' Hamiltonoperator ($\hat{H}_{rr}$) verbunden:

$$H_{rr}^{red} = \hat{U}^{-1}\hat{H}_{rr}\hat{U}. \tag{2.160}$$

Hierbei ist $\hat{U}$ eine unitäre Operation (d.h. $\hat{U}^{-1} = \hat{U}^\dagger$) mit:

$$\hat{U}^{-1} = e^{i\hat{S}_3}e^{i\hat{S}_5}. \tag{2.161}$$

Die Elemente der unitären Transformation $\hat{S}$ haben eine ähnliche Form wie die Gleichung 2.158 mit $p + q + r = n$, wobei n ungerade ist [147].

$$\hat{S} = \sum s_{pqr} \hat{J}_x^p \hat{J}_y^q \hat{J}_z^r + \hat{J}_z^p \hat{J}_y^q \hat{J}_x^r. \tag{2.162}$$

s_{pqr} sind reelle Parameter, wobei die Summe der Koeffizienten $(p + q + r)$ ungerade ist. Demzufolge nehmen $\hat{S}_3$ und $\hat{S}_5$, die den Hamiltonian bis zu $\hat{J}^6$ berücksichtigen, folgende Formen an:

$$\hat{S}_3 = s_{111}(\hat{J}_x\hat{J}_y\hat{J}_z + \hat{J}_z\hat{J}_y\hat{J}_x) \tag{2.163}$$

$$\begin{aligned}\hat{S}_5 &= s_{311}\left(\hat{J}_x^3\hat{J}_y\hat{J}_z + \hat{J}_z\hat{J}_y\hat{J}_x^3\right) \\ &+ s_{131}\left(\hat{J}_x\hat{J}_y^3\hat{J}_z + \hat{J}_z\hat{J}_y^3\hat{J}_x\right) + s_{113}\left(\hat{J}_x\hat{J}_y\hat{J}_z^3 + \hat{J}_z^3\hat{J}_y\hat{J}_x\right).\end{aligned} \tag{2.164}$$

Wir erhalten also folgende Form für den Hamiltonian:

$$\hat{U}^{-1}\hat{H}_{rr}\hat{U} = \widetilde{\hat{H}}_{rr} + \widetilde{\hat{H}}_c^{(4)} + \widetilde{\hat{H}}_c^{(6)} \tag{2.165}$$

mit:

$$\widetilde{\hat{H}}_{rr} = \hat{H}_{rr} \tag{2.166}$$

$$\widetilde{\hat{H}}^{(4)} = \hat{H}_c^{(4)} + i\left[\hat{H}_{rr}, S_3\right] \tag{2.167}$$

$$\widetilde{\hat{H}}_c^{(6)} = \hat{H}_d^6 + i\left[\hat{H}_{rr}, S_5\right] + i\left[\hat{H}_c^{(4)}, S_3\right] - \frac{1}{2}\left[[\hat{H}_{rr}, S_3], S_3\right]. \tag{2.168}$$

Betrachten wir nur den vierten Term $\hat{U}^{-1} = e^{i\hat{S}_3}$ und kürzen $T_{\alpha\alpha} = \tau_{\alpha\alpha\alpha\alpha}$ und $T_{\alpha\beta} = \tau_{\alpha\alpha\beta\beta}$, ergeben sich für den Hamiltonoperator nach der van-Vleck-Transformation [141] folgende Gleichungen:

$$\widetilde{\hat{H}} = \widetilde{B}_x\hat{J}_x^2 + \widetilde{B}_y\hat{J}_y^2 + \widetilde{B}_z\hat{J}_z^2 + \sum_{\alpha,\beta}\widetilde{T}_{\alpha\beta}\hat{J}_y^2 \tag{2.169}$$

$$
\begin{aligned}
\widetilde{H}_{rr} + \widetilde{H}_c^{(4)} = \ & (\widetilde{B}_x - 4\widetilde{R}_6)\hat{J}_x^2 + (\widetilde{B}_y - 4\widetilde{R}_6)\hat{J}_y^2 + (\widetilde{B}_z - 4\widetilde{R}_6)\hat{J}_z^2 \\
& -\widetilde{D}_J \hat{J}^4 - \widetilde{D}_{JK} \hat{J}^2 \hat{J}_z^2 - \widetilde{D}_K \hat{J}_z^4 \\
& -\widetilde{\delta}_J \left[(\hat{J}^+)^2 + (\hat{J}^-)^2 \right] \\
& +\widetilde{R}_5 \left\{ \hat{J}_z^2 \left[(\hat{J}^+)^2 + (\hat{J}^-)^2 \right] + \left[(\hat{J}^+)^2 + (\hat{J}^-)^2 \right] \hat{J}_z^2 \right\} \\
& +\widetilde{R}_6 \left[(\hat{J}^+)^4 + (\hat{J}^-)^4 \right].
\end{aligned}
\tag{2.170}
$$

Die Koeffizienten sind wie folgt definiert:

$$
\widetilde{B}_x = B_x + 4(B_z - B_y)s_{111}
\tag{2.171}
$$

$$
\widetilde{B}_y = B_y + 4(B_x - B_z)s_{111}
\tag{2.172}
$$

$$
\widetilde{B}_z = B_z + 4(B_y - B_x)s_{111}
\tag{2.173}
$$

$$
\widetilde{D}_J = D_J + 1/2(B_x - B_y)s_{111}
\tag{2.174}
$$

$$
\widetilde{D}_{JK} = D_{JK} - 3(B_x - B_y)s_{111}
\tag{2.175}
$$

$$
\widetilde{D}_K = D_K + \frac{5}{2}(B_x - B_y)s_{111}
\tag{2.176}
$$

$$
\widetilde{\delta}_J = \delta_J
\tag{2.177}
$$

$$
\widetilde{R}_5 = R_5 + \frac{1}{2}(B_x + B_y - 2B_z)s_{111}
\tag{2.178}
$$

$$
\widetilde{R}_6 = R_6 + \frac{1}{4}(B_x - B_y)s111.
\tag{2.179}
$$

Die effektiven Rotationskonstanten lauten:

$$
(\widetilde{B}_x - 4\widetilde{R}_6), \ (\widetilde{B}_y - 4\widetilde{R}_6), \ (\widetilde{B}_z - 4\widetilde{R}_6)
\tag{2.180}
$$

2.6.2.1 Die A-Reduktion

Watson [145] [61] setzt für $\widetilde{R}_6 = 0$ und eliminiert damit alle $(K/K + 4)$ Matrixelemente von $\widetilde{H}$. Unter dieser Voraussetzung berechnet sich s_{111} nach

der Gleichung 2.159 (Seite 46):

$$s = -\frac{4R_6}{B_x - B_y}. \tag{2.181}$$

Die Verzerrungskoeffizienten des vierten Terms der A-Reduktion sind definiert als:

$$\Delta_J = \widetilde{D}_J = D_J - 2R_6 \tag{2.182}$$

$$\Delta_{JK} = \widetilde{D}_{JK} = D_{JK} + 12R_6 \tag{2.183}$$

$$\Delta_K = \widetilde{D}_K = D_K - 10R_6 \tag{2.184}$$

$$\delta_J = \widetilde{\delta}_J \tag{2.185}$$

$$\delta_K = -2\widetilde{R}_5 = -2R_5 - \frac{4(2B_z - B_x - B_y)R_6}{B_x - B_y} \tag{2.186}$$

Die Hamiltonian der Gleichung 2.159 verändert sich dann in der A-reduzierten Form folgendermaßen:

$$
\begin{aligned}
H_{rr}^A \quad & = \widetilde{B}_x^{(A)}\hat{J}_x^2 + \widetilde{B}_y^{(A)}\hat{J}_y^2 + \widetilde{B}_z^{(A)}\hat{J}_z^4 - \Delta_J\hat{J}^4 - \Delta_{JK}\hat{J}^2\hat{J}_z^2 - \Delta_K\hat{J}_z^4 \quad (2.187) \\
& -\delta_J\left[(\hat{J}^+)^2 + (\hat{J}^-)^2\right] + \delta_K\left\{\hat{J}_z^2\left[(\hat{J}^+)^2 + (\hat{J}^-)^2\right] + \left[(\hat{J}^+)^2 + (\hat{J}^-)^2\right]\hat{J}_z^2\right\}.
\end{aligned}
$$

2.6.2.2 Die S-Reduktion

Die A-Reduktion kann bei allen nahezu symmetrischen Molekülen zu Problemen führen. In diesen Fällen sind $B_x \approx B_y$ und s_{111} geht entsprechend der Gleichung 2.181 gegen unendlich. Dabei kommt es bei numerischen Computerrechnungen zu Schwierigkeiten. Für diese Moleküle eignet sich die S-Reduzierung von Winnenwisser 2.153, bei der $\widetilde{R}_5 = 0$ gesetzt wird. Dabei rechnet sich dann s_{111} gemäß der Gleichung 2.169:

$$s_{111} = \frac{2R_5}{2B_z - B_x - B_y}. \tag{2.188}$$

Durch die Einführung von σ ergibt sich:

$$\sigma = \frac{2B_z - B_x - B_y}{B_x - B_y}. \tag{2.189}$$

Wir erhalten ähnlich der Gleichungen 2.182 - 2.186 für die S-Reduktion folgende Verzerrungsparameter:

$$\widetilde{D}_J = D_J + \frac{R_5}{\sigma} \tag{2.190}$$

$$\widetilde{D}_{JK} = D_{JK} - \frac{6R_5}{\sigma} \tag{2.191}$$

$$\widetilde{D}_K = D_K + \frac{5R_5}{\sigma} \tag{2.192}$$

$$d_1 = -\delta_J = -\widetilde{\delta}_J \tag{2.193}$$

$$d_2 = \widetilde{R}_6 = R_6 + \frac{R_5}{2\sigma}. \tag{2.194}$$

Für die reduzierten Hamiltonian der S-Reduktion ergibt sich dann:

$$
\begin{aligned}
H_{rr}^{(S)}) \;&= \widetilde{B}_x^{(S)} \hat{J}_x^2 + \widetilde{B}_y^{(S)} \hat{J}_y^2 + \widetilde{B}_z^{(S)} \hat{J}_z^4 - \Delta_J \hat{J}^4 - \Delta_{JK} \hat{J}^2 \hat{J}_z^2 - \Delta_K \hat{J}_z^4 \\
&\quad - d_1 \left[(\hat{J}^+)^2 + (\hat{J}^-)^2 \right] + d_2 \left[(\hat{J}^+)^4 + (\hat{J}^-)^4 \right],
\end{aligned} \tag{2.195}
$$

mit den effizienten Rotationskonstanten der Gleichung 2.168:

$$\widetilde{B}_x^{(S)} = \widetilde{B}_x - 4\widetilde{R}_6 = B_x + \left(4 + \frac{2}{\sigma} \right) R_5 - 4R_6 \tag{2.196}$$

$$\widetilde{B}_y^{(S)} = \widetilde{B}_y - 4\widetilde{R}_6 = B_y + \left(4 + \frac{2}{\sigma} \right) R_5 - 4R_6 \tag{2.197}$$

$$\widetilde{B}_z^{(S)} = \widetilde{B}_z - 4\widetilde{R}_6 = B_z + \frac{rR_5}{\sigma} + 6R_6. \tag{2.198}$$

2.7 Die Linienintensitäten

Die Linienintensität der einzelnen Übergänge wird bestimmt durch den Linienstärkefaktor und den Populationsfaktor bestimmt.

2.7.1 Der Linienstärkefaktor

Der Linienstärkefaktor hängt im Allgemeinen von dem Betrag des Quadrats des Übergangsmatrixelements $R^{n,m}$ ab:

$$S^{n,m} = |R^{n,m}|^2. \tag{2.199}$$

Dieser lässt sich bei dem asymmetrischen Rotor aus dem Dipolmomentoperator μ herleiten lässt:

$$R^{n,m} = \sum_{M',M''} \left\langle mM'|\mu|mM'' \right\rangle. \tag{2.200}$$

Durch die Separation des elektronischen Anteils und des Schwingungsterms wird in folgender Gleichung der reine Rotationsterm dargestellt [92] [151]:

$$\left\langle A(J',\tau',M)|\mu_z|A(J'',\tau'',M'') \right\rangle$$

$$= 3 \sum_M \left| \sum_{K'=-J'}^{J'} \sum_{K''=-J''}^{J''} a_{K'\gamma'}^{J'M'\tau'} a_{K''\gamma''}^{J''M''\tau''} \left\langle J'K'M|\mu_z|J''K''M \right\rangle \right|^2 \tag{2.201}$$

Mit $a_{K\gamma}^{JM\tau}$ als Koeffizient der einzelnen symmetrischen Wellenfunktionen wird die asymmetrische Rotorwellenfunktion durch Linearkombination der symmetrischen Rotorwellenfunktionen gebildet. Der Dipolmomentoperator μ_z in der Gleichung 2.201 muss von dem raumfesten in das molekülfeste Koordinatensystem durch die Richtungskosinusmatrix Φ transformiert werden. Nach Anwendung der Auswahlregeln werden nur die Linienintensitäten ausgewertet, bei denen das Übergangsmatrixelement nicht Null beträgt. Bei einem asymmetrischen Rotator kann das Übergangsdipolmoment aus Komponenten mehrerer Hauptträgheitsachsen bestehen. Man unterscheidet daher a, b

oder c-Typ Banden bzw. Kombinationen aus diesen Typen. Die Intensität der einzelnen Typ-Banden verhält sich zueinander wie deren cos^2, der den Winkel zwischen den jeweiligen Hauptträgheitsachsen und dem Übergangsdipolmoment bildet.

$$S_a : S_b : S_c = cos^2\angle(\mu, a) : cos^2\angle(\mu, b) : cos^2\angle(\mu, c). \tag{2.202}$$

2.7.2 Der Populationsfaktor

Die Boltzmann-Statistik dient zur Beschreibung vom thermischen Besetzungsgrad eines bestimmten Ausgangzustandes:

$$N_i = N g_i e^{-\frac{E_i}{k_b T}}. \tag{2.203}$$

Darin ist g_i der Entartungsgrad des i-ten Niveaus, E_i die Energie des i-ten Niveaus und k_b die Boltzmannkonstante. Im Molekularstrahl kühlen die Rotationszustände ungleichmäßig ab, sodass man ein Zweitemperaturmodell zur Beschreibung des Besetzungsgrades nimmt:

$$N_i = N g_i \left(e^{-\frac{E_i}{k_b T_1}} + w e^{-\frac{E_i}{k_b T_2}} \right). \tag{2.204}$$

w beschreibt hierbei den Wichtungsfaktor der zweiten Tempertatur T_2.

2.7.3 Die Fluoreszenzintensität

Die Linienintensität der Absorption ist proportional zum Populationsfaktor $\left(1 - e^{-\frac{hv}{kT}} \right)$ und zum Linienstärkefaktor S:

$$I_{n'n''} \propto \frac{N g_{n''}}{\sum_{i''} g_{i''} e^{-\frac{E_{i''}}{kT}}} \left(1 - e^{-\frac{hv}{kT}} \right) S_{n'n''}. \tag{2.205}$$

n' steht für die Quantenzahl des angeregten Zustandes und n'' für die Quantenzahl des Grundzustandes. Bei UV-Frequenzen ist die stimulierte Emission

gleich 1, da $hv \gg kT$ und damit der Exponentialausdruck verschwindet. Zusammenfassend ergibt sich für die Intensität der einzelnen Fluoreszenzübergänge:

$$I = I_0 g_{J'' K_a'' K_c''} e^{-\frac{E_{J'' K_a'' K_c''}}{kT_{rot}}} S^{J' K_a' K_c', \ J'' K_a'' K_c''}. \tag{2.206}$$

Bei dem Zweitemperaturmodell berechnet sich die Fluoreszenzintensität wie folgt:

$$I = I_0 g_{J'' K_a'' K_c''} \left(e^{-\frac{E_{J'' K_a'' K_c''}}{kT_{rot1}}} + w \ e^{-\frac{E_{J'' K_a'' K_c''}}{kT_{rot2}}} \right) S^{J' K_a' K_c', \ J'' K_a'' K_c''}. \tag{2.207}$$

2.8 Die Linienverbreiterung

Für einen Übergang zwischen zwei Energieniveaus erwartet man eine definierte Spektrallinie. Tatsächlich jedoch kommt es aufgrund verschiedener unvermeidlicher Störungen zu einer Verbreiterung der Spektrallinien, die sowohl homogen als auch inhomogen sein können.

2.8.1 Das Linienprofil

Die homogene Verbreiterung ist für jedes Molekül im System gleich. Mathematisch lassen sich diese durch die Cauchy-Lorentz-Verbreiterung darstellen [13] [36]:

$$L(x) = \left[\frac{\left(\frac{\gamma}{2\pi}\right)}{(x - x_0)^2 + \left(\frac{\gamma}{2}\right)^2} \right] \tag{2.208}$$

x_0 stellt das Zentrum des Linienprofils dar. γ ist die Halbwertbreite:

$$\Delta\omega_{1/2} = \gamma. \tag{2.209}$$

Durch die Substitution der Kreisfrequenz durch:

$$\omega = 2\pi v, \tag{2.210}$$

und das Einsetzen in die Gleichung 2.209 ergibt sich:

$$\Delta v_{1/2} = \frac{\gamma}{2\pi}. \tag{2.211}$$

Durch die Übernahme der Gleichung 2.211 in die Gleichung 2.200 bekommt man das Lorentz-Profil in Abhängigkeit der Frequenz:

$$L(v) = \left[\frac{\Delta v_{1/2}}{4\pi^2(v - v_0)^2 + (\pi\Delta v_{1/2})^2} \right]. \tag{2.212}$$

Eine Linienverbreiterung, die nicht für alle Moleküle im System gleich ist, nennt man die inhomogene Verbreiterung. Diese lässt sich durch die Gauß-, oder auch die Normalverteilung genannt, beschreiben:

$$G(x) = \frac{1}{2\pi\sigma} e^{-\frac{1}{2}\left(\frac{x-\mu}{\sigma}\right)^2}. \tag{2.213}$$

Durch das Einsetzen der Ursprungfrequenz v_0 für den Mittelwert μ und unter der Berücksichtigung des folgenden Ausdrucks zur Berechnung der Halbwertbreite des Gaußprofils:

$$\Delta v_{1/2} = 2\sigma\sqrt{2ln2}. \tag{2.214}$$

ergibt sich für die Gleichung 2.213:

$$G(x) = \frac{2}{\Delta v_{1/2}} \sqrt{\frac{ln2}{\pi}} e^{-4ln2\left(\frac{v-v_0}{\Delta v_{1/2}}\right)^2}. \tag{2.215}$$

Meist treten mehrere Mechanismen zur Verbreiterung des Linienprofils auf. Das Gesamtprofil berechnet sich durch die Faltung der einzelnen Profilfunktionen:

$$f_{ges}(v) = f_1(v) * f_2(v) * \ldots = \int_{-\infty}^{\infty} f_1(v') * f_2(v - v') * \ldots dv'. \tag{2.216}$$

Die Überlagerung der homogenen Linienverbreiterungen ergibt wieder ein Lorenzprofil. Die resultierende Halbwertbreite berechnet sich aus der Summe der einzelnen Halbwertbreiten:

$$\Delta v_{1/2}^{(L_{ges})} = \Delta v_{1/2}^{(L_1)} + \Delta v_{1/2}^{(L_2)} + \dots \tag{2.217}$$

Aus der Überlagerung der inhomogenen Linienverbreiterungen bekommt man auch hier wieder ein Gaußprofil. Für die Gesamthalbwertsbreite ergibt sich:

$$\Delta v_{1/2}^{(G_{ges})} = \sqrt{(\Delta v_{1/2}^{G_1})^2 + (\Delta v_{1/2}^{G_2})^2 + \dots} \tag{2.218}$$

Die Faltung aus einem homogenen und einem inhomogenen Verbreiterungsprofil führt zu einem Voigtprofil[36]:

$$V(v) = G(v) * L(v) = \int_{-\infty}^{\infty} G(v') * L(v - v')dv' \tag{2.219}$$

Es gibt keine analytische Lösung für das Intergral der Gleichung 2.219. Für die hinreichende Näherung wird die Lösung als Realteil einer imaginären Fehlerfunktion $\overline{\omega}(z)$ wiedergegeben:

$$V(v) = \frac{Re[\overline{\omega}(z)]}{\sigma\sqrt{2\pi}}. \tag{2.220}$$

$$z = \frac{x + i\gamma}{\sigma\sqrt{2}} \tag{2.221}$$

Die Halbwertbreite des Voigtprofils berechnet sich in guter Näherung folgendermaßen [38]:

$$\Delta v_{1/2}^{(V)} = \frac{\Delta v_{1/2}^L}{2} + \sqrt{\frac{\left(\Delta v_{1/2}^L\right)^2}{4} + \left(\Delta v_{1/2}^{(G)}\right)^2}. \tag{2.222}$$

2.8.2   Die Verbreiterungsprofile

2.8.2.1   Die natürliche Lebensdauerverbreiterung

Die begrenzte Lebensdauer τ des angeregten Zustandes stellt die Ursache der
natürlichen Lebensdauerverbreiterung dar, die einem homogenen Lorenzprofil unterliegt.

Mechanismen, welche die begrenzte Lebensdauer verursachen, sind die Zerfallsprozesse erster Ordnung, die spontanen Emissionen, die Internal Conversion, das Intersystem Crossing oder die photochemischen Reaktionen. Die
Bestimmung der Linienbreite. wird durch die Unschärferelation hergeleitet,
wobei $\Delta t = \tau$ gleich gesetzt wird[13]:

$$\Delta E \cdot \Delta t \geq \hbar \tag{2.223}$$

$$\Delta v = \frac{\Delta E}{h} \geq \frac{1}{2\pi\tau}. \tag{2.224}$$

Die Lebensdauer zwischen zwei Niveaus infolge spontaner Emission ist gleich
dem Reziprok des Einsteinkoeffizients A_{nm}, der die Wahrscheinlichkeit der
spontanen Emission aus dem Zustand m in den Zustand n eines Moleküls
wiedergibt[36]:

$$\tau_{sp} = \frac{1}{A_{nm}} = \frac{3hc^2}{64\pi^4 v_{nm}^3 |\langle m|\mu|n\rangle|^2}. \tag{2.225}$$

Durch das Einsetzen dieser Beziehung in die Gleichung 2.224 ergibt sich die
Halbwertsbreite der Lebensdauer:

$$\Delta v_{1/2} \geq \frac{1}{2\pi\tau} = \frac{A_{nm}}{2\pi} = \frac{32\pi^3}{3hc^3} v_{im}^3 |\langle m|\mu|n\rangle|^2. \tag{2.226}$$

Bei der spontanen Emission vom Zustand m in mehrere untere Zustände i
berechnet sich die natürliche Halbwertsbreite aus der Summe der einzelnen
Halbswertsbreiten:

$$\Delta v_{1/2} \geq \frac{1}{2\pi\tau} = \frac{A_{nm}}{2\pi} = \frac{32\pi^3}{3hc^3} \sum_i v_{im}^3 |\langle m|\mu|n\rangle|^2. \tag{2.227}$$

2.8.2.2   Die Druckverbreiterung

Die homogene Linienverbreiterung der Druckverbreiterung wird sowohl durch elastische als auch unelastische Stöße verursacht. Eine detaillierte Beschreibung der Stoßmechanismen findet sich bei Townes und Schawlow [139] sowie Demtröder [36]. Für die niedrigeren Gasdrücke liefert eine einfache semiklassische Analyse ein Lorentzprofil. Die Halbwertbreite berechnet sich proportional zum Gasdruck p und zu einem Druckverbreiterungskoeffizient b, der in der Regel 10MHz/Torr beträgt:

$$\Delta v_{1/2} = bp \tag{2.228}$$

2.8.2.3   Die Dopplerverbreiterung

Die thermische Bewegung der Teilchen bewirkt, dass sich einige der Teilchen entgegen der Einfallsrichtung des Photons bewegen. Durch den optischen Doppler-Effekt verschieben sich dadurch die Photonenfrequenzen. Die Geschwindigkeit der Teilchen in der Gasphase lässt sich mit der Maxwell-Boltzmann-Verteilung darstellen:

$$\frac{n_i}{N} dv = \sqrt{\frac{m}{2\pi kT}} e^{-\frac{mv}{2kT}} dv. \tag{2.229}$$

Das berechnete Linienprofil hat die Form einer Gaußkurve:

$$\sigma = \sqrt{\frac{kT}{mc^2}} v_0. \tag{2.230}$$

Aus dieser Gleichung und der Gleichung 2.214 ergibt sich für die Halbwertsbreite der Dopplerverbreiterung:

$$\Delta v_{1/2} = \frac{v_0}{c} \sqrt{\frac{8kT ln2}{m}}. \tag{2.231}$$

2.8.2.4   Die Flugzeitverbreiterung

Beim Treffen des Laserstahls senkrecht zu einem Molekularstrahl mit einer homogenen Geschwindigkeitsverteilung bestimmen wir die Zeit zwischen der Wechselwirkung von den Molekülen und dem Laserstrahl:

$$\tau = \frac{d}{\text{v}}. \tag{2.232}$$

Die endliche Interaktionszeit zwischen dem Molekül und dem Laserstahl bewirkt eine Verbreiterung der Frequenz für den Übergang. Im Einmodenlaser ist die Feldstärke E nicht konstant, sondern hängt vom Abstand r um die Strahlenachse ab. Diese Abhängigkeit lässt sich durch eine Gaußverteilung beschreiben[32]:

$$E(r,t) = E_0 e^{-\left(\frac{2r}{d}\right)^2} \cos(2\pi vt). \tag{2.233}$$

Die Halbwertbreite berechnet sich somit:

$$\Delta v_{(}1/2) = \frac{\sqrt{8ln2}}{\pi}\frac{\text{v}}{d} \approx 0,75\frac{\text{v}}{d}. \tag{2.234}$$

d beschreibt hierbei die Dicke das Laserstrahls und v die Geschwindigkeit des Molekularstrahls. Bei der genaueren Berechnung der Flugzeitverbreiterung berücksichtigt man die Maxwellsche Geschwindigkeitsverteilung mit:

$$N(\text{v}) = Cv^2 e^{-\frac{m\text{v}^2}{2kT}}. \tag{2.235}$$

2.8.2.5   Die Laserlinienverbreiterung

Durch Schwingungen und thermische Ausdehnung innerhalb des Resonators eines Einmodenlaser kommt es zur Veränderung der Resonatorlängen. Diese verursachen eine Verbreiterung der Laserlinie. Näherungsweise lässt sich die Laserlinienverbreiterung mit dem Gaußprofil wiedergeben. Die Halbwerts-

breite berechnet sich gemäß der Gleichung 2.214:

$$\Delta v_{1/2} = 2\sigma \sqrt{2ln2}. \tag{2.236}$$

Kapitel 3

Der experimentelle Aufbau

Die rotationsaufgelöste elektronische Anregung von Molekülen und Clustern erfordert einen Laser mit einer kleineren Linienbreite als die zu erwartende Linienbreite der Rotationsübergänge der rovibronischen Bande. Außerdem sollten die Moleküle möglichst unter stoßfreien Bedingungen gemessen werden. Durch eine isotropische Expansion ins Vakuum werden die Moleküle bezogen auf ihre Rotations- und Schwingungstemperatur, auf wenige Kelvin abgekühlt, wodurch sich die Spektren deutlich vereinfachen (da nur wenige Rotationsniveaus besetzt sind).

Die Gesamtapparatur ist in folgender Abbildung 3.1 dargestellt. Sie kann in drei Hauptbestandteile aufgeteilt werden:

1. das Lasersystem,

2. die Molekularstrahlapparatur,

3. die Steuerung und Datenerfassung,

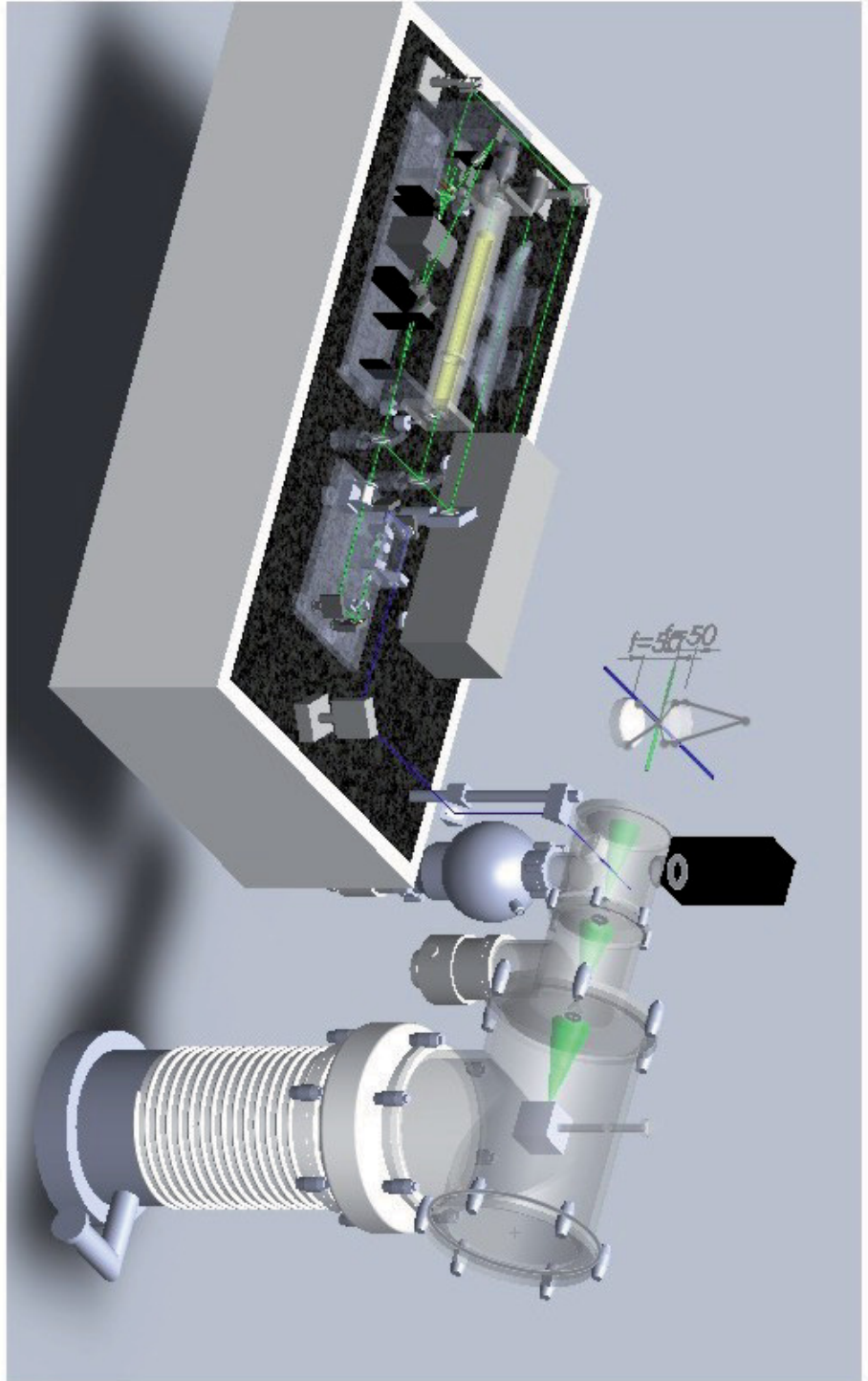die im nächsten Kapitel nacheinander besprochen werden.

Abbildung 3.1: Gesamtaufbau der HRLIF-Apparatur

3.1 Das Laserlabor

Der obere Teil der Abbildung 3.1 zeigt den Aufbau für die Realisierung von schmalbandiger, durchstimmbarer UV-Strahlung, welche die zu untersuchende Substanz elektronisch anregt. Ein frequenzverdoppelter Nd-YAG Laser (Millenia X) pumpt in den Ringfarbstofflaser, dessen emittiertes Laserlicht durch einen Frequenzverdoppler in UV-Licht umgewandelt wird. Für die Bestimmung der relativen Frequenz dient ein Fabry-Perot-Interferometer (FPI). Den absoluten Wert des Spektralbereiches ermittelt man aus der gleichzeitigen Aufnahme des Iodspektrums. Die folgenden Abschnitte widmen sich diesen optischen Elementen.

3.1.1 Der Lasertisch

Ein optischer Tisch, der zur Dämmung von Schwingungen, insbesondere der Vibrationen der Pumpen und der Gebäudeschwingungen dient, wurde in einem angrenzenden Raum, von der Molekularstrahlapparatur getrennt, aufgebaut. Die Tischplatte, auf der sich der Pump- und der Ringlaser, der Frequenzverdoppler, das Referenzetalon und die Iodzelle sowie ein Monochromator zur ungefähren Feststellung der Wellenlänge befinden, besteht aus einer etwa $800kg$ schweren, $2,4m \times 1,1m \times 0,1m$ großen Granitplatte, die zur Minimierung ihrer Eigenschwingungen in ein mehrere Zentimeter dickes Sandbad eingebettet ist. Unterhalb der Sandwanne liegt der $1m$ hohe Styroporblock, der zur Dämpfung von niederfrequenten Gebäudeschwingungen dient. Damit es beim Auslaufen von Lösungsmitteln nicht zur einem seitlichen Abkippen der Sandwanne durch Auflösung des Styropors kommt, sind an der Unterseite der Sandwanne vier Stürze montiert, die bis $5cm$ über dem Boden in das Styropor hinein reichen. Damit wird die Übertragung der Gebäudeschwingungen über diese Stützen an die optischen Elemente verhindert. Zur Minimierung von Staub aus der Umgebungsluft dient ein dreistufiger Strömungsfilter, der die gefilterte Luft über den Tischraum einleitet. Zum zusätzlichen Schutz vor Staub dienen zehn Acrylglasscheiben, die die Seitenflächen vom Laser-

tisch abschließen.

3.1.2   Das Lasersystem

Zum Pumpen des Farbstofflasers wird ein frequenzverdoppelter Nd-YAG Laser verwendet, der bei $532nm$ emittiert. Durch die Absorption werden die Farbstoffe in schwingungsangeregte S_1 Niveaus angeregt. Nach einiger ps relaxieren die Farbstoffmoleküle durch Stöße mit Lösungsmittelteilchen in das niedrigste Schwingungsniveau des S_1-Zustandes. Von hier aus können mehrere Übergänge mit unterschiedlicher Wahrscheinlichkeit stattfinden (Abbildung 3.2. Eine der Möglichkeit ist die Fluoreszenz, bei der unter Ausstrahlung eines Photons das angeregte Molekül in den schwingungsangeregten elektronischen Grundzustand übergeht. Mit einer viel geringeren Wahrscheinlichkeit findet der Übergang zu einem Triplettzustand statt, wobei sich die Anzahl der Moleküle, die für den Laserprozess zur Verfügung stehen, vermindert. Um diesen unerwünschten Triplettübergang zu unterdrücken wird das Millenium X - Laserlicht mit einem rasch strömenden laminaren Strahl einer Lösung des Farbstoffes in Ethylenglykol gekreuzt. Bei der Messung in der vorliegenden Arbeit wurden Rhodamin 6G bzw. Rhodamin 110 als Farbstoff eingesetzt. Durch Kollisionen in der Lösung der Lösung findet eine Verbreiterung sowohl der Absorptionsbande als auch der Emissionsbande statt und ermöglichen damit das kontinuierliche Durchstimmen der Wellenlänge über einen weiten Bereich. Ein Ringresonator mit einer Doppel- Z- Anordnung verhindert die Ausbildung eines Multimodenbetriebs und erlaubt dabei eine schmalbandige Abstimmbarkeit des Lasers [31]. Abbildung 3.3 gibt den Aufbau des Ringresonators mit seinen optischen Komponenten wieder. Die gewünschte Umlaufrichtung ($M4 \rightarrow M5 \rightarrow M1 \rightarrow M3 \rightarrow M4$) gegenüber der 'Rückwärtswelle' wird durch die optische Diode unter Nutzung des magnetptischen Faraday-Effekts realisiert. Zur Selektion einer Wellenlänge dienen drei aufeinander folgende Filter mit unterschiedlichen Finesse F^* und mit unterschiedlichen freien Spektralbereichen (Abbildung 3.4). Die Selektion einer Resonatormode durch diese drei Filter erfolgt durch konstruktive Interferenz zwischen einem
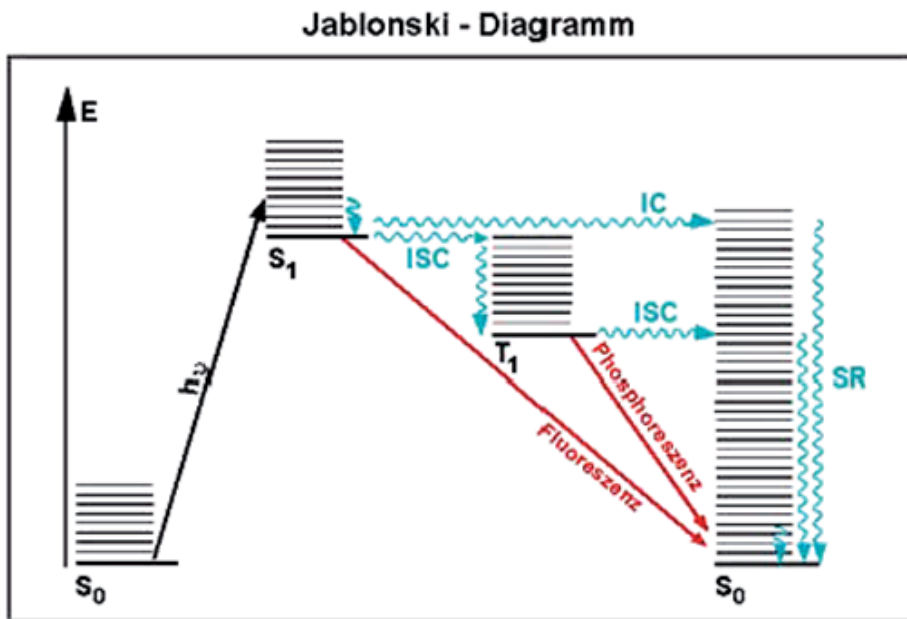
Abbildung 3.2: Jablonski-Diagramm photochemischer Prozesse [137]

Strahl und einem anderen mit um n ganzzahligen Vielfachen verschobenen Phasen. Jedes n kennzeichnet eine Transmissionsordnung; den Abstand zwischen zwei benachbarten Ordnungen nennt man den freien Spektralbereich (free spectral range, FSR). Die Bandbreite eines Transmissionspeaks heißt die volle Halbwertbreite (full width at half maximum, $FWHM$). Die Finesse F^* berechnet sich aus dem Verhältnis zwischen dem Spektralbereich und der Halbwertbreite:

$$F^* = \frac{FRS}{FWHM}. \tag{3.1}$$

Das optische Element mit der kleinsten Finesse und dem größten freien Spektralbereich ist ein doppelbrechendes Filter (birefringent filter), das aus drei doppelbrechenden Platten besteht und einer Halbwertbreite von $2THz$ hat. Die Auswahl einer einzigen longitudinalen Mode geschieht durch die Kombination zweier Etalons, einem dünnen Etalon mit $225GHz$ FSR und $200GHz$ $FWHM$ und einem dicken Etalon, in dem ein fein durchstimmbarer Piezokristall integriert ist. Dadurch können Moden mit einem freien Spektralbe-

reich von $10GHz$ und einer Halbwertbreite von unter $0,5MHz$ durchgescannt werden.

Drei Gründe, die zur Verbreiterung der Laserlinien führen, sind:

1. die Änderung des Brechungsindexes der Umgebungsluft aufgrund der Temperaturschwankungen und der lokalen Druckänderungen,

2. der Sprung in der Resonatorlänge wegen der kurzzeitige Vibration des Laseraufbaus,

3. die Fluktuationen des Farbstoffstrahls.

Ein Regelkreis korrigiert die kurzzeitigen Schwankungen, indem es die aktuelle Wellenlänge mit einem stabilen Referenzresonator vergleicht, daraus ein Regelsignal ermittelt und die Länge des Resonators mit Hilfe eines Piezozylinders am Faltungsspiegel $M3$ variiert. Ferner wird das Regelsignal verwendet, um die Brewsterplatte im Resonator zu kippen, um für die Korrektur der langzeitigen Schwankungen zu sorgen.
 Das Scannen der Mode geschieht in zwei Schritten:

1. Durch Rotation der planparallelen Brewsterplatte vergrößert sich der optische Weg des Laserlichts im Resonator.

2. Der Piezozylinder regelt das Transmissionsmaximum des dicken Etalons auf der aktuellen Lasermode

3.1.3   Das Bestimmen der relativen und der absoluten Frequenz

Der relative Frequenzabstand zwischen dem rovibronischen Übergang und dem elektronischen oder vibronischen Ursprung müssen bei der Berechnung der Rotationskonstante genau ermittelbar sein. Hierzu dient die Aufnahme des Transmissionsspektrums eines quasiplanaren konfokalen Fabry-Perot-Interferometers, das nur für ganzzahlige Vielfache einer charakteristischen
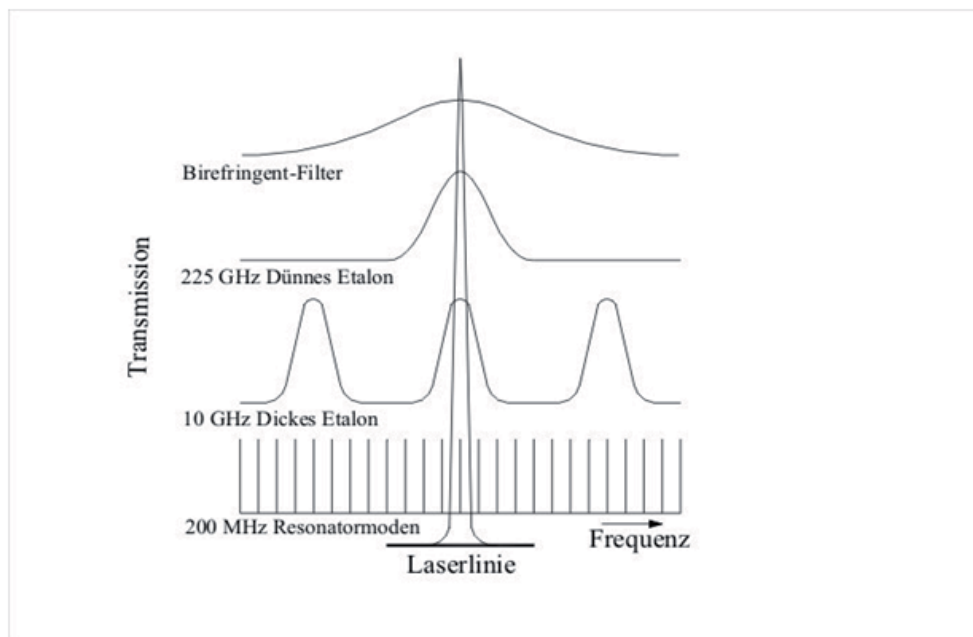
Abbildung 3.3: Modeselektion im Ringfarbstofflaser [31]

Wellenlänge durchlässig ist. Der freie Spektralbereich, der aus exakt gemessenen Mikrowellenübergängen von Indol ermittelt wurde, beträgt 149,9434(56) MHz. Die Bestimmung der absoluten Frequenz geschieht auf zwei Wegen. Zum einen wird ein Teil des Laserstrahls in einen Monochromator zur groben Einstellung der Wellenlänge eingeleitet. Hierbei kann die Mode auf ca. 10 Wellenzahlen bestimmt werden. Zum anderen geschieht die exakte Bestimmung der absoluten Frequenz durch die gleichzeitige Aufnahme eines Jodabsorptionsspektrums und den anschließenden Vergleich mit dem Jodatlas [51] [52]. Dabei wird ein Teil des Laserlichts durch die Jodzelle, die zur Verminderung der Druckverbreiterung der Linien auf unter 1 mbar Restgas evakuiert ist, geleitet und das transmittierte Licht mit einer Photodiode detektiert.
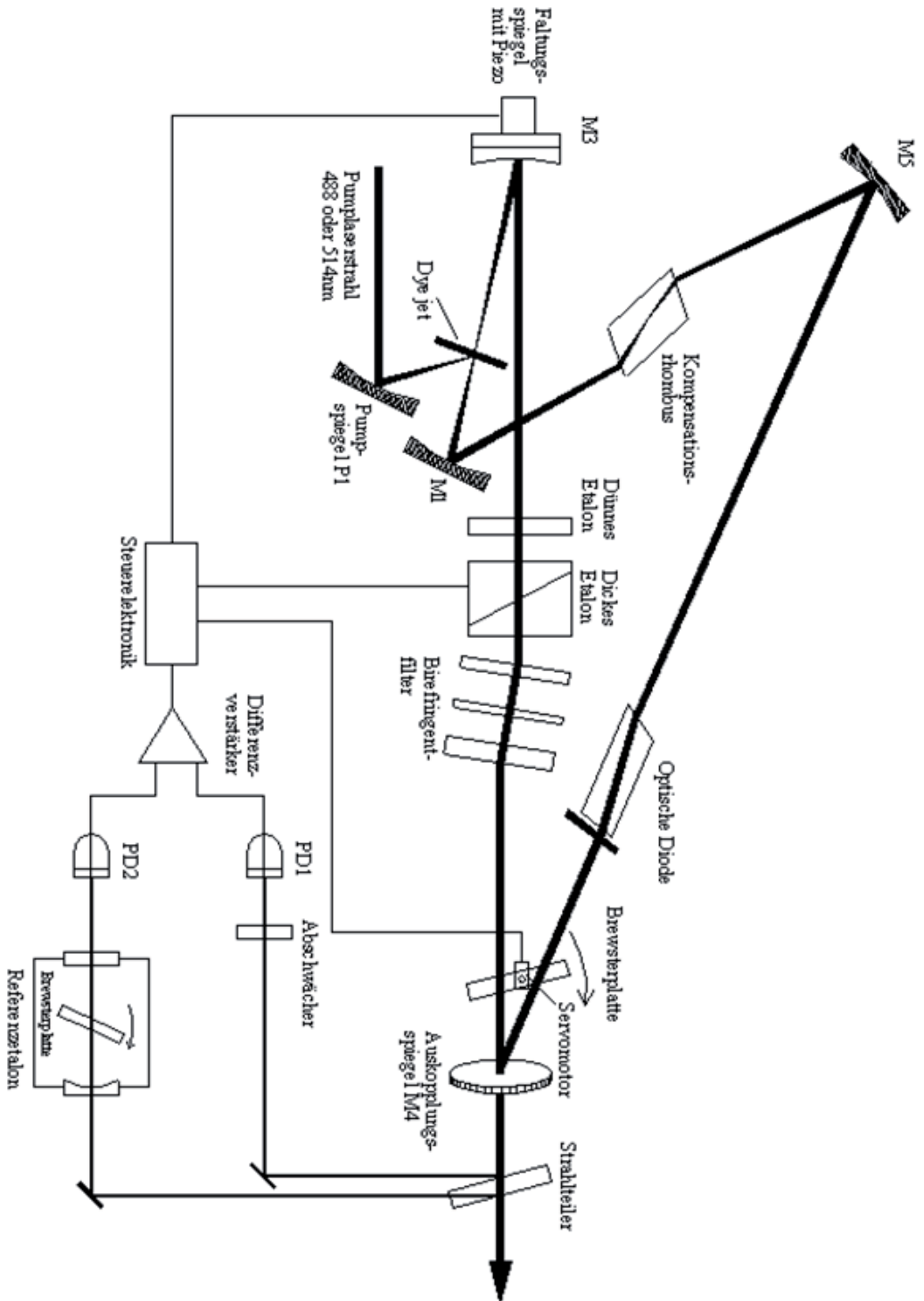
Abbildung 3.4: Schematischer Aufbau des Ringfarbstofflasers [31]

3.1.4 Die Frequenzverdopplung

Licht regt beim Treffen auf eine Materie deren Elektronen zum Schwingen an. Normalerweise schwingt das Elektron mit der gleichen Frequenz wie das eingestrahlte Licht und gibt entsprechende Photonen mit der gleichen Energie wieder ab. Bei Licht mit hoher Intensität, wie es beim Laser der Fall ist, hängt die Polarisation in der Materie nicht nur vom ersten Term der Summe in Gleichung 3.2 ab, sondern setzt sich als Summe mehrerer Beträge zusammen [150]

$$P(E) = \epsilon_0 \sum_n \chi^{(n)} E^n. \tag{3.2}$$

E^n elektrische Feldstärke: $E(t) = E_0 \sin(\omega t)$
ϵ_0 Dielektrizitätskonstante des Vakuums
χ entspricht der dielektrischen Suszeptibilität n - ter Ordnung
Für die Frequenzverdopplung in nichtlinearen optischen Medien, wie zum Beispiel $LiNbO_3$, KDP und BBO, ist der Beitrag des zweiten Summanden verantwortlich:

$$P^{(2)} = \epsilon_0 \left[\chi^{(2)} E_0^2 \sin^2(\omega t) \right]. \tag{3.3}$$

Unter Anwendung des Additionstheorems:

$$\sin^2(\omega t) = \frac{1 - \cos(2x)}{2}. \tag{3.4}$$

ergibt sich die Gleichung 3.3 zu:

$$P^{(2)} = \frac{1}{2} \epsilon_0 \chi^{(2)} E_0^2 - \frac{1}{2} \epsilon_0 \chi^{(2)} E_0^2 \cos(2\omega t). \tag{3.5}$$

Durch die Anregung des Laserlichts wird sowohl die Strahlung der Grundfrequenz als auch solche mit der doppelten Frequenz 2ω erzeugt. Die Intensität der Oberwelle $I_{2\omega}$ ist dem Quadrat der Grundwelle proportional:

$$I_{2\omega} \propto I_\omega^2 = \frac{P^2}{A}. \tag{3.6}$$

Aus der Gleichung 3.5 lässt sich erkennen, dass das Fokussieren des Laserlichts auf eine kleinere Fläche A und die hohe Eingangsleistung P die Leistung der Welle mit der doppelten Frequenz im Output erhöht.

3.1.5   Der Verdopplungsresonator

Das Modell 'Wavetrain' [150], das nach dem 'Delta Concept' als Ringresonator arbeitet, verdoppelt die Frequenz des aus dem Farbstofflaser austretenden Lichtes. Abbildung 3.5 zeigt schematisch den Aufbau des Gerätes. Das senkrecht zum Lasertisch polarisierte Licht wird zuerst durch ein 'Fresnel Rhomb' (FR) um 90 ° gedreht. Die Phasenmodulatoreinheit (PMA), welche sich aus 2 KDP - Kristallen zusammensetzt, wird durch eine Elektronik geregelt, in dem die momentane Modulation durch eine schnelle Photodiode gemessen und die auftretenden Fehler korrigiert werden. Die beiden Linsen $L1$ und $L2$ sowie die beiden Spiegel $BM1$ und $BM2$ fokussieren das modulierte Laserlicht genau in den Verdopplungskristall X, der sich in dem deltaförmigen Ringresonator befindet. Ein piezogelagertes Prisma PZT, dessen Oberflächen genau im Brewsterwinkel zum ein- und ausfallenden Laserstrahl stehen, zwei Spiegel (Einkoppelspiegel $M1$ und Auskoppelspiegel $M2$) und der Verdopplungskristall (BBO) bilden die Einheiten des Resonators. Durch das spezielle Coating der Auskoppelspiegel des Resonators kann nur der frequenzverdoppelte Teil des Laserlichts austreten und wird in die Molekularstrahlapparatur eingeleitet.
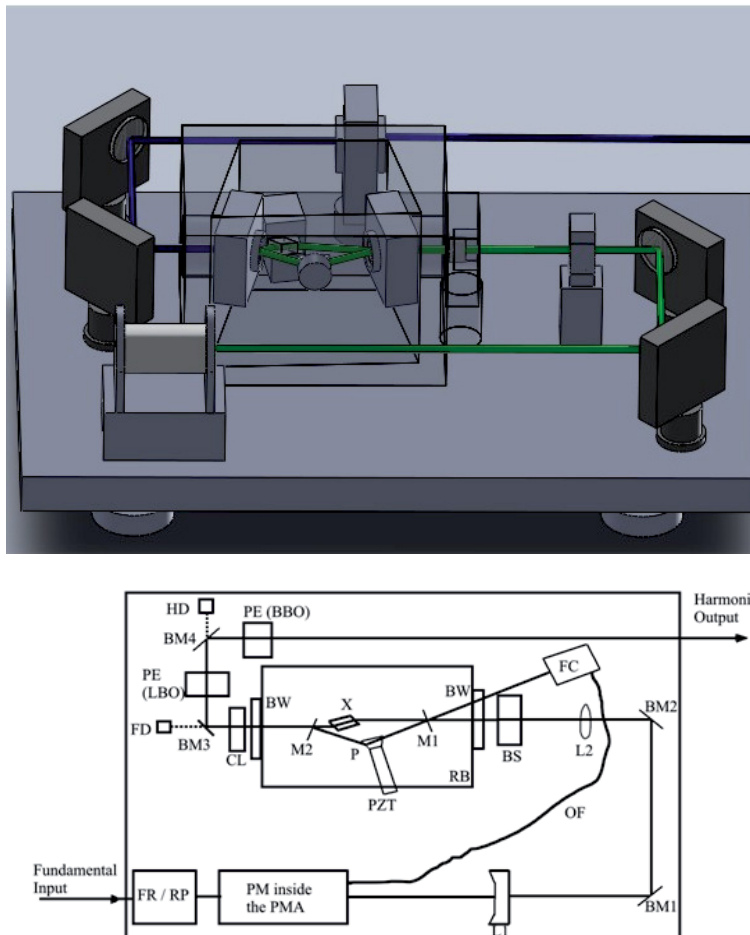
Abbildung 3.5: Der schematische Aufbau des Frequenzverdopplers [150]

3.2 Die Molekularstrahlapparatur

Die Molekularstrahlapparatur (Abbildung 3.6) befindet sich in einem von dem Laserlabor gesonderten Raum, damit die Vibrationen der Vakuumpumpen nicht auf den optischen Aufbau übertragen werden.

Die Molekularstrahltechnik bietet gegenüber anderen Probezufuhren folgende Vorteile:

1. Die Probenmoleküle befinden sich unter fast stoßfreier Bedingung, was

die Bestimmung der molekularen Parameter auch ohne Kenntnis des Wechselwirkungspotenzials mit den Umgebungsmolekülen ermöglicht.

2. Es werden sehr niedrige Translations- und Rotationstemperaturen erreicht und vereinfachen dadurch die zu untersuchenden Spektren.

3. Außerdem bilden sich unter diesen Bedingungen Addukte mit geringer Bindungsenergie, wie zum Beispiel schwach gebundene Cluster, die so untersucht werden können.
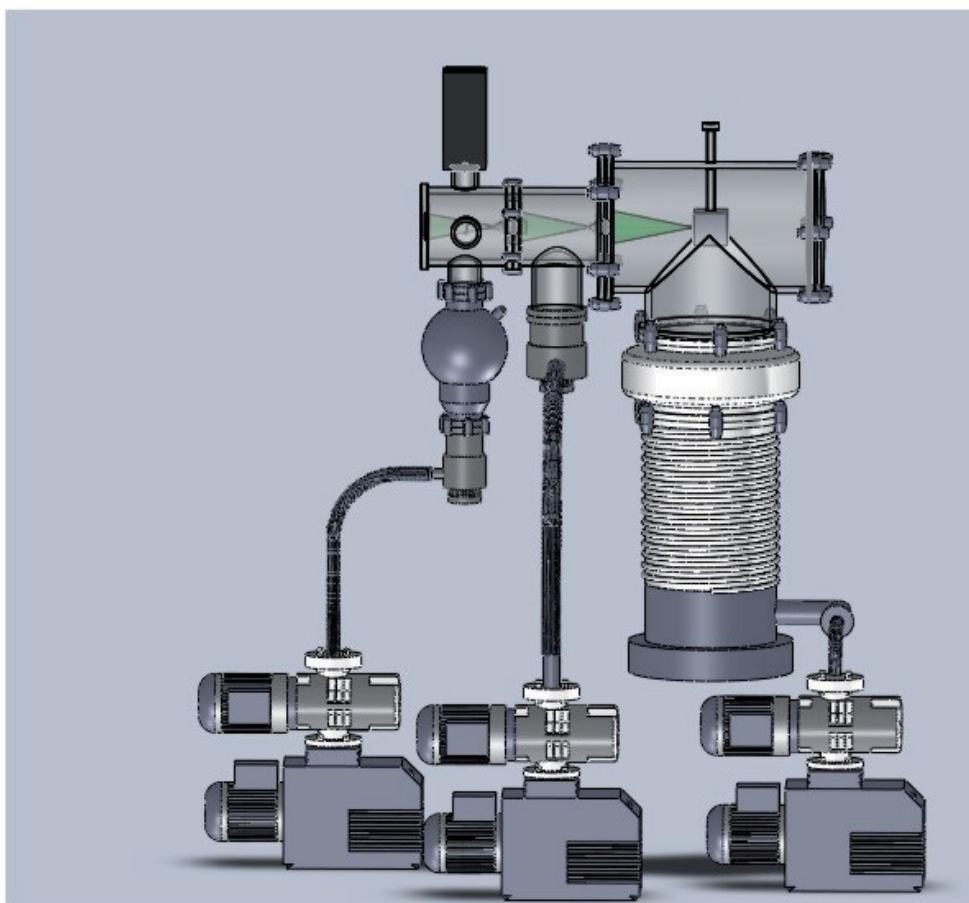
Abbildung 3.6: Schematische Übersicht des Aufbaus der Molekularstrahlapparatur

3.2.1 Der Molekularstrahl
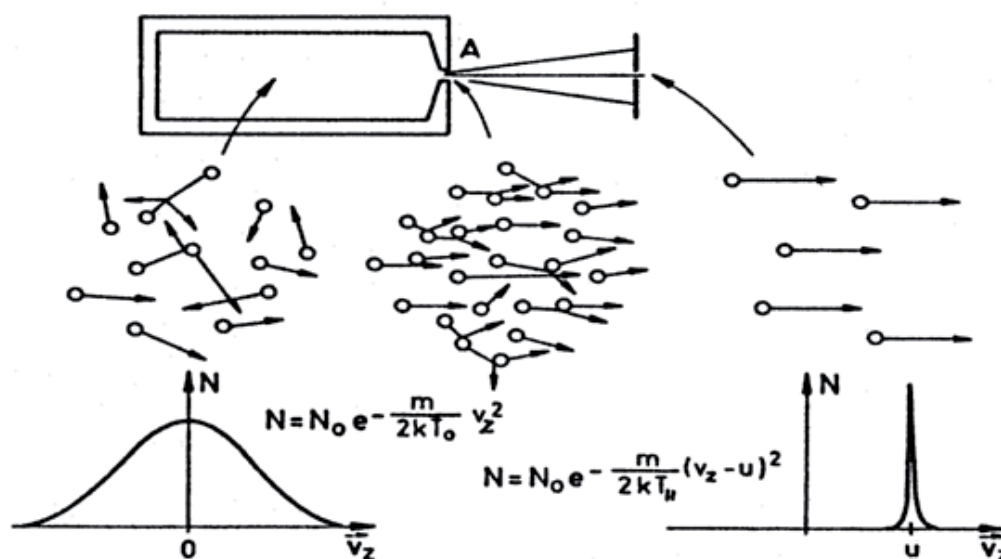
Abbildung 3.7: Geschwindigkeitsverteilungen für den effusiven Strahl (links) und den Überschalldüsenstrahl (rechts)[7]

Jede Expansion durch eine Düse ins Vakuum wird Düsenstrahl (*jet*) genannt. Wenn bei der Expansion ins Vakuum die mittlere freie Weglänge v_0 für Stöße zwischen den Molekülen viel kleiner als der Lochdurchmesser d ist, bildet sich ein Überschalldüsenstrahl (*supersonic jet*). Unter dieser Bedingung finden sehr viele Stöße bei der Molekularstrahlausdehnung statt. Die schnellen Moleküle übertragen einen Teil ihrer kinetischen Energie auf die langsameren Teilchen, was zu einer Verengerung der Geschwindigkeitsverteilung führt. In Abbildung 3.7 ist der Unterschied zu einem effusiven Strahl $\lambda_0 \gg d$, welcher der Maxwell - Boltzmann - Verteilung unterliegt, wiedergegeben. Bei dem Überschalldüsenstrahl verschiebt sich die Geschwindigkeitsverteilung zu höheren Werten und ist stark eingeengt. Dies ist unter den gegebenen Messbedingungen vorteilhaft, weil hierdurch eine geringere Dopplerverbreiterung der Rotationslinien erreicht wird.

3.2.2 Der Aufbau der Molekularstrahlapparatur

Die Abbildung 3.6 zeigt schematisch die Molekularstrahlapparatur. Das Vorvakuum wird durch eine Kombination aus einer Wälzkolbenpumpe und zwei Drehschieberpumpen erzeugt. Eine Öldiffusionspumpe evakuiert die Quellkammer, in der sich eine Probenvorlage befindet. Zwei Turbomolekularpumpen sorgen für den jeweiligen Druck bis zu 10^{-5} mbar und 10^{-7} mbar in den beiden letzten Kammern.

Die Expansion des Molekularstrahls von der Quellkammer über die Pufferkammer zur Messkammer wird durch abnehmende Drücke von Kammer zu Kammer realisiert. Die Kammern sind voneinander durch Skimmer getrennt, die zur Molekularstrahlabschälung dienen. Durch diese Maßnahme wird die Dopplerverbreiterung stark reduziert, weil nur Moleküle mit geringeren Querkomponenten des Ausbreitungsvektors zur jeweils nächsten Kammer durchgelassen werden. Der erste Skimmer, der sich 2 cm hinter der Düse befindet und einen Durchmesser von 1 mm aufweist, schält den größten Teil des aus der Düse expandierten Gases ab. Die mittlere Kammer dient als reine Flugstrecke, um die Quergeschwindigkeit der Moleküle am Messort noch einmal zu reduzieren. Der zweite Skimmer weist einen Durchmesser von 3mm auf.

Durch die Stagnationsleitung werden die zu untersuchenden Substanzen von oben eingefüllt. Ein Wellschlauch verbindet den Probentopf mit der Düse. Probenvorlage, Düsenzuleitung und Düse legen die Richtung der Molekülexpansion fest und können unabhängig voneinander kontrolliert bis 340 °C geheizt werden. Dabei verdampfen die Probenmoleküle und werden mit dem Trägergas ins Vakuum expandiert.

In der Messkammer kreuzt der Molekularstrahl horizontal das Laserlicht. Eine Kombination aus einem Hohlspiegel und zwei plankonvexen Linsen fokussiert einen Teil des Fluoreszenzlichts auf die Kathode eines Photomultipliers, der senkrecht über den Kreuzungspunkt des Molekularstrahls und des

Laserlichts eingebaut ist(Abbildung 3.8).

3.3 Die Experimentsteuerung und die Datenerfassung

Das Ausgangsignal des UV-empfindlichen Photomutipliers wird nach der Vorverstärkung von einem Photonenzähler diskriminiert. Über eine serielle Verbindung gelangt das Signal zum Datenerfassungsrechner. Gleichzeitig registrieren die Photodioden die UV-Leistung, das Jodabsorptionssspektrum und das Interferometersignal mit Hilfe einer 16 Bit AD Konverterkarte. Die Spannungssignale der drei Thermovacs und drei Penningvacs zur Messung der Drücke in den Kammern werden über eine zweite AD Konverterkarte aufgenommen.

Das Messdatenerfassungsprogramm KHiDaq, das in der Diplomarbeit von Marcel Böhm [14] ausführlich behandelt wird, ist ein Echtzeitsystem und kann alle ihm zugewiesenen Aufgaben gleichzeitig bearbeiten.
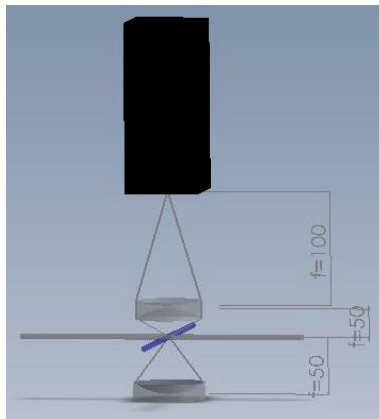
Abbildung 3.8: Die Abbildungsoptik

Kapitel 4

Die Auswertung der rovibronischen Spektren

4.1 Probleme bei der manuellen Auswertung

Bis zur Einführung der automatisierten Spektrenauswertung mit Hilfe der genetischen Algorithmen (GA) wurden die gemessenen Spektren 'manuell', d.h. durch Zuordnung von einzelnen rovibronischen Übergängen zu den entsprechenden Quantenzahlen, ausgewertet. Dieses Verfahren benötigt für die Simulation des Spektrums Startparameter (wie z.B. Rotationskonstanten für beide elektronische Zustände, Ursprungsfrequenz, Übergangsmomentorientierung, Rotationstemperatur), die möglichst genau bekannt sein müssen, um die Errechneten mit den experimentellen Daten vergleichen zu können. Aus den Mikrowellenspektren oder aus den quantenmechanischen Rechnungen, falls vorhanden bzw. durchführbar, kann man die Startparameter für den Grundzustand erhalten. Für den angeregten Zustand existiert als experimentelle Methode zur Ermittlung vorgenannter Parameter nur die Rotationskohärenzspektroskopie, deren Genauigkeit deutlich unter der der rotationsaufgelösten elektronischen Spektroskopie liegt. *Ab initio* Methoden für angeregte Zustände sind im Allgemeinen ebenfalls nicht präzise genug für eine Vorhersage der Rotationskonstanten des angeregten Zustandes. Sind die Startparameter zu

verschieden von den wahren Parametern, unterscheidet sich das simulierte Spektrum gravierend von dem experimentellen Spektrum und eine Zuordnung von Quantenzahlen zu Übergängen wird unmöglich. Außerdem ist es meist nicht möglich, 'manuell' die Übergänge von großen Molekülen oder Clustern zuzuordnen, da ihre Banden keine einzelnen rovibronischen Übergänge darstellen, sondern Überlagerungen von vielen Einzelübergängen.

Aus den oben genannten Gründen erweist sich eine Automatisierung der Auswertung mit Hilfe eines Computers als äußerst vorteilhaft. Bei der Suche nach geeigneten Algorithmen zur Anpassung der molekularen Parameter fiel die Wahl aufgrund verschiedener Vorteile auf die Evolutionsalgorithmen, die im nächsten Abschnitt diskutiert werden.

4.2 Die Evolutionsalgorithmen

Um die Analysis der rotationaufgelösten Spektren zu erleichtern, wurde eine automatische Auswertungsmethode entwickelt: die Evolutionsalgorithmen. Diese Methode basiert auf einem allgemeinen Prinzip der Reproduktion und der natürlichen Selektion in der Natur. Durch die Einführung der Algorithmen wird eine sehr schnelle Analyse ermöglicht. Wir sprechen hier von wenigen Minuten für die Auswertung eines einzelnen Spektrums auf einem Normalcomputer. Daneben gibt es einen viel bedeutenderen Grund, da die Evolutionsalgorithmen auch eine Analyse ermöglichen, auch wenn das Spektrum nicht im Detail verstanden wurde oder eine Überlappung von mehreren Spektren vorliegt. Im Folgenden werden zwei unterschiedliche Umsetzungen dieser Evolutionsalgorithmen vorgestellt: die Genetische Algorithmen(GA) und die evolutionäre Strategie(ES).

4.2.1 Die Genetischen Algorithmen

Das Modell der biologischen Evolution von Charles Darwin, das er in seinem Buch 'The Origin of Species' [33] entwickelte, stellt die Grundidee der ge-

netischen Algorithmen (GA) dar. Sie basiert darauf, dass sich in der Natur die Arten durch das Prinzip der natürlichen Selektion entwickelte, indem in jeden Generationen den besser an ihre Umwelt angepassten Individuen eine größere Überlebenschance zugeschrieben wird. Dadurch besitzen diese eine höhere Wahrscheinlichkeit, ihre Gene an die nächste Generation zu vererben. Bei den GA, die in [[101] [102] und [103] detailliert beschrieben sind, werden innerhalb vorgegebener Grenzen zufällig erzeugte Parameter binär im Gray - Code kodiert und ihre Kostenfunktion berechnet. Jeder binär kodierte Parameter stellt ein Gen dar. Die Gene werden in einem Vektor gesammelt, der als Chromosom bezeichnet wird. Von diesen Chromosomen werden mit Hilfe eines Zufallsgenerators etwa 300 bis 500 erzeugt. Die Kostenfunktion stellt ein Maß für die Übereinstimmung des mit diesen Parametern simulierten Spektrums mit dem experimentellen Spektrum dar (siehe Kapitel 4.4. Die besten Lösungen werden in den Paarungspool übernommen, in dem im nächsten Schritt ein Austausch von Genen zwischen den Chromosomen stattfindet (Crossover). Des Weiteren werden in jeder Generation mit einer gewissen Wahrscheinlichkeit einzelne Bits der Chromosomen zufällig verändert (Mutation) (4.5). Die Tochtergeneration wird erneut über ihre Kostenfunktion bewertet und bildet einen neuen Paarungspool. Der Prozess beginnt dann wieder von neuem. Diese Schleife läuft solange ab bis die vorgegebene Konvergenzkriterien erreicht werden [Abbildung 4.1]. Um zu verhindern, dass durch den Paarungsprozess oder durch Mutation Individuen entstehen, die außerhalb der Grenzwerte liegen, wird im Falle des Auftretens eines solchen Ereignisses einer Spiegelung der Werte in den zulässigen Parameterraum vorgenommen.

4.2.2 Die derandomized -evolutionäre Strategie $[(ES) - DR2]$

Bei der evolutionären Strategie startet man mit einen oder mehreren Mutterchromosomen. Durch die Anwendung eines zufälligen Mutationsvektors auf ein Mutterchromosom entsteht ein neues Individuum. Etwa 200 Individuen

werden auf dieser Weise erzeugt. Die Kostenfunktionen werden sowohl auf
die Eltern- als auch auf die Kinderchromosomen angewendet. Die Individuen
mit der besten Kostenfunktion repräsentieren die Eltern der nächsten Ge-
neration. Der derandomited-DR2 bewirkt, dass die Mutationsvektoren, die
auf einem Elternset angewendet wurden, für ein paar weitere Generationen
gespeichert werden. Im Gegensatz zu den genetischen Algorithmen kann die-
se Strategie die Richtung der besten Lösung merken und somit das globale
Minimum schneller finden.

4.2.3 Covariance Matrix Adaptation Evolution $[CMA-$ $ES]$ Strategie

Noch mehr Vorteile bietet die CMA-ES Strategie(Covariance Matrix Adap-
tation Evolution Strategy). Der Unterschied zu dem DR2 besteht in einem
anderen Mutationsvektor für die Erzeugung der nächsten Elterngeneration.
Bei dieser Strategie wird die ganze Kovarianzmatrix zu jedem Parameter
angepasst.

4.3 Die Eingabedatei

Die Anfangspopulation, die den ersten Paarungspool bildet, wird durch zu-
fälliges Aussuchen von Lösungsmöglichkeiten für das Problem erzeugt.
Die Individuen der Ausgangspopulation erzeugt man aus einem entsprechen-
den Satz Zufallszahlen unter Verwendung von Algorithmen, die die gesetzten
Randbedingungen berücksichtigen. Aus diesem Grund handelt es sich bei
diesen Werten nicht um echte, sondern um determinierte Zufallszahlen.
Die Anzahl der Generationen und der Individuen der Population können un-
abhängig voneinander festgelegt werden, wobei letztere für die Häufigkeit
der Rekombination der Chromosomen ausschlaggebend ist. Eine zu kleine
Anzahl der Generationen bzw. eine zu geringere Populationsgröße verhindert
eine genaue Ermittlung der Parameter im Parameterraum, während zu große

Werte die Rechenzeit exponentiell vergrößern.

Die Tabelle 4.1 zeigt die Erklärung der Parameter. Aus dem Typ des Spektrums kann die Information über die Lage des Übergangsdipolmoments gewonnen werden. Je nachdem wie diese zu der molekülfesten Achse liegen, kann zwischen a-, b-, c-, ab-, ac-, bc- oder abc - Typ gewählt werden. Die Voigt - Linienform stammt aus der Kombination zwischen einer Gaußverbreiterung, die durch Dopplerverbreiterung des Überschallstrahls entsteht, und einer Lorentz-Verbreiterung, die aus der begrenzten Lebensdauer des angeregten Zustandes des Moleküls resultierten. Es empfiehlt sich, am Anfang die Gauß- und die Lorentz-Verbreiterung als Konstante zu nehmen, deren Wert etwa der experimentell beobachtbaren Verbreiterung des Übergangs entspricht, und sie erst wenn alle anderen Parameter gefittet sind, zu variieren. Der maximal besetzte Rotationszustand wird zu Beginn berechnet und kann auch unter dem tatsächlichen Wert gewählt werden, um die Rechenzeit zu verkürzen. Dies ist aber nur bei zu starker Streuung der Ergebnisse, und wenn die größeren Rotationszustände für das Spektrum irrelevant sind, zu empfehlen.

Die Wertebereiche sowohl für die drei Rotationskonstanten als auch für deren Änderung bei der elektronischen Anregung können in der Eingabedatei festgelegt werden. Unter anderem enthält die Eingabedatei zwei weitere wichtige Parameter, die Winkel θ und φ, welche die Lage des Übergangsdipolmomentes angeben.

Die relative Ursprungfrequenz kann meist aus dem experimentellen Spektrum ermittelt werden.

```
┌─────────────────────────────────────────────────────┐
│                    Eingabedatei                       │
└─────────────────────────────────────────────────────┘
                          │
                          ▼
┌─────────────────────────────────────────────────────┐
│      Erzeugen einer zufälligen Anpassungspopulation   │
└─────────────────────────────────────────────────────┘
                          │
                          ▼
┌─────────────────────────────────────────────────────┐
│  Berechnung der Kostenfunktion für jedes einzelnen Individuum  │◄──┐
└─────────────────────────────────────────────────────┘   │
                          │                                  │
                          ▼                                  │
┌─────────────────────────────────────────────────────┐   │
│               Bildung des Paarungspools               │   │
└─────────────────────────────────────────────────────┘   │
                          │                                  │
                          ▼                                  │  Nein
┌─────────────────────────────────────────────────────┐   │
│             Reproduktion durch Crossover              │   │
└─────────────────────────────────────────────────────┘   │
                          │                                  │
                          ▼                                  │
┌─────────────────────────────────────────────────────┐   │
│                     Mutationen                        │   │
└─────────────────────────────────────────────────────┘   │
                          │                                  │
                          ▼                                  │
┌─────────────────────────────────────────────────────┐   │
│               Konvergenz erreicht?                    │───┘
└─────────────────────────────────────────────────────┘
                          │ Ja
                          ▼
┌─────────────────────────────────────────────────────┐
│                      Output                           │
└─────────────────────────────────────────────────────┘
```
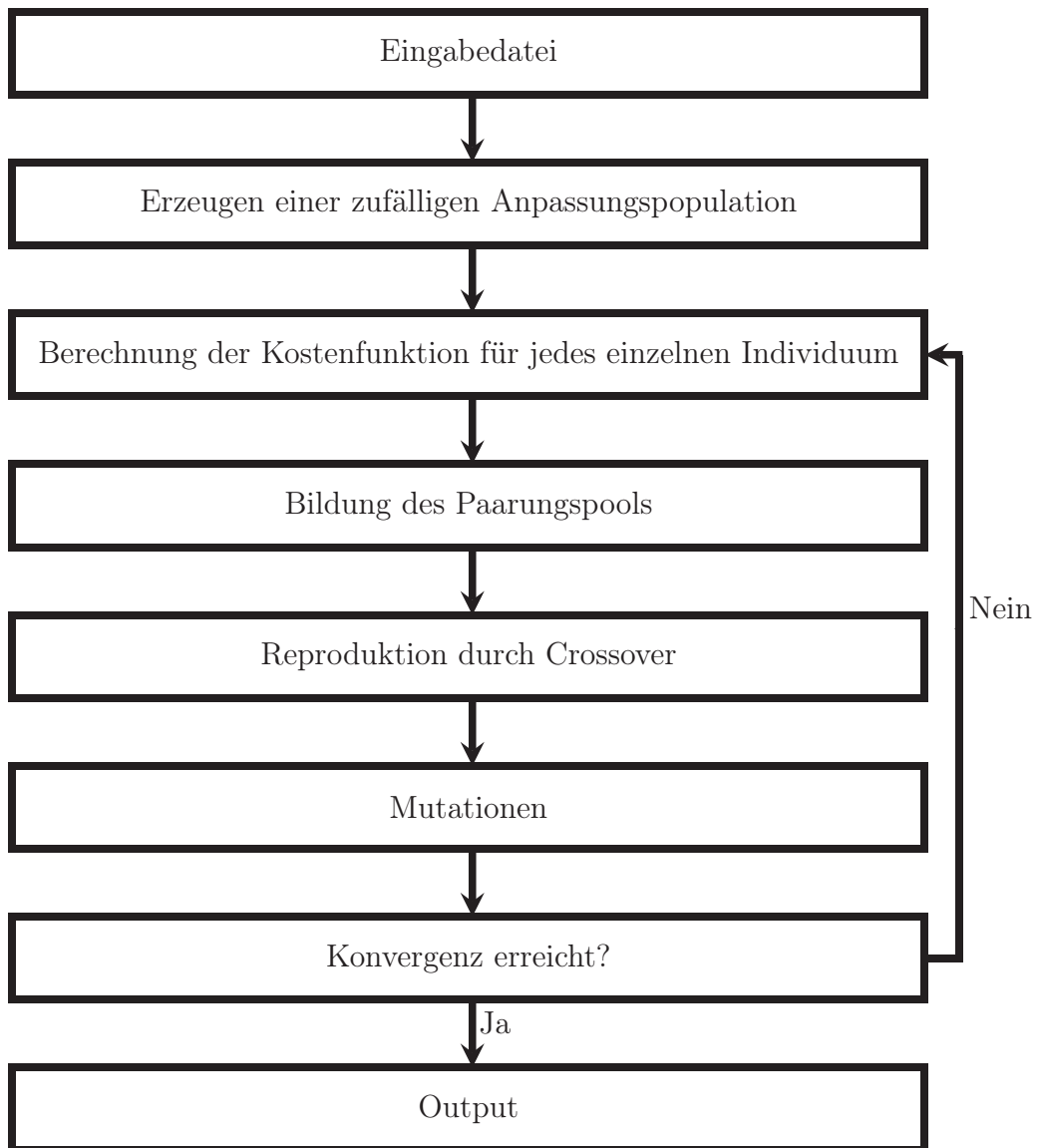
Abbildung 4.1: Schematischer Ablauf der Genetischen Algorithmen

Eingabe	Bedeutung
type of spectrum=abc	Typ des Spektrums
lineshape=Voigt	Art der Linienform
maximum J value=120	Maximal besetzter Rotationszustand
random seeds=50	Zufallszahl zur Erzeugung der ersten Generation
nr generations=300	Anzahl der Generationen
population size=5	Größe der Population
parameter= 1, 2 oder 3 $(A'' B'' oder C'')$	Rotationskonstanten des Grundzustandes
parameter= 82 und 83 (θ und φ)	Winkel des Übergangsmoments mit den Hauptträgheitsachsen
parameter= 90 (T1)	Definition der Temperatur
parameter= 95 (Delta Lorentz)	Größe der Lorentzverbreiterung
parameter= 96 (Delta Gauß)	Größe der Gaußverbreiterung
parameter= 100 (Nu_0)	Ursprungsfrequenz
parameter= 101, 102 und 103 (ΔA, ΔB und ΔC)	$\Delta X = X' - X''$ mit X= A, B oder C

Tabelle 4.1: Definition der Parameter der GA-Eingabedatei

4.4 Die Kostenfunktion

Die durch Zufallskreuzungen entstehenden Lösungen (Chromosomen) werden mit der für das Optimierungsproblem angepassten Kostenfunktion bewertet. Ein optimierter Zyklus mit seinen zugehörigen Kostenfunktionen bildet eine Generation. Die Kostenfunktion C_{fg} steht mit der Fitnessfunktion F_{fg} in folgender Beziehung:

$$C_{fg} = 100(1 - F_{fg}). \tag{4.1}$$

Die Fitnessfunktion für das gefittete Spektrum wurde von Hageman et al. [65] definiert als:

$$F_{fg} = \cos\alpha = \frac{(f,g)}{\|f\|\|g\|} = \sum_{i,j}^{N} \frac{f_i W_{ij} g_j}{\sqrt{\sum_{i,j}^{N} f_i W_{ij} f_j} \sqrt{\sum_{i,j}^{N} g_i W_{ij} f_j}} \tag{4.2}$$

mit

$$(f,g) = f^T W g, \tag{4.3}$$

worin

f	das experimentelle Spektrum
g	das berechnete Spektrum
i,j	die Ordinatenlaufindices und
$W_{ij} = w(|j - i|)$	die Empfindlichkeit der zwei Spektren zueinander

bedeutet. Ferner gilt:

$$W_{ij} = \frac{1 - |i - j|}{1/2 \Delta w} \tag{4.4}$$

für:

$$|i - j| \leq \frac{1}{2}\Delta w \tag{4.5}$$

sonst ist:

$$W_{ij} = 0. \tag{4.6}$$

Für $w(r)$ benutzt man eine Dreieckfunktion mit einer Basisbreite Δw, die wie folgt definiert ist:

$$w(r) = \begin{cases} 1 - |r| / \frac{1}{2}\Delta w & \text{für } |r| \leq \frac{1}{2}\Delta w, \\ 0 & \text{andererseits.} \end{cases}$$

Aus dem Chromosom wird zuerst ein Linienspektrum $\mathbf{L}_{jk}$ berechnet, aus dem man durch Multiplikation mit der Verbreiterungsfunktion $\mathbf{s}_k$ zum berechneten Spektrum $\mathbf{g}_{ij}$ kommt. Es gilt:

$$\mathbf{g}_{ij} = \sum_{k=1}^{N} \mathbf{L}_{jk}\mathbf{s}_k = \mathbf{Ls}. \tag{4.7}$$

Unter dem Gleichsetzen von $g_{ij} = Ls$ und $\widetilde{f} = f^T W L$ ändert sich die Gleichung 4.3 zu 4.7.

$$(f, g) = f^T W L s = \widetilde{f} s \tag{4.8}$$

mit:

$$\widetilde{f} = f^T W L \tag{4.9}$$

Um die Rechenzeit der Kreuzkorrelation (Gleichung 4.2) zu reduzieren sind mehrere Methoden gebräuchlich:

1. Man lässt die Gleichung 4.6 mit dem einmalig berechneten transformierten Strichspektrum über alle N Punkte (also einzelnen Messwerten) des Spektrums laufen ($N \approx 60000 - 250000$;während die Anzahl der Striche $\approx 1000 - 3000$ beträgt).

2. Der Zähler der Gleichung 4.2 wird nur einmal berechnet.

3. Der Benutzer legt in seinem Input den maximal besetzen Rotationszustand (Jmax) fest. Der tatsächliche Wert für Jmax wird zu Beginn des Fits ermittelt und, falls diese Wert von den festgelegten abweicht, gegenbenenfalls nach unten, niemals jedoch nach oben korrigiert.

4.5 Selektion, Reproduktion und Mutation

Nach der Bewertung mit der Kostenfunktion wird eine Rangliste der Chromosomen erstellt, aus der die besten Lösungen den so genannten Paarungspool bilden. Hierbei werden immer 2 Individuen miteinander gepaart und ihre Gene ausgetauscht.

Für die Auswahl der Paare innerhalb des Paarungspools sind folgende Modelle gängig:

1. Top to Bottom: In der Reihe der besten Chromosomen werden immer 2 nebeneinander stehende Spezies miteinander gepaart d.h. (1,2); (3,4); (5,6) . . .

2. Zufallspaarung: Die Paare werden durch Zufall ausgesucht: (1,8); (2,6); . . .

3. gewichtete Zufallspaarung: gute Chromosomen haben größere Chancen, sich mit einem anderen guten Individuum zu paaren.

Die Paarung geschieht durch Crossover von zwei Chromosomen zwischen den Genen. Es gibt drei verschiedene Möglichkeiten, die Gene der zwei ausgesuchten Chromosomen miteinander zu kombinieren. Diese sind in der Tabelle 4.2 ausgeführt. Bei dem One-Point Crossover werden die Bitwerte der zwei Mutterchromosomen einfach ab einer bestimmten, definierten Stelle getauscht. Diese Rekombination rechnet sich sehr schnell und einfach, erweist sich jedoch als unpraktisch, da sie nur begrenzte Kombinationen produziert. Besser ist das Two-Point Crossover, bei dem die Bitwerte zwischen zwei Stellen ausgetauscht werden. Dies ermöglicht alle Kombinationen und wird vorwiegend verwendet. Die dritte Möglichkeit ist das Uniform-Crossover, das eine beliebi-

ge Anzahl der Austauschstellen zulässt. Für die aktuelle Anwendung machen zu lange Rechenzeiten diese Methode jedoch unbrauchbar.

Beim Durchsuchen des Parameterraums könnte der Algorithmus in ein lokales Minimum laufen. Um dies zu verhindern, wird mit einer geringen Wahrscheinlichkeit die Mutation der Chromosomen durch zufälligen Bitaustausch zugelassen. Dabei entsteht ein neues Chromosom, das nicht durch Crossover aus zwei Elternchromosomen entstanden sein kann. Um zu verhindern, dass 'gute' Gene verlorengehen, schließt man das oder die besten Individuen jedoch von diesem Vorgang aus (Elitismus). Die Änderungsrate für die anderen Chromosomen wird typischerweise zwischen 1 % und 5 % festgelegt. Die Mutationen vergrößert die Chance, das globale Minimum herauszufinden.

Crossover	Beispiel
One-Point	1 0 1 · 0 0 1 0 0 0 1 0 1 0 · 1 0 0 1 1 0 0 ↓ 1 0 1 · 1 0 0 1 1 0 0 1 0 1 · 0 0 1 0 0 0 1
Two-Point	1 0 1 · 0 0 1 · 0 0 0 1 0 1 0 · 1 0 0 · 1 1 0 0 ↓ 1 0 1 · 0 0 1 · 1 1 0 0 0 1 0 · 1 0 0 · 0 0 0 1
Uniform	1 · 0 1 · 0 0 1 0 · 0 0 · 1 0 · 1 0 1 · 0 0 1 1 · 0 0 ↓ 1 · 1 0 1 · 0 0 1 1 · 0 0 0 · 0 1 0 · 0 1 0 0 · 0 1

Tabelle 4.2: Möglichkeit des Crossover

Kapitel 5

Veröffentlichungen

5.1   1,4-Benzodioxan

Rotationally Resolved Electronic Spectroscopy of 1,4-Benzodioxan: The Anomeric Effect in the Ground and Electronically Excited State

Thi Bao Chau Vu,[a] Christian Brand,[a] W. Leo Meerts,[b] and Michael Schmitt*[a]

We measured the rotationally resolved electronic spectra of the origin and of three vibronic bands of 1,4-benzodioxan. From comparison to various ab-initio-calculated structures of 1,4-benzodioxan, the twisted C_2 symmetric 1,4-benzodioxan was shown to be responsible for all the observed spectral features. We analyzed the inertial defects in both electronic states as sensitive indicators of the non-planarity of the system. The molecule was found to be more planar in the electronic ground state than in the electronically excited singlet state. This effect can be traced back to an increased puckering of the dioxan ring, which also comprises the oxygen atoms, in the excited state. This observation is discussed in terms of natural bond orbitals.

1. Introduction

1,4-Benzodioxan (BZD) is a flexible molecule, which is formally derived from *ortho*-di-substituted benzenes, the *ortho* positions being bridged by an $-O-(CH_2)_2-O-$ group. Benzene-fused oxygen-containing compounds are of considerable interest as biomolecular building blocks. Most of what we currently know about structure and large-amplitude motions of BZD comes from the groups of Hollas/Gordon[1–4] and Laane.[5–7]

There is a vast literature on the importance of the anomeric effect for the stabilization of the puckered forms of 1,3-dioxole or 1,3-benzodioxole.[8–10] In these molecules the $n_p \rightarrow \sigma^*_{CO}$ interaction involving the nonbonding lone pair with *p*-character at one oxygen atom and the antibonding σ^*_{CO} orbital of the adjacent CO bond have been shown to contribute most of the stabilization energy of the puckered form.[8] A smaller but hitherto important stabilizing contribution comes from the $n_p \rightarrow \sigma^*_{CH}$ interaction with the antibonding CH orbital.[9, 10] In the 1,4-benzodioxan molecule chosen herein, no adjacent CO bond exists; thus, the most important stabilizing contribution in 1,3-benzodioxole is impossible here. Instead, it is the $n_p \rightarrow \sigma^*_{CH}$ interaction which stabilizes the puckered form. This hypothesis can be tested by comparing the extent of the anomeric effect in the ground and electronically excited states. If the electron density is shifted from the oxygen lone pair into the aromatic ring upon electronic excitation, the anomeric effect due to the $n_p \rightarrow \sigma^*_{CH}$ interaction will decrease in the excited state. This effect can be measured via the amount of non-planarity of BZD in both electronic states.

Gordon and Hollas measured the rotational band contour of the 281 nm $\pi\pi^*$ band system of BZD.[1] From symmetry considerations, they determined this system to be due to a A←A transition, as expected for *o*-disubstituted benzenes with C_2 symmetry. From a small inertial defect they deduced a twisted conformation in both electronic states, and the electronic origin ν_0 was determined to be at 35 562.48 cm^{-1}. The same group presented single vibronic level fluorescence (SVLF) spec-

tra of various in-plane and out-of-plane bands.[2] Many modes show a strong Duschinsky effect. Using single vibronic level fluorescence and fluorescence excitation (FE) spectroscopy, the modes with the strongest Duschinsky effect were identified as the bending modes ν_{48} and ν_{47}, the latter being also very anharmonic.[3] A very thorough study was performed by Gordon and Hollas, in which a combination of fluorescence excitation and single vibronic level fluorescence was utilized to assign the ground- and excited-state fundamentals of BZD.[4]

Choo et al. made an assignment of the vibrational spectrum of BZD on the basis of density functional theory using Becke's three-parameter hybrid (B3LYP) method.[11] They calculated the energy difference of twisted and bent structures to be 7.5 kcal mole^{-1}, the latter being a transition state for the interconversion of two twisted forms.

FE and SVLF spectra for several vibronic states were recorded and analyzed by Yang et al.[5] They calculated a barrier to planarity for the twisted structure at the MP2 level of 4095 cm^{-1}. The experimentally determined frequencies of the ring-twisting states were used for a two-dimensional fit of the barrier, including the bending modes. In this model, barriers for the S_0 state of 3906 cm^{-1} and for the S_1 state of 1744 cm^{-1} were obtained. The structures and frequencies for the two lowest singlet states and the lowest triplet state were reported from a density functional analysis by Yang et al.[6]

[a] T. B. Chau Vu, C. Brand, Dr. habil. M. Schmitt
Heinrich-Heine-Universität, Institut für Physikalische Chemie I
40225 Düsseldorf (Germany)
Fax: (+49) 211-81-15195
E-mail: mschmitt@uni-duesseldorf.de

[b] Prof. Dr. W. L. Meerts
Radboud University, Institute for Molecules and Materials
Heyendaalseweg 135, NL-6525 AJ Nijmegen (The Netherlands)

Supporting information for this article is available on the WWW under http://dx.doi.org/10.1002/cphc.201000576.

WILEY ONLINE LIBRARY

These are not the final page numbers! ↗↗

2. Theory

2.1. Ab initio Calculations

Structure optimizations were performed employing the correlation-consistent basis sets of valence triple zeta quality of Dunning (cc-pVTZ) from the TURBOMOLE library.[12, 13] The equilibrium geometries of the electronic ground and the lowest excited singlet states were optimized using the approximate coupled cluster singles and doubles model (CC2) employing the resolution-of-the-identity approximation (RI).[14–16]

Ground- and excited-state energies, dipole moments, and transition dipole moments were calculated using the combined density functional theory multi-reference configuration interaction (DFT/MRCI) method[17] with the same basis sets as that used for the structure optimizations. The configuration state functions (CSFs) in the MRCI expansion are constructed from Kohn–Sham (KS) orbitals, optimized for the dominant closed-shell determinant of the electronic ground state employing the BH-LYP functional.[18, 19] All valence electrons were correlated in the MRCI runs. The lowest five roots in the singlet manifold were calculated. The initial set of CSFs was generated from all single and double excitations out of the five highest occupied molecular orbitals in the KS determinant into the five lowest virtual orbitals and was then iteratively improved. The size of the MRCI expansion was kept moderate by selection of the most important configurations, based on an energy gap criterion,[17] leading to 31 399 configurations with which the calculations where performed.

Additionally, a natural bond orbital analysis using the NBO 3.1 program,[20] implemented in the Gaussian 03 program package (Revision C.02)[21] was performed using the wavefunctions from a (TD) B3LYP-optimized structure using Dunnings cc-pVTZ basis set.

2.2. Evolution Strategies

The rovibronic spectra were fit to an asymmetric rotor Hamiltonian[22] by using the de-randomized (DR) evolution strategy (ES) developed by Ostenmeier et al.[23] A special implementation which we have employed herein represents the second generation of de-randomized ES, abbreviated as DR2.[24] It was recently shown[25] to be a very good alternative to the genetic algorithm-based fits we have employed so far.[26] Evolutionary strategies such as the DR2 algorithm are global optimizers which are inspired by the biological processes of reproduction and natural selection. While classical genetic algorithms aim to find a solution in the parameter space by randomly combining information from a set of trial solutions, the DR2 algorithm can sense in which direction the goodness of the fit (the so-called cost function) increases. In the first step, the DR2 algorithm generates trial solutions (offspring) by using a random distribution around some starting point (parent), each consisting of the complete parameter set which is necessary to simulate the spectrum. Offspring with higher fitness than the parent are kept and used to compute the next generation. The DR2 algorithm makes use of the parameter correlation matrix for successive changes in the parents (mutations). This means that if for some parameter a parent has evolved in the same direction for several generations, resulting in a positive correlation, the most likely solution is assumed to be further in that direction and the next parameter mutation will be larger. Correspondingly, two anticorrelated mutations will lead to a smaller mutation. Compared to classical genetic algorithms, this procedure has been shown to lead to a faster convergence of the parameters.[25]

Experimental Section

1,4-Benzodioxan (purity > 97%) was purchased from Sigma Aldrich and used without further purification.

The experimental setup for the rotationally resolved laser-induced fluorescence is described in detail elsewhere.[27] Briefly, the laser system consisted of a single-frequency ring dye laser (Sirah Matisse DS) operated with Rhodamine 110, pumped with 7 W of a frequency-doubled continuous wave (cw) Nd:YAG laser (Spectra Physics, Millenium X). The dye laser output was coupled to an external folded ring cavity (Spectra Physics Wavetrain) for second-harmonic generation. The resulting output power was constant at about 25 mW during each experiment. The molecular beam was formed by co-expanding 1,4-benzodioxan heated to 120 °C and Ar as carrier gas through a 200 μm nozzle into the vacuum. The molecular beam machine consisted of three differentially pumped vacuum chambers that were linearly connected by skimmers (1 mm and 3 mm, respectively) to reduce the Doppler width to 18 MHz in this setup (full-width-at-half-maximum, FWHM). In the third chamber, 360 mm downstream of the nozzle, the molecular beam crossed the laser beam at a right angle. The imaging optics setup consistd of a concave mirror and two plano-convex lenses to collect the resulting fluorescence onto a photomultiplier tube which was mounted perpendicular to the plane defined by the laser and the molecular beam. The signal output was then discriminated and digitized by a photon counter and transmitted to a PC for data recording and processing. The relative frequency was determined with a quasi-confocal Fabry-Perot interferometer with a free spectral range (FSR) of 149,9434(56) MHz. The absolute frequency was obtained by comparing the recorded iodine absorption spectrum with tabulated lines.

3. Results and Discussion

3.1. Quantum Chemical Calculations

3.1.1. The Electronic Ground State

We calculated three structures with different symmetries [planar (C_{2v}), boat (C_s), and twist (C_2)], which can be assumed to be the minimum structure using CC2-coupled cluster theory with the correlation consistent cc-pVTZ basis set. Table 1 compares the structural parameters (rotational constants and inertial defect) and the relative energies of the three structures. The inertial defect is defined as $\Delta I = I_c - I_a - I_b$, where the I_g are the moments of inertia about the principal inertial axes g. For a planar molecule, it is zero and negative for nonplanar molecules. Vibrational effects actually cause the inertial defects of perfectly planar molecules to deviate slightly from zero. ΔI thus provides a measure for the non-planarity of a molecule.

◄◄ These are not the final page numbers!

Table 1. CC2/cc-pVTZ-calculated relative energies, rotational constants (A,B,C), inertial defects (ΔI), and center frequency of absorption (ν_0) of three different stationary points on the potential energy surface of 1,4-benzodioxan in their electronic ground (doubly primed quantities) and first excited (primed quantities) singlet state.

	Twisted (C_2)	Boat (C_s)	Planar (C_{2v})
E_{rel} [cm^{-1}]	0	2837	4085
A'' [MHz]	2914.9	2859.7	2893.6
B'' [MHz]	1237.8	1241.4	1206.7
C'' [MHz]	892.2	904.8	860.7
$\Delta I''$ [uA^2]	−15.22	−25.28	−6.29
ν_0 [cm^{-1}]	36 114	36 083	35 785
A' [MHz]	2815.5	2836.6	2795.0
B' [MHz]	1232.1	1216.9	1204.0
C' [MHz]	881.3	872.2	850.4
$\Delta I'$ [uA^2]	−16.20	−14.03	−6.27
ΔA [MHz]	−99.4	−23.1	−98.6
ΔB [MHz]	−5.7	−24.5	−2.7
ΔC [MHz]	−10.9	−32.6	−10.3

All three structures exhibit sufficiently different rotational constants to make a straightforward assignment to the experimentally observed form, from a comparison to the experimental rotational constants. Especially the inertial defects ΔI, which give a direct measure for the degree of non-planarity, make the assignment to the twist form straightforward.

The three structures are shown in Figure 1. The lowest energy structure is the twist form. The boat form is higher in energy, by 2837 cm^{-1}, and the planar BZD by 4085 cm^{-1}. The boat form is a first-order saddle point connecting the two enantiomeric twist forms. The planar form represents a second-order saddle point connecting two identical boat forms via the first motion with imaginary frequency and two identical twist forms via the second motion with imaginary frequency.

A comparison of the rotational constants and the inertial defects with the experimental values from Table 3 immediately shows that the twisted structure is responsible for all the features observed in the fluorescence spectra. Also, the changes in the rotational constants upon electronic excitation are in
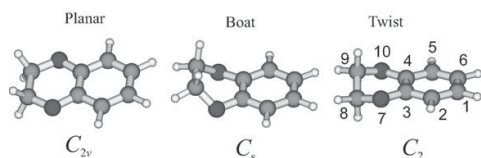
very good agreement with the experimentally determined values for the twisted form.

3.1.2. The Lowest Excited Singlet States

The structures of the two lowest excited singlet states of the twisted, boat, and planar forms of BZD were optimized at the CC2/cc-pVTZ level of theory. The barrier for interconversion of the two enantiomeric twisted forms over the boat transition state amounts to 3930 cm^{-1}, slightly lower than in the electronic ground state. The difference to the second-order transitions state (the planar form) is calculated to be 2768 cm^{-1}, also slightly lower than the value for the S_0 state.

Vertical and adiabatic excitation energies and transition dipole moments of the lowest four electronic singlet states of BZD were calculated at the CC2 level and using DFT/MRCI. The results are compiled in Table 2. The lowest electronically excited singlet state is polarized along the long (a) inertial axis and must therefore be classified as ^1L_b state in the nomenclature of Platt.[28] The excitation is mainly from HOMO to LUMO (17b–18b) and to a lesser extent from HOMO-1 to LUMO+1 (19a–20a), see Figure 2. The second excited singlet state is polarized along the b axis and therefore represents the ^1L_a state. It is mainly a HOMO–LUMO+1 excitation (17b–20a). Two more ex-

Table 2. Calculated vertical and adiabatic singlet excitation energies ΔE [cm^{-1}] and transition dipole moment orientations of BZD. The parameter θ describes the in-plane angle of the TDM with the inertial a axis. All the adiabatic excitation energies are zero-point-energy-corrected at the CC2/cc-pVTZ level of theory.

	$L_b \leftarrow S_0$		θ	$L_a \leftarrow S_0$		θ	$B_b \leftarrow S_0$		θ	$B_a \leftarrow S_0$		θ
	vert.	adiab.		vert.	adiab.		vert.	adiab.		vert.	adiab.	
CC2	38 975	36 114	0	47 108	43 339	90	52 705	48 149	90	52 541	49 884	0
DFT/MRCI	38 245	36 050	0	47 300	44 441	90	53 237	50 055	90	53 369	48 880	0
Exp.		35 560	6									

Table 3. Molecular constants of the origin and three vibration bands of 1,4-benzodioxan obtained from ES-DR2 fits to the experimental spectra.

	Origin	25_0^1	48_0^2	18_0^1
A'' [MHz]	2920.0(4)	2920.1(1)	2919.8(5)	2919.3(3)
B'' [MHz]	1235.22(1)	1235.26(2)	1235.43(3)	1235.34(4)
C'' [MHz]	891.05(1)	891.04(1)	891.08(2)	891.21(2)
$\Delta I''$ [uA^2]	−15.0405	−15.0524	−14.8993	−15.1338
ΔA [MHz]	−92.81(1)	−92.82(1)	−102.04(1)	−93.06(2)
ΔB [MHz]	−6.69(1)	−6.71(1)	−3.35(1)	−7.01(2)
ΔC [MHz]	−9.68(1)	−9.68(1)	−7.14(1)	−9.15(2)
$\Delta I'$ [uA^2]	−16.7226	−16.7362	−17.7377	−17.2907
θ [degree]	6(1)	18(1)	19(1)	2(2)
ϕ [degree]	87(1)	86(1)	87(1)	86(2)
τ [ns]	6.2(1)	6.8(1)	6.3(1)	6.2(1)
T_1	1.55	1.85	1.50	1.50
T_2	2.95	3.45	4.96	2.77
w	0.3	0.12	0.13	0.17
μ_a	0.98	0.98	0.92	1.00
μ_b	0.02	0.02	0.08	0.00
μ_c	0.00	0.00	0.00	0.00
ν_0 [cm^{-1}]	35 560.15(2)	35 699.33(2)	35 718.72(2)	36 262.06(2)
$\Delta\nu$ [cm^{-1}]	0	139.18(2)	158.57(2)	701.91(2)

Figure 1. Structures of the three lowest energy structures of BZD: planar (C_{2v}), boat (C_s), and twisted (C_2), along with the atomic numbering.
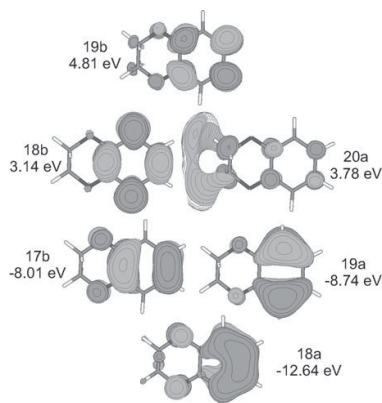
Figure 2. Frontier orbitals of the twisted form of BZD at the CC2/cc-pVTZ level of theory.

cited singlet states have been calculated, namely, the ^1B_a and the ^1B_b states. The first of these is classified as HOMO-2 to LUMO+1 (18a-20a), the next as HOMO to LUMO+1 (17b–20a). The purely electronic ^1B_a and ^1B_b states are quasi-degenerate at the DFT/MRCI level of theory; inclusion of zero-point energy brings the ^1B_a state slightly below the ^1B_b state. Oscillator strengths (f) of 0.0207, 0.0023, 0.7571, and 0.4743 are found for the ^1L_b, ^1L_a, ^1B_b, and ^1B_a states, respectively.

Regarding the large energy gap of more than 8000 cm^{-1} between the ^1L_b and the ^1L_a state and the small oscillator strength of the latter, no vibronic coupling between vibronic bands of the ^1L_b state and the origin of the ^1L_a state is expected.

3.2. The vibrational and Vibronic Spectrum of BZD

The vibrational and vibronic spectra of the twisted form of BZD were calculated at the CC2/cc-pVTZ level of theory. Twenty-five of the 48 vibrations in the C_2 point group transform like the totally symmetric representation *a*, and 23 vibrations like the nontotally symmetric representation *b*. The lowest electronically excited state has its transition dipole moment oriented along the molecular *a* axis. The transition dipole moment transforms like *A* along the inertial *a* axis and like *B* along the *b* and *c* axes. The pure electronic ($\pi\pi^*$) transition is therefore classified as *A←A*. Thus, the totally symmetric vibrational (and vibronic) bands will exhibit *A*-type selections rules, while the nontotally symmetric vibrations will be *BC* hybrid bands.

The calculated ground-state vibrations are given by ascending frequencies in Table S1 of the Supporting Information. The calculated frequencies are compared to experimental vibrational frequencies from ref. [11]. The following columns give the calculated and experimental vibrational frequencies in the first electronically excited state of *A* symmetry. In order to make the assignment of excited-state to ground-state vibrations, we calculated the Duchinsky matrix from the hessians of both electronic states. The normal coordinates Q' of the excit-

ed state and Q'' of the ground state are related by the linear orthogonal transformation given by Duchinsky [Eq. (1)]:[29]

$$\mathbf{Q}'' = \mathbf{SQ}' + \vec{d} \tag{1}$$

where $\vec{d}$ is a displacement vector and **S** is the Duchinsky matrix, which rotates the coordinate system of one state into that of the other state. The largest elements of the complete Duchinsky matrix is given in the last column in Table S1 of the Supporting Information. The lowest nontotally symmetric vibrations Q_{48} and Q_{47} are strongly Duschinsky-mixed, with nearly equal coefficients for both vibrations. This behavior has been inferred by Gordon and Hollas[3] from the massive occurrence of cross-sequences of the form $48_0^x 47_x^0$. While in the low-frequency region strong Duchinsky mixing is found, there is only very little mixing above 500 cm^{-1} and the vibrations retain their identities upon electronic excitation.

3.3. Rotationally Resolved Electronic Spectra

3.3.1. The Electronic Origin

We measured the rotationally resolved electronic spectrum of the electronic origin of BZD in a molecular beam (cf. Figure 3). For the simulation of the rovibronic spectra a rigid asymmetric

Figure 3. Rotationally resolved electronic spectrum of the electronic origin of BZD. The second trace shows the simulation using the best parameters from Table 3. The lowest traces show zoomed-in parts of the experimental spectrum and the simulation.

rotor Hamiltonian was employed.[22] The origin spectrum was fitted to the rotational constants *A*, *B*, and *C* in both electronic states, to the center frequency ν_0, to the orientation of the transition dipole moment with respect to the inertial axes measured by the polar angles θ and ϕ, the rotational temperature in the jet and a Lorentz and Doppler width, for the lineshape profile using an evolutionary strategy approach. The temperature dependence of the intensity is described by a two-temperature model [Eq. (2)]:

$$n(E, T_1, T_2, w) = e^{-E/kT_1} + we^{-E/kT_2} \tag{2}$$

↖↖ These are not the final page numbers!

where E is the energy of the lower state, k is the Boltzmann constant, w is a weighting factor, T_1 and T_2 are the two temperatures.[30] For details of the evolution strategy see Section 2.2.

The molecular parameters from the fit are collected in Table 3. A comparison of the rotational constants and inertial defects of the three BZD structures from Table 1 with the experimental values immediately shows that the observed spectrum is due to the twisted form.

The electronic transition moment is oriented along the (long) inertial a axis. According to Platt's nomenclature, this is the signature of the ^1L_b state, which has the transition moment vector running through the **b**onds, while that of the ^1L_a state runs through the **a**toms.

The change of the inertial defect from -15.04 to -16.72 uA^2 shows that the BZD molecule gets considerably more nonplanar upon electronic excitation. This is exactly the trend which is obtained from the CC2 calculations described in Section 3.1 for the twisted from (increase of ΔI from -15.22 to -16.20 uA^2). Also, the structurally similar 1,3-benzodioxole (BDO), which has been recently investigated in the Pratt[31] and the Laane groups,[8] shows a larger inertial defect in the electronically excited state. There, the increasing non-planarity was attributed to the ability of the p-type lone pair (LP) at the oxygen atom to either conjugate with the π electrons of the benzene ring or interact with the σ* orbital of the adjacent CO and the axial CH bonds. This inverse hyperconjugation (the anomeric effect) is strongly stabilizing and leads to a puckering of the five-membered ring. In the excited state, the weaker interaction of the LP with the aromatic ring leads to an increased anomeric effect and to a stronger non-planarity of the system as has been discussed by Thomas et al.[31]

For BZD, the only possible anomeric interaction is between the oxygen lone pairs (donor) and the the σ* orbitals of the adjacent axial CH bonds (acceptor). The importance of the stabilizing anomeric effect in this molecule can be established from the ab initio calculations in various ways: First, from the CC2 calculations we learn that the C–H bond lengths of the axial H atoms of the bridging CH$_2$ groups are larger than the equatorial ones (1.0936 Å vs. 1.0878 Å) as a consequence of the $\pi(O_{LP}){\rightarrow}\sigma^*(C{-}H_{ax})$ interaction. Secondly, an NBO analysis using the B3-LYP/cc-pVTZ-optimized structure shows a larger Wiberg bond order between the oxygen atom and the axial H atom (0.0215) compared to the equatorial H atom (0.0041). The stabilization energy from a charge transfer from the oxygen LP with 100% p-character to the σ* CH bond [0.6(sp^3)$_C$-0.8(s)$_H$)] amounts to 29.6 kJ mole^{-1}. Figure 4 shows the two natural bond orbitals that are responsible for the interaction which stabilizes the puckered form. On the left-hand side of Figure 4, the p-type oxygen lone pair is shown and on the right-hand
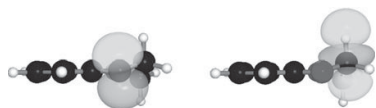
Figure 4. Side view of the p-type oxygen lone pair (left) and the antibonding σ* orbital of the adjacent ÐCH$_2$Ð group (right) in ground-state BZD.

side the antibonding σ* orbital of the adjacent CH$_2$ group as obtained from the NBO analysis.

Upon electronic excitation, the electron density is shifted from the oxygen lone pair to the aromatic ring, such as in the case of phenol[33] (cf. also Figure 2). This effect is also quantified through the ab initio calculations: The Wiberg bond order (NBO) index between the oxygen atom and the axial H atom decreases upon electronic excitation from 0.0215 to 0.0204, while the bond order between the oxygen and the adjacent ring carbon atom increases from 0.9781 to 0.9871. The charge-transfer stabilization from the oxygen lone pair to the antibonding σ* CH bond is smaller (28.4 kJ mole^{-1}) than in the electronic ground state. Thus, it can be inferred from the calculations that the explication given in refs. [8,31] for the increased non-planarity upon electronic excitation in BDO does not apply for BZD.

Comparison of the ground- and excited-state structures of BZD reveals an important detail: While the O atoms in ground-state BZD are situated in the plane of the aromatic ring (upper trace in Figure 5), they are slightly out-of-plane in the excited
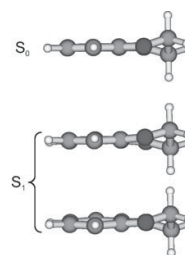
Figure 5. Side view of the ground-state structure (upper trace) and of two different side views of the lowest excited singlet state.

state. The O$_7$O$_{10}$C$_4$C$_3$ dihedral angle from the CC2 calculations is 0.5° in the ground state and 5° in the excited state. The lower two traces of Figure 5 give two different side views of excited-state BZD: the first projection shows that one of the O atoms is located above the aromatic ring, the other below. The second projection places the two O atoms in the line of view. In this perspective, it can be seen that the heterocyclic six-ring adopts a half-chair configuration as found for the non-aromatic analogue 2,3-dihydro-1,4-dioxin.[32] Since electronic excitation reduces the bond orders in the aromatic ring due to the ππ* excitation, the forced co-planarity of the aromatic ring and the oxygen atoms in the electronic ground state is released in favor of the sterically more stable nonplanar form.

3.3.2. Higher Vibronic Bands

Figure 6 shows the rotationally resolved spectrum of the A vibration Q_{25} at 0,0 + 139 cm^{-1}. The parameters from the best fit are compiled in Table 3. The band is a pure a-type band, such as the electronic origin. This is what can be expected for the vibrations with A-symmetry. The change of the inertial defect upon electronic excitation nearly matches the one of the elec-
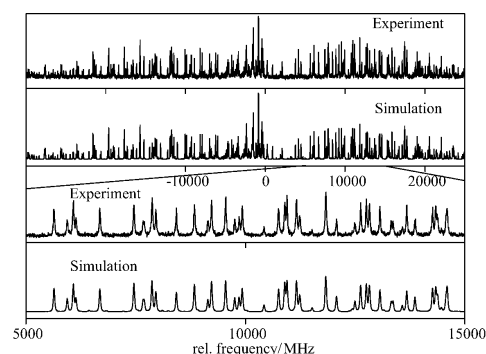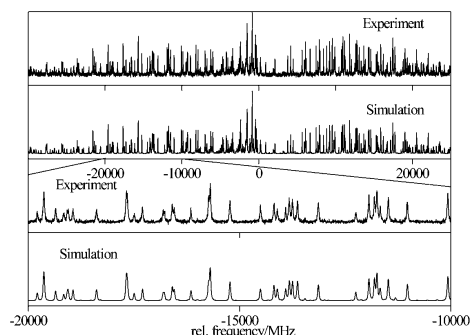
Figure 6. Rotationally resolved electronic spectrum of the 139 cm^{-1} band of BZD. The second trace shows the simulation using the best parameters from Table 3. The lowest traces show zoomed-in parts of the experimental spectrum and the simulation.

tronic origin, thus giving further evidence for the assignment of this band as being of *A* symmetry.

Figure S1 of the Supporting Information shows the rotationally resolved spectrum of the first overtone of the *B* vibration Q_{48} at 0,0 + 159 cm^{-1}. The parameters from the best fit are also compiled in Table 3. The overtone of this *B* vibration is also of *A* symmetry as the electronic origin, and shows consequently an *a*-type contour. For this band a considerably larger change of the inertial defect upon electronic excitation is found than for the origin and the 0,0 + 139 cm^{-1} bands.

The rotationally resolved spectrum of the *A* vibration Q_{18} at 0,0 + 702 cm^{-1} is shown in Figure S2 of the Supporting Information. The parameters from the best fit are compiled in Table 3. This band was previously assigned as Q_{21}. As a result of our normal-mode and Duchinsky analysis we reassign this band as being due to Q_{18}.

The excited-state lifetimes of the electronic origin and of all the vibronic bands investigated herein were determined from the Lorentz contribution of the Voigt profiles of the rovibronic lines. They are remarkably similar, around 6.5 ns.

4. Conclusions

The rotationally resolved electronic spectra of BZD have shown that this molecule exists in the twisted form in both electronic states. The main factor for the stabilization of the twisted form is the steric repulsion of the adjacent CH$_2$ groups. The non-planarity of BZD in both states has been measured through the inertial defect. It is shown that BZD is more planar in the electronic ground state than in the electronically excited state. The reason for the larger non-planarity of the system is the reduced C—C bond order in the aromatic ring upon electronic $\pi\pi^*$ excitation. The O atoms, whose *p*-type lone pairs can be partially delocalized into the aromatic ring, adopt a structure with less steric strain in the excited state and therefore leave the aromatic plane, thereby leading to a larger inertial defect.

[1] R. D. Gordon, J. M. Hollas, *J. Mol. Spectrosc.* **1992**, *156*, 415 – 420.
[2] R. D. Gordon, J. M. Hollas, *J. Mol. Struct.* **1993**, *293*, 193 – 196.
[3] R. D. Gordon, J. M. Hollas, *J. Chem. Phys.* **1993**, *99*, 3380 – 3389.
[4] R. D. Gordon, J. M. Hollas, *J. Mol. Spectrosc.* **1994**, *163*, 159 – 179.
[5] J. Yang, M. Wagner, J. Laane, *J. Phys. Chem. A* **2007**, *110*, 9805 – 9815.
[6] J. Yang, J. Choob, O. Kwon, J. Laane, *Spectrochim. Acta Part A* **2007**, *68*, 1170 – 1173.
[7] J. Yang, J. Laane, *J. Mol. Struct.* **2006**, *798*, 27 – 33.
[8] J. Laane, E. Bondoc, S. Sakurai, K. Morris, N. Meinander, J. Cho, *J. Am. Chem. Soc.* **2000**, *122*, 2628.
[9] S. Moon, Y. Kwon, J. Lee, J. Choo, *J. Phys. Chem. A* **2001**, *105*, 3221 – 3225.
[10] D. Suárez, T. L. Sordo, J. A. Sordo, *J. Am. Chem. Soc.* **1996**, *118*, 9850 – 9854.
[11] J. Choo, S. Yoo, S. Moon, Y. Kwon, H. Chung, *Vib. Spectrosc.* **1998**, *17*, 173 – 182.
[12] R. Ahlrichs, M. Bär, M. Häser, H. Horn, C. Kölmel, *Chem. Phys. Lett.* **1989**, *162*, 165 – 169.
[13] A. Schäfer, C. Huber, R. Ahlrichs, *J. Chem. Phys.* **1994**, *100*, 5829 – 5835.
[14] C. Hättig, F. Weigend, *J. Chem. Phys.* **2000**, *113*, 5154 – 5161.
[15] C. Hättig, A. Köhn, *J. Chem. Phys.* **2002**, *117*, 6939 – 6951.
[16] C. Hättig, *J. Chem. Phys.* **2002**, *118*, 7751 – 7761.
[17] S. Grimme, M. Waletzke, *J. Chem. Phys.* **1999**, *111*, 5645 – 5655.
[18] A. D. Becke, *J. Chem. Phys.* **1993**, *98*, 1372 – 1377.
[19] C. Lee, W. Yang, R. Parr, *Phys. Rev. B* **1988**, *37*, 785 – 789.
[20] E. D. Glendening, A. E. Reed, J. E. Carpenter, F. Weinhold, *NBO Version 3.1*, Madison.
[21] *Gaussian 03* (Revision C.02), M. J. Frisch, G. W. Trucks, H. B. Schlegel, G. E. Scuseria, M. A. Robb, J. R. Cheeseman, J. A. Montgomery, Jr., T. Vreven, K. N. Kudin, J. C. Burant, J. M. Millam, S. S. Iyengar, J. Tomasi, V. Barone, B. Mennucci, M. Cossi, G. Scalmani, N. Rega, G. A. Petersson, H. Nakatsuji, M. Hada, M. Ehara, K. Toyota, R. Fukuda, J. Hasegawa, M. Ishida, T. Nakajima, Y. Honda, O. Kitao, H. Nakai, M. Klene, X. Li, J. E. Knox, H. P. Hratchian, J. B. Cross, V. Bakken, C. Adamo, J. Jaramillo, R. Gomperts, R. E. Stratmann, O. Yazyev, A. J. Austin, R. Cammi, C. Pomelli, J. W. Ochterski, P. Y. Ayala, K. Morokuma, G. A. Voth, P. Salvador, J. J. Dannenberg, V. G. Zakrzewski, S. Dapprich, A. D. Daniels, M. C. Strain, O. Farkas, D. K. Malick, A. D. Rabuck, K. Raghavachari, J. B. Foresman, J. V. Ortiz, Q. Cui, A. G. Baboul, S. Clifford, J. Cioslowski, B. B. Stefanov, G. Liu, A. Liashenko, P. Piskorz, I. Komaromi, R. L. Martin, D. J. Fox, T. Keith, M. A. Al-Laham, C. Y. Peng, A. Nanayakkara, M. Challacombe, P. M. W. Gill, B. Johnson, W. Chen, M. W. Wong, C. Gonzalez, J. A. Pople, Gaussian, Inc., Wallingford, CT, **2004**.
[22] H. C. Allen, P. C. Cross, *Molecular Vib-Rotors*, Wiley, New York, **1963**.
[23] "Step-Size Adaptation Based on Non-Local Use of Selection Information": A. Ostermeier, A. Gawelczyk, N. Hansen in *Lecture Notes in Com-*

puter Science: Parallel Problem Solving from Nature (PPSN III) (Eds.: Y. Davidor, H.-P. Schwefel, R. Männer), Springer, Heidelberg, **1994**.

[24] "The Second Harmonic Generation Case Study as a Gateway for ES to Quantum Control Problems": O. M. Shir, T. Bäck in *Proceedings of the Genetic and Evolutionary Computation Conference*, ACM Press, London, **2007**.

[25] I. Kalkman, C. Vu, M. Schmitt, W. L. Meerts, *ChemPhysChem* **2008**, *9*, 1788–1797.

[26] W. L. Meerts, M. Schmitt, *Int. Rev. Phys. Chem.* **2006**, *25*, 353–406.

[27] M. Schmitt, J. Küpper, D. Spangenberg, A. Westphal, *Chem. Phys.* **2000**, *254*, 349–361.

[28] J. R. Platt, *J. Chem. Phys.* **1949**, *17*, 484–495.

[29] F. Duschinsky, *Acta Physicochim. URSS* **1937**, *7*, 551–577.

[30] Y. R. Wu, D. H. Levy, *J. Chem. Phys.* **1989**, *91*, 5278–5284.

[31] J. A. Thomas, L. Alvarez-Valtierra, D. W. Pratt, *Chem. Phys. Lett.* **2010**, *490*, 109–115.

[32] F. Freeman, C. Lee, W. J. Hehre, H. N. Po, *J. Comput. Chem.* **1997**, *18*, 1392–1406.

[33] C. Ratzer, J. Küpper, D. Spangenberg, M. Schmitt, *Chem. Phys.* **2002**, *283*, 153–169.

[34] M. A. R. Matos, C. C. S. Sousa, V. M. F. Morais, *J. Phys. Chem. A* **2008**, *112*, 7961–7968.

These are not the final page numbers! ↗↗

ARTICLES

T. B. Chau Vu, C. Brand, W. L. Meerts, M. Schmitt*

■■ – ■■

Rotationally Resolved Electronic Spectroscopy of 1,4-Benzodioxan: The Anomeric Effect in the Ground and Electronically Excited State
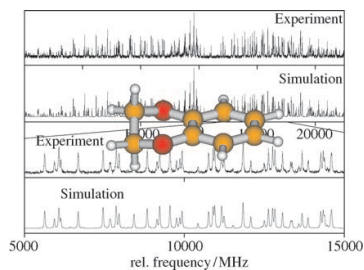
The structure of 1,4-benzodioxan is studied in the ground and first electronically excited singlet state using rotationally resolved electronic spectroscopy (see figure). The molecule is found to be more planar in the electronic ground state than in the electronically excited singlet state. This can be traced back to an increased puckering of the dioxan ring—which also comprises the oxygen atoms—in the excited state. The effect is discussed in terms of natural bond orbitals.

↖↖ **These are not the final page numbers!**

5.2   7-Azaindol Wasser-Cluster

Rotationally resolved electronic spectroscopy of water clusters of 7-azaindole

Thi Bao Chau Vu,[1] Ivo Kalkman,[2] W. Leo Meerts,[2] Yuriy N. Svartsov,[3] Christoph Jacoby,[1] and Michael Schmitt[1,a)]

[1]*Institut für Physikalische Chemie I, Heinrich-Heine-Universität, D-40225 Düsseldorf, Germany*
[2]*Department of Molecular and Laser Physics, Institute for Molecules and Materials, Radboud University Nijmegen, P.O. Box 9010 NL-6500 GL Nijmegen, The Netherlands*
[3]*Institut für Anorganische Chemie, Johannes Kepler Universität Linz, Altenbergerstraße 69, A-4040 Linz, Austria*

The rotationally resolved electronic spectra of the electronic origin of the 7-azaindole-$(H_2O)_1$ and of the 7-azaindole-$(H_2O)_2$ clusters have been measured in a molecular beam. From the rotational constants the structures in the S_0 and S_1 electronic states were determined as cyclic with the pyrrolo NH and the pyridino N atoms being bridged by one and two water molecules, respectively. Excited state lifetimes of about 10 ns for both clusters have been found. In the spectrum of the 7-azaindole-$(H_2O)_2$ cluster a splitting of the rovibronic band is observed, which can be traced back to a large amplitude motion, involving the out-of-plane hydrogen atoms of the water chain. Both the changes of the rotational constants upon electronic excitation and the orientation of the transition dipole point to a solvent induced state reversal between the L_a and the L_b states upon microsolvation. © *2008 American Institute of Physics*. [DOI: 10.1063/1.2928637]

I. INTRODUCTION

In a preceding theoretical study on the lowest electronically excited states of 7-azaindole and the 7-azaindole$(H_2O)_{1,2}$ clusters, the geometries, excitation energies, transition dipole orientations, and natures of the excited states have been predicted at the RICC2 and DFT/MRCI level of theory.[1] In the following some of these theoretical predictions will be tested, using rotationally resolved electronic spectroscopy of the 7-azaindole$(H_2O)_{1,2}$ clusters.

Laser spectroscopic investigations of the structures and photophysical properties of azaindole and its hydrogen and van der Waals bound clusters range back to the early 80s of the last century. Fuke *et al.*[2] measured mass-resolved ionization spectra and fluorescence excitation spectra of 7-azaindole, 7-azaindole$(H_2O)_{1,2}$, and (7-azaindole)$_2$. From the large spectral redshift (1285 cm^{-1}) they proposed a considerable distortion of the geometry upon electronic excitation of the water clusters.

Kim and Bernstein[3] presented mass-resolved excitation spectra of 7-azaindole and its clusters with Ar, CH_4, NH_3, H_2O, D_2O, CH_3OH, and C_2H_5OH. For the azaindole-water cluster they deduced a structure in which the water moiety is bound to the π-system instead of a hydrogen bonded structure.

Nakajima *et al.*[4] investigated the geometric structures of 7-azaindole$(H_2O)_{1-3}$ and of the 7-azaindole dimer using laser-induced fluorescence spectroscopy with high resolution (~0.01 cm^{-1}, equivalent to 300 MHz). They deduced a planar ring structure of 7-azaindole$(H_2O)_1$ from the rotational analysis of the spectrum and from *ab initio* calculations. For

the $n=2$ and 3 clusters, also cyclic hydrogen bonded ring structures with the water oxygen atoms in the aromatic plane were suggested.

In the work of Fomer *et al.* pump-probe experiments have been performed on the $n=2$, 3, and 4 water clusters of azaindole, which yield for the doubly and triply hydrated clusters biexponential decays with a short component (a few hundred femtoseconds) and a long component (6 ps). They attribute this behavior to a stepwise proton transfer from the $1H$ to the $7H$ position in the $n=2$ and 3 cluster, while a single exponential decay for the $n=4$ cluster was believed to be the signature of a concerted proton transfer.[5]

Yokoyama *et al.* performed IR-UV double resonance spectroscopy on 7-azaindole-water clusters together with *ab initio* molecular orbital calculations.[6] From their results hydrogen bonded single ring structures for the 7-azaindole$(H_2O)_n$ cluster with $n=1-3$ was deduced in the electronic ground state.

The structural changes of the 7-azaindole$(H_2O)_1$ cluster upon electronic excitation were determined from a Franck–Condon analysis of the emission spectra obtained via pumping of several vibronic bands.[7] The distances of both the $O \cdots H$ and the $H \cdots N$ hydrogen bond are found to decrease upon electronic excitation, accompanied by a distortion of the monomer geometry.

Dispersed fluorescence spectra of 7-azaindole$(H_2O)_{1-3}$ clusters were presented by Hara *et al.*[8] No visible emission from the proton transferred tautomers could be observed in their experiment, excluding the excited state proton transfer (ESPT) taking place in the gas phase on a time scale comparable to the fluorescence lifetime.

The geometrical changes of the 7-azaindole monomer itself were investigated using rotationally resolved electronic
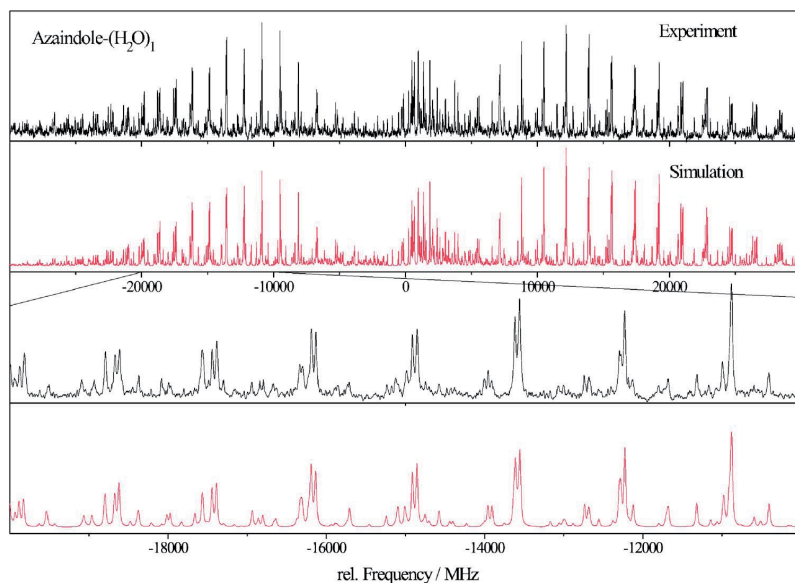
a)Electronic mail: mschmitt@uni-duesseldorf.de.

FIG. 1. (Color online) Rotationally resolved spectrum of the electronic origin of the 7-azaindole-$(H_2O)_1$ water cluster and simulation of the spectrum using the molecular parameters from the best GA fit, given in Table I. The lower two traces show an expanded view in the range of $-20\,000$ to $-10\,000$ MHz relative to the electronic origin.

spectroscopy of four different isotopomers of 7-azaindole[9,10] as well as a Franck–Condon analysis.[11] In Ref. 9 the nature of the electronically excited state has been shown to be predominantly of L_b character. Recently, the excited state dipole moment of 7-azaindole has been determined by Kang *et al.* from the Stark effect in a rotationally resolved LIF spectrum.[12]

II. EXPERIMENTAL METHODS

The experimental setup for the rotationally resolved laser-induced fluorescence is described in detail elsewhere.[13] Briefly, it consists of a ring dye laser (Coherent 899-21) operated with Kiton Red, pumped with 7 W of the frequency doubled output of a diode pumped Yb:YAG disc laser (TCFKA ELS). About 600–700 mW of the fundamental dye laser output is coupled into an external folded ring cavity (Spectra Physics) for second harmonic generation.

The molecular beam is formed by expanding azaindole heated to 100 °C and seeded in 300–700 mbars of argon through a 100 μm hole into the vacuum. The molecular beam machine consists of three differentially pumped vacuum chambers that are connected by two skimmers (1 and 3 mm, respectively) in order to reduce the Doppler width to 25 MHz. The molecular beam is crossed at right angles in the third chamber with the laser beam 360 mm downstream of the nozzle. The resulting fluorescence is collected perpendicular to the plane defined by laser and molecular beam by an imaging optics setup consisting of a concave mirror and two plano-convex lenses. The fluorescence is detected by a UV enhanced photomultiplier tube whose output is recorded by a PC based photon counter IO card. The relative frequency is determined with a quasiconfocal Fabry–Perot interferometer. The absolute frequency was determined by recording the iodine absorption spectrum and comparison the transitions to the tabulated lines.[14]

III. EXPERIMENTAL RESULTS

A. 7-azaindole($H_2O)_1$

Figure 1 shows the rotationally resolved spectrum of the electronic origin of 7-azaindole-$(H_2O)_1$. The spectrum spans about 60 GHz and displays a well resolved rovibronic structure with predominantly *ab*-hybrid type.

The molecular parameters obtained from a genetic algorithm (GA) based automated fit of the spectrum are given in Table I, and are compared to the results of various *ab initio* calculations for both electronic states. For details about the fitting procedure using the GA technique see Refs. 15–17. Although, as in the case of the azaindole monomer,[9] a simple rigid rotor Hamiltonian without axis reorientation was employed, all intensities and line positions are well reproduced (cf. Fig. 1). The slightly negative inertial defect ΔI and the negligible change of ΔI upon electronic excitation ($\Delta\Delta I$) point to nearly planar structures with at most one hydrogen atom pointing out of the molecular plane in both electronic states. The transition dipole moment, determined from the relative intensities of a and b lines in the spectrum, makes an angle of $\pm 27°$ with the inertial a axis, slightly different from the value, which has been obtained from a fit to the rovibronic contour ($\pm 16°$) taken at much lower resolution (300 MHz).[7] The polar angle ϕ, which introduces c-type character in the vibronic band was determined to be $\pm 86°$, meaning less than 1% c type. Thus, the transition dipole moment is located in the plane of the chromophore. For the discussion of the sign of the TDM angle θ, cf. Sec. IV B. The line shape was fitted to a Voigt profile with a Doppler contribution of 25 MHz, resulting in a Lorentz contribution of 15 ± 4 MHz.

The agreement between the experimental and computed rotational constants in both electronic states is very good for the time dependent density functional theory and the coupled cluster RICC2/TZVP *ab initio* calculations from Ref. 1

TABLE I. Comparison of the molecular parameters from the fit to the rotationally resolved electronic spectrum of 7-azaindole(H$_2$O)$_1$ shown in Fig. 1 to the results of *ab initio* calculations. (TD)DFT and RICC2 were performed with the TZVP basis. For details of the DFT/MRCI calculations, cf. part I of the present study (Ref. 1).

	Expt.	(TD)B3-LYP[a]	RICC2[a]	DFT/MRCI[a]	CAS(10,9)[b]
A'' (MHz)	1761.75	1775	1784	1784[c]	1780
B'' (MHz)	1342.80	1349	1353	1353[c]	1288
C'' (MHz)	762.89	768	771	771[c]	749
ΔI (amu Å^2)	−0.77	−1.31	−1.04	−1.04	−1.56
θ (°)	±27	−17	−3	+19	−89
ϕ (°)	±86	+90	+90	+89	+90
μ_a^2	0.777	0.914	0.995	0.896	0.000
μ_b^2	0.217	0.085	0.005	0.104	1.000
μ_c^2	0.006	0.000	0.000	0.000	0.000
ν_0 (cm^{-1})	33 340.43	32 360	33 288	33 214	37 320
ΔA (MHz)	35.97	25	35	35	−13[c]
ΔB (MHz)	15.34	15	14	14	−22[c]
ΔC (MHz)	11.80	9	11	11	−10[c]
$\Delta\Delta I$ (amu Å^2)	−0.09	0.45	−0.15	−0.15	0.23

[a]Calculations described in Ref. 1.
[b]Calculations described in Ref. 7.
[c]Structure used for the DFT/MRCI calculations is the RICC2/TZVP relaxed structure.

which are also given in Table I for comparison. The complete active space CAS(10,9)/cc-pVDZ calculations[7] agree well in the electronic ground state, but even the signs of the changes of the rotational constants upon electronic excitation are predicted wrongly for all rotational constants at this level of theory. The rotational constants reported for DFT/MRCI calculations are the ones of the relaxed RICC2 geometry, at which DFT/MRCI has been performed.[1]

The transition properties such as excitation energies and transition dipole moments are quite satisfactorily reproduced at RICC2/TZVP and even better at DFT/MRCI level, while the CASSCF calculations predict the band type completely wrong, and also the adiabatic excitation energy, which is off by nearly 4000 cm^{-1}.

B. 7-azaindole(H$_2$O)$_2$

Due to the large oscillator strength of transitions to the lowest electronically excited state of 7-azaindole, and the large stability of the hydrogen bonded water clusters, also higher water clusters can be observed with rotationally resolved electronic spectroscopy. Figure 2 shows the spectrum of the electronic origin of the 7-azaindole(H$_2$O)$_2$ cluster. In contrast to the case of the 1:1 cluster, the spectrum of the 1:2 cluster consists of two closely spaced components, with a splitting of 29 469 MHz, which can easily be determined in an autocorrelation of the spectrum. The spectrum has been fit using a rigid rotor Hamiltonian without axis reorientation, for each of the components using the GA technique, as for the 1:1 water cluster.

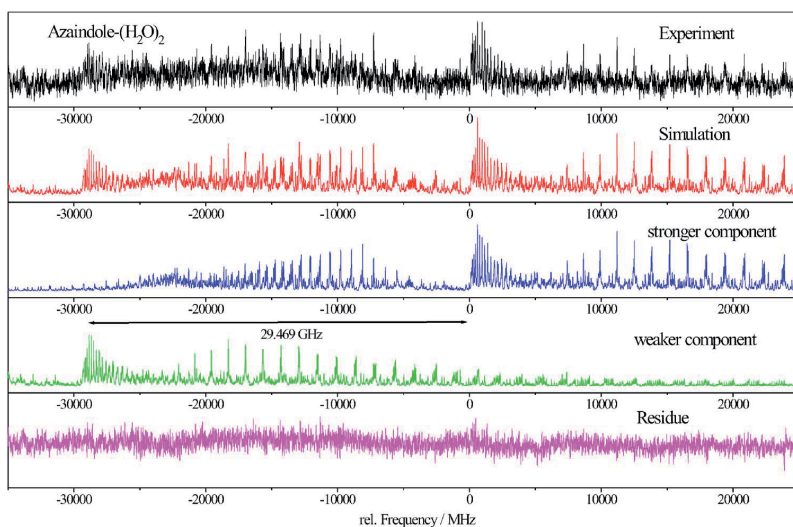FIG. 2. (Color online) Rotationally resolved spectrum of the electronic origin of 7-azaindole(H$_2$O)$_2$ and simulation of the spectrum using the molecular parameters from the best GA fit, given in Table II. The last trace shows the residue of the sum of the individual fits of the subcomponents and the experimental spectrum. Frequencies in megahertz are given relative to the origin of the stronger component.

TABLE II. Comparison of the molecular parameters from the fit with the rotationally resolved electronic spectrum of 7-azaindole(H_2O)$_2$ shown in Fig. 2 to the results of *ab initio* calculations. The (TD)DFT and RICC2 calculations are performed with the TZVP basis. For details of the calculations, cf. part I of the present study (Ref. 1).

	Expt. band 1	Expt. band 2	(TD)B3-LYP	RICC2	DFT/MRCI
A'' (MHz)	1413.81(25)	1415.46(52)	1424	1425	1425
B'' (MHz)	827.61(9)	828.00(18)	856	842	842
C'' (MHz)	524.02(5)	524.15(8)	537	533	533
ΔI (amu Å^2)	−3.7	−3.2	−5.0	−6.9	−6.9
θ (°)	±34	±35	−22	+16	+33.7
ϕ (°)	±74	±66	+90	+90	+87.1
μ_a^2	0.6336	0.5594	0.8536	0.9200	0.690
μ_b^2	0.2956	0.2805	0.1463	0.0799	0.307
μ_c^2	0.0708	0.1600	0.0001	0.0001	0.003
ν_0 (cm^{-1})	32 632.10	⋯	32 850	29 358	32 751
$\Delta\nu_0$ (MHz)	⋯	29469	⋯	⋯	⋯
ΔA (MHz)	9.35(3)	9.47(2)	+30	+5	+5
ΔB (MHz)	27.54(2)	27.38(5)	+31	+28	+28
ΔC (MHz)	12.59(2)	12.48(1)	+16	+16	+16
$\Delta\Delta I$ (amu Å^2)	−0.6	−0.5	−0.3	−0.7	−0.7

The rotational constants for both electronic states are given in Table II and are compared to the results of *ab initio* calculations. The agreement with the results of the time dependent DFT and the RICC2 calculations is as satisfying as for the $n=1$ cluster. The considerably larger inertial defect in both electronic states points to a slightly out-of-plane geometry for at least one of the heavy atoms. Comparison to the calculated structures shows that the oxygen atoms of both water moieties in the hydrogen bond chain are slightly out of plane—one being below, the other above the aromatic plane.

As can be already inferred from the strong and unusually sharp correlation side peak at a shift of 29 469 MHz relative to the unshifted autocorrelation, the rotational constants of the two subbands are very similar, cf. Table II. The nature of the large amplitude motion, responsible for the splitting in the spectrum will be investigated in detail in Sec. IV D.

The characteristics of the electronic excitation (adiabatic excitation energy and orientation of the transition dipole moment orientation are again well reproduced at the DFT/MRCI level of theory. The angle θ between the TDM and the a axis is determined to be ±34° from the intensities in the experimental spectrum and to +33.7 from the DFT/MRCI calculations.

As for the 7-azaindole(H_2O)$_1$ cluster, the line shape was fitted to a Voigt profile with a Doppler contribution of 25 MHz, resulting in a Lorentz contribution of 15±6 MHz.

C. Determination of the cluster structures

The partial intermolecular structures of the $n=1,2$ clusters have been determined from the rotational constants given in Tables I and II using the program PKRFIT.[18,19] The structures of the 7-azaindole monomer in both electronic states was taken from a combined structural fit to rotational constants of four different isotopomers and to the Franck–Condon intensities of 107 emission bands.[11] The OH distance in the water moiety was set to 96 pm, and the water HOH angle to 104°. Only three geometry parameters could

be determined, because for each cluster the rotational constants of only one isotopomer have been measured. For the $n=1$ cluster, the H_1O_8 bond length, the $N_1H_1O_8$ angle, and the $N_1H_1O_8H_{8b}$ dihedral angle have been chosen. The definitions of the distances, angles, and dihedral angles are given in Fig. 3. The second hydrogen bond length N_7H_{8a} was not included in the fit, but is obtained implicitly from the definition of the Z matrix used in the fit. A distinct shortening of both hydrogen bonds upon electronic excitation is found.

Table III presents the results of the fit. In addition to the three fitted parameters, the other three values which determine the intermolecular geometry are given for completeness.

For the $n=2$ cluster the restriction of the geometry model due to the small number of inertial parameters is even more unsatisfying. As for the binary cluster, the geometry of the monomer for both electronic states was taken from the Franck–Condon analysis presented in Ref. 11. Two hydrogen bond distances and the angle, which describes the deviation of the N-$H_1 \cdots O_8$ hydrogen bond from linearity were fitted.
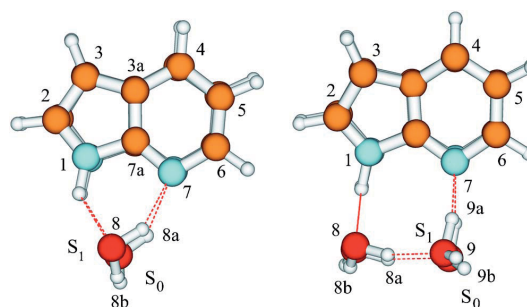

FIG. 3. (Color online) Structures of 7-azaindole(H_2O)$_1$ and 7-azaindole(H_2O)$_2$ in the ground and first excited singlet states from the fit to the rotational constants. The structures for both states are overlayed, with a maximum of congruence for the azaindole moiety. In each case, the upper structure shows the excited state.

TABLE III. S_0 and S_1 state geometry parameters (r_0) of the 7-azaindole(H_2O)$_{1,2}$ clusters, from the fit to the experimental rotational constants. All bond lengths are given in picometers, angles and dihedral angles are given in degrees.

| r_0 | 7-AI(H_2O)$_1$ | | r_0 | 7-AI(H_2O)$_2$ | |
	S_0	S_1		S_0	S_1
H_1O_8 [a]	215.3	195	H_1O_8 [b]	175.2	169.3
$N_1H_1O_8$ [a]	131	127	$H_{8a}O_9$ [a]	170.2	167.9
$N_1H_1O_8H_{8b}$ [a]	139	95	$O_8H_1N_1$ [a]	167	162
N_7H_{8a}	228.1	211.7	$O_9H_{8a}O_8$ [b]	167	162
$N_7H_{8a}O_8$	116	124	$H_{9a}N_7$	214.1	181.8
$H_1O_8H_{8b}$	110	110	$H_{9a}N_7O_9$	156	166

[a]Used in the fit.
[b]The angle $O_9H_{8a}O_8$ was kept fix at the fitted value of $O_8H_1N_1$.

Again, the last hydrogen bond length $H_{9a}N_7$ results automatically from the definition of the internal coordinates. As in the case of the 1:1 cluster, all hydrogen bond lengths decrease upon electronic excitation. Spectra of a much larger number of isotopomers will be necessary to completely unravel the structure of the $n=2$ cluster in both electronic states in the future.

IV. DISCUSSION

A. The structures of the clusters in ground and excited states

The comparison to calculated rotational constants shows, that both for the ground state and the excited state the $1H$ tautomer is experimentally observed, although the $7H$ tautomer is found to be considerably more stable in the S_1 state. Comparison to the results of the RICC2/TZVP calculations in Ref. 1 shows a large change of the geometry of the aza-indole monomer moiety upon water complexation in the electronically excited state, while the ground state geometry of 7-azaindole in the monomer and the water cluster is nearly the same. The reason for this strange behavior in the excited state is a solvent induced state reversal between the L_b and L_a states, the former being the S_1 state in the monomer, the latter in the 1- and 2-water clusters. Of special interest for future experiments will be the determination of selected geometry parameters of the monomer in the cluster, using isotopically substituted species and Kraitchmans equations. These present a direct access to the question of the electronic nature of the excited states.

Both hydrogen bond lengths in the 7-azaindole(H_2O)$_1$ cluster (H_1O_8 and N_7H_{8a}) are considerably shortened upon electronic excitation which can be explained by the increased excited state acidity of the pyrrole moiety and the increased basicity of the pyridine moiety in the first electronically excited $\pi-\pi^*$ state.[20] Figure 3 shows the simultaneous decrease of both hydrogen bonds in the excited state.

For the 7-azaindole(H_2O)$_2$ cluster, the H_1O_8 bond length also decreases upon electronic excitation. The hydrogen bond length between the two water moieties $H_{8a}O_9$ decreases slightly, due to polarization effects on both water moieties, mediated by the basicity increase of the pyridino N atom and the increase in acidity of the pyrrolo N(H) site.[21]

B. Orientation of the transition dipole

The orientation of the transition dipole moment in the 7-azaindole monomer was experimentally determined to be −14° (Ref. 10) or −20° (Ref. 9) with respect to the a axis. The minus sign refers to a orientation, in which the TDM points in direction of the pyrrolic NH group [orientation I in Fig. 4(a)]. The DFT/MRCI calculations, reported in part I (Ref. 1) of the present investigation, however, predict a TDM orientation of +20° [orientation II in Fig. 4(a)].

The orientation of the TDM in the water cluster is determined in the present work to be ±27° with respect to the a axis of the cluster. The RICC2/TZVP calculations, reported in part I (Ref. 1) which reproduce the experimental excited state rotational constants better than 1%, show that the angle of the inertial a-axis in the cluster with the $C_{3a}C_{7a}$ bond (cf.
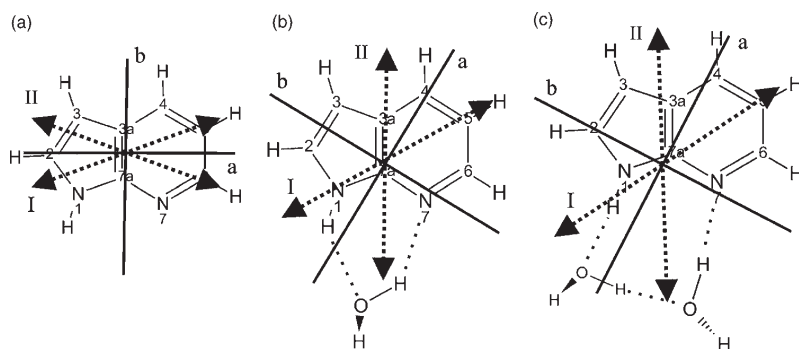

FIG. 4. Inertial axis systems and TDM orientations of 7-azaindole, 7-azaindole (H_2O)$_1$, and 7-azaindole (H_2O)$_2$.

Fig. 4) is 30°. In the monomer the angle between the *a* axis and the $C_{3a}C_{7a}$ bond is found to be 90°. Therefore, the inertial axis system in the frame of the azaindole monomer is rotated counterclockwise by 60° upon cluster formation, as shown in Fig. 4. The inertial axes of the monomer and the water clusters are shown with the azaindole monomer moieties oriented equally in Fig. 4.

If the positive sign of the TDM orientation in the $n=1$ cluster applies, as predicted by the DFT/MRCI calculations, the TDM would make an angle with the *a* axis of the monomer of −33° [orientation I in Fig. 4(b)]. If on the other hand the negative sign would apply, then the angle of the TDM with the *a* axis in the monomer geometry would be 87° (orientation II). This orientation is completely different from both orientations I and II in the 7-azaindole monomer.

For the $n=2$ cluster the rotation of the inertial axes upon water complexation is calculated from the geometries of the RICC2 calculations to be −70° [cf. Fig. 4(c)]. The experimentally determined angle of the TDM with the *a* axis in the inertial system of the cluster is ±34°, while DFT/MRCI predict in very good numerical agreement a value of +35°. In the inertial system of the monomer, this would correspond to angles of −35° for the + sign (close to orientation I in the monomer) or to 105° for the − sign (different from both orientations I and II). Again, the positive direction gives an orientation, similar to orientation I in the monomer.

Comparison of the experimental rotational constants of the azaindole monomer and the water clusters to the results of the RICC2 calculations for the lowest excited states showed that the excited state of the clusters has a completely different geometry from that of the monomer, while the ground state geometry is similar.[1] This points to a change of the ordering of the lowest two excited states upon cluster formation.

Summarizing these findings, it appears as if the TDM angle in the monomer should have a positive sign, as predicted by the DFT/MRCI calculations, but in contradiction to previous experiments. Since these experiments were performed independently in two different groups, the reason for this discrepancy is not easily allegeable. Maybe the assumption made in Refs. 9 and 10 in the interpretation that deuteration leaves the molecule electronically unchanged and rotates only the inertial axes is not correct. If one looks into the theoretical results for the other tautomer of 7-azaindole (the H being at the 7-position instead of the 1-position), the direction of the TDM is reversed between L_a and L_b compared to the "normal" 1*H* tautomer. If we now assume tunneling between the two positions (N_1 and N_7) to occur, the resulting TDM orientation might deviate from that of the pure 1*H*-7-azaindole. Since the barrier is high, most of the contribution to the TDM comes from the "normal" tautomer, but a small fraction is induced by the other tautomer. In the case of the deuterated isotopomer, tunneling is quenched, and the orientation is governed exclusively by the one of the "normal" tautomer. This means that the reason for the change of the angle might be different from what was assumed in both analyses (a pure effect of deuteration on the inertial axes).

C. Excited state lifetimes

The Voigt profiles of single rovibronic lines in the 7-azaindole$(H_2O)_1$ and 7-azaindole$(H_2O)_2$ spectra exhibit both Lorentz components of 15 ± 5 MHz. This broadening corresponds to an excited state life time of about 10 ns. This value is considerably larger than the excited state life time in the 7-azaindole monomer of 2.5 ns.[9] Huang *et al.* reported lifetimes of 8.1 ns for 7-azaindole$(H_2O)_1$ and of 6.6 ns for 7-azaindole$(H_2O)_2$ using time-correlated single-photon counting.[22] Folmer *et al.* found a biexponential decay with time constants of 360 and 6 ps in the excited state of 7-azaindole$(H_2O)_2$ using pump-probe spectroscopy.[5] They suggested that the existence of two different time constants points to a stepwise proton transfer reaction in the excited state. Later, Hara *et al.* showed that, in the fluorescence emission spectra of the 7-azaindole$(H_2O)_{1–3}$ clusters in a molecular beam, no visible fluorescence could be detected.[8] From that, they concluded that ESPT does not occur on the time scale of direct (resonant) fluorescence emission in the gasphase. Our present investigations sustain this conclusion. The much shorter transients, shown in Fig. 2 of Ref. 5, are recorded only up to 7 ps. Thus, it is possible that a much longer time component is contained in their transient. By-eye extrapolation of the data in Fig. 2 of Ref. 5 points to a remaining intensity offset, which might be a reminiscence of the slow component, observed in our cw experiment. Alternatively, the transients, which were observed on the different mass channels of the clusters in Ref. 5 might be contaminated by fragmentation from higher cluster sizes, thus yielding an averaged lifetime of many cluster sizes, including very large ones.

D. Internal motion in the 7-azaindole$(H_2O)_2$ cluster

The splitting, which is observed in the spectrum of the 7-azaindole$(H_2O)_2$ cluster, might be caused by the existence of two different conformers of the cluster, with a small spectral shift due to different zero-point-energy differences. Regarding the fact that the splitting is very small, the chromophore of the two conformers and its close vicinity must be very similar. One possibility for two different conformers in the 7-azaindole$(H_2O)_2$ cluster is shown in Fig. 5. Here, we plotted the potential energy for the tunneling motion, which interchanges the up and down hydrogen atoms in the water chain, projected to a one-dimensional reduced coordinate. The line of view is from the central hydrogen bond $(H_{8a} \cdots O_9)$ to the azaindole moiety, oriented as shown in Fig. 3. The global minimum has an up/down or down/up arrangement of the two H atoms of the water moieties. From this minimum, a transition state is reached, in which one of the two hydrogen atoms is in plane. By further rotation of this H atom in the same direction, a second (local) minimum is reached, in which both H atoms point down(up)wards. Both local minima with the hydrogens pointing both up or both down have the same energy as the up/down and down/up conformations of the global minimum. The stationary points along this coordinate have been calculated at the RICC2/TZVP level of theory for both electronic states. All energies, relative to the global minimum, are given at the
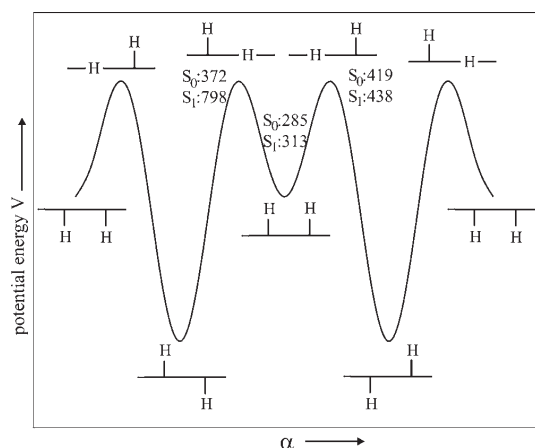
FIG. 5. One-dimensional potential energy curve of the tunneling coordinate in the 7-azaindole(H_2O)$_2$ cluster. The conformations of the stationary points have been depicted symbolically with the line of sight into the plane of the hydrogen bond ring and the azaindole monomer. The two out-of-plane hydrogen atoms are labeled by 8b and 9b in Fig. 3.

respective stationary points in Fig. 5. From the relative energies of the transition states in Fig. 5, it is clear that the arrangement with the in-plane hydrogen atom at the pyrrolo side has a slightly different energy than at the pyridino side.

A normal mode analysis at the level of structure optimization has been performed to check the right number of imaginary and nonimaginary frequencies for the minima and the transition states. The splitting in the spectrum would then arise from two transitions, connecting the global and the local minima in each electronic state [cf. Fig. 6(a)]. Since the ground state energy difference between the two conformers amounts only to 285 cm^{-1} (including zero-point-energy correction) and the barrier separating them is calculated to be 372 cm^{-1}, both conformers might be frozen out in the course
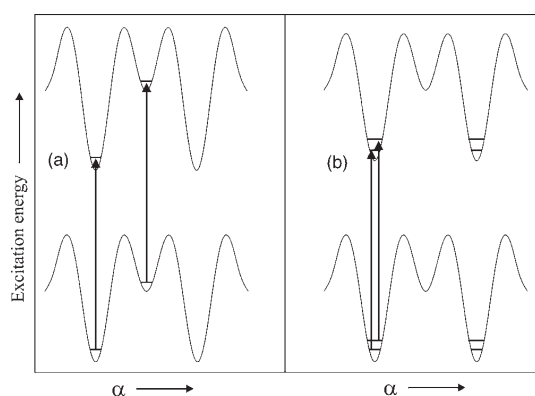

FIG. 6. Energy level scheme for the possible transitions in 7-azaindole(H_2O)$_2$. (a) Transitions between different conformers. The assumption is made that under the expansion conditions both conformers are frozen out simultaneously. (b) Transitions between different tunneling components of the most stable conformer, which in this model is frozen out exclusively in the supersonic expansion.

of the expansion, forming an intensity ratio between the two bands which is governed by the expansion conditions.

If on the other hand, only the most stable conformer is exclusively frozen out in the supersonic expansion; an alternative explanation for the splitting can be given on the basis of a tunneling splitting of the lowest vibrational level in the potential energy curve of Fig. 5, which differs from the excited state splitting by the absolute value of the observed splitting.

In the following we estimate the order of magnitude of the splitting. Since the energy differences of the various transition states (at least in the electronic ground state) are small, it is possible to approximate the potential by an expansion in cosine terms,

$$V_4 = \tfrac{1}{2}(V_2(1 - \cos 2\alpha) + V_4(1 - \cos 4\alpha)), \qquad (1)$$

with $V_2 = -290$ cm^{-1} and $V_4 = +200$ cm^{-1} in the electronic ground state.

Using the potential given above and a reduced torsional constant B of 23 cm^{-1}, which is typical for a hydroxy torsion,[23] a ground state torsional level splitting of 0.4 cm^{-1} is obtained using the analytical solutions from Ref. 24 of the Schrödinger equation with the Hamiltonian

$$H_T = B\frac{d^2}{d\alpha^2} + \tfrac{1}{2}\sum_n V_n(1 - \cos n\alpha), \qquad (2)$$

as implemented in the program HTORFIT, which is described in Ref. 25. For the excited state, a negligible splitting results due to the much higher barrier. Therefore, the very crude approximation that the potential in the excited state is also approximated by a sum of cosine terms does not influence the result. Inspection of Fig. 5 shows that, while the minima with the hydrogen pointing "ud" and "du" are exactly equal, there is a large difference in the relative transition state energies for the hydrogen atom at the pyrrolo side or at the pyridino side being in plane, respectively. Thus, a potential containing cosine and sine terms would be more appropriate. According to the fact that the barrier is much higher in the excited state a very small splitting would result in any of the model potential chosen. Regarding the fact that the above estimation contains a few very rough approximations, the appraised splitting is surprisingly close to the experimentally determined one. Nevertheless, one has to keep in mind that the estimation presented here is only meant to show the right order of magnitude for the splitting expected from the tunneling motion.

The two possible explanations for the splitting of the electronic origin of the 7-azaindole(H_2O)$_2$ cluster are depicted in Fig. 6. A distinction between these two possibilities seems to be difficult. In case (b), the relative intensities of the subbands will only depend on the spin statistical weights of the two components but not on the expansion conditions, since both transitions originate from the same ground state potential energy minimum. In case (a) the expansion conditions should alter the relative intensities. In none of the experiments we performed does a change of the relative intensities could be observed, which would point to case (b). Nevertheless, the range in which the expansion conditions

can be varied without loosing the cluster signal are quite small for the 7-azaindole(H_2O)$_2$ cluster. Thus, at the present moment, no definite answer can be given to this question. Since the chance of the difference of the two excitations originating from different minima on the potential energy surface shown in Fig. 6(a) being as small as observed experimentally, we strongly prefer the tunneling model [case (b)].

V. CONCLUSIONS

The structures of the 7-azaindole(H_2O)$_{1,2}$ clusters were determined in the S_0 and the S_1 state. Both in the ground and excited state cyclic hydrogen bonded clusters of the 1H tautomer were found, although in the excited state the 7H tautomer is more stable one. Of course, this is not in the Franck–Condon region for transitions from the 1H ground state.

Contrary to the case of the 7-azaindole monomer, we find the S_1 state in the microsolvated clusters to be of L_a character in Platts nomenclature (HOMO→LUMO). This conclusion can be drawn on the basis of the excited state structures, the transition dipole moment orientations and the adiabatic excitation energies.

The increased acidity of the pyrrolic NH group and the increased basicity of the pyridino N atom in the electronically excited state leads to a considerable shortening of both hydrogen bonds in the cyclic 7-azaindole(H_2O)$_1$ cluster.

Excited state lifetimes of 10 ns have been determined from the Lorentz contribution to the line profiles for both clusters, which are orders of magnitude larger that the two time constants for a biexponential decay, that has been measured by pump-probe spectroscopy.

The spectral splitting observed in the 7-azaindole(H_2O)$_2$ cluster can be explained on the basis of a tunneling motion, which interconverts the two out-of-plane hydrogen atoms of the hydrogen bond.

ACKNOWLEDGMENTS

[1] Y. N. Svartsov and M. Schmitt, J. Chem. Phys. **128**, 214310 (2008).
[2] K. Fuke, H. Yoshiuchi, K. Kaya, Y. Achiba, K. Sato, and K. Kimura, J. Phys. Chem. **88**, 5840 (1984).
[3] S. K. Kim and E. R. Bernstein, J. Phys. Chem. **94**, 3531 (1990).
[4] A. Nakajima, M. Hirano, R. Hasumi, K. Kaya, H. Watanabe, C. C. Carter, J. Williamson, and T. A. Miller, J. Phys. Chem. A **101**, 392 (1999).
[5] D. E. Folmer, E. S. Wisniewski, J. R. Stairs, and J. A. W. Castleman, J. Phys. Chem. A **104**, 10545 (2000).
[6] H. Yokoyama, H. Watanbe, T. Omi, S. Ishiuchi, and M. Fujii, J. Phys. Chem. A **105**, 9366 (2001).
[7] R. Brause, D. Krügler, M. Schmitt, K. Kleinermanns, A. Nakajima, and T. A. Miller, J. Chem. Phys. **123**, 224311 (2005).
[8] A. Hara, K. Sakota, M. Nakagaki, and H. Sekiya, Chem. Phys. Lett. **407**, 30 (2005).
[9] M. Schmitt, C. Ratzer, K. Kleinermanns, and W. L. Meerts, Mol. Phys. **102**, 1605 (2004).
[10] C. Kang, J. T. Yi, and D. W. Pratt, J. Chem. Phys. **123**, 094306 (2005).
[11] R. Brause, M. Schmitt, D. Spangenberg, and K. Kleinermanns, Mol. Phys. **102**, 1615 (2004).
[12] C. Kang, J. T. Yi, and D. W. Pratt, Chem. Phys. Lett. **423**, 7 (2006).
[13] M. Schmitt, J. Küpper, D. Spangenberg, and A. Westphal, Chem. Phys. **254**, 349 (2000).
[14] S. Gerstenkorn and P. Luc, *Atlas du Spectre d' Absorption de la Molécule d' iode* 14 800–20 000 cm^{-1} (CNRS, Paris, 1986).
[15] W. L. Meerts, M. Schmitt, and G. Groenenboom, Can. J. Chem. **82**, 804 (2004).
[16] W. L. Meerts and M. Schmitt, Phys. Scr. **73**, C47 (2005).
[17] W. L. Meerts and M. Schmitt, Int. Rev. Phys. Chem. **25**, 353 (2006).
[18] C. Ratzer, J. Küpper, D. Spangenberg, and M. Schmitt, Chem. Phys. **283**, 153 (2002).
[19] M. Schmitt, D. Krügler, M. Böhm, C. Ratzer, V. Bednarska, I. Kalkman, and W. L. Meerts, Phys. Chem. Chem. Phys. **8**, 228 (2006).
[20] J. Catalán and J. L. G. de Paz, J. Chem. Phys. **122**, 244320 (2005).
[21] J. Catalán, P. Pérez, J. C. del Valle, J. L. G. de Paz, and M. Kasha, Proc. Natl. Acad. Sci. U.S.A. **99**, 5799 (2002).
[22] Y. Huang, S. Arnold, and M. Sulkes, J. Phys. Chem. **100**, 4734 (1996).
[23] G. Berden, W. L. Meerts, M. Schmitt, and K. Kleinermanns, J. Chem. Phys. **104**, 972 (1996).
[24] J. D. Lewis, T. B. Malloy, Jr., T. H. Chao, and J. Laane, J. Mol. Struct. **12**, 427 (1972).
[25] C. Jacoby and M. Schmitt, ChemPhysChem **5**, 1686 (2004).

5.3   5-Methoxytryptamin

The conformational landscape of 5-methoxytryptamine studied by rotationally resolved fluorescence spectroscopy and resonant ionization spectroscopy

Thi Bao Chau Vu,[a] Ivo Kalkman,[b] W. Leo Meerts,[b] Christian Brand,[a]
Yuriy N. Svartsov,[a] Sascha Wiedemann,[a] Rainer Weinkauf[a] and Michael Schmitt*[a]

Rotationally resolved electronic spectra of three different conformers of 5-methoxytryptamine were recorded in a molecular beam. 5-Methoxy substitution reduces the number of observed conformers to three compared to seven that have been reported for tryptamine. Quantum chemical calculations indicate that *anti*-rotamers of the methoxy-group are more stable relative to the *syn*-forms. Two *gauche* structures (Gpy(in) and Gph(in)) of the ethylamino group with respect to the indole chromophore were found to be less stable than the other seven. The lowest electronically excited state has been identified as the ^1L_b one for all observed conformers which was confirmed by quantum-chemical calculations. Based on the comparison of rotational constants obtained from fits using evolutionary algorithms with those from calculations, the three observed conformers were determined to be the Gpy(up), Gph(up), Gpy(out) ethylamino side-chain conformations.

1. Introduction

Ethylamino substituted indole derivatives like tryptamine (2-(1H-indol-3-yl)ethanamine), serotonin (3-(2-aminoethyl)-1H-indol-5-ol), melatonin (N-[2-(5-methoxy-1H-indol-3-yl)ethyl]-ethanamide) and mexamin (2-(5-methoxy-1H-indol-3-yl)ethanamine) have found considerable interest due to their effect as neuro-transmitters, radiation protecting agents or sedatives. The present publication presents an investigation of the conformational isomers of mexamin (also called 5-methoxytryptamine) using a combination of low resolution ionization spectroscopy, rotationally resolved electronic spectroscopy, and *ab initio* theory.

The crystal structure of 5-methoxytryptamine has been determined to be monoclinic by X-ray crystallography. The ethylamino side-chain was found to be bent into the *gauche* or synclinal conformation.[1] Bayari and Ide presented a vibrational analysis of 5-methoxytryptamine in KBr using FTIR spectroscopy. Additionally they took the X-ray diffraction pattern of 5-methoxytryptamine and determined the preferential conformation in the crystal to be in *anti* position.[2]

Tryptamine has become a model system, for which the conformational landscape has been studied intensively over a long period.[3–10] The rotationally resolved electronic spectrum of tryptamine in a molecular beam has been reported several times in the past few years at increasingly good resolutions, thus unravelling more details of its conformational landscape.[6–10] Caminati determined the rotational constants of the A and B conformers of tryptamine in the electronic ground state using microwave spectroscopy and made an assignment to the structures based on *ab initio* calculations.[11] Dian *et al.* determined the energy thresholds between the different conformers of tryptamine using stimulated emission pumping-hole filling and stimulated emission pumping-induced population transfer spectroscopy.[12,13]

Improved theoretical methods for the description of electronically excited states facilitate the computation of various properties like structure, adiabatic excitation energies, permanent and transition dipole moments, *etc.* with nearly spectroscopic accuracy.[14]

Much less structural information can be found for serotonin and melatonin. LeGreve *et al.* performed laser induced fluorescence (LIF), resonance enhanced multiphoton ionization (REMPI), UV–UV double resonance (UV–UV DR) and resonant ion-dip infrared (RIDIR) spectroscopy on serotonin and identified 8 different conformers.[15] For melatonin Florio *et al.*[16] found and assigned five different conformers on the basis of IR–UV double resonance spectroscopy.

It has been found that small changes in the system like water attachment to flexible molecules can considerably change the energetics of the conformational landscape.[9] In this paper we address the question how a methoxy substitution in position 5 of the indole ring changes the conformational landscape of tryptamine. Since the distance between the methoxy and the ethylamino groups is considerably large, one would expect a very weak direct interaction and hence a negligible effect on conformational preferences. We will show in this paper that this is not the case.

[a] *Heinrich-Heine-Universität, Institut für Physikalische Chemie I, D-40225 Düsseldorf, Germany. E-mail: mschmitt@uni-duesseldorf.de*
[b] *Molecular and Biophysics Group, Institute for Molecules and Materials, Radboud University Nijmegen, NL-6500 GL Nijmegen, The Netherlands*

2.   Techniques

2.1   Experimental procedures

5-Methoxytryptamine (98%) was purchased from Sigma Aldrich and used without further purification. The experimental setup for the rotationally resolved laser induced fluorescence is described in detail elsewhere.[17] Briefly, the laser system consists of a single frequency ring dye laser (Coherent 899-21) operated with Kiton Red, pumped with 7 W of the 515 nm line of a frequency doubled cw Nd:YAG laser. The dye laser output is coupled into an external folded ring cavity (Spectra Physics Wavetrain) for second harmonic generation. The resulting output power was constant at about 15 mW during each experiment. The molecular beam is formed by co-expanding 5-methoxytryptamine, heated to 200 °C, and 200 mbar of argon through a 200 µm nozzle into the vacuum. The molecular beam machine consists of three differentially pumped vacuum chambers that are linearly connected by skimmers (1 and 3 mm, respectively) in order to reduce the Doppler width. The resulting resolution is 25 MHz in this setup (FWHM). In the third chamber, 360 mm downstream of the nozzle, the molecular beam crosses the laser beam at a right angle. The imaging optics setup consists of a concave mirror and two plano-convex lenses to collect the resulting fluorescence onto a photomultiplier tube, which is mounted perpendicular to the plane defined by the laser and molecular beam. The signal output is then discriminated and digitized by a photon counter and transmitted to a PC for data recording and processing. The relative frequency is determined with a quasi-confocal Fabry–Perot interferometer. The absolute frequency is obtained by comparing the recorded iodine absorption spectrum with tabulated lines.[18]

The experimental setup for the low-resolution REMPI experiment is described in detail elsewhere.[19] In short, the sample molecules are heated to 110 °C to form a suitable partial pressure in a pulsed valve (General Valve) flooded with 4 bar Ar carrier gas. The pulsed supersonic beam is pulsed into a first vacuum chamber, then skimmed after 30 mm and finally ionized ca 200 mm downstream the valve in a second vacuum chamber. Ions are accelerated in a two-stage ion source and mass detected in a linear time-of-flight mass spectrometer. For REMPI spectroscopy the gated ion signal is recorded in dependence on the laser wavelength. The excitation light was provided by a frequency-doubled conventional Nd:YAG laser-pumped dye laser (7 ns pulse width). The laser was used without lens to avoid saturation in the excitation processes (100 µJ pulse^{-1}, 4 mm^2 laser beam size).

2.2   Computational methods

2.2.1   Quantum mechanical calculations.
Structure optimizations were performed employing the valence triple zeta basis set with polarization functions (d,p) from the TURBOMOLE library.[20,21] The equilibrium geometries of the electronic ground states were optimized at the level of density functional theory using the B3-LYP-D functional[22] corrected for long range dispersion interactions.[23,24] These dispersion interactions account for interactions of the ethylamino side-chain with the π-system of the chromophore, present in the four *gauche* conformers. Zero-point energy correction was accounted for through vibrational harmonic frequencies which have been calculated through analytical second derivatives of the B3-LYP energies using the aoforce module[25,26] implemented in Turbomole Version 5.9.

2.2.2   The evolutionary algorithms for fitting of the rovibronic spectra.
The rotationally resolved electronic spectra were fit to a simple asymmetric rotor Hamiltonian using the derandomized-ES DR2 algorithm, an evolutionary strategy developed by Ostenmeier *et al.*[27] which has been shown recently to be a very good alternative for the automated assignment of rotationally resolved electronic spectra of molecules which are highly congested[28] compared to the genetic algorithm based fits we have employed so far.[29–32] Both strategies—the derandomized-ES DR2 algorithm and the genetic algorithm—belong to the category of global optimizers whose concepts are copied from evolutionary concepts in nature.

Their main difference lies in the fact that while the genetic algorithm tries to find a solution in parameter space by randomly combining information from a set of trial solutions, the steps in the DR2 algorithm are influenced by their history. In a first step, some trial solutions are generated from a random distribution around some starting point, each consisting of the complete parameter set necessary to describe the spectrum, and the quality of each solution is analyzed using a fitness function. If one of the solutions, obtained in the combination of information is better than the original one, this solution is selected and used to compute the next parent generation, which then serves as the starting point for an iteration of this cycle. In the calculation of the parent for the next generation the DR2 algorithm makes use of the correlation matrix for successive changes in the parents (mutations). This means that whenever for some parameter a parent has evolved in the same direction for several generations, so that their correlation in this parameter is positive, the most likely solution is assumed to be further in that direction and the next parameter mutation step will be larger. Correspondingly, two *anti*-correlated mutations will lead to a smaller mutation size.

3.   Results

3.1   Computational results

The structures of fourteen different conformers of 5-methoxy-tryptamine have been optimized at the B3-LYP-D/TZVP level of theory using dispersion corrected functionals from Grimme.[23,24] Using the notation of Carney *et al.*, these are labelled as Gpy(out), Gpy(up), Gph(out), Gph(up), Anti(py), Anti(ph), and Anti(up) conformers describing the orientation of the ethylamino side-chain with respect to the indole ring (*gauche* on the pyrrole side, *gauche* on the phenyl side or *anti*), and the orientation of the amino lone pair (pointing up, out, to the phenyl side or to the pyrrole side). Like in tryptamine itself, the (in) conformers of Gph and Gpy with the lone pair pointing to the aromatic ring are of much higher energy and will not be considered here. The number of possible conformers compared to tryptamine is doubled in
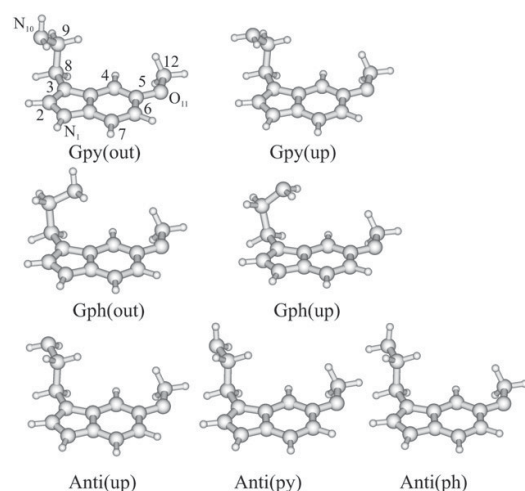
Fig. 1 DFT-D optimized *anti(OMe)* structures of seven conformers of 5-methoxytryptamine. The Gpy(out) structure contains the atomic numbering used in this publication.

5-methoxytryptamine, because the methoxy group in 5-position can be oriented in the direction of the ethylamino side-chain (*anti(OMe)*) or opposing the side-chain (*syn(OMe)*). All *syn(OMe)* conformers are at least 3.5 kJ/mole higher in energy than their *anti(OMe)* counterparts.

Fig. 1 shows the seven optimized *anti(OMe)* structures, Table 1 gives the rotational constants, inertial defects and relative energies of all rotamers (*syn(OMe)* and *anti(OMe)*) at the B3-LYP-D/TZVP level of theory. A complete analysis and comparison of the methoxytryptamine and serotonin conformational space is performed and will be published soon.[33]

While density functional theory does not account properly for the dispersive interactions between the ethylamino side-chain and the π-system of the chromophore and thus underestimates the energy differences of the *gauche* and the *anti* conformers, Møller–Plesset perturbation theory on second order (MP2) has been shown in related molecules like

tryptamine[12,14,34] and serotonin[15] to give the correct energy ordering of the conformers. Nevertheless, MP2 calculations are computationally very expensive compared to DFT methods. We therefore decided to use the dispersion corrected Becke-3LYP-D functional which has been shown to correctly account for dispersive van der Waals interactions.[23]

In contrast to the tryptamine case, where the Gpy(out) conformer was found to be the most stable one, we predict for 5-methoxytryptamine the Gph(out) conformer to be the most stable one. This agrees with MP2 calculations of LeGreve *et al.*[15] on 5-hydroxytryptamine conformers which find the Gph(out) conformer as most stable one, followed by the Gpy(out) conformer. DFT calculations, performed in the same work put the energy ordering as in the tryptamine case. This (incorrect) ordering was also found in a DFT study by van Mourik *et al.*[35] and shows the necessity of considering the dispersion forces correctly.

The quite large stabilization of the *gauche* conformers relative to the *anti* conformers is a consequence of the consideration of the long range dispersions and shows the advantage of the dispersion corrected density functionals over the standard ones, for the description of the conformational stabilities.

The vibrational frequencies of the Gpy(out) conformer in the range of the large amplitude torsional motions have been calculated for the electronic ground state using analytical second derivatives of the RIMP2 energy using the Aoforce module from the Turbomole package. The lowest frequency at 39.2 cm^{-1} can be assigned to the torsional motion τ_1 of the C3C8 bond. The energetically following vibration at 68.2 cm^{-1} is a bending motion of the ethylamino side-chain relative to the indole ring (β_1) with an admixture of methoxy bending. The vibration at 96.2 cm^{-1} is a combined methoxy and ethylamino bending mode. The torsional motion τ_2 about the C8C9 bond is found at 124.7 cm^{-1}. Further bands at 153.2 and 267.4 cm^{-1} can be assigned to combinations of bending and torsional motions mainly localized in the methoxy group and inversion motion at the indolic NH group. Out-of-plane vibrations of the indole chromophore at 169.9 and 212.1 cm^{-1} are assigned to the 10b and 10a vibrations in

Table 1 DFT-D (B3-LYP-D/TZVP) calculated rotational constants (*A*, *B*, *C*) the inertial defects (ΔI) and relative energies (ΔE) of fourteen conformers of 5-methoxytryptamine in their electronic ground state. Stabilization energies contain zero-point corrections using the B3-LYP/TZVP harmonic frequencies

Aoforce	Anti(OMe)						
	Gpy(out)	Gpy(up)	Gph(out)	Gph(up)	Anti(py)	Anti(ph)	Anti(up)
A/MHz	979	965	908	916	850	848	847
B/MHz	512	517	585	572	525	529	527
C/MHz	367	368	380	380	336	337	336
ΔI/amu Å^2	−126.2	−127.9	−90.5	−105.3	−53.1	−51.7	−51.5
ΔE/cm^{-1}	93.4	89.0	0	203.9	554.1	501.1	765.8

Anti	Syn(OMe)						
	Gpy(out)	Gpy(up)	Gph(out)	Gph(up)	Anti(py)	Anti(ph)	Anti(up)
A/MHz	1155	1141	1056	1064	990	991	989
B/MHz	443	445	496	491	448	449	447
C/MHz	348	349	358	360	318	318	318
ΔI/amu Å^2	−126.1	−130.5	−85.8	−100.4	−49.3	−46.3	−52.4
ΔE/cm^{-1}	408.9	420.6	509.8	529.7	829.1	859.4	458.1

Table 2 Vibrational frequencies below 300 cm^{-1} of the seven most stable Anti(OMe) conformers of 5-methoxytryptamine

Mode	Gpy(out)	Gpy(up)	Gph(out)	Gph(up)	Anti(py)	Anti(ph)	Anti(up)
τ_1	39.2	36.9	54.4	42.0	48.5	49.0	48.8
β_1	68.2	67.0	80.5	73.6	66.7	66.4	66.9
β_1	96.2	95.0	92.6	86.7	92.6	90.4	92.7
τ_2	124.7	119.1	126.8	124.2	98.3	98.3	97.9
$N_{inv.}$	153.2	153.2	152.7	152.2	153.3	153.2	153.4
10b	169.9	168.8	177.1	175.6	175.5	175.6	176.3
10a	212.1	209.8	220.3	209.1	202.9	201.0	201.1
$N_{inv.}$	267.4	266.7	262.8	266.6	239.0	239.6	261.3

the classification scheme of Varsanyi.[36] Most of the modes strongly couple methoxy and ethylamino torsional motions, so that no unequivocal description of the mode as in the case of tryptamine can be given. The approximate descriptions of the modes given in Table 2 have been taken from ref. 37. Table 2 compares the vibrational frequencies below 300 cm^{-1} of the seven Anti(OMe) conformers.

3.2 Low resolution R2PI spectra of 5-methoxytryptamine

Low-resolution R2PI spectra were recorded to obtain overview spectra and to identify spectral contributions of clusters with water. Fig. 2 shows the R2PI spectrum of 5-methoxytryptamine in the range between 32 450 and 32 950 cm^{-1}. Trace (a) shows the R2PI spectrum at m/z = 190 Da (the methoxytryptamine mass) using the methoxytryptamine sample as obtained. In a next step, to avoid contamination by methoxytryptamine–water cluster peaks, the sample was thoroughly dried. All peaks red to 32 700 and blue to 32 900 practically vanished as shown in trace (b). Trace (c) finally shows the R2PI spectrum with addition of 18 mbar of water to the Ar carrier gas, recorded at the mass channel of methoxytryptamine + water

(m/z = 208 Da). None of these bands could be detected on higher mass channels from larger water clusters. Thus, we tentatively assign all bands shown in trace (c) to the 5-methoxytryptamine(H$_2$O)$_1$ cluster. The spectrum is governed by long progressions in low frequency modes and differs considerably from the R2PI spectra of tryptamine(H$_2$O)$_1$[38] and indole(H$_2$O)$_1$.[39]

Four different bands can be assigned on the basis of the R2PI spectrum of Fig. 2b to belong to the 5-methoxytryptamine monomer. They are labelled by A–D according to their intensities. Band D at 32 844.73 cm^{-1} was too weak to obtain a rotationally resolved spectrum with a sufficiently good signal/noise ratio for assignment. Anyhow, from the frequency of 36.6 cm^{-1} relative to the origin of the A conformer, it is probable that this band represents a vibrational mode of the A conformer due to the torsional motion of the ethylamino side-chain about the C8C9 bond, *cf.* Table 2. Nevertheless, we cannot exclude completely a forth conformer for being responsible for this band. Rotationally resolved spectra of the three bands A–C will be presented in section 3.

3.3 High resolution spectra of conformers of 5-methoxytryptamine

Fig. 3 shows the rotationally resolved spectrum of the conformer A of 5-methoxytryptamine along with a simulation,

Fig. 2 (a) R2PI spectrum taken on the mass channel of 5-methoxytryptamine (m/z = 190 Da). (b) R2PI spectrum taken on the mass channel of 5-methoxytryptamine (m/z = 190 Da) after thorough drying of the sample. (c) R2PI spectrum taken on the mass channel of 5-methoxytryptamine(H$_2$O)$_1$ (m/z = 208 Da) after addition of 18 mbar of water to the Ar carrier gas. (d) Conditions like in (c), but spectrum taken at the mass channel 190 Da.

Fig. 3 Rotationally resolved electronic spectrum of the A band of 5-methoxytryptamine. The second trace shows the simulation using the best parameters from Table 3. The lowest traces show zoomed-in parts of the experimental spectrum and the simulation.

Table 3 Molecular constants of the three conformers of 5-methoxy-tryptamine obtained from ES-DR2 fits to the experimental spectra. The changes of the ground state rotational constants A'', B'', and C'' upon electronic excitation are defined as: $\Delta A = A' - A''$ etc., where A' are the rotational constants in the electronically excited state. ΔI is the inertial defect in amu Å^2 and $\Delta\Delta I$ its change upon electronic excitation

Exp.	Conf. A	Conf. B	Conf. C
A''/MHz	990.88(12)	914.40(11)	976.85(12)
B''/MHz	500.27(9)	569.18(8)	504.49(9)
C''/MHz	361.57(9)	376.74(8)	362.65(9)
ΔI/amu Å^2	−122.49	−99.14	−125.41
θ/°	78(6)	77(6)	80(6)
ϕ/°	40(6)	46(6)	45(6)
μ_a^2	57	46	49
μ_b^2	39	49	48
μ_c^2	4	5	3
τ/ns	11.2(24)	10.2(20)	—
ν_0/cm^{-1}	32 808.13(2)	32 733.82(2)	32 763.49(2)
ΔA/MHz	−5.44(3)	−7.45(3)	−5.09(3)
ΔB/MHz	−3.22(4)	−2.38(4)	−3.06(4)
ΔC/MHz	−2.49(4)	−2.23(4)	−2.18(4)
$\Delta\Delta I$/amu Å^2	−122.14	−99.40	−125.80

using the best parameters from the derandomized-ES DR2 fit given in Table 3. The uncertainties of the parameters are given in parentheses and are obtained as standard deviations by performing a quantum number assigned fit. In this fit those transitions obtained from the derandomized-ES DR2 fit are included that would be used in a typical manual assignment of the spectra, that is transitions with intensity larger than 5% of the maximum intensity and with rotational quantum numbers up to $J = 10$.

Even what appears to be single rovibronic lines in the P or R branch of the simulated spectrum are superpositions of some ten rovibronic transitions. This fact highlights the necessity for an automated fitting technique like the evolutionary strategies employed here. Band A at 32808.13 cm^{-1} is predominantly an ab hybrid type transition. with 57% a-type, 39% b-type, and 4% c-type character. The lifetime is determined to be around 10 ns from a Lorentz contribution of 14 MHz to the full Voigt

line width. From the rotational constants an inertial defect of −122.5 amu Å^2 for the ground state and of −122.1 amu Å^2 for the electronically excited state is calculated.

The high resolution spectrum of the B band of 5-methoxytryptamine at 32 733.8 cm^{-1} is shown in Fig. 4. Like band A, this transition is predominantly polarized in the ab plane, with an excited state lifetime of approximately 10 ns. The inertial defect in the ground state is −99.14 amu Å^2 and in the excited state −99.40 amu Å^2, considerably smaller than in the A conformer.

Fig. 5 shows the high resolution spectrum of band C at 32763.5 cm^{-1}. This band consists of two rovibronic spectra, separated by ca 2000 MHz. One of these spectra is unambiguously fitted with the molecular parameters given in Table 3. The spectral features of the other component are too different ($cf.$ the lowest trace in Fig. 5, which gives the residue of the experimental and simulated spectrum) to be due to another 5-methoxytryptamine conformer. It consists more or less only of a pronounced Q-branch structure, with hardly any P or R band intensity. The mass spectrum shows a mass of 161 coming up, while scanning over band C. This might be a fragment from 5-methoxytryptamine, formed by thermal decomposition in the source, cleaving a CH–NH$_2$ fragment, and leaving 3-methyl-5-methoxyindole. Since the chromophore and its direct surrounding are the same to 5-methoxytryptamine it is not improbable that the absorption takes place spectrally very close.

The density of lines in band C of methoxytryptamine is so high (mainly due to the overlapping second band), that no reliable Lorentzian width can be determined and, consequently, no lifetime is given in Table 3. The inertial defect of band C is −125.41 amu Å^2 in the ground state and −125.80 amu Å^2 in the electronically excited state, thus the largest of all three conformers.

The changes of the rotational constants upon electronic excitation of the three conformers are all negative, quite small and similar, in contrast to the changes in tryptamine.[9]
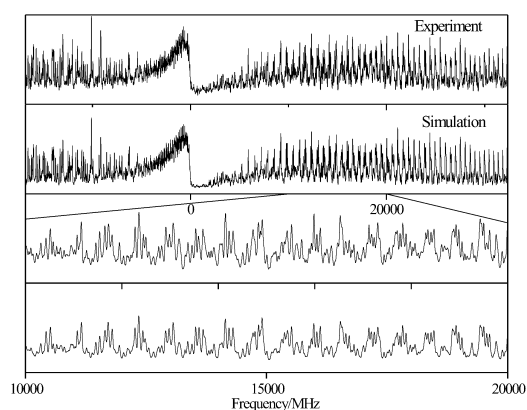

Fig. 4 Rotationally resolved electronic spectrum of band B of 5-methoxytryptamine. The second trace shows the simulation using the best parameters from Table 3. The lowest traces show zoomed-in parts of the experimental spectrum and the simulation.
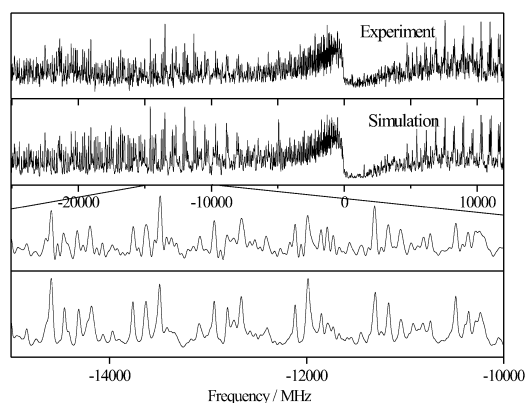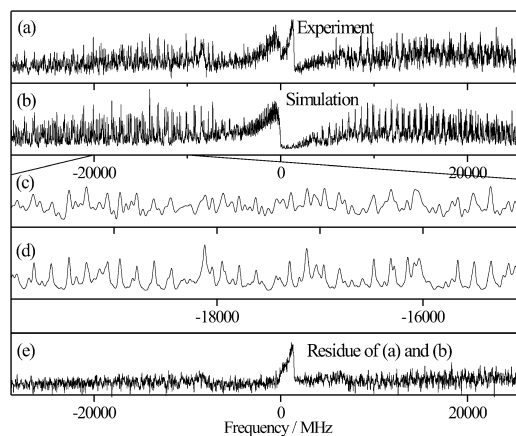

Fig. 5 Rotationally resolved electronic spectrum of band C of 5-methoxytryptamine. The second trace shows the simulation using the best parameters from Table 3. The next two traces show zoomed-in parts of the experimental spectrum and the simulation. The lowest trace gives the residue of the experimental and simulated spectrum.

4. Discussion

The R2PI spectra of 5-methoxytryptamine show a considerable number of bands, which belong to the clusters with water. Differing from the tryptamine case a number of cluster bands appear. Although the clusters with water are not the central topic of this publication we also tried to record the rotationally resolved spectra of the clusters. Unfortunately, we did not succeed in getting any high resolution spectrum of the clusters of methoxytryptamine with water. This is probably due to the very different expansion conditions in the pulsed R2PI and the continuous LIF experiment. Further work is on the way, to adapt the expansion conditions in the cw experiment in order to be able to record the high resolution spectra of the clusters with water as well.

4.1 Assignment of the conformers

The assignment of the three origin bands of 5-methoxytryptamine conformers to the structure only on the basis of their rotational constants is difficult, because the calculated differences within the Gpy, the Gph, and the Anti families are small (*cf.* Table 1), while the distinction between the *syn*(*OMe*) and *anti*(*OMe*) structures poses no problems. Table 4 gives the χ^2 values for the calculated and experimental rotational constants for the four different *Anti*(*OMe*) *gauche* conformers.

The assignment for band B, being due to the *Anti*(*OMe*)-Gph(up) conformer from the χ^2 value is straightforward. The assignment of structures to bands A and C on the basis of the least squares of the rotational constants only is not so unambiguous, because both Gpy(out) and Gpy(up) structures have small χ^2 values for the A as well as for band C.

Therefore, in addition to the least squares of the calculated and the experimental rotational constants, we also employed the differences of rotational constants between the conformers under consideration and the inertial defects of the conformers. Table 5 shows the differences of the experimental rotational constants and inertial defect of conformers A and C compared to the difference of the calculated Gpy(out) and Gpy(up) rotational constants and their inertial defect. Since differences of calculated rotational constants show less errors as the absolute numbers, we present the differences of the experimental and calculated rotational constants between A and C in Table 5. The good agreement and the correct sign show that this assignment is right. Note that a reversed assignment would especially lead to switching of the signs.

Table 4 χ^2 values $((A_{\exp} - A_{calc})^2/\sigma_A^2 + (B_{\exp} - B_{calc})^2/\sigma_B^2 + (C_{\exp} - C_{calc})^2/\sigma_C^2)$ obtained from experimental rotational constants ($A_{\exp}$, $B_{\exp}$, and $C_{\exp}$) and their standard deviations (σ_A, σ_B, and σ_C) from Table 3 for the three different bands A, B and C and calculated rotational constants (A_{calc}, B_{calc}, and C_{calc}) from Table 1 for the *Anti*(OMe) conformers of Gpy(out), Gpy(up), Gph(out), and Gph(up)

Conf.	Gpy(out)	Gpy(up)	Gph(out)	Gph(up)
A	30 428	86 171	1 405 272	1 066 519
B	870 580	648 966	44 151	3115
C	9620	32 606	1 166 582	856 963

Table 5 Ground state difference of the rotational constants ($\Delta A'' = A''$(conformer A)–A''(conformer C); $\Delta B''$, and $\Delta C''$, respectively) and difference of the inertial defect ($\Delta\Delta I''$) of conformer A and conformer C ($\Delta\Delta I'' = \Delta I''$(conformer A)–$\Delta I''$(conformer C)) compared to the respective calculated difference of *gauche* pyrrole out and up obtained from the DFT-D calculations

	Gauche pyrrole	
	Experiment	Calculated
	conf.*A*–conf.*C*	out-up
$\Delta A''$/MHz	14.1	14
$\Delta B''$/MHz	−4.8	−5
$\Delta C''$/MHz	−1.1	−1
$\Delta\Delta I''$/amu Å^2	3.0	1.69

4.2 Determination of the structure parameters

The determination of only three rotational constants for each conformer allows of course only the determination of three geometrical parameters, keeping all others fixed. We performed a fit of angle α_1 (C8C9N10), the dihedral angles dih$_2$ (C3C8C9N10), and dih$_3$ (C2C3C8C9) (*cf.* Fig. 1 for the atomic numbering) with all other geometry parameters held fixed at the values of the DFT-D optimized structures using the program pKrFit.[40,41] The resulting structural parameters in Table 6 are r_0 parameters, incorporating the effects of zero-point motions. Further investigations with other isotopomers have to be performed to further refine these results.

4.3 Orientation of the transition dipole moment

The transition dipole moment (TDM) in all three conformers is located in the *ab* plane, and oriented as shown in Fig. 6 and Table 7. There are two possible orientations of the transition dipole moment (I and II in Fig. 6), since the relative intensities of the rovibronic bands in the experimental spectra depend on the projection of the TDM onto the inertial axes. Comparing this orientation to the results of DFT/MRCI calculations on TDDFT/TZVP optimized structures,[33] and to the orientation of the transition dipole moment in the lowest electronically excited state of tryptamine[5] and 5-methoxyindole[42] it is found that orientation I is observed, which corresponds to that of the L_b state. Thus, like for tryptamine itself, the lowest electronically excited state is L_b. The experimental adiabatic excitation energy for the Gph(up) conformers is 32 734 cm^{-1}, for Gpy(out) 32 808 cm^{-1}, and for Gpy(up) 32 763 cm^{-1}.

They are compared in Table 7 to the excitation energies of the respective tryptamine conformers. The relative excitation energies have the same energetic ordering as in tryptamine, thus further confirming the assignment of the absorption features to the geometries of the described conformers.

Table 6 Fitted geometry parameters of the three 5-methoxytryptamine conformers studied in this work. For the definition of the angles and dihedral angles *cf.* Fig. 1

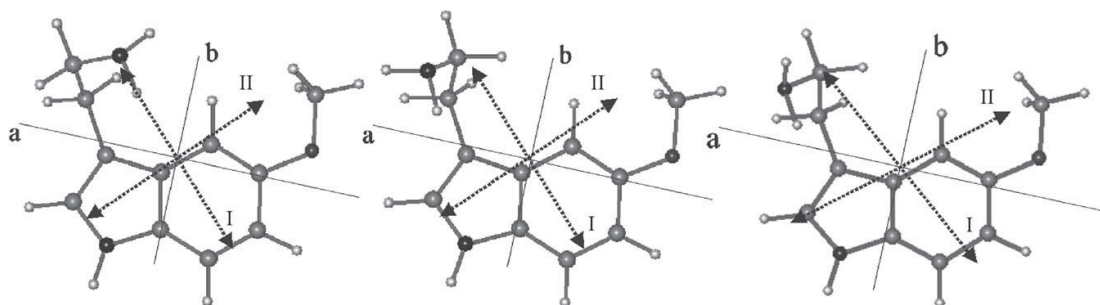|	α_1 C8C9N10	dih$_2$ C3C8C9N10	dih$_3$ C2C3C8C9
Gpy(out)	111.08(20)	−65.58(4)	102.23(2)
Gph(up)	112.86(23)	68.85(3)	90.72(1)
Gpy(up)	116.57(22)	−63.38(4)	103.8(2)

Fig. 6 Orientation of the transition dipole moment in the inertial frame of the Gph(up), Gpy(up), and Gpy(out) conformers of 5-methoxytryptamine.

Table 7 Comparison of adiabatic excitation energies and transition dipole moment orientations in tryptamine and 5-methoxytryptamine

(OMe)	Tryptamine				5-Methoxytryptamine			
	ν_0	$\Delta\nu_0$	ϕ	θ	ν_0	$\Delta\nu_0$	ϕ	θ
Gph(up)	34 832	0	81	14	32 734	0	77	46
Gpy(up)	34 896	64	72	22	32 763	29	80	46
Gpy(out)	34 916	84	72	14	32 808	74	80	39

5. Conclusions

The rotationally resolved electronic spectra of three different conformers of 5-methoxytryptamine were analyzed and assigned to the Gph(up) (band B), the Gpy(out) (band A), and the Gpy(up) (band C) structures. Band D can be tentatively assigned to the torsional motion τ_1 of the ethylamino side-chain of conformer A. The experimental frequency is 36.6 cm^{-1}, the calculated frequency (RIMP2/TZVP) of the Gpy(out) conformer 39.2 cm^{-1}. The same vibrational band for the Gph(up) conformer is calculated to be 42 cm^{-1} and shows very weakly up in the red wing of band C, while for the Gpy(up) conformer it is calculated to be 36.9 cm^{-1}, weakly showing up red to the origin of band A. The origin bands of all three conformers belong to the ^1L_b electronic state. Good agreement is found between the experimental rotational constants and those extracted from optimized structures, using dispersion corrected density functionals. These structures closely resemble the experimentally found ones, with an energy ordering of Gph(out) < Gpy(up) < Gpy(out) < Gph(up) < Anti(ph) < Anti(py) < Anti(up). This energetic ordering of conformers is the same that LeGreve et al.[15] have found for the similar 5-hydroxytryptamine system, showing the reliability of the dispersion correction for examination of the conformational spaces of this class of molecules. The three most stable structures are in good agreement with the experiment.

In 5-methoxytryptamine only *Anti(OMe)* structures of the methoxy group and *gauche* structures of the ethylamino side-chain are found. Since tryptamine itself has already 7 low-lying thermally populated conformers and the methoxy group in 5-methoxytryptamine adds one more conformational dimension to this, one would expect to observe even more than 7 conformers. Instead, only 3 conformers of 5-methoxytryptamine are found in the experiment. It is improbable that some of the

conformers have much shorter lifetimes which may prevent them from being observed in a highly resolving experiment. Therefore, the reason for the preferential stabilization of the *gauche* conformers in methoxytryptamine must be a changed electrostatic interaction of the ethylamino side-chain with the indole chromophore upon substitution with a methoxy group in 5-position.

References

1 W. G. Quarles, D. H. Templeton and A. Zalkin, *Acta Crystallogr., Sect. B*, 1974, **30**, 95–98.
2 S. Bayari and S. Ide, *Spectrochim. Acta*, 2003, **A59**, 1255–98.
3 Y. D. Park, T. R. Rizzo, L. A. Peteanu and D. H. Levy, *J. Chem. Phys.*, 1986, **84**, 6539–6549.
4 J. R. Carney and T. S. Zwier, *J. Phys. Chem. A*, 2000, **104**, 8677.
5 L. Pei, J. Zhang, C. Wu and W. Kong, *J. Chem. Phys.*, 2006, **125**, 024305-1–024305-8.
6 L. A. Philips and D. H. Levy, *J. Chem. Phys.*, 1988, **89**, 85–90.
7 Y. R. Wu and D. H. Levy, *J. Chem. Phys.*, 1989, **91**, 5278–5284.
8 T. Nguyen, T. Korter and D. Pratt, *Mol. Phys.*, 2005, **103**, 1603–1613.
9 M. Schmitt, M. Böhm, C. Ratzer, C. Vu, I. Kalkman and W. L. Meerts, *J. Am. Chem. Soc.*, 2005, **127**, 10356–10364.

10 T. Nguyen and D. Pratt, *J. Chem. Phys.*, 2006, **124**, 054317-1–054317-6.
11 W. Caminati, *Phys. Chem. Chem. Phys.*, 2004, **6**, 2806–2809.
12 J. R. Clarkson, B. C. Dian, L. Moriggi, A. DeFusco, V. McCarthy, K. D. Jordan and T. S. Zwier, *J. Chem. Phys.*, 2005, **122**, 214311-1–214311-15.
13 B. C. Dian, J. Clarkson and T. S. Zwier, *Science*, 2004, **303**, 1169–1173.
14 M. Schmitt, R. Brause, C. Marian, S. Salzmann and W. L. Meerts, *J. Chem. Phys.*, 2006, **125**, 124309-1–124309-10.
15 T. A. LeGreve, E. E. Baquero and T. S. Zwier, *J. Am. Chem. Soc.*, 2007, **129**, 4028–4038.
16 G. M. Florio, R. A. Christie, K. D. Jordan and T. S. Zwier, *J. Am. Chem. Soc.*, 2002, **124**, 10236–10247.
17 M. Schmitt, J. Küpper, D. Spangenberg and A. Westphal, *Chem. Phys.*, 2000, **254**, 349–361.
18 S. Gerstenkorn and P. Luc, *Atlas Du Spectre D'absorption De La Molécule D'iode*, CNRS, Paris, 1982.
19 S. Wiedemann, A. Metsala, D. Nolting and R. Weinkauf, *Phys. Chem. Chem. Phys.*, 2004, **6**, 2641–2649.
20 R. Ahlrichs, M. Bär, M. Häser, H. Horn and C. Kölmel, *Chem. Phys. Lett.*, 1989, **162**, 165–169.
21 A. Schäfer, C. Huber and R. Ahlrichs, *J. Chem. Phys.*, 1994, **100**, 5829–5835.
22 A. D. Becke, *J. Chem. Phys.*, 1993, **98**, 5648–5652.
23 S. Grimme, *J. Comput. Chem.*, 2007, **25**, 1463–1473.
24 S. Grimme, *J. Comput. Chem.*, 2006, **27**, 1787–1799.
25 H. Horn, H. Weiss, M. Häser, M. Ehrig and R. Ahlrichs, *J. Comput. Chem.*, 1991, **12**, 1058.
26 P. Deglmann, F. Furche and R. Ahlrichs, *Chem. Phys. Lett.*, 2002, **362**, 511–518.
27 A. Ostenmeier, A. Gawelcyk and N. Hansen, in *Parallel Problem Solving from Nature, PPSN III*, ed. Y. Davidor, H.-P. Schwefel and R. Männer, Springer, Berlin/Heidelberg, 1994.
28 I. Kalkman, C. Vu, M. Schmitt and W. L. Meerts, *ChemPhysChem*, 2008, **9**, 1788–1797.
29 J. A. Hageman, R. Wehrens, R. de Gelder, W. L. Meerts and L. M. C. Buydens, *J. Chem. Phys.*, 2000, **113**, 7955–7962.
30 W. L. Meerts, M. Schmitt and G. Groenenboom, *Can. J. Chem.*, 2004, **82**, 804–819.
31 W. L. Meerts and M. Schmitt, *Phys. Scr.*, 2005, **73**, C47–C52.
32 W. L. Meerts and M. Schmitt, *Int. Rev. Phys. Chem.*, 2006, **25**, 353–406.
33 Y. Svartsov and M. Schmitt, in preparation, 2009.
34 Y. K. Sturdy and D. C. Clary, *Phys. Chem. Chem. Phys.*, 2007, **9**, 2065–2074.
35 T. van Mourik and L. E. V. Emson, *Phys. Chem. Chem. Phys.*, 2002, **4**, 5863–5871.
36 G. Varsanyi, *Assignments for Vibrational Spectra of 700 Benzene Derivatives*, Wiley, New York, 1974.
37 M. Schmitt, K. Feng, M. Böhm and K. Kleinermanns, *J. Chem. Phys.*, 2006, **125**, 144303-1–144303-9.
38 L. A. Peteanu and D. H. Levy, *J. Chem. Phys.*, 1988, **92**, 6554–6561.
39 J. R. Carney and T. S. Zwier, *J. Phys. Chem. A*, 1999, **103**, 9943–9957.
40 C. Ratzer, J. Küpper, D. Spangenberg and M. Schmitt, *Chem. Phys.*, 2002, **283**, 153–169.
41 M. Schmitt, D. Krügler, M. Böhm, C. Ratzer, V. Bednarska, I. Kalkman and W. L. Meerts, *Phys. Chem. Chem. Phys.*, 2006, **8**, 228–235.
42 B. Albinsson and B. Nordén, *J. Phys. Chem.*, 1992, **96**, 6204.

5.4 Tryptamin

J|A|C|S

A R T I C L E S

Structural Selection by Microsolvation: Conformational Locking of Tryptamine

Michael Schmitt,*,† Marcel Böhm,† Christian Ratzer,† Chau Vu,† Ivo Kalkman,‡ and W. Leo Meerts*,‡

Contribution from the Institut für Physikalische Chemie, Heinrich-Heine-Universität, D-40225 Düsseldorf, Germany, and Molecular and Biophysics Group, Institute for Molecules and Materials, Radboud University Nijmegen, P.O. Box 9010, NL-6500 GL Nijmegen, The Netherlands

Received April 7, 2005; E-mail: mschmitt@uni-duesseldorf.de; Leo.Meerts@science.ru.nl

Abstract: The conformational space of tryptamine has been thoroughly investigated using rotationally resolved laser-induced fluorescence spectroscopy. Six conformers could be identified on the basis of the inertial parameters of several deuterated isotopomers. Upon attaching a single water molecule, the conformational space collapses into a single conformer. For the hydrogen-bonded water cluster, this conformer is identified unambiguously as tryptamine *A*. In the complex, the water molecule acts as proton donor with respect to the amino group. An additional interaction with one of the aromatic C−H bonds selectively stabilizes the observed conformer more than all other conformers. Ab initio calculations confirm much larger energy differences between the conformers of the water complex than between those of the monomers.

Introduction

Conformation of molecules plays an important role in reactions of organic and biochemically relevant molecules. Still, little is known about the effect of solvents on conformations, in particular, in small systems. The conformational landscape even of small aromatic molecules with an ethylamine side chain like tryptamine comprises many structurally different, but nearly equally stable conformations. Tryptamine possesses 27 conformers from three 3-fold rotations in and of the alkylamino side chain (cf. Figure 1): two around the C−C single bonds, and one around the C−N bond. In 9 of these 27 conformers, the $C_\alpha H_2$−NH_2 tail of the alkylamino group is oriented perpendicular to the aromatic plane. These nine conformers have been calculated to have energies considerably lower than those of the remaining ones.[1] Surprisingly, the multitude of conformers reduces to a single one upon complex formation with just one water molecule.[2] In the present work, we study the reason for this locking of the conformational variety to a single structure. This is an interesting subproblem in the more general context of the induced fit principle,[3] which describes the predisposition of a flexible ligand toward a coordination partner or of the lock and key principle,[4] which describes the static behavior of a preorganized ligand toward one or more coordination partners. A more flexible model for describing these kinds of conformational complementarities has been proposed by Kumar et al.[5]
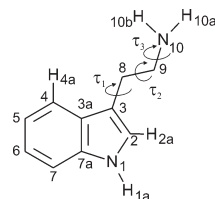
Figure 1. Atomic numbering and definitions of the geometry parameters used in the fit. τ_1 is the dihedral angle defined by the atoms C_2,C_3,C_8,C_9, τ_2 for C_3,C_8,C_9,N_{10}, and τ_3 for the dihedral angle C_8,C_9,N_{10},H_{10b}, where H_{10b} designates the hydrogen atom that is closest to the indole ring.

All three models have far reaching implications for molecular recognition processes.

Pioneering experimental work on the different conformers of tryptamine was performed in a molecular beam using rotationally resolved LIF spectroscopy by Philips and Levy at a spectral resolution of 0.07 cm^{-1}.[6] The triply deuterated conformers were investigated by Wu and Levy[7] of the same group. The conformers were analyzed using the rotational constants[8] of undeuterated and deuterated tryptamines. Seven different conformers were identified on the basis of rotational contours and were named *A*, *B*, *C*(1), *C*(2), *D*, *E*, and *F*.[9] A conformational analysis of tryptamine was reported from

† Heinrich-Heine-Universität.
‡ Radboud University Nijmegen.
(1) Carney, J. R.; Zwier, T. S. *J. Phys. Chem. A* **2000**, *104*, 8677.
(2) Sipior, J.; Sulkes, M. *J. Chem. Phys.* **1988**, *88*, 6146−6156.
(3) Koshland, D. E. *Proc. Natl. Acad. Sci. U.S.A.* **1958**, *44*, 98−123.
(4) Fischer, E. *Ber. Dtsch. Chem. Ges.* **1894**, *27*, 2985−2993.

(5) Kumar, S.; Ma, B.; Tsai, C.-J.; Sinha, N.; Nussinov, R. *Protein Sci.* **2000**, *9*, 10−19.
(6) Philips, L. A.; Levy, D. H. *J. Chem. Phys.* **1988**, *89*, 85−90.
(7) Wu, Y. R.; Levy, D. H. *J. Chem. Phys.* **1989**, *91*, 5278−5284.
(8) The rotational constants determine the structure of the molecule in a given electronic state since the rotational constant along the *g*-inertia axis of the molecule (*g* = *a*, *b*, *c*) is defined as $A_g = h/8\pi^2 I_g$, with I_g the moment of inertia along the *g*-axis.
(9) Park, Y. D.; Rizzo, T. R.; Peteanu, L. A.; Levy, D. H. *J. Chem. Phys.* **1986**, *84*, 6539−6549.

rotational coherence spectra taken by Connell et al.[10] Caminati published the microwave structure of the *A* and *B* conformer of tryptamine and made an assignment based on ab initio calculations.[11] A more thorough investigation of all seven conformers was given by Carney and Zwier based on resonant ion dip infrared (RIDIR) spectra in the region of the CH alkyl stretch vibrations and by UV−UV hole-burning spectroscopy.

Carney and Zwier[1] proposed a schematic nomenclature of the nine tryptamine conformers with the $C_\alpha H_2$−NH_2 tail out of plane, based on the amino group positions relative to the indole ring and the orientations of the amino group lone pair. We use their nomenclature throughout this publication. The two conformations with the amino lone pair pointing downward to the aromatic ring were found to be much less stable than the other seven conformers. Recently, Dian et al. measured directly the energy thresholds between the different conformers of tryptamine using stimulated emission pumping-hole filling and stimulated emission pumping-induced population transfer spectroscopy.[12]

Microsolvated clusters of tryptamine have been less investigated than have the monomers. Park et al. found that the multitude of conformations of tryptamine collapses into one conformer upon complexation with methanol.[9] The binary water, methanol, and ethanol clusters were investigated by Sipior and Sulkes by LIF spectroscopy, and all were shown to collapse into one prominent conformer peak.[2] Peteanu and Levy investigated the water, methanol, chloroform, and dioxane complexes of tryptamine by two-color two-photon ionization spectroscopy.[13] They observed very different behavior of the dioxane cluster compared to the water and methanol clusters. Rotational constants for the cluster with one water molecule were reported by Felker[14] and Connell et al.[15] using rotational coherence spectroscopy on two isotopomers of the cluster. They deduced a bridged cluster for the cluster with one water molecule. The clusters with two and three water molecules were studied by Carney et al. using RIDIR spectroscopy.[16] They proposed that the preference for a certain conformer is due to a water bridge between the amino and the pyrrolic NH sites of the molecule for clusters with more than one water molecule. We report here a high-resolution laser-induced fluorescence study of the complex of tryptamine with a single water molecule and the origin of the conformational locking in this cluster.

Techniques

Experimental Procedures. The experimental setup for the rotationally resolved LIF is described elsewhere.[17] Briefly, it consists of a ring dye laser (Coherent 899-21) operated with rhodamine 110, pumped with 6 W of the 514 nm line of an Ar^+ ion laser. Its output is coupled into an external folded ring cavity (Spectra Physics) for second harmonic generation (SHG). The molecular beam is formed by co-expanding tryptamine, heated to 160 °C and argon (250−500 mbar, see below) through a 100 μm nozzle into the vacuum. The molecular beam machine consists of three differentially pumped vacuum chambers that are

linearly connected by skimmers (1 and 3 mm, respectively) in order to reduce the Doppler width. The molecular beam is crossed at right angles in the third chamber with the laser beam 360 mm downstream of the nozzle, and the resulting fluorescence is collected perpendicular to the plane defined by laser and molecular beam by an imaging optics. The Doppler width in this setup is 25 MHz (fwhm). A photomultiplier tube detects the integrated molecular fluorescence, and its output is discriminated and digitized by a photon counter and transmitted to a PC for data recording and processing. Relative frequencies are determined with a quasi confocal Fabry−Perot interferometer with a free spectral range (FSR) of 149.9434(56) MHz. The absolute frequency was obtained from a recording of the iodine absorption spectrum and comparing it to the tabulated lines.[18]

Tryptamine was purchased from Merck Schuchard (p.A.) and used without further purification. The mixed isotopomers were produced by refluxing tryptamine with a 3-fold excess of DCl (38%) for 1 h. The solution was then neutralized using a solution of NaOD in D_2O, and washing the precipitation twice with D_2O. The precipitation was then dried over silica gel and stored under nitrogen. This resulted in a more or less equal amount of the different deuteration grades. The triply deuterated isotopomer could be produced nearly exclusively by co-expanding with D_2O, kept at 0 °C. Higher water temperatures led to strong signal reduction due to the formation of the water cluster, and lower temperatures resulted in mixed isotopomers. Another explication for the signal decrease at higher temperatures of the D_2O sample might be deuterium exchange also in positions of the benzene ring, as has been shown to take place under comparable conditions for 4-hydroxyindole.[19] Nevertheless, the aromatic CH-deuterated isotopomers have generally a quite large shift and are well outside the observed spectral range.

Computational Methods

Ab Initio Calculations. The structures of the conformers of tryptamine in the electronic ground state have been optimized at the MP2/6-311G(d,p) level with the Gaussian 98 program package (revision 11).[20] The SCF convergence criterion used throughout the calculations was an energy change below 10^{-8} Hartree, while the convergence criterion for the gradient optimization of the molecular geometry was $\partial E/\partial r < 1.5 \times 10^{-5}$ Hartree/Bohr and $\partial E/\partial \varphi < 1.5 \times 10^{-5}$ Hartree/degree, respectively. Two conformers with the amino lone pair pointing down to the ring have been shown by Carney et al.[1] to be much higher in energy and have not been further investigated here. Vibrational corrections have been made using the ZPE from B3LYP/6-311G(d,p) calculations. The water cluster is optimized at the MP2/6-311G(d,p) level of theory. The starting geometries for the structure optimizations have been obtained by attaching a water to all seven conformers at four different positions: to the pyrrolic NH group, acting as proton donor, to both amino hydrogen atoms, acting as proton donors, and to the N atom of the amino group, acting as proton acceptor. Thus, 28 different starting geometries have been used. Their relative energies were investigated at the HF/6-311G(d,p) level. The amino group acceptor structures of each conformer have then been further refined at the MP2/6-311G(d,p) level of theory. Basis set superposition errors were corrected using the counterpoise method of Boys and Bernardi,[21] and zero-point energy corrections have been performed with the vibrational frequencies of a B3LYP/6-311G(d,p) normal-mode analysis using analytical gradients.

Genetic Algorithms. A fit using genetic algorithms (GA) mimics the concepts of natural reproduction and selection processes. For a detailed description of the GA, the reader is referred to the original literature on evolutionary or genetic algorithms.[22−24]

(10) Connell, L. L.; Corcoran, T. C.; Joireman, P. W.; Felker, P. *Chem. Phys. Lett.* **1990**, *166*, 510−516.
(11) Caminati, W. *Phys. Chem. Chem. Phys.* **2004**, *6*, 2806−2809.
(12) Dian, B. C.; Clarkson, J.; Zwier, T. S. *Science* **2004**, *303*, 1169−1173.
(13) Peteanu, L. A.; Levy, D. H. *J. Chem. Phys.* **1988**, *92*, 6554−6561.
(14) Felker, P. M. *J. Phys. Chem.* **1992**, *96*, 7844−7857.
(15) Connell, L. L.; Corcoran, T. C.; Joireman, P. W.; Felker, P. *J. Phys. Chem.* **1990**, *94*, 1229−1232.
(16) Carney, J. R.; Dian, B. C.; Florio, G. M.; Zwier, T. S. *J. Am. Chem. Soc.* **2001**, *123*, 5596−5597.
(17) Schmitt, M.; Küpper, J.; Spangenberg, D.; Westphal, A. *Chem. Phys.* **2000**, *254*, 349−361.

(18) Gerstenkorn, S.; Luc, P. *Atlas du spectre d'absorption de la molécule d'iode* CNRS, Paris, 1982.
(19) Huang, Y.; Sulkes, M. *Chem. Phys. Lett.* **1996**, *254*, 242−248.
(20) Frisch, M. J. et al. *Gaussian 98*, revision a.11; Gaussian, Inc.: Pittsburgh, PA, 2001.
(21) Boys, S. F.; Bernardi, F. *Mol. Phys.* **1970**, *19*, 553.

The molecular parameters are encoded binary, each parameter to be optimized representing a gene. A vector of all genes, which contains all molecular parameters, is called a chromosome. In an initial step, the values of all parameters are set to random values between lower and upper limits, which are chosen by the user. The quality of the solutions then is evaluated by a fitness function. A proper choice of this fitness function is of vital importance for the success of the GA convergence. In refs 25 and 26, the fitness function F_{fg} has been defined as:

$$F_{fg} = \frac{(\mathbf{f,g})}{||\mathbf{f}|| \; ||\mathbf{g}||} \tag{1}$$

Here, $\mathbf{f}$ and $\mathbf{g}$ are the vector representations of the experimental and calculated spectrum, respectively. The inner product $(\mathbf{f,g})$ is defined with the metric $\mathbf{W}$, which has the matrix elements $W_{ij} = w(|j - i|) = w(r)$ as:

$$(\mathbf{f,g}) = \mathbf{f}^T \mathbf{W} \mathbf{g} \tag{2}$$

and the norm of $\mathbf{f}$ as $||\mathbf{f}|| = \sqrt{(\mathbf{f,f})}$; similar for $\mathbf{g}$. For $w(r)$, we used a triangle function[25] with a width of the base of Δw:

$$w(r) = \begin{cases} 0 - |r|/\left(\frac{1}{2}\Delta w\right) & \text{for } |r| < \frac{1}{2}\Delta w \\ 0 & \text{otherwise} \end{cases} \tag{3}$$

One optimization cycle, including evaluation of the fitness of all solutions, is called a generation. Pairs of chromosomes are selected for reproduction, and their information is combined via a crossover process. Since crossover combines information from the parent generations, it basically explores the error landscape. The value of a small number of bits is changed randomly by a mutation operator. For the simulation of the rovibronic spectra, a rigid asymmetric rotor Hamiltonian was employed.[27]

Results

The Tryptamine Monomer. Figure 1 shows the atomic numbering used for designation of the isotopomers and the clusters used in this publication. The rotationally resolved electronic origin of the *A* conformer of tryptamine at 34915.64 cm^{-1} is shown in Figure 2 along with a fit based on the genetic algorithms (GA). The technique has been shown before to work reliably even for strongly overlapping bands, where a standard assigned fit would be impossible.[25,26] The origin band is a hybrid with mainly *a*-type character.

Table 1 reports the molecular parameters obtained from the fit and the comparison to previously reported constants of the *A* conformer, either from microwave spectroscopy for the electronic ground state[11] or from LIF spectroscopy for ground and excited states.[6] A'', B'', and C'' designate the rotational constants in the electronic ground state, A', B', and C' are those of the excited state. ΔA, ΔB, and ΔC are the changes of rotational constants upon electronic excitation.[8] θ and ϕ are the spherical coordinate angles of the transition moment vector in

(22) Holland, J. H. *Adaption in Natural and Artificial Systems*; MI, The University of Michigan Press: Ann Arbor, MI, 1975.
(23) Goldberg, D. E. *Genetic Algorithms in Search, Optimisation and Machine Learning*; Addison-Wesley: Reading, MA, 1989.
(24) Rechenberg, I. *Evolutionsstrategie: Optimierung technischer Systeme nach Prinzipien der biologischen Evolution*; Frommann-Holzboog: Stuttgart, Germany, 1973.
(25) Hageman, J. A.; Wehrens, R.; de Gelder, R.; Meerts, W. L.; Buydens, L. M. C. *J. Chem. Phys.* **2000**, *113*, 7955−7962.
(26) Meerts, W. L.; Schmitt, M.; Groenenboom, G. *Can. J. Chem.* **2004**, *82*, 804−819.
(27) Allen, H. C.; Cross, P. C. *Molecular Vib-Rotors*; Wiley: New York, 1963.
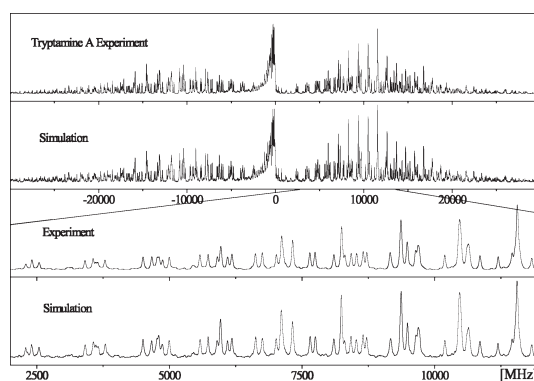
Figure 2. Rovibronic spectrum of the electronic origin of tryptamine *A* at 34915.64 cm^{-1}. The upper trace shows the experimental spectrum, the following shows the simulation with the best molecular parameters from the GA fit. The following traces present an enlarged portion of the spectrum.

the molecular fixed frame (*a*, *b*, *c*). The μ_a, μ_b, and μ_c designate the components of the transition dipole moment to the inertial axis of the cluster.[28] They are given for comparison to the respective parameters in ref 6. τ (ns) is the excited-state lifetime, calculated from the Lorentzian width. The ground-state rotational constants of the *A* and *B* conformers agree within their uncertainties with the microwave values from Caminati.[11] Deviations are due to the implicitly higher accuracy of the microwave data and the utilization of a different Hamiltonian, including centrifugal distortion in ref 11. The deviations to the ground-state rotational constants from Philips and Levy range between 50 MHz for the *A* rotational constant of the *A* conformer to 170 MHz for the *A* rotational constant of the *E* conformer.[6] Given the small differences between the rotational constants of the conformers, an unambiguous assignment to the respective structures requires the accuracy of nearly fully resolved rovibronic spectra. On the other hand, the differences of the rotational constants upon electronic excitation agree very well with the previously reported values of Philips and Levy.[6] The quite large deviations in the ground-state rotational constants are mainly due to the lower resolution (75 MHz) in the experiments of ref 6. Convolution of our spectra with an additional contribution of about 70 MHz made the assignment quite hard, even for the automated GA technique described above.

Since three rotational constants are not sufficient to give an unambiguous assignment to which conformation band *A* belongs, we recorded the spectra of several deuterated isotopomers. Deuteration with DCl as described in the experimental procedures section in Techniques resulted in a mixture of up to eight different isotopomers. Under these conditions, the highest deuteration grade which can be achieved is the triply deuterated d$_3$. If all deuteration grades are formed, the spectrum of each conformer consists of the undeuterated, three different singly deuterated, three different doubly deuterated, and one triply deuterated isotopomer. With the atomic numbering given in Figure 1, these eight isotopomers are tryptamine, [1b-D]-tryptamine-*d*$_1$, [10a-D]tryptamine-*d*$_1$, [10b-D]tryptamine-*d*$_1$, [1b-

(28) The components of the transition dipole moment along the inertial axis are defined by: $\mu_a = \mu \sin \phi \cos \theta$, $\mu_b = \mu \sin \phi \sin \theta$, and $\mu_c = \mu \cos \phi$.

Table 1. Molecular Parameters for the Conformers *A*−*F* of Tryptamine Determined from GA Fits, as Described in the Text

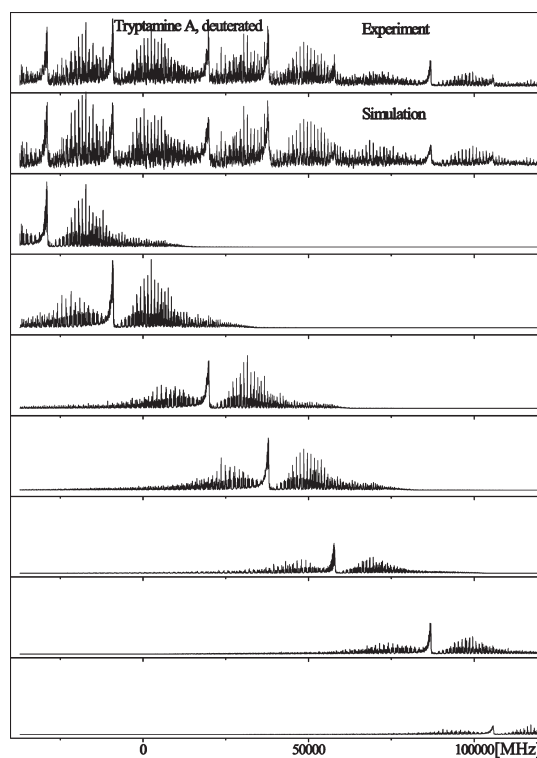|	*A* band			*B* band			*C* band		*D* band		*E* band		*F* band	
	this work	ref 11	ref 6	this work	ref 11	ref 6	this work	ref 6	this work	ref 6	this work	ref 6	this work	ref 6
A'' (MHz)	1731.02	1730.197	1783.8	1710.25	1709.438	1777.8	1594.16		1767.74	1933.6	1761.40	1930.7	1605.11	1636.9
B'' (MHz)	682.04	681.86	674.5	682.22	681.87	665.5	755.84		617.78	611.6	614.75	608.6	737.84	722.5
C'' (MHz)	551.56	551.48	551.6	551.10	550.84	548.6	561.39		477.00	473.6	475.58	473.6	561.51	584.6
θ (°)	71.92			72.25			76.85		75.03		77.43	80.71		
ϕ (°)	14.24			22.28			18.17		5.54		10.90	13.92		
μ_A	0.9234		0.88	0.8812		0.88	0.9317		0.9246	0.85	0.9185	0.85	0.9176	0.77
μ_B	0.2271		0.37	0.3611		0.37	0.2634		0.0087	0.32	0.0341	0.32	0.0564	0.42
μ_C	0.3093		−0.29	0.3050		−0.29	0.2502		0.0667	−0.42	0.0474	−0.42	0.0261	−0.47
$\Delta_{Lor.}$ (MHz)	25.3			29.9			24.3		32.08		25.5	25.2		
τ (ns)	6.2			5.3			6.5		5.0		6.2	6.3		
A' (MHz)	1724.02		1777.8	1703.62		1783.8	1587.38		1754.07	1918.7	1748.47	1915.7	1592.77	1624.9
B' (MHz)	672.68		665.5	672.92		674.5	743.08		612.34	605.6	609.26	602.6	728.49	716.5
C' (MHz)	544.58		545.6	544.54		554.6	554.20		473.44	470.7	472.16	470.7	555.25	572.6
ΔA (MHz)	−7.00		−6.0	−6.63		−6.0	−6.78		−13.67	−14.9	−12.9	−15.0	−12.34	−12.0
ΔB (MHz)	−9.36		−9.0	−9.30		−9.0	−12.76		−5.44	−6.0	−5.5	−6.0	−9.35	−6.0
ΔC (MHz)	−6.98		−6.0	−6.56		−6.0	−7.19		−3.56	−3.0	−3.4	−3.0	−6.26	−12.0

D][10a-D]tryptamine-d_2, [1b-D][10b-D]tryptamine-d_2, [10a-D]-[10b-D]tryptamine-d_2, and [1b-D][10a-D][10b-D]tryptamine-d_3. For the *A* conformer, we were only able to observe seven out of the eight possible isotopomers. Using the mixed deuteration grades, a serious problem arises for the assignment of single rovibronic lines, due to strong overlap of the different isotopomeric origins. Using the GA, it is possible to automatically fit several bands simultaneously, as we have shown for the overlapping origins of phenol−nitrogen clusters[29] and differently deuterated azaindoles.[30] Figure 3 shows the experimental spectrum of the seven isotopomers of the *A* conformer together with the fit of all bands and the individual results for each origin band.

To verify the correctness of the rotational constants derived from the spectrum of Figure 3, we selectively produced the triply deuterated tryptamine as described in the experimental procedures section of Techniques. The fit to this single spectrum reproduced the values obtained from the overall fit of all isotopomers. The resulting inertial parameters of all isotopomers are given in Table 2 and will be used in this section for the determination of the exact conformation of each conformer. Since seven different isotopomers contribute a total of 21 rotational constants, sufficient information for an unambiguous assignment is present.

A very good agreement between simulation and experiment is also observed for the electronic origin of the *B* conformer at 34895.91 cm^{-1} given in Figure 4. The resulting rotational constants are compiled in Table 1.

For the *B* conformer, all eight possible isotopomers (vide infra) could be observed. As in the case of the *A* conformer, the origins overlap strongly due to similar zero-point energies in the ground and excited states of the isotopomers. The spectra are shown in Figure 5; the resulting rotational constants of all isotopomers are given in Table 2. Again, like for conformer *A*, the results for the rotational constants were cross-checked against the triply deuterated *B* conformer, produced selectively by the method described above.

The spectra of the undeuterated and triply deuterated *C*, *D*, *E*, and *F* conformers are shown in the Supporting Information. Here, we will report only the molecular constants that were

(29) Schmitt, M.; Ratzer, C.; Meerts, W. L. *J. Chem. Phys.* **2004**, *120*, 2752−2758.
(30) Schmitt, M.; Ratzer, C.; Kleinermanns, K.; Meerts, W. L. *Mol. Phys.* **2004**, *102*, 1605−1614.

Figure 3. Rovibronic spectra of the electronic origins of seven isotopomers of the *A* conformer of tryptamine.

obtained from the GA assigned spectra. The electronic origins of the *C* (34879.22 cm^{-1}) and *D* conformers (34884.26 cm^{-1}) are spectrally very close, so that the mixed deuterated isotopomers would overlap even between the two different conformers. For this reason, we took only the undeuterated and triply deuterated spectra. The electronic origins of the spectra of the d_3-*C* (34885.80 cm^{-1}) and d_3-*D* conformers (34886.32 cm^{-1}) are even closer and overlap considerably. Also, here, the GA made it possible to fit both subspectra independently. Philips and Levy[6] and Carney et al.[1] reported the existence of two different origins of the *C* conformer, namely, *C*(1) and *C*(2). The two *C* conformers were identified by Philips and Levy

Table 2. Rotational Constants for the Isotopomers of the Tryptamine Conformers *A*−*F*. Conformers with an Asterisk Had Larger Uncertainties in the Inertial Parameters and were Excluded from the Structural Fits (Rotational Constants Are Given in MHz, and the Origin Frequencies in cm^{-1})

conformer	isotopomer	A″	B″	C″	A′	B′	C′	ν_0
A	h$_3$	1731.02	682.04	551.56	1724.02	672.68	544.58	34915.64
	[1a-D]	1683.25	682.41	546.52	1675.83	672.75	539.66	34917.20
	[10a-D]	1709.03	667.03	543.53	1702.37	658.08	536.82	34916.30
	[10b-D]	1712.32	675.26	548.85	1706.28	665.69	541.82	34917.27
	[1a-D][10a-D]	1685.30	671.65	542.79	1681.36	662.71	535.49	34918.84
	[1a-D][10b-D]*	1676.44	671.58	538.31	1673.41	662.32	527.94	34917.87
	d$_3$	1646.11	659.05	534.89	1640.28	649.8	528.27	34919.47
B	h$_3$	1710.25	682.22	551.10	1703.62	672.92	544.54	34895.91
	[1a-D]	1661.92	681.38	545.19	1655.52	671.68	538.85	34897.66
	[10a-D]	1701.67	667.02	541.27	1695.50	657.87	534.75	34894.89
	[10b-D]	1694.79	674.03	547.37	1688.44	664.74	540.73	34896.85
	[1a-D][10a-D]*	1657.24	673.39	541.89	1651.83	664.06	535.37	34898.49
	[1a-D][10b-D]*	1640.31	678.05	559.93	1631.19	675.62	556.19	34897.55
	[10a-D][10b-D]	1689.51	661.71	537.75	1683.13	652.48	531.26	34896.74
	d$_3$	1641.98	659.18	533.12	1636.75	650.06	526.69	34898.38
C	h$_3$	1594.16	755.84	561.39	1587.38	743.08	554.20	34879.22
	d$_3$	1509.11	737.12	545.22	1503.43	724.67	538.28	34885.80
D	h$_3$	1767.74	617.78	477.00	1754.07	612.34	473.44	34884.26
	d$_3$	1648.46	584.20	454.74	1635.78	579.25	451.61	34886.32
E	h$_3$	1761.40	614.75	475.58	1748.47	609.26	472.16	34868.34
	d$_3$	1650.34	557.33	429.34	1630.52	542.65	418.75	34869.98
F	h$_3$	1605.11	737.84	561.51	1592.77	728.49	555.25	34831.95
	d$_3$	1522.25	725.63	546.97	1511.10	716.32	540.71	34838.31
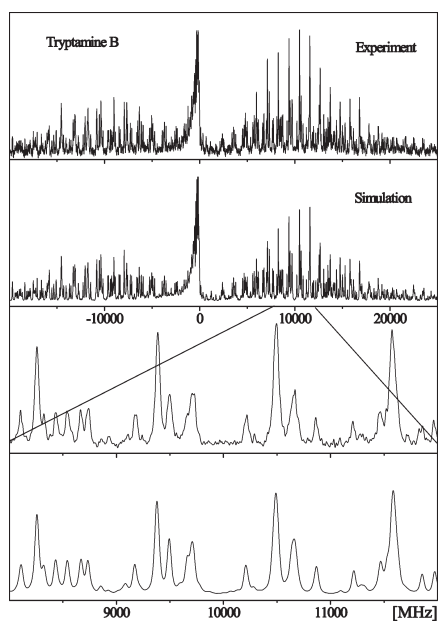
Figure 4. Rovibronic spectrum of the electronic origin of tryptamine *B* at 34895.91 cm^{-1}. The upper trace shows the experimental spectrum, the following shows the simulation with the best molecular parameters from the GA fit. The following traces present an enlarged portion of the spectrum.

Figure 5. Rovibronic spectra of the electronic origins of the fully protonated and seven deuterated isotopomers of the *B* conformer of tryptamine. Trace *a* shows the experimental spectrum, and the other traces show the simulations of the individual isotopomers. The electronic origin of the undeuterated tryptamine *B*, shown in trace *c*, is at 34895.91 cm^{-1}. Trace *b* represents the isotopomer [10b-D]tryptamine-*d*$_1$, trace *d* [1b-D][10a-D]-tryptamine-*d*$_2$, trace *e* [1b-D]tryptamine-*d*$_1$, trace *f* [1b-D][10b-D]tryptamine-*d*$_2$, trace *g* [10a-D]tryptamine-*d*$_1$, trace *h* [1b-D][10a-D][10b-D]tryptamine-*d*$_3$, and trace *i* the [10a-D][10b-D]tryptamine-*d*$_2$ isotopomer.

through their different Q-branches in the rotationally resolved LIF spectrum, approximately 0.6 cm^{-1} apart. This finding was confirmed by Carney et al.[1] via different resonant ion dip infrared (RIDIR) spectra taken through two vibronic bands that were shown to belong to the *C* spectrum by UV−UV hole-burning. We carefully scanned the respective region of the *C* conformer, but we were able to identify only one band, absorbing in this range in contrast to the findings of Philips

and Levy[6] and Carney et al.[1] The signal-to-noise ratio in our experiment would have allowed for the detection of a band at least by a factor of 50 smaller than the origin of the *C* conformer at 34879.22 cm^{-1}. We changed the expansion conditions over a large range in order to rule out the possibility that different cooling conditions in the molecular beam were responsible for

Table 3. Comparison of Rotational Constants of the MP2/6-311G(d,p) Optimized Structures of Seven Conformers of Tryptamine with the Experimentally Determined Rotational Constants

	Gpy(out)	Gpy(up)	anti(py)	Gph(out)	anti(ph)	anti(up)	Gph(up)
$E_{rel.}$ (kJ/mol)	0.4083	0.5445	6.8644	0	6.8143	5.6123	1.3709
A'' (MHz)	1729.9	1711.5	1767.0	1578.9	1756.2	1753.2	1588.7
B'' (MHz)	687.4	686.8	614.7	772.0	619.1	616.0	753.5
C'' (MHz)	556.6	555.9	476.7	564.8	478.3	476.9	566.9
experiment	*A*	*B*	*D*	*C*		*E*	*F*
A'' (MHz)	1731.02	1710.25	1767.74	1594.16		1761.40	1605.11
B'' (MHz)	682.04	682.22	617.78	755.84		614.75	737.84
C'' (MHz)	551.56	551.10	477.00	561.39		475.58	561.51

the "disappearance" of the second *C* band. Under no experimental conditions, we could find any trace of an additional band with a Q-branch around 34879.2 ± 0.6 cm^{-1}.

The electronic origins of the *E* (34868.34 cm^{-1}) and *F* (34831.95 cm^{-1}) conformers are much weaker than the *A* and *B* origins. Therefore, we were only able to record the undeuterated and the triply deuterated conformers. Nevertheless, the six rotational constants for each conformer are sufficient for an unambiguous assignment of the structure, which needs, in principle, only three rotational constants for the three dihedral angles. The parameters from the best fits are given in Table 1. The spectra of the *E* and *F* conformers were taken at considerably lower backing pressures than the other conformers. The optimum expansion conditions for observation of conformers *A* to *D* were 500 mbar of Ar and a temperature of the tryptamine sample container of 160 °C. Optimum conditions for the *E* and *F* conformers were at a backing pressure of 200−250 mbar.

Comparison of the rotational constants of the undeuterated tryptamine conformers with the results of ab initio calculations gives a first clue to the assignment to a specific structure. Table 3 compares the rotational constants of the optimized MP2/6-311G(d,p) structures with the experimentally obtained rotational constants. The best agreement is found by relating band *A* to the Gpy(out) conformer, band *B* to Gpy(up), band *D* to anti-(py), band *C* to Gph(out), band *E* to anti(up), and band *F* to Gph(up). This assignment agrees with the findings of Carney et al. but is still not able to remove their ambiguity in the distinction of the anti(ph) and anti(py) structures. Therefore, the information has to be combined with the rotational constants of the deuterated isotopomers. This will be performed in the following section. Figure 6 shows the six observed conformers.

A comparison of the relative energies of the seven conformers, calculated in this study at MP2/6-311G(d,p), with the B3LYP/aug-ccVTZ results of Carney and Zwier shows important differences. The energies of all anti conformers are quite similar, while the energies of the gauche conformers differ considerably between both methods. For the correlated MP2 method, the Gph(out) conformer becomes the most stable one, while this conformer is only the third most stable one at density functional level. Of course, one would expect the largest differences for the conformers with a potential interaction between the amino group and the aromatic ring. This is the case for all gauche conformers, but not the anti conformers. The relative intensities of the individual tryptamine bands in the low-resolution spectra of refs 6 and 1 seem to favor energetically the Gpy(out) (*A*) and the Gpy(up) (*B*) conformers over the Gph-(out) (*C*) conformer. Nevertheless, this comparison of relative intensities relies on the assumption of equal or nearly equal oscillator strengths for all conformers. It is well-known that the
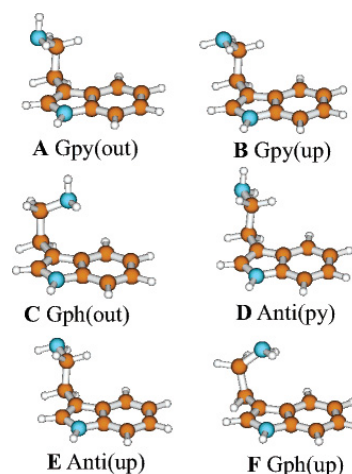
Figure 6. Structure of the six tryptamine conformers identified in the rovibronic analysis of the present publication. Gpy represents conformers in which the amino group position is gauche to the pyrrole side of the indole ring. Anti is for a position anti to the indole ring, and Gph for a position gauche to the phenyl side. The orientations of the amino lone pair are designated by "out" and "py", depending on the direction of the lone pair of the amino group with respect to the rings ($\pm 60°$), or "up" (180°). This nomenclature follows the suggestion of Carney and Zwier.[1]

orientation of the transition dipole moment depends strongly on the conformational orientation of a flexible group, attached to a benzene chromophore.[31,32] This interaction takes place both by "through bond" and "through space" interactions.

Determination of the Monomer Structure Parameters. The program pKrFit[33] was used to determine the structure of the tryptamine isotopomers and the water cluster in the electronic ground state. We performed a structural fit for the different conformers, in which the different vibrational contributions from the different isotopomers are completely neglected and which is based on the following assumption:

$$I_0^g = I_{rigid}^g(r_0) \qquad (4)$$

In this equation, the three I_0^g are the (experimentally determined) zero-point averaged moments of inertia with respect to the inertial axes *g*. The function $I_{rigid}^g(r_0)$ is calculated from the structural parameters r_0 using rigid-molecule formulas. The resulting structure is called the r_0-structure.

(31) Kroemer, R. T.; Liedl, K. R.; Dickinson, J. A.; Robertson, E. G.; Simons, J. P.; Borst, D. R.; Pratt, D. W. *J. Am. Chem. Soc.* **1998**, *120*, 12573−12582.
(32) Richardson, P. R.; Bates, S. P.; Jones, A. C. *J. Phys. Chem. A* **2004**, *108*, 1233−1241.
(33) Ratzer, C.; Küpper, J.; Spangenberg, D.; Schmitt, M. *Chem. Phys.* **2002**, *283*, 153−169.

Table 4. Results of the Structural Fits of the Tryptamine Conformers for the Electronic Ground State (Dihedral Angles $\tau_1 - \tau_3$ Are Defined in Figure 1)

	A	B	D	D	C	E	F
	Gpy(out)	Gpy(up)	anti(py)	anti(ph)	Gph(out)	anti(up)	Gph(up)
τ_1	101.9	103.7	104.7	104.6	93.1	107.6	85.5
τ_2	−63.9	−65.3	179.5	182.3	63.5	−11.2	62.8
τ_3	75.1	−59.1	118.8	−147.1	166.6	−102.0	−40.6
χ^2	4	4	6	4	4	10	3

The first step was a simulation of the rotational constants for the different isotopomers, based on the results of the ab initio calculations described above. The assignment of the different isotopomers of the *A* conformer is very straightforward since the differences between calculated and experimental rotational constants are small. Starting with the known isotopomers, h_3 and d_3, it was possible to assign all other isotopomers. The assignment of the bands in the order of their appearance in the spectrum is given in Table 2. In all cases, the agreement between the rotational constants of the isotopomers predicted from the ab initio structures is stunning. The next step is the determination of the structural Z-matrix parameters to be fit to the rotational constants. The first choice is, of course, the dihedral angles, which determine the position and orientation of the amino group. Therefore, the three dihedral angles, τ_1, τ_2, and τ_3 (cf. Figure 1 for definition), have been varied to fit the rotational constants. Table 4 presents the results for the best ground-state structure.

The Tryptamine−Water Cluster. Low-resolution spectra showed that despite the richness of the potential energy landscape of the tryptamine monomer, only a single band at $34\,957$ cm^{-1} appears upon addition of water,[2] which can be attributed to the binary water cluster. The water molecule might attach to each of the seven conformers that have similar energies in the ab initio calculations. Four attaching positions of the water molecules have been considered for the starting geometries: the pyrrolic NH group, which acts as proton donor with respect to the water molecule, the amino group, which might act with each of its H-atoms as proton donor, and the amino group, which might act as a proton acceptor. Without considering any van der Waals bound structures, there are 28 different geometries possible. Nevertheless, only one shows up in the high-resolution UV spectrum. Figure 7 shows the rotationally resolved spectrum of the electronic origin of tryptamine−water at $34\,957.11$ cm^{-1}. The molecular parameters obtained from the GA fit of this spectrum are given in Table 5 and are compared to the values obtained by Felker[14] and Connell and Felker[10] using rotational coherence spectroscopy. The angle θ of 23 °, given in ref 14 for the angle of the TDM with the a-axis, has been converted into components of the TDM along the inertial axes in Table 5 for better comparison.

Comparison of the experimental rotational constants with rotational constants of Hartree−Fock optimized structures (Table 6) reveals that only the Gpy(out) conformer with the water binding as proton donor to the amino group (Figure 6) can be responsible for the observed band. All other calculated rotational constants are too far off to be considered. In the Hartree−Fock calculations, not all 28 starting geometries converged into an equivalent structure. Clusters in which the H-atom of the amino group that is pointing in direction of the aromatic ring acts as proton donor with respect to the water do not converge at all. Clusters in which the H-atom of the amino group is pointing
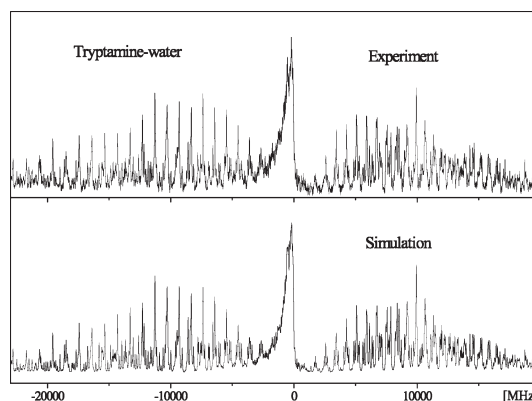

Figure 7. Rovibronic spectrum of the electronic origin of tryptamine−water at 34957.11 cm^{-1} along with the simulation using the best parameters given in Table 5.

Table 5. Molecular Parameters for the Tryptamine−Water Cluster Determined from GA Fits, as Described in the Text. *A*, *B*, and *C* are the Rotational Constants of the Molecule in the Ground State. ΔA, ΔB, and ΔC are the Changes of the Rotational Constants upon Electronic Excitation[8] (μ_a, μ_b, and μ_c Designate the Components of the Transition Dipole Moment to the Inertial Axis of the Cluster, and τ (ns) Is the Excited State Life Time)

tryptamine−water	this work	ref 14
A'' (MHz)	1465.78	1465
B'' (MHz)	483.43	479
C'' (MHz)	397.99	379
μ_a	0.8063	0.847
μ_b	0.0221	0.153
μ_c	0.1715	0
τ (ns)	4.8	
ΔA (MHz)	−6.82	
ΔB (MHz)	−4.71	
ΔC (MHz)	−3.72	

away from the aromatic ring converge for all Gph and Gpy conformers into the respective structure, while for all anti conformers, they converge into the structure with the amino group being proton acceptor. It is intriguing that the calculated energy differences between the conformers complexed with a single water molecule are much larger than those for the respective monomers.

To investigate the physical origin of the structural selection by microsolvation of tryptamine with one water molecule we reoptimized the most stable Hartree−Fock structure for each conformer with Møller−Plesset perturbation theory. The results of the ab initio calculations are summarized in Table 6. The energy differences between the different conformer clusters are much larger than those for the respective monomers using the same method and basis set. If one expresses the energy differences in temperature units, the observed monomer energies differ by less than kT at room temperature, while for the complexes, the energy differences grow much larger than kT at room temperature. What is the reason for the pronounced stabilization of the *A* conformer with respect to all other conformers upon water complexation?

Figure 8 shows the structure of the most stable water cluster. The distance between the O-atom of the water moiety and H_{2a} at the pyrrole moiety of the indole ring (cf. Figure 1 for atomic numbering of the monomer) is only 238.1 pm. This is already

Table 6. HF/6-31G(d,p) Optimized Structures of Different Tryptamine−Water Clusters. The Numbers in Parentheses Give the MP2/6-311G(d,p) Values Where Applicable. The Relative MP2 Energies Contain Corrections of the Basis Set Superposition Error Using the Counterpoise Method of Boys and Bernardi[21] and Zero-Point Energy Corrections

|	Gpy(out)			Gpy(up)		
	NH(py)	NH$_2$(a)	NH$_2$(d)	NH(py)	NH$_2$(a)	NH$_2$(d)
$E_{rel.}$ (kJ/mol)	12.535	0 (0)	17.140	14.291	11.313 (8.088)	24.325
A'' (MHz)	917.0	1469.4 (1483.0)	1160.8	804.1	1163.9 (1079.8)	1399.7
B'' (MHz)	548.7	470.8 (488.2)	566.2	591.0	412.9 (490.3)	445.7
C'' (MHz)	373.0	387.0 (402.7)	524.4	370.3	356.4 (397.9)	365.4
	anti(py)			Gph(out)		
	NH(py)	NH$_2$(a)	NH$_2$(d)	NH(py)	NH$_2$(a)	NH$_2$(d)
$E_{rel.}$ (kJ/mol)	15.294	10.58 (13.228)		14.526	5.457 (4.354)	16.832
A'' (MHz)	1035.8	1629.3 (1584.0)		1003.0	1058.7 (1095.1)	1047.1
B'' (MHz)	466.1	377.0 (402.2)		538.6	602.4 (617.9)	643.9
C'' (MHz)	332.7	316.8 (330.9)		375.8	420.4 (437.2)	523.1
	anti(ph)			anti(up)		
	NH(py)	NH$_2$(a)	NH$_2$(d)	NH(py)	NH$_2$(a)	NH$_2$(d)
$E_{rel.}$ (kJ/mol)	15.345	8.149 (12.425)		15.472	12.784 (13.183)	
A'' (MHz)	1038.6	1169.1 (1185.7)		1031.7	1342.2 (1231.8)	
B'' (MHz)	466.4	509.7 (522.1)		466.4	341.6 (386.9)	
C'' (MHz)	333.2	373.1 (381.1)		332.9	304.6 (346.9)	
	Gph(up)					
	NH(py)	NH$_2$(a)	NH$_2$(d)		experiment	
$E_{rel.}$ (kJ/mol)	16.035	12.694 (7.099)	23.826			
A'' (MHz)	968.2	1231.5 (1247.8)	1065.1		1465.81	
B'' (MHz)	542.8	405.5 (430.6)	621.8		483.37	
C'' (MHz)	378.1	351.1 (371.0)	520.3		398.02	
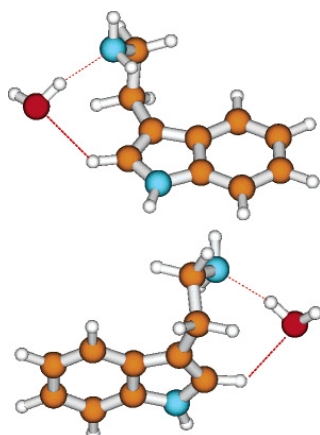
Figure 8. Structure of the tryptamine−water complex in the electronic ground state obtained from the fit of the water distance and the water orientation to the experimentally determined rotational constants. The lower half gives a back-view of the complex. The fitting procedure is described in detail in the Supporting Information.

a distance that allows for a weak hydrogen bond, thus selectively stabilizing this conformer. What about the other conformers? Clusters of water with conformers in which the amino lone pair is pointing up do not have the possibility to form an additional hydrogen bond. The same holds for all anti structures in which the ethyl amino side chain points away from the indole ring system.

Thus, the only two structures which might be additionally stabilized are Gpy(out) (the *A* conformer) and Gph(out) (the *C* conformer). In case of the *C* conformer cluster, the additional stabilizing interaction takes place between the water O-atom and H$_{4a}$ at the benzene moiety of the indole ring. The hydrogen

bond distance is larger (248.4 pm), explaining the lower stability of this cluster relative to the *A* conformer cluster. The stronger bonding interaction in the *A* conformer cluster reflects the increased acidity of the C$_2$−H bond compared to that of the C$_4$−H bond.

Determination of the Cluster Structure Parameters. Since the ab initio calculations guided us in deciding which conformer is present in the water cluster, we determined the structural parameters only for the Gpy(out) geometry with the water molecule attached to the amino group, which acts as acceptor in this cluster. The three rotational constants have been used for a fit of the O$_{water}$N distance, the O$_{water}$NC$_\alpha$ angle, and the O$_{water}$NC$_\alpha$C$_\beta$ dihedral angle. The structures of the tryptamine and water moieties have been kept fixed at the respective monomer geometries. A hydrogen bond length of 301.3 pm and a nearly linear hydrogen bond was obtained from the fit. This value is similar to the O$_{water}$N hydrogen bond lengths of the ammonia−water complex (298.3 pm)[34] and the aniline−water complex (303 pm).[35] The structure shown in Figure 8 is very similar to the structure that was derived by Felker[14] and Connell and Felker[10] based on the rotational constants of the normal isotopomer and the d_3-tryptamine−D$_2$O cluster, which were obtained by rotational coherence spectroscopy.

Conclusions

It is surprising that the microsolvation of tryptamine with a single water molecule freezes out one specific conformer of the possible 27 in tryptamine. While the barriers separating the individual conformers that can be observed in the experiment amount to several times the thermal energy kT at room temperature, the energy *difference* between these isotopomers

(34) Herbine, P.; Dyke, T. R. *J. Chem. Phys.* **1985**, *83*, 3768−3774.
(35) Spoerel, U.; Stahl, W. *J. Mol. Struct.* **1998**, *190*, 278−289.

is smaller than or of the order of the magnitude of kT. Thus, if one compares the stabilities of isolated conformational species, nearly all minima on the potential energy surface are accessible thermally, and the respective conformations should all be considered. On the other hand, complexation with a single water molecule already increases the energy differences between the conformers to several times the thermal energy at room temperature. We have traced back the origin of the selective stabilization of one conformer to an additional bonding in the water complex, which can only occur in the A conformer.

Supporting Information Available: Spectra of the normal isotopomer and the triply deuterated C, D, E, and F conformers of tryptamine, along with a simulation using the best parameters from the GA fits. Cartesian coordinates of the MP2/6-311G-(d,p) optimized structures of the seven tryptamine conformers described in the text. Complete ref 20. This material is available free of charge via the Internet at http://pubs.acs.org.

JA0522377

5.5 Benzoesäure-Dimer

Tunneling Splittings in the S_0 and S_1 States of the Benzoic Acid Dimer Determined by High-Resolution UV Spectroscopy

Ivo Kalkman,[a] Chau Vu,[b] Michael Schmitt,*[b] and W. Leo Meerts*[a]

Five different isotopologues of the benzoic acid dimer and a vibronic band located 57 cm^{-1} above the electronic origin, which is assigned to the out-of-plane butterfly motion, are studied by rotationally resolved UV spectroscopy. From these measurements a ground-state structure with C_{2h} symmetry is deduced, whereas the symmetry is lowered to C_s in the S_1 state. The increase in the center-of-mass distance between the two monomers that is found on electronic excitation indicates a decrease in hydrogen-bond strength. The tunneling splittings in the S_0 and S_1 states are 1385.2 ± 0.7 and 271.2 ± 0.7 MHz, respectively, corresponding to an increase in barrier height by 7.2 % on electronic excitation.

1. Introduction

Hydrogen bonding is very important in biological systems and has therefore been the subject of considerable research. Some systems employ multiple hydrogen bonds to connect molecular subunits; most notable among these is DNA, the base pairs of which are connected by double or triple hydrogen bonds. Because of their high symmetry, the dimers of carboxylic acids such as formic acid, acetic acid, and benzoic acid have become model systems for double hydrogen bonding. Their carboxyl groups link to create an eight-membered ring and, in the above examples, a ground-state dimer structure of C_{2h} symmetry. This doubly hydrogen-bonded structure is so strong that even at room temperature mostly dimers are present.

Since many biologically relevant processes involve proton transfer, an interesting aspect of carboxylic acid dimers is the possibility of double proton tunneling. The tunneling path has long been the subject of debate, however, and theoretical estimates of proton transfer times span several orders of magnitude (e.g., see Madeja and Havenith[1] and references therein). Early calculations agreed that extensive geometry optimization of the transition state is necessary and that the transition itself is strongly coupled to a deformation of the whole molecular frame, but the predicted barrier heights differed significantly.[2, 3] Anomalous isotope effects observed for two vibrations of formic acid dimer led Maréchal to conclude that the transfer of protons can not be described as a simple tunneling motion in a double-minimum potential.[4] Recent direct dynamics calculations with a single multidimensional coordinate system could explain a variety of gas-phase and crystal data by carefully considering the contributions of various zero-point vibrations to the tunneling rates and assuming a negligible splitting in the electronically excited state.[5] Coupling between the tunneling mode and transverse modes was calculated to result in a more than 20-fold increase in the tunneling splitting. Recently, ^{1}H NMR relaxometry and quasi-elastic neutron scattering have shown conclusively that proton transfer in the benzoic acid crystal is a strongly correlated motion of the two protons, while the tunneling path is little affected by deuteration in the carboxyl group.[6] Fillaux et al. deduced from spectra of powdered crystals that the potential barrier for the transfer of a single proton is already on the order of 5000 cm^{-1}, which means that semiclassical jumping over the top is negligible.[7] In conclusion, the picture that has emerged is that double proton transfer in carboxylic acid dimers is a pure tunneling motion that occurs in concert, initiated by a zero-point vibrationally induced symmetric decrease of the distance between the two monomer units.

Experimental data on the barriers for concerted proton tunneling reflect the sensitive dependence on the vibrations in both monomer units. In one of the earliest measurements on such systems, Costain and Srivastava found that the barrier height is larger than 6000 cm^{-1} in $CF_3COOH\cdots HCOOH$, but less than 5000 cm^{-1} in $CF_3COOH\cdots CH_3COOH$.[8] From fluid-phase absorption spectra the barrier heights in dimers of formic acid and acetic acid were deduced to be in the range 6500–7000 cm^{-1} when a symmetric double-minimum potential is assumed.[9] By means of high-resolution gas-phase IR spectroscopy on various isotopologues of the formic acid dimer, ground-state tunneling splittings of 375 and 474 MHz were observed

[a] I. Kalkman, Prof. W. L. Meerts
Molecular and Biophysics Group
Institute for Molecules and Materials, Radboud University Nijmegen
P.O. Box 9010, 6500 GL Nijmegen (The Netherlands)
Fax: (+31) 24-365-33-11
E-mail: Leo.Meerts@science.ru.nl

[b] C. Vu, Dr. M. Schmitt
Institut für Physikalische Chemie und Elektrochemie I
Mathematisch-Naturwissenschaftliche Fakultät
Heinrich-Heine-Universität Düsseldorf
Universitätsstraße 26.43.02.43, 40225 Düsseldorf (Germany)
Fax: (+49) 211-81-15195
E-mail: Mschmitt@uni-duesseldorf.de

for the $(DCOOH)_2$ and $(HCOOH)_2$ dimers, respectively, whereas for the $(DCOOD)_2$ dimer an upper limit of 60 MHz was deduced.[1,10,11] This corresponds well with an effective barrier height of 6940 cm^{-1} for the fully protonated dimer.[5]

Attempts to determine the magnitude of the tunneling splitting in the benzoic acid dimer have mainly been made by using crystallographic methods. Although the crystal of benzoic acid is composed of dimeric units, its lattice structure destroys the symmetry between the two monomers, and this results in two inequivalent potential minima and an inability to determine the tunneling splitting. However, with a suitable dopant the inequivalence between the two minima can be nearly lifted locally to allow a coarse estimate. The values found with thioindigo and selenoindigo as dopants were 8.4 ± 0.1 and 6.5 ± 1.5 GHz, respectively.[12,13] Remmers et al.[14] studied the gas-phase dimer using high-resolution UV spectroscopy. The spectrum they recorded consisted of two rigid-rotor components separated by 1107 ± 7 MHz, which they assumed to be the difference between the tunneling splittings in the S_0 and S_1 states. These data were later re-analyzed by using genetic algorithms to yield a more accurate value of 1116 ± 3 MHz.[15] Smedarchina et al. theoretically reproduced this value quite well (1920 MHz) by assuming that it was due solely to the ground-state splitting, taking it to be zero in the excited state, and showed that it corresponds to an effective tunneling barrier of 5793 cm^{-1}.[5]

Electronic coupling between the two monomer units in a doubly hydrogen-bonded system depends very sensitively on the nature of the hydrogen bonds. Perhaps the most striking example of this is the 7-azaindole dimer, in which electronic excitation was shown to be localized on one of the monomer units in all isotopologues, with the exception of a single asymmetric, doubly deuterated structure, in which it was found to be completely delocalized.[16,17] This is remarkable, since the last-named structure only differs from two others by monodeuteration in the aromatic ring. Fortunately, in many other systems the situation seems to be more clear-cut. In the 2-pyridone dimer the excitation is completely delocalized,[18,19] whereas in carboxylic acids the excitation generally seems to be localized.[20–22] By observing a vibronic band in the gas-phase benzoic acid dimer split into four components on partial deuteration, Poeltl et al. showed that also in this system electronic excitation resides on a single half of the complex.[23,24]

Localization of excitation raises the question how feasible excitation transfer is. Very interesting in this respect is the existence of a vibronic band around 57 cm^{-1} above the origin of the benzoic acid dimer. This band is shared with many other carboxylic acid dimers, including that of anthranilic acid, for which it was recently found that, although there is a strong Franck–Condon progression in this mode, the dispersed fluorescence spectrum shows intensity only in even members of the progression.[20] By means of DFT calculations, the band was assigned as the intermolecular geared bend mode, and the anomalous intensity patterns were explained by the possibility of excitation transfer between the two monomers, altering the selection rules.[25] Due to large intramolecular geometry changes on excitation of a monomer unit, however, the exci-

ton splitting could not be observed directly. The corresponding vibronic band of the benzoic acid dimer shows the same anomalous intensity pattern, but a detailed analysis of intramolecular vibrational relaxation (IVR) rates in isotopically mixed dimers led to the conclusion that excitation transfer is only appreciable at higher excess energies.[24] Still, due to the absence of an intramolecular hydrogen bond, the intramolecular geometry changes on electronic excitation are much smaller in the benzoic acid dimer than in the anthranilic acid dimer, which means an exciton splitting might be observable in the vibronic band of benzoic acid dimer. This was also suggested by Baum et al., though given their upper limit of 0.3 cm^{-1}, such a measurement would require high resolution.[26]

The assignment of this band is the topic of some debate. Poeltl et al. initially suggested it to be the intermolecular geared bend mode. This was because it forms strong combination bands with other vibrations ascribed to internal motions in the carboxyl group, and due to the observation that in the completely ring-deuterated (d_5–d_5) dimer the vibrational frequency remains virtually unchanged.[23] They later favored reassignment as either the out-of-plane bending motion or torsion, given that its frequency is unchanged in the electronically excited state.[24] Dispersed fluorescence spectra of this band led Tomioka et al. to assume that it is the torsion mode.[27] Quantum chemical calculations seem to disagree among each other to the same extent. Based on DFT calculations, Nandi et al. assigned it as the geared bend motion,[28] while Antony et al. claimed that it is the torsion mode,[29] and according to Florio et al. it could be either the geared bend or tilting motion.[30,31] Bakker et al. found that the difficulties in accurately describing the hydrogen-bonded modes also play a role in the calculation of higher vibrations (500–1900 cm^{-1}).[32]

Herein, we determine the intermolecular structure in both the ground and electronically excited state from seven different dimer origins in high-resolution spectra. Of particular interest is the question whether a decrease in the carboxyl O···O distance can be observed, as has been suggested,[8,11] and whether the excited state has a bent structure, as was proposed earlier.[14] Furthermore, analysis of a high-resolution spectrum of the 57 cm^{-1} vibronic band should show whether exciton splitting is present and which vibration is involved. Lastly, this assignment should allow us to determine the splittings of the S_0 and S_1 states separately, as well as the relative tunneling barrier height.

Experimental Section

Experimental Procedures: The experimental setup for rotationally resolved laser-induced fluorescence (LIF) is described elsewhere.[33] Briefly, it consists of a ring dye laser (Coherent 899-21) containing Rhodamine 110, pumped with 6 W of a frequency-doubled Yb:YAG laser. The second harmonic of the dye-laser output is generated in an external folded ring cavity (Spectra Physics Wavetrain). The resulting output power is typically between 30 and 40 mW and is constant during each experiment. The molecular beam is formed by co-expanding benzoic acid, heated to 390 K, and argon through a 100 µm nozzle into the vacuum by using a backing pressure of 220 mbar. The molecular-beam equipment consists of three differ-

entially pumped vacuum chambers that are linearly connected by skimmers (1 and 3 mm in diameter, respectively) in order to reduce the Doppler width. In the third chamber, 360 mm downstream of the nozzle, the molecular beam is crossed at right angles by the UV laser beam. Imaging optics focus the total undispersed fluorescence from the excited molecules onto a photomultiplier tube mounted perpendicularly to the plane defined by the laser and the molecular beam, the output of which is then discriminated and digitized by a photon counter and transmitted to a PC for data recording and processing. The resulting Doppler width in this setup is 25 MHz (FWHM). Relative frequencies are determined with a quasiconfocal Fabry–Perot interferometer with a free spectral range (FSR) of 149.9434(56) MHz. The absolute frequency was obtained by comparing the recorded absorption spectrum of iodine with tabulated lines.[34]

Materials: Benzoic acid was purchased from Caelo (p.A.), and [D_5]benzoic acid (99.2%) was obtained from CDN isotopes. Both were used without further purification. [D_1]Benzoic acid was produced by refluxing benzoic acid with an excess of D_2O and subsequent removal of the solvent.

Ab Initio Calculations: Structure optimizations were performed by employing the valence triple-zeta basis set with one set of polarization functions per atom (TZVP) from the TURBOMOLE library.[35,36] The equilibrium geometries of the electronic ground and the lowest excited singlet states were preoptimized by (time-dependent) density functional theory with the B3LYP functional and subsequently optimized at the CC2 level within the resolution-of-the-identity approximation.[37,38] To ensure that the optimized structure is a real minimum we numerically calculated the second derivatives. We obtained no imaginary frequencies for any of the normal modes, that is, all optimized structures are minima.

The singlet-state energies and wavefunctions were calculated by the combined DFT/multireference configuration interaction (DFT/MRCI) method of Grimme and Waletzke.[39] The configuration state functions in the MRCI expansion are constructed from Kohn–Sham (KS) orbitals, optimized for the dominant closed-shell determinant of the electronic ground state by employing the BHLYP[40,41] functional. All valence electrons were correlated in the MRCI runs, and the eigenvalues and eigenvectors of eight singlet states were determined. The initial set of reference configuration state functions was generated automatically in a complete active-space-type procedure (including all single and double excitations from the five highest occupied molecular orbitals in the KS determinant to the five lowest virtual orbitals) and was then iteratively improved.

The first-order transition state for double proton transfer was preoptimized at the B3LYP level with the 6-31G(d,p) basis set by using the QST3 method[42] as implemented in the Gaussian03 program package.[43] With the thus-obtained structure the S_0 transition state was optimized at the RICC2 level by using the trust radius image minimization (TRIM) method[44] implemented in the STATPT module from TURBOMOLE V5.8 with the same basis sets as for the minimum structures.

The Derandomized ES DR2 Algorithm: Spectra were fitted to a simple asymmetric rotor Hamiltonian by using a derandomized (DR) evolutionary strategy (ES) which was developed in the mid-90s by Ostenmeier et al.[45] This special implementation, which is also used herein, represents the second generation of derandomized ES and is abbreviated in the following as DR2.[46] It is shown here to be a very good alternative to the genetic algorithm based fits we have employed so far.[47,48]

Both evolutionary strategies like the DR2 algorithm and the genetic algorithm belong to the category of global optimizers known as evolutionary algorithms, which were inspired by the biological processes of reproduction and natural selection. However, whereas the genetic algorithm tries to find a solution in parameter space by combining information from a set of trial solutions with the aim of creating better ones, the DR2 algorithm can sense in which direction the fitness increases. In a first step of the DR2 algorithm, some trial solutions are generated (offspring) by using a random distribution around some starting point (parent), each consisting of the complete parameter set necessary to describe the spectrum, and the quality of each solution is analyzed by means of a fitness function.[47,48] Provided one of the offspring is better than the parent, this solution is selected and used to compute the next parent, which then serves as the starting point for an iteration of this cycle (generation). In calculating the parent for the next generation, the DR2 algorithm makes use of the correlation matrix for successive changes in the parents (mutations). In essence, this means that if for some parameter a parent has evolved in the same direction for several generations, so that their correlation in this parameter is positive, the most likely solution is assumed to be further in that direction and the next parameter mutation will be larger. Correspondingly, two anticorrelated mutations will lead to a smaller mutation. By discriminating between mutation rates of different parameters, the DR2 algorithm can reliably find the optimal solution within a relatively small number of generations.[45]

The usefulness of the DR2 algorithm in solving physical problems was shown by Shir et al., who tested several evolutionary algorithms for their ability to find the theoretical alignment of a sample of molecules in space with shaped laser pulses.[49] The DR2 algorithm proved to be not only the fastest but also the most reliable algorithm for this task, and it even outperformed several more advanced algorithms such as DR3 and CMA–ES. Given their success they then turned their attention to the problem of second harmonic generation (SHG) which, although much more difficult, showed that the DR2 algorithm again performed best.[46] When used to fit our spectra, the DR2 algorithm succeeded in obtaining good fits with a smaller population and within fewer generations compared to the genetic algorithm (GA). Although the evaluation of a single trial solution in the DR2 algorithm is more expensive, this led to a reduction in the total computation time by a factor of two compared to the GA.

2. Results and Discussion

2.1. The Dimer Origin

The rotationally resolved spectrum of the $S_1 \leftarrow S_0$ origin of the benzoic acid dimer has been reported before,[14,15] but was measured again for this study. It is a b-type spectrum and shows doubling of all lines due to concerted proton tunneling in the double hydrogen bond. The size of this splitting is $\Delta = 1114.0 \pm 1.0$ MHz. The spectrum is very congested, and each apparent transition typically consists of some ten individual rovibrational transitions. The transitions in these K stacks all share the same ΔK_a, but differ in the ground-state level from which they originate. Under our experimental conditions, transitions originating from ground-state levels with J values up to 130 are needed to reproduce contributions to the spectrum with an intensity of at least 0.5% of the strongest transitions. Since there is no thermal equilibrium in the molecular beam,

we employ a two-temperature Boltzmann model to describe the energy distribution. This resulted in rotational temperatures of $T_1 = 3.5$ K and $T_2 = 5.3$ K with a relative T_2 weight factor of 0.29.

Besides the d_0–d_0 dimer we measure the $S_1 \leftarrow S_0$ origin of four more isotopologues, which give rise to six additional spectra. These are the d_1–d_1 and d_5–d_5 homodimers, where the former is deuterated in the hydrogen bonds and the rings of the latter are completely deuterated, and the d_0^*–d_1/d_1^*–d_0 and d_0^*–d_5/d_5^*–d_0 mixed dimers. Here the asterisk denotes the electronically excited moiety. Due to the weak electronic coupling between the two monomer units, the electronic excitation is localized on one of them, and as a result both mixed dimers have two separate origins depending on which monomer is excited.[23] However, since the isotopic shifts upon deuteration are small, the origins of these mixed dimers (with the exception of the d_5^*–d_0) are not spectrally separated from the homodimers consisting of the excited monomer and have therefore not been resolved in previous studies. As an example the spectrum of the d_0^*–d_5 dimer is shown in Figure 1 together with a simulated spectrum. The simulation consists of two components: the spectrum of d_0–d_0, for the simulation of which the molecular constants are held fixed to the optimal values determined there, and the spectrum of d_0^*–d_5 itself, blueshifted by 0.67 cm^{-1}. All other spectra and their simulations can be found in the Supporting Information.

Within the experimental uncertainty all initial simulations produce transition dipole moment directions corresponding to pure b-type spectra, and no a-type or c-type components can be incorporated unambiguously. Therefore, to obtain the final results a pure b-type asymmetric rotor Hamiltonian is used. Also, for d_0^*–d_1 and d_1^*–d_0 as well as d_0^*–d_5 and d_5^*–d_0, the
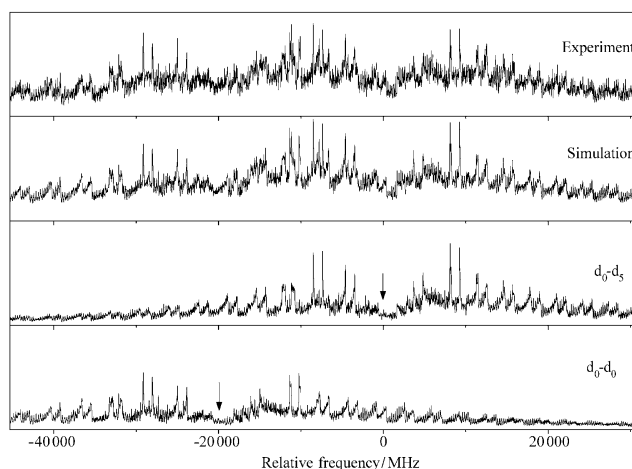

Figure 1. Electronic origin of the benzoic acid d_0^*–d_5 dimer at 35724.456 cm^{-1}. In the upper two traces the measured spectrum and the best simulation are shown. The lower two traces show the two components present in the simulation, that is, the d_0^*–d_5 spectrum and the d_0–d_0 spectrum, for the latter of which the molecular parameters deduced from the analysis of a separate measurement were used. The arrows indicate the spectral origins.

ground-state rotational constants for each set are the same within their experimental uncertainties, that is, both spectra in each of these two sets indeed originate from a common ground state structure. In a final fit the ground-state rotational constants for both spectra in each set are therefore forced to be equal. The parameters obtained from the final fits are given

Table 1. Origins and molecular parameters for the isotopologues of the benzoic acid dimer determined from fits using evolutionary algorithms.

	This work	d_0–d_0 Ref. [14]	Ref. [15]	d_0–d_0 + 57 cm^{-1}	d_1–d_1	d_5–d_5
A'' [MHz]	1925.00(20)	1923(16)	1926.87(50)	1925.04(21)	1905.94(18)	1686.92(16)
B'' [MHz]	128.05(14)	127(8)	128.19(10)	128.08(14)	127.73(14)	118.91(14)
C'' [MHz]	120.14(14)	114(8)	120.27(10)	120.17(14)	119.79(14)	111.16(14)
A' [MHz]	1908.95(16)	1908(16)	1910.70(50)	1920.48(17)	1890.16(15)	1672.95(13)
B' [MHz]	127.53(14)	–	127.67(10)	127.57(14)	127.18(14)	118.42(14)
C' [MHz]	119.63(14)	–	119.76(10)	119.64(14)	119.24(14)	110.68(14)
ΔA [MHz]	−16.05(9)	−15(10)	−16.17(20)	−4.56(9)	−15.78(8)	−13.98(7)
ΔB [MHz]	−0.52(12)	–	−0.52(1)	−0.52(12)	−0.55(12)	−0.48(12)
ΔC [MHz]	−0.51(12)	–	−0.51(1)	−0.53(12)	−0.55(12)	−0.48(12)
Δ [MHz]	1114.0(10)	1107(7)	1116(3)	1656.4(11)	< 45	1077.0(10)
Origin [cm^{-1}][a]	35723.786(1)	35723.82(5)	–	35781.091(1)	35737.416(1)	35874.324(1)

	d_0^*–d_1		d_1^*–d_0	d_0^*–d_5	d_5^*–d_0
A'' [MHz]	1915.76(32)		1915.76(17)	1798.21(14)	1798.21(15)
B'' [MHz]	127.91(15)		127.91(14)	123.42(14)	123.42(14)
C'' [MHz]	119.98(15)		119.98(14)	115.58(14)	115.58(14)
A' [MHz]	1899.65(26)		1900.51(14)	1784.55(12)	1782.50(12)
B' [MHz]	127.39(15)		127.33(14)	122.95(14)	122.90(14)
C' [MHz]	119.50(15)		119.42(14)	115.11(14)	115.07(14)
ΔA [MHz]	−16.11(16)		−15.25(10)	−13.66(6)	−15.72(7)
ΔB [MHz]	−0.50(12)		−0.57(12)	−0.46(12)	−0.52(12)
ΔC [MHz]	−0.50(12)		−0.56(12)	−0.48(12)	−0.51(12)
Δ [MHz]	136.7(12)		98.9(11)	1137.0(10)	1116.9(11)
Origin [cm^{-1}][a]	35722.789(1)		35737.574(1)	35724.456(1)	35872.481(1)

[a] In the spectra with splitting, the origin of the reddest component is given.

in Table 1. The estimated lifetime broadening of the transitions is 20 ± 10 MHz, corresponding to an excited state lifetime of 8 ± 4 ns. Unfortunately, the congested nature of the spectra prohibits a more accurate determination.

Immediately obvious is that the changes in the rotational constants (ΔB_g; $g = a$, b, c) are largely independent of deuteration, and thus the spectra are qualitatively very similar in appearance. Strikingly, both for the d_0^*–d_1/d_1^*–d_0 and the d_0^*–d_5/d_5^*–d_0 mixed dimers, the two spectra originating from the same ground state show substantially different tunneling splittings. In the case of d_1–d_1 no splitting is observed. From test calculations we estimate how large the separation between two closely spaced spectral components must be in order to observe both. This results in a value of 45 MHz, which indicates an upper value for the splitting.

2.2. The 57 cm^{-1} Vibronic Band

Figure 2 shows the rotationally resolved spectrum of the vibronic band located 57 cm^{-1} above the electronic origin of the d_0–d_0 dimer. Although the signal-to-noise ratio is more than an order of magnitude lower than that of the origin spectrum, the agreement between simulation and experiment is clearly still very good. On comparison with the origin spectrum it is also apparent that the amount by which all lines are split due to tunneling is substantially larger; the fit yields a value of 1656.4 ± 1.1 MHz, which corresponds to an increase of almost 50%. The molecular parameters resulting from this fit are listed in Table 1.

2.3. Determination of the Cluster Structure Parameters

The RICC2 optimizations of the S_0 state structure with imposed C_1 and C_{2h} symmetry restrictions are performed with the TZVP basis sets. The results of both calculations are identical within
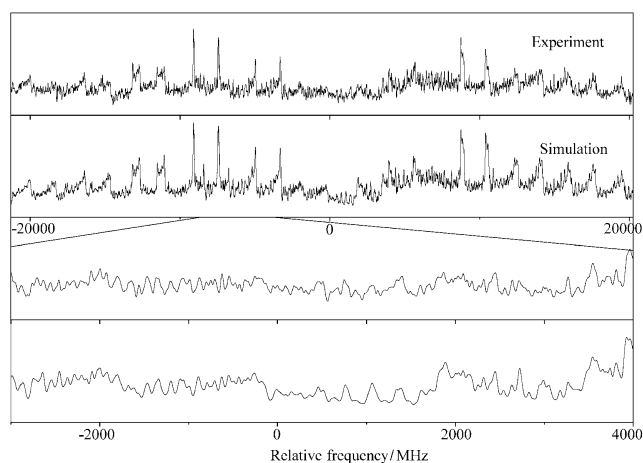
the accuracy of the calculation, and this confirms the symmetry of the equilibrium structure. The rotational constants resulting from the constrained calculations are listed in Table 2 along with the experimental rotational constants from this study and the optimized geometric parameters. The agreement between calculated and experimental inertial parameters is very good, with the calculated constants differing from the measured ones by less than half a percent. Since the experimentally determined rotational constants are effective values rather than equilibrium values, we ascribe the difference to effects of zero-point energy vibrational averaging and assume the calculated structure to be the best possible fit to our measurements. The S_1 state optimizations at the same level of theory result in rotational constants close to those of the ground state. The A constant is found to decrease by 16 MHz on electronic excitation, which compares to a difference of 19 MHz between the RICC2/TZVP calculations of the excited state and the electronic ground state.

The atomic numbering of the benzoic acid dimer used in the discussion of the structural parameters of the monomers and the hydrogen-bond parameters is shown in Figure 3. The
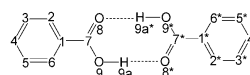
Figure 3. Atomic numbering of the benzoic acid dimer used in Table 2. The asterisks mark the electronically excited benzoic acid moiety.

calculated geometric parameters for both benzoic acid moieties are equal for the ground state (C_{2h} symmetry), while they differ considerably for the electronically excited state, reflecting the localized excitation with a reduction of the symmetry to C_s. The electronically excited benzoic acid moiety (marked with asterisks in the bond definitions in Table 2) shows an increase of the average C—C bond length from 139.4 pm in the ground state to 143.0 pm, which is typical for benzenoid aromatic compounds. The unexcited moiety of the electronically excited dimer has an average C—C bond length of 139.6 pm, which is nearly the same as in the ground state and confirms localization of excitation on one of the benzoic acid moieties. The decrease of the C1—C7 bond length, indicating quinoidal character in the S_1 state, is also found in other monosubstituted benzenes.

The hydrogen-bond geometric parameters show the same behavior: two equal O9—H9a bond lengths and equal O9-H9a-O8* angles, which define

Figure 2. Vibronic band at 35781.091 cm^{-1}, around 57 cm^{-1} above the electronic origin of the benzoic acid d_0–d_0 dimer.

the deviation from linearity of the hydrogen bonds in the electronic ground state, while both geometric parameters differ considerably in the excited state. The COH···OC* hydrogen bond is considerably shorter than in the electronic ground state (-5.2 pm), while the *COH···OC bond is longer by 1.8 pm. These opposite changes of the hydrogen-bond lengths, which are founded in the decreased OH acidity on electronic excitation, result in in-plane tilting of the monomer moieties in the excited state. The amount by which the structure is bent cannot be determined in the same way as was done by Remmers et al.,[14] since they assumed both monomer geometries were retained in the dimer, which is not the case and leaves their bending angle ill-defined. When we instead define the bending angle as C4-CM-C4*, where CM stands for the center of mass of the dimer, a value of $0.7 \pm 0.2°$ results. Since the decrease in length of the shortened hydrogen bond is larger than the increase in length of the elongated one, these results are consistent with the reduction in the average carboxyl O···O distance found in earlier work.[8, 11]

Table 2. Rotational constants and S_0- and S_1-state geometric parameters of the benzoic acid dimer calculated at the RICC2/TZVP level of theory. The atomic numbering refers to Figure 3. All bond lengths are given in picometers, and angles in degrees. Atoms marked with an asterisk belong to the electronically excited benzoic acid moiety.

	S_0			S_1	
	RICC2	Crystal data[53]	Exptl.[a]	RICC2	Exptl.[a]
A'' [MHz]	1919	–	1925	1900	1909
B'' [MHz]	128	–	128	127	127
C'' [MHz]	120	–	120	119	120
C1–C2	139.9	139.2	–	140.0	–
C2–C3	139.2	140.1	–	139.3	–
C3–C4	139.5	138.4	–	139.6	–
C4–C5	139.6	137.9	–	139.6	–
C5–C6	139.1	138.7	–	139.2	–
C6–C1	139.9	139.0	–	140.0	–
C1–C7	148.3	148.4	–	148.6	–
C7–O8	124.0	126.3	–	124.2	–
C7–O9	130.0	127.5	–	132.8	–
O9–H9a	100.3	ca. 100	–	100.2	–
C–H (av)	108.3	–	–	108.4	–
C2-C1-C7	121.3	118.8	–	121.3	–
O8-C7-O9	123.8	123.2	–	124.0	–
C1-C7-O8	122.2	120.2	–	121.9	–
C7-O9-H9a	108.5	–	–	108.8	–
C1*–C2*	139.9	139.2	–	143.4	–
C2*–C3*	139.2	140.1	–	143.2	–
C3*–C4*	139.5	138.4	–	141.9	–
C4*–C5*	139.6	137.9	–	142.9	–
C5*–C6*	139.1	138.7	–	143.1	–
C6*–C1*	139.9	139.0	–	143.4	–
C1*–C7*	148.3	148.4	–	144.3	–
C7*–O8*	124.0	126.3	–	125.7	–
C7*–O9*	130.0	133.1	–	134.5	–
O9*–H9a*	100.3	ca. 100	–	100.0	–
C*–H* (av)	108.3	–	–	108.3	–
C2*-C1*-C7*	121.3	118.8	–	122.8	–
O8*-C7*-O9*	123.8	123.2	–	123.6	–
C1*-C7*-O1*	122.2	120.2	–	122.2	–
C7*-O9*-H9a*	108.5	–	–	108.2	–
H9a–O8*	165.4	ca. 160	–	160.2	–
O8–H9a*	165.4	ca. 160	–	167.2	–
O8–O9*	265.7	263.3	–	267.2	–
O9–O8*	265.7	263.3	–	260.4	–
O9-H9a-O8*	179.0	–	–	177.5	–
O9*-H9a*-O8	179.0	–	–	179.1	–

[a] Experimental values from this study. For exact values and accuracies, see Table 1

2.4. Determination of the Center-of-Mass Distance

An easy approach to the change of the cluster structure upon electronic excitation can be made by using the center-of-mass (COM) distance of the monomer moieties in the cluster, as has been shown by Connell et al.[50] The COM distance of two monomer moieties in a dimer is given by Equation (1)

$$R = \sqrt{\frac{\sum_g I_g^{Dimer} - \sum_g I_g^{Monomer1} - \sum_g I_g^{Monomer2}}{2\mu}} \quad (1)$$

where μ is the reduced mass of the two moieties, and I_g are the respective moments of inertia, described by their superscripts, which are calculated from experimentally determined rotational constants. The COM distances for d_0–d_0 and d_1–d_1 in

the ground state were calculated by using the monomer rotational constants, taken from the microwave work of Onda et al.,[51] for both moieties. The difference between the COM distances of d_0–d_0 and d_1–d_1 can be traced back to the different vibrational averaging in these isotopologues.

While the determination of the COM distance in the electronic ground state is conceptually easy, two problems arise for the electronically excited state: first, the rotational constants of the excited state of the monomer are not known. Second, it is not known a priori whether the excitation is local or delocalized over both moieties. In the first case different rotational constants must be used in Equation (1) for Monomer1 and Monomer2. One of the monomers would then have the

rotational constants of benzoic acid in the ground state, and the other the rotational constants of the electronically excited state. Since these rotational constants are not available, we use the ground state rotational constants of both monomers for a rough model (model 1).

Because we conclude that the electronic excitation is localized, a more accurate COM distance can be derived when the rotational constants of the monomer excited state are used. These can be obtained by calculating the structure of the benzoic acid monomer by DFT with the B3LYP functional for the ground state and with time-dependent (TD)DFT for the excited state. The difference between the two sets of rotational constants closely matches the change in the rotational constants on electronic excitation, while the absolute values are less reliable. We therefore added the difference between the calculated rotational constants from the DFT and TDDFT calculations to the microwave rotational constants to get the inertial parameters for the excited monomer moiety, and used these in a more accurate model (model 2).

Table 3 compares the COM distances in the ground and electronically excited states of the benzoic acid dimer for both monomer models. For both isotopologues and independent of the model used we find an increase in the COM distance, that is, a decrease of the hydrogen-bond strength on electronic excitation.

Table 3. Center-of-mass distance [pm] of the d_0–d_0 and the d_1–d_1 isotopologues of the benzoic acid dimer in the ground and electronically excited states.

		d_0–d_0	d_1–d_1
S_0		712.6	708.9
S_1	model 1	714.6	713.3
S_1	model 2	713.1	711.7
Δ	model 1	2.0	4.4
Δ	model 2	0.5	2.8

2.5. Symmetry

Both the $S_1 \leftarrow S_0$ spectrum and the vibronic band 57 cm^{-1} above it are b-type spectra consisting of two components. Interestingly, the separation between these components is larger in the vibronic spectrum than in the origin spectrum. Figure 4 shows the three possible ways to combine these two observations: a) the ground-state splitting is very small, b) the S_1-state
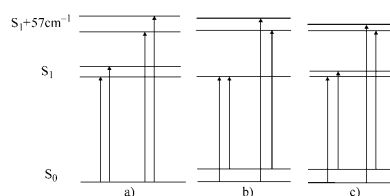
splitting is very small, or c) both are appreciable. Since it is expected from theory that the splitting in the electronically excited state is smaller than that in the ground state due to the weakening of one of the hydrogen bonds (e.g., see ref. [5]) we hold the first option for unlikely and will therefore not explore it further. For the other two options, some of the arrows drawn in Figure 4b and c are not unique; the relative sizes of the tunneling splittings are equally unknown. However, it is clear that without any selection rules restricting the possibilities, the vibronic band would consist of four components, and in case c the same would hold for the origin transition. This is clearly not what we observe, so a closer look at the symmetry of the dimer system is warranted. For a large part the group theory for this system is the same as for the formic acid dimer, which has been described in detail by Madeja et al.[1] We therefore focus on the main differences and conclusions here; more information can be found in their article. Additionally, we will consider case b to be the limiting case for the energy-level ordering shown in Figure 4c and no longer consider it separately.

As shown in Section 2.3, the ground-state structure is of C_{2h} symmetry and if we assume a synchronous tunneling motion, the transition state is of D_{2h} symmetry, which means we must describe the ground state using the molecular symmetry group G_8. For the electronically excited state, however, we already concluded that the electronic excitation is localized on one monomer unit. This immediately lowers the symmetry to C_s with a C_{2v} transition state (with the A axis as the C_2 axis) so that we must describe the excited state using G_4. The energy-level diagram and allowed transitions that result for the origin and the seven lowest-frequency vibrations (see Section 2.6) are shown in Figure 5. Note that all levels have two symmetry labels due to the unresolved K-type doubling in this system.

If in addition to the localization of the electronic excitation the excited state has a bent structure, then the system has $C_s(M)$ symmetry (isomorphic with C_s) and all energy-level labels are transformed into A′/A″. This means all transitions would become possible again, in contradiction with our observations.

Figure 4. Three possible energy-level schemes for explaining the observed $S_1 \leftarrow S_0$ and $S_1 + 57$ cm$^{-1} \leftarrow S_0$ spectra.
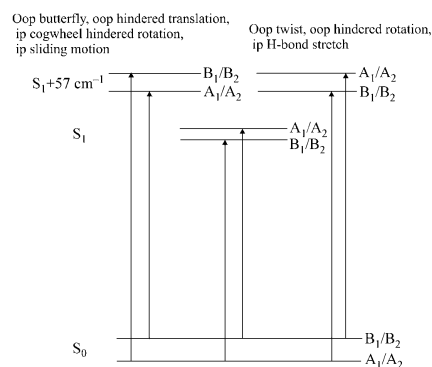

Figure 5. Energy-level ordering and allowed transitions for the electronic origin and seven lowest-frequency vibrations under C_{2v} symmetry; vibrational nomenclature after ref. [30]. Out-of-plane vibrations are designated as oop, and in-plane vibrations as ip.

Clearly the bending angle for the excited-state geometry we deduced in Section 2.3 is small enough to approximate the system as G_4-symmetric.

The assumption of G_4 symmetry also affects the intensity ratios between different transitions. The effect, however, is small: when the K-type doubling cannot be resolved (as in our case) a ratio between $\Delta K_a \Delta K_c$ (even/even) and (even/odd) to (odd/odd) and (odd/even) transitions of 31:33 results. This effect is further diminished by the crowdedness of the spectrum, which mixes different transitions under each apparent line shape, and leads to our inability to decide on the correctness of this assumption based on nuclear statistics.

2.6. Vibronic Band Assignment

For a correct assignment of the 57 cm^{-1} band we need the calculated frequencies for the vibrations indicated in Figure 5; they are given for the S_0 state in Table 4. MOLDEN frequency files containing the optimized geometry and all intra- and intermolecular vibrations can be found in the Supporting Information.

We know from earlier work by Poeltl et al.[24] that for this particular vibration the excited-state frequency is practically the same as that in the ground state, which allows us to use these ground-state frequencies for our assignment. They were derived under C_{2h} symmetry and the corresponding symmetry labels are given. However, as was described in Section 2.5, due to the feasibility of the tunneling motion and the localization of electronic excitation, we should use the G_4 symmetry group, which is isomorphic to C_{2v}, to describe possible transitions. For this reason G_4 symmetry labels were also added. The last three columns list the calculated changes in rotational constants for these vibrations in the harmonic approximation.

Since the splitting observed in the vibronic-band spectrum is larger than that in the origin spectrum (1656.4 vs 1114.0 MHz) it is clear that an assignment to a vibration having the same selection rules as the origin transition (those on the right-hand side in Figure 5) is only possible if the vibration itself increases the tunneling rate. Since the out-of-plane twisting motion and the out-of-plane hindered rotation leave the

hydrogen-bonding network practically unaffected, these are ruled out. The in-plane hydrogen-bond stretch is expected to increase the tunneling rate, but the motion itself would lead to a change in the B and C rotational constants. Since this contradicts our measurements, we also exclude the in-plane H-bond stretching motion as a possibility, forcing us to conclude that the selection rules for the 57 cm^{-1} vibronic band must be reversed.

Examining the four vibrations listed on the left-hand side of Figure 5, the same argument excludes the in-plane sliding motion, as it is expected to affect the B and C rotational constants as well as A, contrary to our observations. This leaves us with only three possible assignments: the out-of-plane butterfly motion, the out-of-plane hindered translation, and the in-plane cogwheel hindered rotation. Without additional information to discriminate between these modes, we opt to trust the calculated frequencies and assign the 57 cm^{-1} band as the out-of-plane butterfly motion, in excellent agreement with calculations (58 cm^{-1}). It also agrees with the observation that the frequency is virtually unchanged in the d_5–d_5 dimer,[23] and with the assignment made in reference [24]. Unfortunately, however, the effect of this vibration on the A rotational constant does not agree with our measurements. Indeed, even the sign of the predicted change is wrong. Although the vibrational effects on the rotational constants were calculated in the harmonic approximation and it is well-known that the vibrations in the benzoic acid dimer are highly anharmonic,[30] we infer that this vibration must be accompanied by a structural change that is not predicted by our calculations.

2.7. Splittings

Interestingly, the out-of-plane butterfly mode involves practically no motion of the hydrogen-bonding network. If we assume that this means the effect on the tunneling rate is negligible, we can deduce the sizes of the S_0- and S_1-state tunneling splittings. As can be seen in Figure 5 the splitting observed in the vibronic band spectrum would then be the sum of the S_0 and S_1 tunneling splittings, whereas the separation between the two components in the origin spectrum would be equal to the difference. If we now, as in Section 2.5, take the S_0 splitting to be larger than the S_1 splitting, it immediately follows that $\Delta(S_0) = 1385.2 \pm 0.7$ MHz and $\Delta(S_1) = 271.2 \pm 0.7$ MHz. In the case of a pure, coherent tunneling motion in a simple symmetric double-minimum potential well, we can now calculate the effective potential barrier V_{eff} in the WKB approximation.[52] The imaginary frequency at the top of the barrier ω_i and the corresponding ground-state frequency ω_F were deduced from a normal-mode analysis of the S_0

Table 4. RICC2/TZVP calculated frequencies for the seven lowest S_0 state vibrations of the d_0–d_0 and d_5–d_5 benzoic acid dimers including their symmetry labels under the C_{2h} point group and the G_4 molecular symmetry group. Also given are the calculated changes in rotational constants to which they lead in the harmonic approximation. The MOLDEN frequency files containing the optimized geometry and all intra- and intermolecular vibrations are mandatory for the description of the vibrations. They can be found in the Supporting Information.

Vibration	Frequency [cm^{-1}]		Symmetry		Δg; $g = A, B, C$ [MHz]		
	d_0–d_0	d_5–d_5	C_{2h}	G_4	ΔA	ΔB	ΔC
Observed	57.31	–	–	–	11.49	0.00	−0.02
Oop butterfly	58.1	56.5	a_u	B_1	−14.26	−0.06	0.00
Oop hindered translation	88.6	86.7	b_g	B_1	−18.17	−0.08	0.00
Ip cogwheel hindered rotation	97.9	93.5	b_u	B_2	−8.93	−0.01	−0.05
Oop twist	110.9	101.4	a_u	A_2	−7.78	−0.03	0.00
Ip H-bond stretch	116.8	113.8	a_g	A_1	−9.57	5.40	4.69
Ip sliding motion	134.1	129.5	a_g	B_2	2.09	1.58	1.40
Oop hindered rotation	171.7	171.2	b_g	A_2	−13.33	−0.06	0.00

transition state and ground state RICC2 structures, respectively. Using the resulting values of $\omega_i = 1122$ cm^{-1} and $\omega_F = 3167$ cm^{-1} we find an S_0-state potential barrier of 6224 cm^{-1} (7.45 kJ mol^{-1}). Because no reliable S_1-state transition frequency was calculated, we assume the same frequencies to calculate the S_1-state potential barrier, which results in a value of 6672 cm^{-1} (7.99 kJ mol^{-1}).

Since the approximation used here is quite crude, we do not expect these barrier heights to be very accurate, even though the S_0-state barrier is quite close to that of 6.93 kJ mol^{-1} found in the most extensive calculation done until now.[5] However, we do expect the ratio of the S_1 to S_0 barrier heights to be relatively accurate. Thus, we can conclude that the barrier height increases by about 7.2% on electronic excitation.

The fact that the splitting observed in the 57 cm^{-1} band spectrum can be interpreted as arising from proton tunneling while no further splitting has been observed leads to the conclusion that exciton splitting does not show up in our spectra. This leads to an upper limit of 45 MHz for the exciton splitting and confirms the conclusion from earlier work that excitation transfer only becomes important at higher excess energies.[24]

3. Conclusions

From a measurement of the rotationally resolved spectra of five different isotopologues we observed two separate origins for each of the mixed dimers. Together with the observation that the ground-state rotational constants are the same for both of these spectra, this provides unequivocal proof that the electronic excitation is localized on one of the monomer units. From our structural analysis it can be deduced that this leads to an asymmetry in the geometry of the hydrogen-bonding network and lowering of the dimer symmetry to C_s. We also found an increase in the center-of-mass distance between the two monomer moieties, from which we conclude that the hydrogen bond is weakened upon electronic excitation. Analysis of a vibronic band located 57 cm^{-1} above the electronic origin leads us to the conclusion that it should be assigned to the out-of-plane butterfly motion and allows separate deduction of the S_0- and S_1-state splittings. From the resulting splittings, $\Delta(S_0) = 1385.2 \pm 0.7$ MHz and $\Delta(S_1) = 271.2 \pm 0.7$ MHz, it can be concluded that the barrier height in the S_1 state is 7.2% larger than that in the S_0 state. No evidence for excitation transfer was found.

Acknowledgements

[1] F. Madeja, M. Havenith, *J. Chem. Phys.* **2002**, *117*, 7162–7168.

[2] F. Graf, T.-K. Ha, R. R. Ernst, *J. Chem. Phys.* **1981**, *75*, 2914–2918.

[3] S. Nagaoka, N. Hirota, T. Matsushita, K. Nishimoto, *Chem. Phys. Lett.* **1982**, *92*, 498–502.

[4] Y. Maréchal, *J. Chem. Phys.* **1987**, *87*, 6344–6353.

[5] Z. Smedarchina, A. Fernández-Ramos, W. Siebrand, *J. Chem. Phys.* **2005**, *122*, 134309-1–134309-12.

[6] Q. Xue, A. J. Horsewill, M. Johnson, H. Trommsdorff, *J. Chem. Phys.* **2004**, *120*, 11107–11119.

[7] F. Fillaux, M. H. Limage, F. Romain, *Chem. Phys.* **2002**, *276*, 181–210.

[8] C. C. Costain, G. P. Srivastava, *J. Chem. Phys.* **1964**, *41*, 1620–1627.

[9] H. Morita, S. Nagakura, *J. Mol. Spectrosc.* **1972**, *42*, 536–546.

[10] M. Ortlieb, M. Havenith, *J. Phys. Chem. A* **2007**, *111*, 7355–7363.

[11] A. Gutberlet, G. W. Schwaab, M. Havenith, *Chem. Phys.* **2008**, *343*, 158–167.

[12] A. Oppenländer, C. Rambaud, H. P. Trommsdorff, J.-C. Vial, *Phys. Rev. Lett.* **1989**, *63*, 1432–1435.

[13] C. Rambaud, H. P. Trommsdorff, *Chem. Phys. Lett.* **1999**, *306*, 124–132.

[14] K. Remmers, W. L. Meerts, I. Ozier, *J. Chem. Phys.* **2000**, *112*, 10890–10894.

[15] W. L. Meerts, M. Schmitt, *Int. Rev. Phys. Chem.* **2006**, *25*, 353–406.

[16] K. Sakota, H. Sekiya, *J. Phys. Chem. A* **2005**, *109*, 2718–2721.

[17] K. Sakota, H. Sekiya, *J. Phys. Chem. A* **2005**, *109*, 2722–2727.

[18] A. Held, D. W. Pratt, *J. Chem. Phys.* **1992**, *96*, 4869–4876.

[19] A. Müller, F. Talbot, S. Leutwyler, *J. Chem. Phys.* **2002**, *116*, 2836–2847.

[20] C. A. Southern, D. H. Levy, J. A. Stearns, G. M. Florio, A. Longarte, T. S. Zwier, *J. Phys. Chem. A* **2004**, *108*, 4599–4609.

[21] G. Meijer, M. S. de Vries, H. E. Hunziker, H. R. Wendt, *J. Chem. Phys.* **1990**, *92*, 7625–7635.

[22] C. K. Nandi, M. K. Hazra, T. Chakraborty, *J. Chem. Phys.* **2004**, *121*, 5261–5271.

[23] D. E. Poeltl, J. K. McVey, *J. Chem. Phys.* **1983**, *78*, 4349–4355.

[24] D. E. Poeltl, J. K. McVey, *J. Chem. Phys.* **1984**, *80*, 1801–1811.

[25] C. A. Southern, D. H. Levy, G. M. Florio, A. Longarte, T. S. Zwier, *J. Phys. Chem. A* **2003**, *107*, 4032–4040.

[26] J. C. Baum, D. S. McClure, *J. Am. Chem. Soc.* **1980**, *102*, 720–727.

[27] Y. Tomioka, H. Abe, N. Mikami, M. Ito, *J. Phys. Chem.* **1984**, *88*, 2263–2270.

[28] C. K. Nandi, T. Chakraborty, *J. Chem. Phys.* **2004**, *120*, 8521–8527.

[29] J. Antony, G. von Helden, G. Meijer, B. Schmidt, *J. Chem. Phys.* **2005**, *123*, 014305-1–014305-11.

[30] G. M. Florio, E. L. Sibert III, T. S. Zwier, *Faraday Discuss.* **2001**, *118*, 315–330.

[31] G. M. Florio, T. S. Zwier, E. M. Myshakin, K. D. Jordan, E. L. Sibert III, *J. Chem. Phys.* **2003**, *118*, 1735–1746.

[32] J. M. Bakker, L. M. Aleese, G. von Helden, G. Meijer, *J. Chem. Phys.* **2003**, *119*, 11180–11185.

[33] M. Schmitt, J. Küpper, D. Spangenberg, A. Westphal, *Chem. Phys.* **2000**, *254*, 349–361.

[34] S. Gerstenkorn, P. Luc, *Atlas du Spectre d'Absorption de la Molécule d'Iode*, Laboratoire Aimé-Cotton CNRS II, Paris, **1982**.

[35] R. Ahlrichs, M. Bär, M. Häser, H. Horn, C. Kölmel, *Chem. Phys. Lett.* **1989**, *162*, 165–169.

[36] A. Schäfer, C. Huber, R. Ahlrichs, *J. Chem. Phys.* **1994**, *100*, 5829–5835.

[37] C. Hättig, A. Köhn, *J. Chem. Phys.* **2002**, *117*, 6939–6951.

[38] C. Hättig, *J. Chem. Phys.* **2002**, *117*, 7751–7761.

[39] S. Grimme, M. Waletzke, *J. Chem. Phys.* **1999**, *111*, 5645–5655.

[40] A. D. Becke, *J. Chem. Phys.* **1993**, *98*, 1372.

[41] C. Lee, W. Yang, R. Parr, *Phys. Rev. B* **1988**, *37*, 785–789.

[42] C. Peng, H. B. Schlegel, *Israel J. Chem.* **1994**, *33*, 449.

[43] M. J. Frisch, G. W. Trucks, H. B. Schlegel, G. E. Scuseria, M. A. Robb, J. R. Cheeseman, J. A. Montgomery, Jr., T. Vreven, K. N. Kudin, J. C. Burant, J. M. Millam, S. S. Iyengar, J. Tomasi, V. Barone, B. Mennucci, M. Cossi, G. Scalmani, N. Rega, G. A. Petersson, H. Nakatsuji, M. Hada, M. Ehara, K. Toyota, R. Fukuda, J. Hasegawa, M. Ishida, T. Nakajima, Y. Honda, O. Kitao, H. Nakai, M. Klene, X. Li, J. E. Knox, H. P. Hratchian, J. B. Cross, C.

Adamo, J. Jaramillo, R. Gomperts, R. E. Stratmann, O. Yazyev, A. J. Austin, R. Cammi, C. Pomelli, J. W. Ochterski, P. Y. Ayala, K. Morokuma, G. A. Voth, P. Salvador, J. J. Dannenberg, V. G. Zakrzewski, S. Dapprich, A. D. Daniels, M. C. Strain, O. Farkas, D. K. Malick, A. D. Rabuck, K. Ragha-vachari, J. B. Foresman, J. V. Ortiz, Q. Cui, A. G. Baboul, S. Clifford, J. Cioslowski, B. B. Stefanov, G. Liu, A. Liashenko, P. Piskorz, I. Komaromi, R. L. Martin, D. J. Fox, T. Keith, M. A. Al-Laham, C. Y. Peng, A. Nanayakkara, M. Challacombe, P. M. W. Gill, B. Johnson, W. Chen, M. W. Wong, C. Gonzalez, J. A. Pople, *Gaussian03 (Revision a.1)*, Gaussian, Inc., Pittsburgh, PA, **2003**.

[44] T. Helgaker, *Chem. Phys. Lett.* **1991**, *182*, 503–510.

[45] A. Ostenmeier, A. Gawelcyk, N. Hansen in *Parallel Problem Solving from Nature—PPSN III* (Eds.: Y. Davidor, H.-P. Schwefel, R. Männer), Springer, Berlin/Heidelberg, **1994**.

[46] O. M. Shir, T. Bäck, *The Second Harmonic Generation Case Study as a Gateway for ES to Quantum Control Problems*, Proceedings of the Genetic and Evolutionary Computation Conference, ACM Press, London, UK, **2007**.

[47] J. A. Hageman, R. Wehrens, R. de Gelder, W. L. Meerts, L. M. C. Buydens, *J. Chem. Phys.* **2000**, *113*, 7955–7962.

[48] W. L. Meerts, M. Schmitt, G. Groenenboom, *Can. J. Chem.* **2004**, *82*, 804–819.

[49] O. M. Shir, C. Siedschlag, T. Bäck, M. J. J Vrakking, *Opt. Commun.* **2006**, *264*, 511–518.

[50] L. L. Connell, S. M. Ohline, P. W. Joireman, T. C. Corcoran, P. M. Felker, *J. Chem. Phys.* **1992**, *96*, 2585–2593.

[51] M. Onda, M. Asai, K. Takise, K. Kuwae, K. Hayami, A. Kuroe, M. Mori, H. Miyazaki, N. Suzuki, I. Yamaguchi, *J. Mol. Struct.* **1999**, *482*, 301–303.

[52] J. Bicerano, H. F. Schaefer III, W. H. Miller, *J. Am. Chem. Soc.* **1983**, *105*, 2550–2553.

[53] G. Bruno and L. Randaccio, *Acta Crystallogr. B* **1980**, *36*, 1711–1712.

5.6   Phenol-Argon-Cluster

The structure of phenol-Ar$_n$ (n=1,2) clusters in their S_0 and S_1 states

Ivo Kalkman,[1] Christian Brand,[2] Thi-Bao Chau Vu,[2] W. Leo Meerts,[1] Yuriy N. Svartsov,[2] Otto Dopfer,[3] Xin Tong,[4] Klaus Müller-Dethlefs,[4] Stefan Grimme,[5] and Michael Schmitt[2,a)]

[1]*Molecular and Biophysics Group, Institute for Molecules and Materials, Radboud University Nijmegen, NL-6500 GL Nijmegen, The Netherlands*
[2]*Institut für Physikalische Chemie I, Heinrich-Heine-Universität, Universitätsstraße 26.43.02.43 D-40225 Düsseldorf, Germany*
[3]*Institut für Optik und Atomare Physik, Technische Universität Berlin, Hardenbergstraße 36, D-10623 Berlin, Germany*
[4]*The Photon Science Institute, The University of Manchester, Alan Turing Building, Manchester M13 9PL, United Kingdom*
[5]*Organisch-Chemisches Institut der Universität Münster, Corrensstrasse 40, D-48149 Münster, Germany*

The structures of the van der Waals bonded complexes of phenol with one and two argon atoms have been determined using rotationally resolved electronic spectroscopy of the $S_1 \leftarrow S_0$ transition. The experimentally determined structural parameters were compared to the results of quantum chemical calculations that are capable of properly describing dispersive interactions in the clusters. It was found that both complexes have π-bound configurations, with the phenol-Ar$_2$ complex adopting a symmetric $(1|1)$ structure. The distances of the argon atoms to the aromatic plane in the electronic ground state of the $n=1$ and $n=2$ clusters are 353 and 355 pm, respectively. Resonance-enhanced multiphoton ionization spectroscopy was used to measure intermolecular vibrational frequencies in the S_1 state and Franck–Condon simulations were performed to confirm the structure of the phenol-Ar$_2$ cluster. These were found to be in excellent agreement with the $(1|1)$ configuration. © 2009 American Institute of Physics. [DOI: 10.1063/1.3149780]

I. INTRODUCTION

Intermolecular interactions of aromatic molecules are vital for chemical and biological recognition.[1] A detailed understanding of these interactions at the molecular level requires accurate knowledge of the intermolecular potential energy surface. Essential parameters of such a surface include the interaction energy and the geometry of the global minimum, as well as the occurrence of less stable local minima. The fruitful interplay of high-resolution spectroscopy of isolated clusters in molecular beams and high-level quantum chemical calculations provides the most direct access to these potential parameters.[2–9] Clusters of phenol with neutral ligands, denoted phenol-L_n, are attractive model systems to investigate the competition of two different fundamental types of intermolecular forces, namely hydrogen bonding to the acidic OH group (H-bond) and van der Waals (vdW) bonding (stacking) to the highly polarizable π electron system of the aromatic ring (π-bond, vdW bond). It turns out that the relative interaction strengths of both binding motifs strongly depend on the type of ligand (L), the degree of solvation (n), and the degree of electronic excitation or ionization. Hence, a plethora of spectroscopic and theoretical studies have been carried out on phenol-bearing clusters in order to determine the preference for stacking or hydrogen bonding interactions.

The present work reports high-resolution electronic spectra of phenol-Ar$_n$ clusters with $n=1$ and 2 in a molecular beam expansion, along with quantum chemical calculations. An analysis of vibrational frequencies from new resonance-enhanced multiphoton ionization (REMPI) spectra of the phenol-Ar$_n$ ($n=1–2$) clusters will corroborate the results. The analysis of the $S_1 \leftarrow S_0$ spectra obtained at the level of rotational resolution provides for the first time clear-cut information about the geometry and preferential binding motif of these prototype clusters, which are model systems for an acidic polar molecule interacting with a nonpolar solvent. Despite numerous spectroscopic studies on phenol-Ar$_n$ clusters reported in the past, the structural binding motif of this simple system has not been identified unambiguously for the neutral electronic states.

In the following, the present knowledge about phenol-Ar$_n$ will be briefly reviewed. In 1985, initial spectroscopic data about phenol-Ar$_n$ ($n=0–2$) came from one-color REMPI spectra of the $S_1 \leftarrow S_0$ transition and two-color photoionization efficiency (PIE) spectra of the cation ground state (D_0) recorded via the S_1 state origins by Gonohe *et al.*[10] On the basis of nearly additive shifts in the $S_1 \leftarrow S_0$ transition energies (-33 and -68 cm^{-1}) and ionization potentials (-152 and -297 cm^{-1}) upon complexation with one and two argon atoms, the authors concluded that both argon ligands are π-bonded to phenol on opposite sides of the aromatic ring, denoted $(1|0)$ and $(1|1)$ structure, respectively.[10] The intermolecular vibrational structures observed in the $S_1 \leftarrow S_0$ electronic spectra of phenol-Ar$_1$ (Refs. 11 and 12) and

phenol-Ar$_2$ (Ref. 13) have subsequently been assigned assuming π-bonded $(1|0)$ and $(1|1)$ structures, respectively.

Almost negligible complexation-induced frequency shifts of the O–H stretch (ν_{OH}) and other skeletal vibrations in the S_0 state of phenol-Ar$_1$ observed via stimulated Raman[14] and IR dip spectroscopy[15,16] have been indicative for a π-bonded $(1|0)$ geometry for the $n=1$ complex. In addition, high-level quantum chemical calculations of the potential energy surface in the S_0 state yield a π-bonded global minimum, and it is unclear at present whether the H-bonded structure is a shallow local minimum or a transition state.[17–20] Comparison of rotational constants derived from a rotational band contour fit of the S_1 origin spectrum with *ab initio* rotational constants obtained at the MP2/6-31G(d,p) level also support a π-bonded $(1|0)$ geometry for $n=1$.[21] Meerts *et al.*[6] presented the fully rotationally resolved electronic spectrum of the 7D-phenol-Ar$_1$ cluster, without a detailed structural analysis. The rotational constants of the S_0 state are close to those of the S_1 state, implying similar π-bonded geometries in both electronic states. Mass-analyzed threshold ionization (MATI) and zero-kinetic-energy (ZEKE) photoelectron spectroscopy have been employed to derive the binding energies of π-bonded phenol-Ar$_1$ in the D_0, S_1, and S_0 states as 535 ± 3, 397 ± 13 and 364 ± 13 cm^{-1}, respectively, and to measure and assign the intermolecular vibrational modes in the D_0 cation state.[22–25] The intermolecular frequencies are consistent with the π-bonded phenol-Ar$_1$ geometry. Similarly, the ν_{OH} frequency of phenol$^+$-Ar$_1$ derived from IR photodissociation of the cation dimer generated by REMPI is compatible only with a π-bonded isomer.[15,26]

Until recently, all spectroscopic studies indicated that phenol$^+$-Ar$_1$ has a π-bonded equilibrium structure in the S_0, S_1, and D_0 states and no signature of a H-bonded phenol$^+$-Ar$_1$ isomer had been detected. In 2000, however, the IR photodissociation spectrum of phenol$^+$-Ar$_1$ generated in an electron impact (EI) ion source clearly demonstrated that the H-bonded isomer is the global minimum on the potential energy surface of the cation cluster, with a characteristic ν_{OH} frequency strongly redshifted from isolated phenol$^+$ by H-bonding.[27–31] This result was confirmed by quantum chemical calculations, which predict the H-bonded isomer as global minimum in the D_0 state, whereas the π-bonded structure is only a local minimum.[20,28,32] The reason why the most stable H-bonded isomer of phenol$^+$-Ar$_1$ had completely escaped previous spectroscopic detection (MATI, PIE, ZEKE, REMPI-IR),[10,21,23–26] arises from the fact that the phenol$^+$-Ar cation in the D_0 state had been prepared by REMPI of the neutral π-bonded precursor, which is governed by the restrictions of minimal geometry changes imposed by the Franck–Condon (FC) principle. In contrast, the EI cluster ion source predominantly produces the most stable isomer of a given phenol$^+$-Ar$_n$ cation cluster because the reaction sequence begins with EI ionization of the phenol monomer, which is followed by three body cluster aggregation reactions.[29,31] As the H-bond in phenol$^+$-Ar$_1$ is more stable than the π-bond, the energetically most favorable isomers of larger phenol$^+$-Ar$_n$ clusters $(n>1)$ have one H-bonded ligand and $(n-1)$ π-bonded ones.[29]

The ionization-induced $\pi \rightarrow H$ switch in the preferred phenol$\cdots$Ar binding motif has recently been probed by time-resolved IR spectroscopy of the phenol$^+$-Ar$_2$ complex prepared by REMPI.[33,34] These studies revealed that after ionization of π-bonded phenol-Ar$_2$, one Ar ligand isomerizes from the π-bonded site toward the H-bonded site on a time scale of several picoseconds. However, it was noted that for a full understanding of this dynamic process, one must know whether the neutral phenol-Ar$_2$ precursor complex has a symmetric $(1|1)$ structure with one Ar above and the other symmetrically below the aromatic plane or a $(2|0)$ structure with both Ar atoms at the same side of the aromatic ring. Unfortunately, no reliable calculations are available for the potential energy surface of phenol$^+$-Ar$_2$. Moreover, spectroscopic evidence for the geometric structure of neutral phenol-Ar$_2$ is scarce and not unambiguous as it relies on vibrationally resolved spectra only.[10,13,25,35] Recent hole-burning spectra of phenol-Ar$_n$ with $n=1$ and 2 demonstrated that all spectral features observed in the $S_1 \leftarrow S_0$ REMPI spectra indeed arise from single isomers in the molecular beam expansion, which have been assigned to π-bonded structures for both $n=1$ and $n=2$. The refined analysis of the intermolecular vibrational structure observed for phenol-Ar$_2$ was, however, compatible with both a $(1|1)$ and a $(2|0)$ structure.[35] The main purpose of the present work is to provide the definitive answer to the question of the geometry of the phenol-Ar$_2$ trimer.

II. METHODS

A. Experimental procedures

The experimental setup for rotationally resolved laser induced fluorescence spectroscopy is described in detail elsewhere.[36] Briefly, it consists of a ring dye laser (Coherent 899-21) operated with Rhodamine 110, pumped with 7 W of the frequency-doubled output of a diode pumped Yb:YAG (yttrium aluminum garnet) disk laser (ELS Versadisk). About 600–700 mW of the fundamental dye laser output is coupled into an external folded ring cavity (Spectra Physics) for second harmonic generation. The typical output power is 20 mW and is constant during each experiment. The molecular beam is formed by expanding phenol, heated to 365 K, and seeded in 600 mbars of argon, through a 230 μm hole into the vacuum. The molecular beam machine consists of three differentially pumped vacuum chambers that are connected by two skimmers (1 and 3 mm diameter, separated approximately 200 mm) in order to reduce the Doppler width to 25 MHz. The molecular beam is crossed at right angles with the laser beam in the third chamber, 360 mm downstream of the nozzle. The resulting fluorescence is collected perpendicular to the plane defined by the laser and the molecular beam by an imaging optics setup consisting of a concave mirror and two planoconvex lenses. The fluorescence is detected by a UV enhanced photomultiplier tube whose output is recorded by a PC based photon counter card. The relative frequency is determined with a quasiconfocal Fabry–Pérot interferometer. The absolute frequency is determined by recording the iodine absorption spectrum and comparison of the transitions with tabulated lines.[37]

The experimental apparatus for REMPI spectroscopy has been described in detail previously.[38] Phenol-Ar$_n$ clusters were produced in a skimmed supersonic expansion by passing argon gas over a heated phenol sample (330–350 K) in an internal sample holder located directly behind the valve. The pressure of argon gas can be varied up to 8 bars in order to optimize the production of phenol-Ar$_n$ clusters. The rotational temperature of the molecules is approximately 4 K after the expansion.[21] The molecular beam interacts with the counterpropagating, frequency-doubled output of two Nd:YAG pumped dye lasers (Radiant Dyes, Narrow Scan) using Coumarin 153 for excitation, while a mixture of sulforhodamine B and 4-dicyanomethylene-2-methyl-6-p-dimethylaminostyryl-4H-pyran (DCM) was used for the ionization laser to achieve a wide tuning range. The lasers were calibrated (± 0.02 cm^{-1}) with reference to simultaneously recorded iodine absorption spectra, corrected from air to vacuum.

Phenol was purchased from Riedel–de Haën and was used without further purification. 7D-phenol was produced by refluxing phenol with an excess of D$_2$O and subsequent removal of solvent.

B. Computational methods

1. Quantum chemical calculations

Quantum chemical calculations were performed with the TURBOMOLE (Ref. 39) and ORCA (Ref. 40) program packages. The Gaussian atomic orbital basis sets were taken from the TURBOMOLE library.[41,42] The economic triple-zeta Ahlrichs-type sets with different numbers of polarization functions (TZVP or TZVPP) as well as the triple and quadruple-zeta sets of Dunning[43] including diffuse basis functions (aug-cc-pVTZ and aug-cc-pVQZ) have been employed. Using these sets a detailed basis set dependence study has been performed for the structure of phenol-Ar$_2$. The equilibrium geometries of the electronic ground and the lowest excited singlet states were optimized at the level of the approximate coupled cluster singles and doubles model (CC2) employing the resolution-of-the-identity approximation.[44,45] The CC2 method represents the simplest reliable *ab initio* treatment of electron correlation consistent for both ground and excited states, which is necessary to describe noncovalently bound complexes. In addition, we also considered the currently most accurate density functional theory (DFT) approach for noncovalent interactions, namely, a double-hybrid functional including empirical dispersion corrections (B2PLYP-D).[46,47] This method explicitly includes nonlocal correlation effects and yields very accurate results close to those of CCSD(T) for the widely used S22 benchmark set of vdW complexes. Full geometry optimizations using analytical B2PLYP-D gradients[48] were performed for this method and only ground states were considered.

2. Franck–Condon simulations

The change in a molecular geometry on electronic excitation can be determined from the intensities of absorption or emission bands using the FC principle. According to the FC principle the relative intensity of a vibronic band depends on
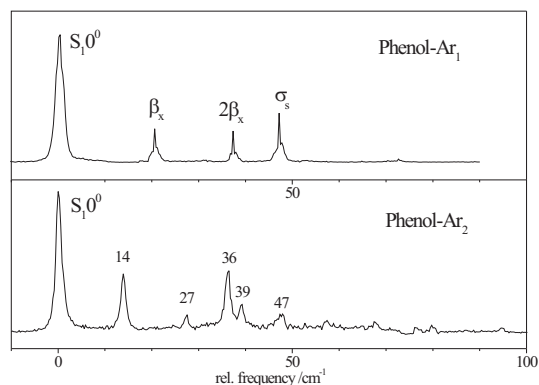

FIG. 1. Two-color $(1+1')S_1 \leftarrow S_0$ REMPI excitation spectra of phenol-Ar$_n$ (n=1–2). The spectra were recorded with the probe laser set to 32 210 cm^{-1}. Assignments of intermolecular modes are included for the n=1 complex. Frequencies are relative to the electronic origin of the n=1 cluster at 36 315.05 and of the n=2 cluster at 36 280.94 cm^{-1}.

the overlap integral of the vibrational wave functions in both electronic states, which is determined by the relative shift of the two potential energy curves connected by the vibronic transition along the normal coordinates Q of both states and the vibrations involved,

$$FC = \left| \int [\Psi'(Q')]^* \Psi''(Q'') dQ' \right|^2$$
$$= \langle v', \ldots, v'_N | v'', \ldots, v''_N \rangle^2, \tag{1}$$

where the $\Psi(Q)$ are the N-dimensional vibrational wave functions. The normal coordinates Q' of the excited state and Q'' of the ground state are related by the linear orthogonal transformation given by Duschinsky.[49]

The program FCFIT (Ref. 50) determines the structural changes on electronic excitation from the experimentally determined intensity pattern. Simultaneously, the changes in the rotational constants are used in the fit to assess the ge-
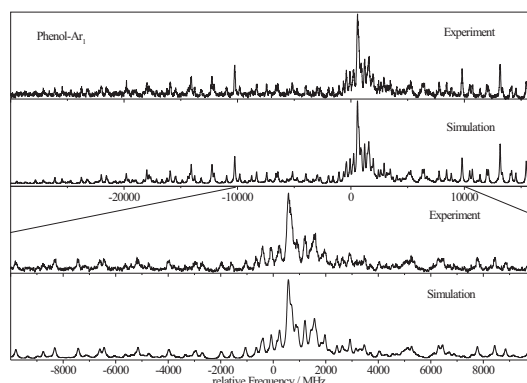

FIG. 2. Rotationally resolved spectrum of the electronic origin of the phenol-Ar$_1$ cluster at 36 315.05 cm^{-1} and simulation of the spectrum using the molecular parameters from the best ES fit, given in Table I. The lower two traces show an expanded view in the range from −10 000 to +10 000 MHz relative to the electronic origin.

TABLE I. Comparison of the molecular parameters from the fit to the rotationally resolved electronic spectrum of phenol-Ar_1 (Fig. 2) and 7D-phenol-Ar_1 (not shown), to the results of *ab initio* calculations. For the definition of the parameters, see text.

	Phenol-Ar_1			7D-phenol-Ar_1		
	Expt.	CC2[a]	B2PLYP-D[b]	Expt.	CC2[a]	B2PLYP-D[b]
A''/MHz	1818.7(5)	1804.00	1827.00	1780.1(5)	1760.85	1784.28
B''/MHz	1124.9(5)	1210.25	1200.86	1120.2(5)	1202.34	1191.87
C''/MHz	917.5(14)	973.25	971.28	905.5(7)	958.00	955.70
ϕ/(deg)	0[c]	0.36	$\cdots$	0[c]	0.37	$\cdots$
ΔA/MHz	$-43.94(6)$	-37.12	$\cdots$	$-43.44(3)$	-34.61	$\cdots$
ΔB/MHz	24.40(3)	31.66	$\cdots$	25.19(2)	31.30	$\cdots$
ΔC/MHz	23.35(2)	32.16	$\cdots$	23.26(2)	31.44	$\cdots$

[a]With the TZVP basis set.
[b]With the aug-cc-pVTZ basis set.
[c]Fixed to zero in the fit.

ometry change on excitation. The program was used to fit the intensities in the absorption spectrum using only the experimentally determined changes in the rotational constants. The necessary Hessians for ground and excited states were taken from the CC2/TZVP calculations.

3. Evolutionary strategies

The rotationally resolved electronic spectra were fit to an asymmetric rigid rotor Hamiltonian with the help of evolutionary strategies (ESs). Contrary to most previous applications of genetic algorithm techniques[51–53] in the evaluation of molecular parameters from rotationally resolved electronic spectra[6,54–56] a different ES with mutative step size control was used in the present work. Mutative step size control adapts the speed at which the parameter space is explored with each optimization step. It tends to work well for the adaptation of a global step size but tends to fail when it comes to the step size of each individual parameter due to several disruptive effects.[57] The derandomized algorithm DR2 used here[58] is aiming at the accumulation of information about the correlation or anticorrelation of past mutation vectors that connect trial solutions in order to tackle this problem. The high effectiveness of this approach for spectral analysis has been demonstrated recently.[59]

III. RESULTS AND DISCUSSION

A. REMPI spectra of phenol-Ar_{1-2}

REMPI spectra of the phenol-Ar_n ($n=1-2$) clusters are shown in Fig. 1. Spectroscopic results are in agreement with previous studies[23,25] but show considerable improvement in signal-to-noise ratio.

In the REMPI spectra of the phenol-Ar_1 cluster [Fig. 1(a)], the most intense feature, the S_1 band origin, appears at $36\,316.4 \pm 0.5$ cm^{-1}, in very good agreement with the previous value of $36\,316 \pm 0.5$ cm^{-1}.[23,25] The position of the origin transition represents a redshift of 33 cm^{-1} with respect to the S_1 origin of the phenol monomer at $36\,348.7$ cm^{-1}.[60] The spectrum also exhibits a number of vdW vibrational modes at 23, 42, and 53 cm^{-1} above the

band origin. They have been previously assigned as the bending mode β_x, its overtone, $2\beta_x$, and the intermolecular stretch σ_s.[21]

The most prominent spectral feature in the phenol-Ar_2 spectrum [Fig. 1(b)] at $36\,282.1 \pm 0.5$ cm^{-1} is assigned to the $S_1 \leftarrow S_0$ origin. Relative to the phenol-Ar_1 band origin, this peak is redshifted by 34 cm^{-1}, suggesting that the argon atom solvates the phenol molecule at a similar binding site to that in phenol-Ar_1. In a previous study[35] several smaller visible features in the spectrum were assigned to a progression in an intermolecular bending vibration (β_x, $2\beta_x$, and $3\beta_x$ at 14, 27, and 39 cm^{-1}) and excitation of the intermolecular stretch (σ_s at 36 cm^{-1}). It was argued that this vibronic assignment is not unique and an asymmetric $(2|0)$ structure cannot be excluded for the phenol-Ar_2 cluster.[35]

B. Rotationally resolved electronic spectrum of phenol-Ar_1

The rotationally resolved electronic spectrum of the electronic origin of the phenol-Ar_1 cluster at $36\,315.05$ cm^{-1} is shown in Fig. 2. It is a nearly pure c-type spectrum which is dominated by a strong central Q-branch, shown in an expanded view in the lower trace of Fig. 2. Since no a- or b-type transitions could be incorporated unambiguously into the fit, the final fit was made to a pure c-type asymmetric rotor Hamiltonian. The same is true for the other high-resolution spectra discussed below.

Close agreement between the experimental spectrum and the simulation is obtained. The parameters deduced from this fit, listed in Table I, are the rotational constants in the S_0 state (A'', B'', C''), the change in rotational constants on electronic excitation ($\Delta(A, B, C)$), the frequency of the $S_1 \leftarrow S_0$ origin transition, and the direction of the transition dipole moment with respect to the system's main inertial a-axis (expressed in the angle ϕ).[56] The rotational temperature of the molecules in the molecular beam was described using a two temperature model[61,56] with $T_1 = 2.1$ K, $T_2 = 6.5$ K, and a relative weight factor of 0.01 for T_2. The Lorentzian width cannot be transformed into an excited state lifetime in this case, since the spectrum contains an unresolved torsional splitting due to the OH torsion and serves only to obtain
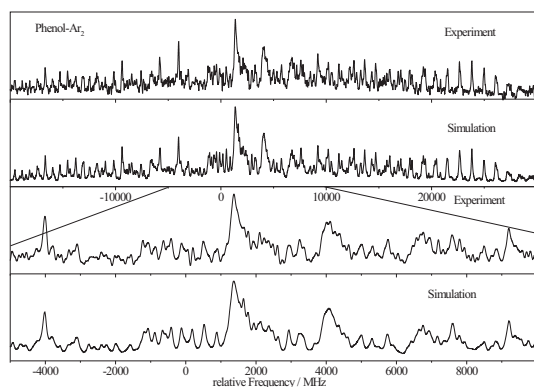
FIG. 3. Rotationally resolved spectrum of the electronic origin of phenol-Ar$_2$ at 36 280.94 cm^{-1} and simulation of the spectrum using the molecular parameters from the best ES fit, given in Table II. The lower two traces show an expanded view in the range of −9000 to +10 000 MHz relative to the electronic origin.
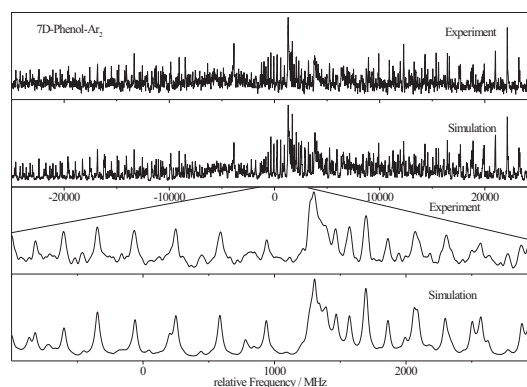

FIG. 4. Rotationally resolved spectrum of the electronic origin of 7D-phenol-Ar$_2$ at 36 278.62 cm^{-1} and simulation of the spectrum using the molecular parameters from the best ES fit (Table II). The lower two traces show an expanded view in the range of −1000–3000 MHz relative to the electronic origin.

good agreement between simulation and experiment.[62] The rotational constants of the ground state of phenol-Ar$_1$ determined from the high-resolution spectrum show significant deviations from those obtained from a contour fit to a low-resolution spectrum (with deviations of up to 4%),[21] demonstrating the limits of the latter technique for the extraction of quantitative structural information.

The second isotopologue which has been investigated is the 7D-phenol-Ar$_1$ cluster, which has its electronic origin at 36 312.74 cm^{-1} (spectrum not shown here). The linewidth of the rovibronic transitions in the deuterated cluster is considerably smaller than that of the undeuterated cluster, as is the case in the bare monomer.[60] A comparison of the molecular parameters obtained from the ES fits of the phenol-Ar$_1$ and 7D-phenol-Ar$_1$ spectra with the results of quantum chemical calculations is also given in Table I.

C. Rotationally resolved electronic spectrum of phenol-Ar$_2$

Figure 3 shows the rotationally resolved electronic spectrum of the phenol-Ar$_2$ origin at 36 280.94 cm^{-1}. As for the

phenol-Ar$_1$ cluster, the spectrum is dominated by a strong Q-branch and can fully be simulated using selection rules for c-type bands. At 36 278.62 cm^{-1} the origin of its hydroxy deuterated isotopologue is found (Fig. 4). Also displayed are the simulations using the best fit parameters from Table II. Table II compares the molecular parameters obtained from ES fits of the phenol-Ar$_2$ and 7D-phenol-Ar$_2$ spectra with the results of quantum chemical calculations at different levels of theory and using different basis sets. For details about the calculations, cf. Sec. III E.

D. The structures of the phenol-Ar$_{1,2}$ clusters

The comparison of the experimental and calculated rotational constants of phenol-Ar$_1$ confirms that the cluster has a π-bound structure. Calculations also indicate the existence of a second stable structure, in which the argon atom is hydrogen bonded to the phenol OH group. However, this structure was not observed in the experiment. Both structures are depicted in Fig. 5. The structure of the phenol-Ar$_2$ cluster observed experimentally, however, has not been unequivocally determined yet. The most important clue concerning its

TABLE II. Comparison of the molecular parameters from the fit to the rotationally resolved electronic spectrum of phenol-Ar$_2$ and 7D-phenol-Ar$_2$ shown in Figs. 3 and 4, respectively, to the results of *ab initio* calculations of the (1|1) structure.

	Phenol-Ar$_2$			7D-phenol-Ar$_2$		
	Expt.	CC2[a]	B2PLYP-D[b]	Expt.	CC2[a]	B2PLYP-D[b]
A''/MHz	1777.6(5)	1774.10	1779.87	1726.4(5)	1724.23	1729.10
B''/MHz	462.5(3)	496.74	494.08	462.1(2)	496.41	493.77
C''/MHz	420.7(5)	449.69	447.42	417.8(2)	446.67	444.38
ϕ/(deg)	0[c]	0.35	⋯	0[c]	0.35	⋯
ΔA/MHz	−18.44(2)	−25.92	⋯	−15.45(2)	−22.76	⋯
ΔB/MHz	12.33(2)	19.23	⋯	12.31(2)	19.21	⋯
ΔC/MHz	13.23(2)	18.97	⋯	13.19(2)	18.85	⋯

[a]With the TZVP basis set.
[b]With the aug-cc-pVTZ basis set.
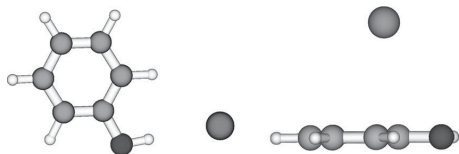[c]Fixed to zero in the fit.

FIG. 5. Geometries of both considered phenol-Ar$_1$ isomers: The hydrogen bonded structure (left) and the vdW bonded structure (right).

structure is the rotationally resolved electronic spectrum of its S_1 origin. The rotational constants that can be expected for the different possible configurations (Fig. 6) are given in Table III. For the hydrogen bonded structure no changes in the rotational constants upon electronic excitation are given since no stable S_1 state minimum was found. Comparison with the experimental parameters from Table II provides unambiguous evidence for the $(1|1)$ structure of this cluster.

E. Structural parameters

The performance of different methods and basis sets for the prediction of the rotational constants and the distance of the argon atom(s) to the aromatic plane is compared in Table IV. Comparing the experimental with the calculated rotational constants, one has to bear in mind that the rotational constants from the calculations represent B_g^e ($g=a,b,c$) values based on the r_e structure, while the experimental values are B_g^0 values based on the vibrationally averaged r_0 struc-
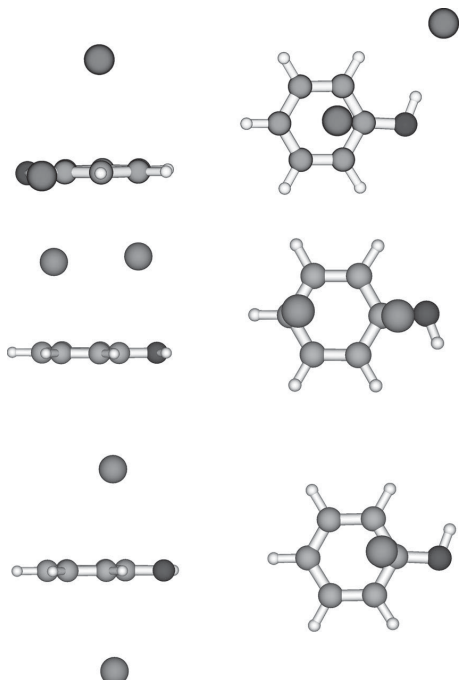

FIG. 6. Calculated geometries of various phenol-Ar$_2$ clusters (CC2/TZVP): the hydrogen bonded structure (top), the $(2|0)$ structure (middle), and the $(1|1)$ structure (bottom).

TABLE III. CC2/TZVP calculated rotational constants for several possible phenol-Ar$_2$ complexes (Fig. 6).

	VdW		
	$(1|1)$	$(2|0)$	Hydrogen bound
A''/MHz	1774.1	1095.4	1133.3
B''/MHz	496.7	651.7	443.3
C''/MHz	449.7	512.4	384.9
ΔA/MHz	−25.9	93.1	⋯
ΔB/MHz	19.2	−52.0	⋯
ΔC/MHz	19.0	−15.1	⋯

ture. We used Dunning's triple- and quadruple-ζ basis sets augmented with diffuse functions (aug-cc-pVTZ and aug-cc-pVQZ) as well as the Karlsruhe triple-ζ basis sets, augmented with single and double sets of polarization functions (TZVP and TZVPP) at the CC2 level. The argon atoms are located on the inertial a-axis, thus the motion of the argon atoms in the very shallow potentials parallel to the plane of phenol (the β_x and β_y vibrations, described in Sec. III F) will have a considerable effect on the B and C rotational constants. Especially, since the mean squared deviation due to zero-point vibration from the hypothetical equilibrium structure is positive, the experimental B and C rotational constants are expected to be smaller than the calculated ones. This is certainly the case here. A more thorough comparison of the effects of basis set size thus requires a correction of the calculated structure by zero-point vibrational effects in these weakly bound clusters. Calculations are on the way in order to obtain anharmonically corrected vibrationally averaged rotational constants on the respective level of theory. Since this procedure requires the computation of cubic and some of the quartic force constants at the respective level, this approach is extremely time-consuming and exceeds the scope of this article.

The intermolecular structures of the vdW bonded phenol-Ar$_{1,2}$ clusters were determined from the experimental rotational constants by means of a pseudo-Kraitchman fit[63] as described by Schmitt *et al.*[64] using the normal and hydroxy deuterated isotopologues. The use of pseudo-Kraitchman geometry parameters (r_s) has the advantage that the difference in the r_e structural parameters is smaller than for the rotational constants, which are based on r_0 values.[65,66]

For the $n=1$ cluster the perpendicular distance of the argon atom to the aromatic plane is given in Table IV and compared to the respective results from the B2PLYP-D/aug-cc-pVTZ and CC2/TZVP optimized structures. On electronic excitation, the argon distance decreases by more than 6 pm. This decrease can be traced back to the expected increase of dispersion energy for excited state complexes and to favorable orbital interactions that are repulsive in the ground state due to the Pauli exclusion principle.

For the $n=2$ cluster a slightly larger distance (about 2 pm) of the argon atom to the aromatic plane is observed for both the ground and the electronically excited state than for the $n=1$ cluster (cf. Table IV). For the *pseudo*-Kraitchman fit the distance of both argon atoms to the ring system was chosen to be the same. The experimentally determined dis-

TABLE IV. Calculated rotational constants and distance d of the argon atoms from the phenol plane obtained from a pseudo-Kraitchman fit in phenol-Ar$_1$ and phenol-Ar$_2$.

	CC2				B2PLYP-D (aug-cc-pVTZ)	Expt.
	TZVP	TZVPP	aug-cc-pVTZ	aug-cc-pVQZ		
			Phenol-Ar$_1$			
A''/MHz	1804.0	1813.1	1814.2	1815.8	1827.00	1818.7
B''/MHz	1210.3	1200.5	1225.9	1227.8	1200.86	1124.9
C''/MHz	973.3	969.5	986.8	988.9	971.28	917.5
$d(S_0)$/pm	340	341	337	338	341	352.6(9)
$d(S_1)$/pm	334	334	⋯	⋯	⋯	346.1(8)
			Phenol-Ar$_2$			
A''/MHz	1774.1	1755.6	1751.4	1757.5	1779.9	1777.6
B''/MHz	496.7	495.1	509.2	509.9	494.1	462.5
C''/MHz	449.7	447.2	458.5	459.2	447.4	420.7
$d(S_0)$/pm	344	345	336	336	342	354.5(2)
$d(S_1)$/pm	336	336	⋯	⋯	⋯	348.5(4)

tances in the $n=1$ and $n=2$ clusters agree reasonably well with the calculated parameters, with all experimental values being larger by 10–18 pm compared to the calculated values depending on the level of theory and basis set employed. A similar overestimation of binding energy and corresponding underestimation of intermolecular distances as known for MP2 (Ref. 67) can be expected with CC2 for the here considered phenol-Ar$_n$ complexes. Thus, also the currently most accurate DFT approach for noncovalent interactions, a double-hybrid functional including empirical dispersion corrections[47] is included in Table IV and is compared to the CC2 values. It yields for both clusters better agreement than CC2 with the most appropriate basis set (aug-cc-pVQZ). The shorter distances of the calculations compared to the experiments have to be traced back to both overestimation of binding energy and the lack of inclusion of vibrational zero-point averaging in the calculations. Both typically contribute 5 pm in the intermolecular distances, yielding a very good agreement with the experimental value.

In order to understand why the distance of the argon atoms to the phenol ring is larger for the $n=2$ cluster, a decomposition of the total binding energy of the argon atoms to the phenol ring into its constituents [energy decomposition analysis (EDA), for details see, e.g., Ref. 68] is presented in Table V. Calculations were done at the B97-D/def2-TZVP EDA level of theory using the CC2/aug-cc-pVTZ optimized geometry. To enable this comparison the geometry used for the phenol-Ar$_1$ complex was that of the Phenol-Ar$_2$ complex with one of the argon atoms removed. The contribution per argon atom due to dispersion interaction is exactly equal for

both $n=1$ and $n=2$ clusters due to the DFT-D approximation used in this analysis. The Pauli exchange repulsion is nearly equal due to the fixed geometries employed, and only the induction and electrostatic terms are notably different. While the electrostatic term tends to stabilize the $n=2$ cluster even more, the induction term overcompensates this effect. Half of the sum of electrostatic and induction interactions for the $n=2$ cluster is about 0.05 kcal/mol smaller than the sum of electrostatic and induction for the $n=1$ cluster. This small but significant decrease in binding energy for the phenol-Ar$_2$ complex is consistent with a longer phenol-argon distance. The most likely explanation for the smaller induction component is that the symmetry of the phenol-Ar$_2$ complex does not allow for the existence of an induced dipole moment perpendicular to the phenol plane.

Finally, we note that the total binding energy of 0.903 kcal/mol (316 cm^{-1}) for phenol-Ar$_1$ is consistent with the experimental value of 364 ± 13 cm^{-1},[23] demonstrating that this theoretical level accounts in a semiquantitative fashion for the intermolecular forces in this cluster.

F. Vibrational frequencies

Table VI compares the vibrational frequencies for the phenol-Ar$_2$ cluster obtained from its REMPI spectrum (Fig. 1) with the CC2 S_1-state vibrational frequencies for the $(1|1)$ cluster. The frequencies are somewhat overestimated, but on the whole the agreement is satisfactory. To test whether the assignments given in Table VI are reasonable a FC simulation was performed using the geometries and the Hessian

TABLE V. Decomposition of the different contributions to the binding energy (in kcal/mol) of argon atoms to the phenol ring in the electronic ground state at the DFT-B97-D/def2-TZVP level. The dispersion contribution is exactly additive (compare values in last column, first and last rows) in the DFT-D treatment used.

Complex	Total	Pauli	Electrostatic	Induction	Electrostatic+induction	Dispersion
Phenol-Ar$_1$	−0.903	3.632	−1.382	−0.675	−2.057	−2.478
Phenol-Ar$_2$	−1.684	7.273	−2.822	−1.178	−4.000	−4.956
$\frac{1}{2}$phenol-Ar$_2$	−0.849	3.636	−1.411	−0.589	−2.000	−2.478

TABLE VI. Phenol-Ar$_2$ intermolecular vibrational frequencies (in cm^{-1}) as determined from Fig. 1 compared with CC2/TZVP calculated S_1-state vibrational frequencies for the (1|1) cluster.

Experiment	CC2	Assignment
14	15	β_x^1
20[a]	19	β_y^1
27	28[b]	β_x^2
⋯	26	λ_x^1
36	51	σ_s^1
39	42[b]	β_x^3
⋯	61	λ_y^1
⋯	68	σ_a^1
47	69[b]	$\sigma_s^1 + \beta_x^1$

[a]From Ref. 35.
[b]Harmonic combination and overtone bands.

matrix from the CC2 calculations of both electronic states and the changes in the rotational constants given in Table II. From the rotational constants of the two isotopologues phenol-Ar$_2$ and 7D-phenol-Ar$_2$ the changes of six rotational constants upon excitation are obtained and can be used in the fit. With these six changes in the rotational constants, five modes have been used as basis for the geometry distortion upon excitation. These modes are the lowest five intermolecular modes from Table VI. The result displayed in Fig. 7 shows good agreement with experiment, confirming the assignments of Table VI. In order to facilitate the comparison of the experimental and FC fitted spectrum the theoretical frequencies have been set to the values of the experimental ones.

The vibrational assignments show that all peaks in the REMPI spectrum can be explained as progressions and combinations of just two modes, β_x and σ_s. For transitions from the ground state, these two modes are the only ones that are allowed in C_{2v} symmetry, which is a near-symmetry group for the (1|1) cluster.[35] Under its proper symmetry group, C_s, β_y also becomes allowed, although its transition strength is expected to be low. Indeed, this mode has been detected at
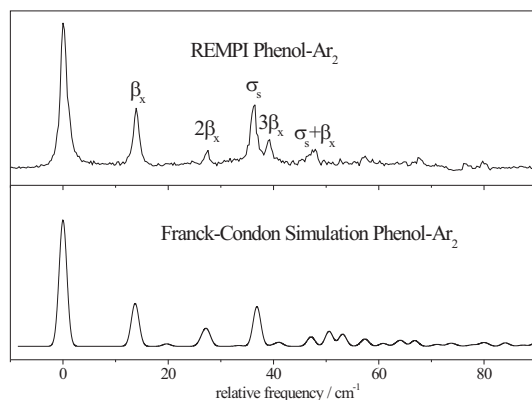
20 cm^{-1} in the hole-burning spectrum of phenol-Ar$_2$ due to intensity enhancement arising from saturation effects of weak transitions. In contrast, the (2|0) structure has C_1 symmetry and all six intermolecular vibrations are allowed in this isomer. The vibrational assignments of Table VI are therefore in agreement with the (1|1) structure of the observed cluster.[35]

IV. CONCLUSIONS

The intermolecular structure of the phenol-Ar$_n$ ($n = 1, 2$) clusters has been investigated with high-resolution UV spectroscopy. From the rotational constants it could be deduced that in both clusters the argon atoms are vdW bonded to the phenol ring, with the $n = 2$ cluster adopting a (1|1) conformation where one argon atom is located on each side of the ring. Further evidence for these structures was extracted from REMPI spectra with the help of FC simulations. Quantum chemical calculations at the CC2 and B2PLYP-D levels of theory were performed to identify the most stable isomers, which are in full agreement with these assignments.

The distance between the argon atoms and the phenol ring was found to be slightly larger in the $n = 2$ cluster than in the $n = 1$ cluster. A decomposition of the cluster binding energy into individual contributions showed that this is due to a smaller inductive force between the ring and the argon atom in the $n = 2$ cluster, arising from noncooperative three body induction interactions. Since the dominant inductive force arises from dipole-induced dipole interaction it was concluded that a small contribution to the induced dipole moment perpendicular to the phenol plane, which is forbidden by symmetry in the $n = 2$ cluster, is most likely responsible for the smaller distance in the $n = 1$ cluster.

FIG. 7. FC simulation of the phenol-Ar$_2$ REMPI spectrum shown in Fig. 1(b). Frequencies are given with respect to the $S_1 \leftarrow S_0$ origin transition at 36 280.94 cm^{-1}. The corresponding peak assignments are given in Table VI.

[1]E. A. Meyer, R. K. Castellano, and F. Diederich, Angew. Chem., Int. Ed. **42**, 1210 (2003).
[2]D. J. Nesbitt, Annu. Rev. Phys. Chem. **45**, 367 (1994).
[3]H. J. Neusser and K. Siglow, Chem. Rev. (Washington, D.C.) **100**, 3921 (2000).
[4]H. J. Neusser and H. Krause, Chem. Rev. (Washington, D.C.) **94**, 1829 (1994).
[5]E. J. Bieske and O. Dopfer, Chem. Rev. (Washington, D.C.) **100**, 3963 (2000).
[6]W. L. Meerts, M. Schmitt, and G. Groenenboom, Can. J. Chem. **82**, 804 (2004).
[7]M. Schmitt, C. Ratzer, and W. L. Meerts, J. Chem. Phys. **120**, 2752 (2004).
[8]T. M. Korter, J. Küpper, and D. W. Pratt, J. Chem. Phys. **111**, 3946 (1999).
[9]J. E. Braun, T. L. Grebner, and H. J. Neusser, J. Phys. Chem. A **102**, 3273 (1998).
[10]N. Gonohe, H. Abe, N. Mikami, and M. Ito, J. Phys. Chem. **89**, 3642 (1985).
[11]E. J. Bieske, M. W. Rainbird, I. M. Atkinson, and A. E. W. Knight, J. Chem. Phys. **91**, 752 (1989).
[12]M. Mons, J. L. Calve, F. Piuzzi, and I. Dimicoli, J. Chem. Phys. **92**, 2155

(1990).

[13] M. Schmidt, M. Mons, and J. L. Calve, Z. Phys. D: At., Mol. Clusters **17**, 153 (1990).

[14] G. V. Hartland, B. F. Henson, V. A. Venturo, and P. M. Felker, J. Phys. Chem. **96**, 1164 (1992).

[15] A. Fujii, M. Miyazaki, T. Ebata, and N. Mikami, J. Chem. Phys. **110**, 11125 (1999).

[16] T. Ebata, A. Iwasaki, and N. Mikami, J. Phys. Chem. A **104**, 7974 (2000).

[17] J. Makarewicz, J. Chem. Phys. **111**, 084310 (1999).

[18] F. Tran and T. A. Wesolowski, Int. J. Quantum Chem. **101**, 854 (2005).

[19] J. Cerny, X. Tong, P. Hobza, and K. Müller-Dethlefs, J. Chem. Phys. **128**, 114319 (2008).

[20] M. A. Vincent, I. H. Hillier, C. A. Morgado, N. A. Burton, and X. Shan, J. Chem. Phys. **128**, 044313 (2008).

[21] M. S. Ford, S. R. Haines, I. Pugliesi, C. E. H. Dessent, and K. Müller-Dethlefs, J. Electron Spectrosc. Relat. Phenom. **112**, 231 (2000).

[22] X. Zhang and J. L. Knee, Faraday Discuss. **97**, 299 (1994).

[23] C. E. H. Dessent, S. R. Haines, and K. Müller-Dethlefs, Chem. Phys. Lett. **315**, 103 (1999).

[24] C. E. H. Dessent and K. Müller-Dethlefs, Chem. Rev. (Washington, D.C.) **100**, 3999 (2000).

[25] S. R. Haines, C. E. H. Dessent, and K. Müller-Dethlefs, J. Electron Spectrosc. Relat. Phenom. **108**, 1 (2000).

[26] A. Fujii, T. Sawamura, S. Tanabe, T. Ebata, and N. Mikami, Chem. Phys. Lett. **225**, 104 (1994).

[27] N. Solca and O. Dopfer, Chem. Phys. Lett. **325**, 354 (2000).

[28] N. Solca and O. Dopfer, J. Mol. Struct. **563–564**, 241 (2001).

[29] N. Solca and O. Dopfer, J. Phys. Chem. A **105**, 5637 (2001).

[30] N. Solca and O. Dopfer, Chem. Phys. Lett. **369**, 68 (2003).

[31] O. Dopfer, Z. Phys. Chem. **219**, 125 (2005).

[32] J. Cerny, X. Tong, P. Hobza, and K. Müller-Dethlefs, Phys. Chem. Chem. Phys. **10**, 2780 (2008).

[33] S. Ishiuchi, M. Sakai, Y. Tsuchida, A. Takeda, Y. Kawashima, M. Fujii, O. Dopfer, and K. Müller-Dethlefs, Angew. Chem., Int. Ed. **44**, 6149 (2005).

[34] S. Ishiuchi, M. Sakai, Y. Tsuchida, A. Takeda, Y. Kawashima, O. Dopfer, K. Müller-Dethlefs, and M. Fujii, J. Chem. Phys. **127**, 114307 (2007).

[35] S. Ishiuchi, Y. Tsuchida, O. Dopfer, K. Müller-Dethlefs, and M. Fujii, J. Phys. Chem. A **111**, 7569 (2007).

[36] M. Schmitt, J. Küpper, D. Spangenberg, and A. Westphal, Chem. Phys. **254**, 349 (2000).

[37] S. Gerstenkorn and P. Luc, *Atlas du Spectre D'Absorption de la Molécule D'iode* 14 800–20 000 cm^{-1} (CNRS, Paris, 1986).

[38] S. R. Haines, W. D. Geppert, D. M. Chapman, M. J. Watkins, C. E. H. Dessent, M. C. R. Cockett, and K. Müller-Dethlefs, J. Chem. Phys. **109**, 9244 (1998).

[39] R. Ahlrichs, M. Bär, and H.-P. Baron, TURBOMOLE (version 5.7), Univer-

sität Karlsruhe, Germany, 2002.

[40] F. Neese, ORCA, an *ab initio*, density functional and semiempirical program package, University of Bonn, Germany, 2007.

[41] R. Ahlrichs, M. Bär, M. Häser, H. Horn, and C. Kölmel, Chem. Phys. Lett. **162**, 165 (1989).

[42] A. Schäfer, C. Huber, and R. Ahlrichs, J. Chem. Phys. **100**, 5829 (1994).

[43] J. T. H. Dunning, J. Chem. Phys. **90**, 1007 (1989).

[44] C. Hättig and A. Köhn, J. Chem. Phys. **117**, 6939 (2002).

[45] C. Hättig, J. Chem. Phys. **118**, 7751 (2003).

[46] S. Grimme, J. Chem. Phys. **124**, 034108 (2006).

[47] T. Schwabe and S. Grimme, Phys. Chem. Chem. Phys. **9**, 3397 (2007).

[48] F. Neese, T. Schwabe, and S. Grimme, J. Chem. Phys. **126**, 124115 (2007).

[49] F. Duschinsky, Acta Physicochim. URSS **7**, 551 (1937).

[50] D. Spangenberg, P. Imhof, and K. Kleinermanns, Phys. Chem. Chem. Phys. **5**, 2505 (2003).

[51] J. H. Holland, *Adaption in Natural and Artificial Systems* (The University of Michigan Press, Ann-Arbor, MI, 1975).

[52] D. E. Goldberg, *Genetic Algorithms in Search, Optimisation and Machine Learning* (Addison-Wesley, Reading, MA, 1989).

[53] I. Rechenberg, *Evolutionsstrategie: Optimierung Technischer Systeme Nach Prinzipien der biologischen Evolution* (Frommann-Holzboog, Stuttgart, 1973).

[54] J. A. Hageman, R. Wehrens, R. de Gelder, W. L. Meerts, and L. M. C. Buydens, J. Chem. Phys. **113**, 7955 (2000).

[55] W. L. Meerts and M. Schmitt, Phys. Scr. **73**, C47 (2006).

[56] W. L. Meerts and M. Schmitt, Int. Rev. Phys. Chem. **25**, 353 (2006).

[57] N. Hansen and A. Ostenmeier, Evol. Comput. **9**, 159 (2001).

[58] A. Ostenmeier, A. Gawelcyk, and N. Hansen, *Step-Size Adaptation Based on Non-Local Use of Selection Information*, Parallel Problem Solving From Nature, Vol. 3 (Springer, Berlin/Heidelberg, 1994).

[59] I. Kalkman, C. Vu, M. Schmitt, and W. L. Meerts, ChemPhysChem **9**, 1788 (2008).

[60] C. Ratzer, J. Küpper, D. Spangenberg, and M. Schmitt, Chem. Phys. **283**, 153 (2002).

[61] Y. R. Wu and D. H. Levy, J. Chem. Phys. **91**, 5278 (1989).

[62] G. Berden, W. L. Meerts, M. Schmitt, and K. Kleinermanns, J. Chem. Phys. **104**, 972 (1996).

[63] P. Nösberger, A. Bauder, and H. H. Günthard, Chem. Phys. **1**, 418 (1973).

[64] M. Schmitt, D. Krügler, M. Böhm, C. Ratzer, V. Bednarska, I. Kalkman, and W. L. Meerts, Phys. Chem. Chem. Phys. **8**, 228 (2006).

[65] C. Costain, J. Chem. Phys. **29**, 864 (1958).

[66] J. K. G. Watson, J. Mol. Spectrosc. **48**, 479 (1973).

[67] T. B. W. Klopper, H. P. Lüthi, and A. Bauder, J. Chem. Phys. **101**, 9747 (1994).

[68] S. Grimme, J. Antony, T. Schwabe, and C. Mück-Lichtenfeld, Org. Biomol. Chem. **5**, 741 (2007).

5.7   o-Toluidine

Structure and internal rotation in the S_0 and S_1 states of *o*-toluidine studied by high resolution UV spectroscopy

Ivo Kalkman,[a] Chau Vu,[b] Michael Schmitt*[b] and W. Leo Meerts*[a]

The rotationally resolved spectrum of the *o*-toluidine $S_1 \leftarrow S_0$ origin was measured using laser induced fluorescence spectroscopy. From the resulting spectrum torsional barriers to internal rotation of the methyl group were derived, which resulted in S_0 state values of $V_3 = 699 \pm 11$ cm^{-1} and $V_6 = 64 \pm 11$ cm^{-1} with an effective rotational constant F of 5.38 ± 0.04 cm^{-1} while for the S_1 state the result was $V_3 = 40.87 \pm 0.14$ cm^{-1} and $V_6 = -16.8 \pm 0.8$ cm^{-1} with $F = 5.086 \pm 0.001$ cm^{-1}. The S_1 state structure was found to be severely distorted, with the methyl group making a 7.7° degree angle with the benzene ring. Evidence of an excited state precessional motion of the methyl group was found.

1. Introduction

One of the fundamental motifs in organic chemistry are aromatic rings, and substituted benzenes have therefore been studied vigorously over the years using a plethora of spectroscopic techniques. Some of the more interesting substitutions involve flexible groups which give rise to dynamics, such as an amino group (aniline) or a methyl group (toluene). In this paper the dynamics in *o*-toluidine (also named *o*-methylaniline), where both these groups are attached to the benzene ring in neighbouring positions, will be investigated.

From aniline it is known that in the ground state its amino group is pyramidal with respect to the benzene plane but that its structure is quasi-planar in the S_1 state.[1,2] From far-infrared (FIR) spectra the inversion barrier was determined to be around 525 cm^{-1}.[3,4] High resolution laser induced fluorescence (LIF) spectra were unable to resolve a tunneling splitting corresponding to the inversion motion, in keeping with this high barrier.[5,6] The situation for the toluidines is very similar. The NH$_2$ inversion barriers in *o*-, *m*- and *p*-toluidine were measured to be 558, 528 and 588 cm^{-1}, respectively, all a little higher than in aniline due to a higher electron density on the amino nitrogen atom.[7] High-resolution spectroscopy of *p*-toluidine did not reveal a tunneling splitting due to the inversion motion.[8] Such a splitting is therefore not expected to show up in the *o*-toluidine spectrum.

The barrier to internal rotation of the methyl group in substituted toluenes has been investigated for a large number of substituents and substitution positions; a nice overview can be found in a paper by Zhao *et al.*[9] Looking through the tables in this paper a general trend can be observed: for ortho-substituted toluenes electronic excitation dramatically reduces an initially high threefold barrier, whereas for meta-substituted toluenes the methyl group rotation is almost free

in the S_0 state but becomes severely hindered in the S_1 state. Since the *para*-substituted toluenes have no threefold barrier due to their higher symmetry their barriers are generally lower, but the same general effect as in *meta*-substituted toluenes can be observed. This means that the barrier height depends much more on the substitution position than on the exact nature of the substituent, and an explanation for these effects is most likely connected to the electronic configuration of these substances. When the substituents considered here, which are all electron donating groups, are replaced with an electron withdrawing group we would therefore expect to see very different behavior, as was confirmed in later experiments on tolunitrile.[10] In the case of *o*-toluidine the barriers to internal rotation were determined from fluorescence excitation and dispersed fluorescence spectra by Okuyama *et al.* which resulted in $V_3 = 703$ cm^{-1}, $V_6 = 62$ cm^{-1} in the S_0 state and $V_3 = 40$ cm^{-1}, $V_6 = -11$ cm^{-1} in the S_1 state.[11] The barrier in the cation was measured to be $V_3 = 649$ cm^{-1}, $V_6 = 19$ cm^{-1}.[12,13]

Calculations on various substituted toluenes have been quite successful in reproducing measured barriers by relating its height to the Hammett σ constant of the substituent combined with substitution position[14] and the difference in π-bond order between both ring carbon bonds geminal to the methyl rotor.[15] These calculations show that the molecular structure changes with rotation of the methyl group, regardless of substituent or substitution position. The molecular geometries and conformational preferences of toluidines are therefore closely connected to the barriers to internal rotation.

p-Toluidine has been studied most extensively since steric hindrance between the methyl and amino groups is absent and it is highly symmetric.[8,16–19] The electronic effects described in the previous paragraph are found to induce a precession of the methyl group with its rotation. Moving to *m*- and *o*-toluidine steric hindrance enhances this precessional motion and leads to distortions of both the methyl and amino groups.[20–23] Simulations by Brodersen *et al.* have revealed that typical changes in rotor axis orientation in substituted toluenes are on the order of 1.5 degrees.[24]

[a] *Molecular- and Biophysics Group, Institute for Molecules and Materials, Radboud University Nijmegen, P.O. Box 9010, NL-6500 GL, Nijmegen, The Netherlands. E-mail: Leo.Meerts@science.ru.nl*
[b] *Heinrich-Heine-Universität, Institut für Physikalische Chemie, D-40225, Düsseldorf, Germany. E-mail: mschmitt@uni-duesseldorf.de*

In this paper the rotational constants of *o*-toluidine in its S_0 and S_1 states will be determined from rotationally resolved UV LIF spectra and these will be used to derive an exact molecular structure. Furthermore, accurate barriers to internal rotation of the methyl group will be derived from the spectra and possible evidence for a precessional motion of the methyl rotor will be discussed.

2. Methods

2.1 Experimental procedures

The experimental setup for the rotationally resolved LIF is described elsewhere.[25] Briefly, it consists of a frequency doubled Nd:YAG laser which pumps a ring dye laser (Coherent 899-21) operated with Rhodamine 6G. The dye laser output is coupled into an external folded ring cavity (Spectra Physics Wavetrain) for second harmonic generation. The typical output power is 20 mW and is constant during each experiment.

The molecular beam is formed by co-expanding argon at a backing pressure of 340 mbar and room temperature *o*-toluidine into the vacuum through a 320 μm nozzle. The molecular beam machine consists of three differentially pumped vacuum chambers that are linearly connected by skimmers (1 mm and 3 mm diameter, respectively). In the third chamber, 360 mm downstream of the nozzle, the UV laser beam crosses the molecular beam at right angles. Imaging optics focus the total undispersed fluorescence from the excited molecules onto a photo-multiplier tube mounted perpendicular to the plane defined by the laser and the molecular beam. Its output is discriminated and digitized by a photon counter card inside a personal computer. The Doppler width of measured transitions is 25 MHz (FWHM). Relative frequencies are determined with a quasi-confocal Fabry-Perot interferometer with a free spectral range (FSR) of 149.9434(56) MHz. The absolute frequency is obtained by comparing the recorded iodine absorption spectrum with tabulated lines.[26]

o-Toluidine (≥ 99%) was obtained from Aldrich and used without further purification.

2.2 Computational methods

2.2.1 *Ab initio* calculations.
Structure optimizations were performed employing the valence triple zeta basis set with polarization functions (d,p) from the TURBOMOLE library.[27,28] The equilibrium geometries of the electronic ground and the lowest excited singlet states were optimized at the CC2 level within the resolution-of-the-identity approximation.[29,30] Ground state vibrational frequencies have been calculated through analytical second derivatives using the AOFORCE module[31,32] implemented in Turbomole Version 5.8. Excited state vibrational frequencies were calculated using numerical differentiation of analytic gradients using the NumForce script of Turbomole Version 5.8.

The singlet state energies, wavefunctions, and transition dipole moments were calculated using the combined density functional theory/multi-reference configuration interaction (DFT/MRCI) method by Grimme and Waletzke.[33] The configuration state functions (CSFs) in the MRCI expansion are constructed from Kohn–Sham (KS) orbitals, optimized for the dominant closed shell determinant of the electronic ground state employing the BH-LYP functional.[34,35] All valence electrons were correlated in the MRCI runs and the eigenvalues and eigenvectors of the lowest singlet state were determined. The initial set of reference configuration state functions was generated automatically in a complete active space type procedure (including all single and double excitations from the five highest occupied molecular orbitals in the KS determinant to the five lowest virtual orbitals) and was then iteratively improved. The MRCI expansion was kept moderate by extensive configuration selection. The selection of the most important CSFs is based on an energy gap criterion as described by Grimme and Waletzke.[33] Only those configurations were taken into account whose energy did not exceed a certain cutoff energy. The energy of a given configuration was estimated from orbital energies within the selection procedure. The cutoff energy was given by the energy of the highest desired root as calculated for the reference space plus a cutoff parameter $\delta E_{sel} = 1.0 E_H$. This choice has been shown to yield nearly converged results.[33]

2.2.2 Spectral analysis.
To describe the *o*-toluidine spectrum a torsion–rotation Hamiltonian of the following form was used:[36]

$$H_{tr} = F(p - \vec{\rho}\vec{J})^2 + V(\alpha) + AJ_a^2 + BJ_b^2 + CJ_c^2. \quad (1)$$

In this equation A, B and C are the molecule's rotational constants, J_a, J_b, J_c are the projections of the total angular momentum $\vec{J}$ onto the main inertial axes a, b and c, respectively, and $V(\alpha)$ is the torsional potential, which takes the form:

$$V(\alpha) = \frac{V_3}{2}(1 - \cos 3\alpha) + \frac{V_6}{2}(1 - \cos 6\alpha). \quad (2)$$

Furthermore, $p = -i\hbar\frac{\partial}{\partial\alpha}$ is the angular momentum operator conjugate to the torsional angle α and F is the internal rotation constant, which is related to the moment of inertia of the internal rotor I_α and its torsional constant, F_{top}, via:

$$F = \hbar^2/2rI_\alpha = F_{top}/r, \quad (3)$$

with

$$r = 1 - I_\alpha \sum_g \cos^2(\eta_g)/I_g. \quad (4)$$

I_g ($g = a,b,c$) are the moments of inertia of the entire molecule and cos η_g are the direction cosines of the methyl top axis with respect to the main inertial axes. Finally, the parameter ρ in eqn (1) is related to these direction cosines through the equation:

$$\rho_g = (I_\alpha/I_g)\cos \eta_g. \quad (5)$$

This equation can be rewritten in terms of the polar angles (ζ,η), where ζ is the angle between the methyl top axis and the *c*-axis and η is the angle between the projection of the methyl top axis onto the *ab*-plane and the *a*-axis. When this is done the components of ρ are given by:

$$\rho_a = (I_\alpha/I_a)\sin \zeta \cos \eta$$
$$\rho_b = (I_\alpha/I_b)\sin \zeta \sin \eta \quad (6)$$
$$\rho_c = (I_\alpha/I_c)\cos \zeta.$$

It will be shown in section 3 that the torsional splitting in the ground state is too small to be measured in the experiment described here, which means that no information on the corresponding ground state parameters can be derived. The only information on the torsional potential that can be extracted from the spectrum are the values of V'_3, F', η' and ζ'. An initial fit of the rotationally resolved spectrum was performed with the Evolutionary Algorithm (EA) automatic fitting program[37–39] using the recently implemented DR2 algorithm.[40] For this fit the values of V''_3, V''_6, F'' and V'_6 were taken from Okuyama et al.[11] while the values for η'' and ζ'' were fixed to those that resulted from RICC2 calculations. In a second step the resulting V'_3, F', η' and ζ' were used in combination with torsional transition frequencies measured by laser induced fluorescence[23] and dispersed fluorescence[11] spectroscopy to determine the values of the torsional parameters that were kept fixed in the first fit. This was done with the program HTorFit.[41]

3. Results and discussion

Fig. 1 shows the rotationally resolved S1 ← S$_0$ origin spectrum of o-toluidine. It consists of two spectral components separated by 98 584 ± 5 MHz. As has been shown previously[22,23] these result from transitions between the two lowest torsional levels which arise from internal rotation of the methyl group. The lower of the two components is due to transitions between nondegenerate levels of a_1 symmetry while the upper one results from transitions between doubly degenerate torsional levels of e symmetry. Shown in the panel below the spectrum is the best fit. The correspondence between the two is excellent, as is also evidenced by the enlarged portion depicted in the two panels below it. The bottom panel of Fig. 1 shows a stick spectrum of the strongest transitions in the simulation and a convolution of these with a Lorentzian function with a width (FWHM) of 0.3 cm^{-1}; the resulting spectrum matches the rotational contour spectra from Ballesteros and Santos[23] quite well.

From the ordering of the two torsional components it can immediately be concluded that the barrier to internal rotation must be lower in the S$_1$ state than it is in the S$_0$ state. To obtain exact values for the barriers to internal rotation a combined fit of this spectrum with the torsional bands measured in previous work[11,23] was performed as described in section 2.2.2. The molecular parameters deduced from this analysis, together with the values obtained from ab initio calculations, are given in Table 1. Calculated torsional transitions are compared with measured ones in Table 2. From the second table it can be seen that, again, the deduced parameters are in excellent agreement with experiment.

A two-temperature model[42] was used to describe the rotational temperature in the molecular beam, which yielded T_1 = 2.1 K and T_2 = 3.6 K with a relative T_2 weight of 0.14. From a 26.8 MHz Lorentzian contribution to the total linewidth the excited state lifetime is found to be around 6.0 ns, which is substantially longer than the 3.5 ns lifetime in p-toluidine[8] and much closer to the 7.2 ns measured in aniline.[2]

3.1 Transition dipole moment

The value of ϕ in Table 1 indicates that the transition dipole moment (TDM) lies in the plane of the benzene ring. While the sign of the angle θ normally cannot be determined from the experiment since the relative intensities in the spectrum only depend on the square of the transition dipole moment components, its sign can be determined in molecules that possess an internal rotor. This happens because the intensities of some of the E-type transitions depend on the relative signs of θ and η.[43–45] Since the sign of η is known from geometrical considerations this fixes the absolute sign of θ. In the case at hand the result is that the TDM orientation has to be in the direction of the methyl group, which corresponds to the plus sign in Fig. 2.

From a comparison of the measured rotational constants with those resulting from RICC2 calculations it can be seen that the correspondence is satisfactory, and as will be discussed in section 3.3 the calculations indicate that the amino group is nonplanar in the S$_0$ state and becomes more planar in the S$_1$ state. This effect is also observed in aniline, where the transition dipole moment is perpendicular to the amino group CN bond.[2,46] Because the methyl group has a relatively small influence on the benzene π-electron system compared to the amino group (inductive vs. mesomeric effect) it therefore seems reasonable to conclude that the electronic excitation must be similar to that in aniline and the transition dipole moment is directed towards the methyl group, which only induces a moderate change in the TDM direction with respect to that in aniline.

As can be seen from Table 1, the RICC2 calculations also predict the torsional barriers very accurately. Since the torsional barrier in o-toluidine is very sensitive to the local electronic environment at the ring carbon atom the methyl group is attached to, this is another indication that the ab initio results are reliable. However, Table 1 shows that it doesn't predict the S$_1$ ← S$_0$ excitation energy very accurately. Moreover, no information on the sign of the θ angle can be extracted from it. A single point DFT/MRCI calculation at the RICC2 optimized S$_1$ state geometry was therefore performed, the results of which were added to Table 1. Both the size and the direction of the resulting TDM as well as the excitation energy agree very well with experiment.

3.2 The methyl rotor

The last piece of information that results from the spectral analysis concerns the methyl rotor geometry contained in the parameters F, η and ζ. To avoid confusion both the values for F and F_{top} defined in eqn (3) are given in Table 1. Immediately apparent is the fact that the parameter ζ has a value which is very different from 90° in the S$_1$ state. This is certainly not expected and the possibility that the rotor actually makes an 18.4° angle with respect to the ab-plane is ruled out by the inertial defect, which points to an almost planar structure. This interpretation is therefore disregarded, and since a reasonable correspondence between model and experiment could only be obtained with the parameter values given in Table 1 it seems that an alternate model is needed.
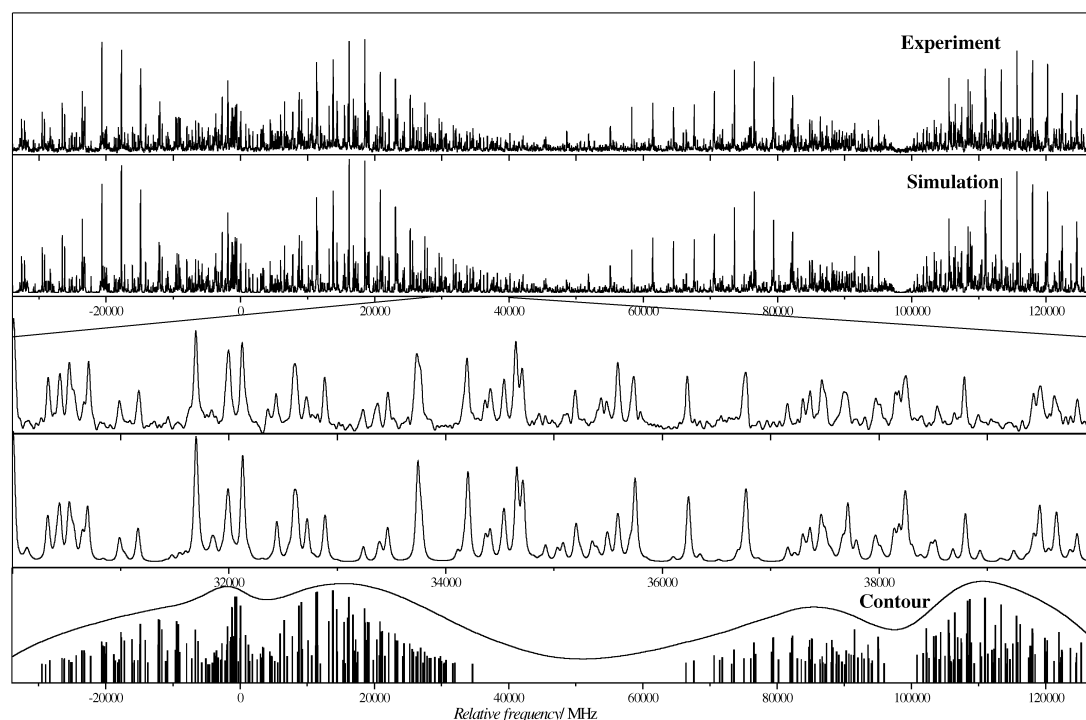
Fig. 1 The electronic origin of *o*-toluidine at 34 316.848 cm^{-1}. The upper two traces show the measured spectrum and the best simulation. In the two traces below that an enlarged part of the spectrum is shown. The bottom trace shows a stick spectrum which contains the strongest transitions from the simulation shown in the second trace and a convolution of these with a Lorentz function (FWHM 0.3 cm^{-1}).

Table 1 Molecular parameters of *o*-toluidine as determined from the fits to the $S_1 \leftarrow S_0$ origin transition shown in Fig. 1. For a description of the fitting procedure see section 2.2.2. Also listed are the results of *ab initio* calculations at the RICC2/TZVP and DFT/MRCI levels of theory

	S_0			S_1				$\Delta(S_1 - S_0)$
	Exp.	RICC2	Ref. 11	Exp.	RICC2	Ref. 11	Ref. 21	Exp.
A/MHz	3229.60(17)	3268	—	3121.92(14)	3098	—	—	−107.68(18)
B/MHz	2188.49(16)	2219	—	2181.97(13)	2187	—	—	−6.52(22)
C/MHz	1316.82(9)	1334	—	1296.03(12)	1295	—	—	−20.79(13)
ΔI/amu Å^2	−3.62(4)	−3.59	—	−3.60(5)	−4.00	—	—	0.02(5)
V_3/cm^{-1}	699(11)	657	703	40.87(14)	120	40	35	−658(11)
V_6 (cm^{-1})	64(11)	—	62	−16.8(8)	—	−11	28	−81(11)
F_{top}/cm^{-1}	5.28(4)	5.51	5.18	5.086(1)	5.48	5.30	5.1	−0.19(4)
F/cm^{-1}	5.38(4)	5.62	5.28	5.184(1)	5.59	5.40	5.2	−0.19(4)
η/°	28.7^a	28.7	—	28.14(12)	26.1	—	—	7.1(23)
ζ/°	89.5^a	89.5	—	71.6(7)	88.1	—	—	−18.3(6)

	Exp.	RICC2	DFT/MRCI	Ref. 11	Ref. 21
θ/°	+ 37.47(26)	±31.5	+ 38.9	—	—
ϕ/°	89.3(8)	90.0	88.9	—	—
ν_0/cm^{-1}	34 316.848(1)	36 137	34 706	34 316	34 316
$\nu_0(E) - \nu_0(A_1)$/MHz	98 584(5)	—	—	≈90 000	≈105 000
$\Delta_{Lorentz}$/MHz	26.8(10)	—	—	—	—
$\tau_{1/2}$/ns	5.95(22)	—	—	—	—

^{a} Fixed to RICC2 calculated value.

For the interpretation of *p*-toluidine spectra Tan *et al.*[8] were forced to use a modified Hamiltonian which accounts for a precessional motion of the methyl rotor axis. Although in the case considered here a fit to the data is possible without inclusion of a precession angle it cannot be ruled out that a second, physically more acceptable solution is possible when it is included. The appropriate form of this Hamiltonian, including a V_3 potential term, was therefore used in an attempt to obtain

Table 2 Torsional transitions used in the determination of some of the internal rotor parameters of *o*-toluidine given in Table 1. For a description of the fitting procedure see section 2.2.2. All values are relative to the $0a_1 \leftarrow 0a_1$ transition, where $\nu\sigma(S_1) \leftarrow \nu\sigma(S_0)$ indicates an absorption band and $\nu\sigma(S_1) \rightarrow \nu\sigma(S_0)$ an emission band

Transition	Exp.	Fit	Diff.	
$1e \leftarrow 1e$	98584(5)[a]	98 584	0	MHz
$1e \leftarrow 2e$	27.8(3)[b]	27.4	−0.4	cm^{-1}
$0a_1 \leftarrow 3a_2$	45.0(3)[b]	45.5	+0.5	cm^{-1}
$0a_1 \leftarrow 3a_1$	56.2(3)[b]	57.5	+1.3	cm^{-1}
$1e \leftarrow 4e$	86.8(3)[b]	87.8	+1.0	cm^{-1}
$1e \leftarrow 5e$	132.1(3)[b]	134.0	+1.9	cm^{-1}
$0a_1 \leftarrow 6a_1$	196.6(3)[b]	190.9	−5.7	cm^{-1}
$1e \rightarrow 2e$	182(6)[c]	189	+7	cm^{-1}
$0a_1 \rightarrow 3a_1$	361(6)[c]	358	−3	cm^{-1}
$1e \rightarrow 4e$	362(6)[c]	355	−7	cm^{-1}
$1e \rightarrow 5e$	472(10)[c]	489	+17	cm^{-1}
$0a_1 \rightarrow 6a_1$	578(10)[c]	578	0	cm^{-1}
$1e \rightarrow 7e$	589(10)[c]	602	+13	cm^{-1}
$1e \rightarrow 8e$	684(10)[c]	669	−15	cm^{-1}

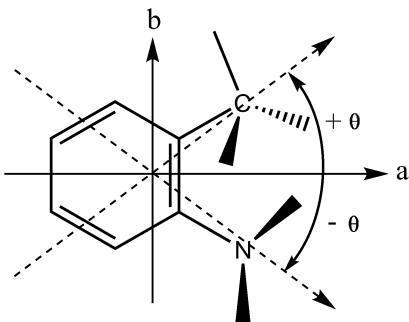[a] This work. [b] Ballesteros and Santos.[23] [c] Okuyama *et al.*[11]

Fig. 2 Definition of the transition dipole moment direction with respect to the main interial axes.

a fit, but this resulted in a zero degree precession angle. However, this does not rule out the possibility that precessional motion is responsible for the observed effective value of ζ. As was pointed out by Brodersen and Gordon[24] this Hamiltonian does not allow for any motion of the methyl carbon atom with the torsional angle and it is therefore still possible that the observed effect is due to motion of the *whole* methyl group. They showed that this results in a marked decrease of the effective rotational constant F with respect to its equilibrium value, and that a precession angle of $1.5°$ is typical of substituted toluenes. Looking at Table 1, indeed it can again be seen that the measured values are much smaller than the calculated ones and that the difference between the two is much larger in the S_1 state than it is in S_0. The fact that the *ab initio* results predict that the angle ζ becomes $88.1°$ on electronic excitation, which would mean that the methyl group comes out of the plane by $1.9°$, can be viewed as further evidence to support this theory. For this situation the Hamiltonian used in the present analysis (given in eqn (1)) is only approximate and, as a result, the value of ζ found here should not be viewed as a geometric parameter but rather as an effective parameter which includes perturbation effects.

3.3 Molecular structure

As was already noted in section 3.1 the rotational constants that result from RICC2 calculations compare favourably with those obtained from the experiment, which adds credibility to the structure derived from them. A list of geometric parameters is given in Table 3; the corresponding atomic numbering is depicted in Fig. 3.

For the S_0 state it can be seen that, with the exception of the C_8H_{8a} bond, all bond lengths are shorter than in either of the two calculations performed so far. In the S_1 state the opposite is found, and most bond lengths tend to be longer. In combination with the observation that almost all bond lengths increase on electronic excitation, this means that the effect the excitation has on the *o*-toluidine geometry is much greater than previously thought. This picture is confirmed by the bond angles: whereas in the ground state they coincide very well with the values from previous work, they differ substantially in the electronically excited state.

When the detailed benzene ring geometry is investigated it can be seen that in the S_0 state the ring carbon bond between both atoms the substituents attach to, C_1C_2, is longest whereas the one on the opposite side of the ring, C_4C_5, is shortest. Furthermore, the $C_1C_2C_3$ angle is only $118.5°$ whereas the $C_2C_3C_4$ angle is $122.0°$. These all act to tilt the methyl group away from the amino group. Since the amino group is electron withdrawing in nature, an attempt to explain this using only natural hybrid orbitals (NHOs), as was done for *o*-chlorotoluene and *o*-fluorotoluene by Lu *et al.*,[15] would lead us to expect that the $C_6C_1C_2$ angle is substantially larger than $120°$. This is not the case, with its actual value at $119.6°$ even slightly smaller than $120°$. Moreover, NHOs have a local effect on the ring structure and cannot explain the fact that the C_4C_5 bond is shorter than both its neighbours. These results are therefore viewed as evidence that, unlike in *o*-chlorotoluene and *o*-fluorotoluene, steric hindrance is an important factor for the *o*-toluidine structure.

The approximate C_2 symmetry axis (from an inertial point of view) which the benzene ring possesses in the ground state, intersecting both the C_1C_2 and the C_4C_5 bonds, is retained on electronic excitation. Simultaneously, all ring CC bond lengths increase, which corresponds to an expansion of the ring. With respect to the average ring CC distance, the C_2C_3 and C_6C_1 bonds are elongated while the C_2C_3 and C_5C_6 bonds are shortened. Combined with the fact that both the C_2C_8 and the C_1N_7 bonds lengths increase, this means that the S_1 state is strongly *ortho*-quinoidal in character. From the ring dihedral angles it can be deduced that the ring geometry also becomes distorted in the out-of-plane direction and adopts a chair conformation similar to that of cyclohexane. Interestingly, while the difference between both CC bond lengths geminal to the methyl group (C_1C_2 and C_2C_3) is 0.3 pm smaller in the excited state than it is in the ground state, they are by no means equal. This means that the barrier to internal rotation of the methyl group is low in the S_1 state even though good, local C_{2v} symmetry at the C_2 carbon atom is absent. This confirms the conclusion from earlier work that the barrier is mostly electronic in nature and that steric effects are only of secondary importance.[14,15]

Table 3 Rotational constants and S_0 and S_1 state geometric parameters for *o*-toluidine. The calculated values from this work were obtained at the RICC2/TZVP level of theory. The atomic numbering refers to Fig. 3

	S_0				S_1		
	Exp.[a]	RICC2[a]	MP2[b]	HF[c]	Exp.[a]	RICC2[a]	CIS[b]
A/MHz	3229.60	3268	3228	—	3121.92	3098	3196
B/MHz	2188.49	2219	2178	—	2181.97	2187	2240
C/MHz	1316.82	1334	1313	—	1296.03	1295	1328
Bond lengths/pm							
C_1C_2	—	139.8	141.1	140.1	—	142.9	142.7
C_2C_3	—	138.3	140.0	138.8	—	144.1	137.0
C_3C_4	—	138.4	139.8	138.8	—	141.9	140.0
C_4C_5	—	138.0	139.8	138.5	—	141.6	139.8
C_5C_6	—	138.1	139.6	138.5	—	142.2	136.3
C_6C_1	—	138.7	140.3	139.2	—	143.5	143.6
C_1N_7	—	139.9	141.0	140.1	—	137.2	131.1
C_2C_8	—	150.8	150.5	151.1	—	149.4	150.1
CH (ring)[d]	—	107.5	108.9	107.6	—	108.4	107.3
N_7H_{7a}	—	99.5	101.7[d]	99.8[d]	—	101.1	100.4[d]
N_7H_{7b}	—	99.5	101.7[d]	99.8[d]	—	101.1	100.4[d]
C_8H_{8a}	—	108.8	109.6[d]	108.6[d]	—	109.9	108.4[d]
C_8H_{8b}	—	108.5	109.6[d]	108.6[d]	—	109.3	108.4[d]
C_8H_{8c}	—	108.2	109.6[d]	108.6[d]	—	109.4	108.4[d]
C_1C_4	—	278.4	281.0	279.3	—	281.3	278.8
Bond angles/°							
$C_1C_2C_3$	—	118.5	118.6	118.5	—	116.7	117.4
$C_2C_3C_4$	—	122.0	121.6	122.0	—	119.0	121.9
$C_3C_4C_5$	—	118.9	119.2	118.9	—	122.4	121.0
$C_4C_5C_6$	—	120.1	120.0	120.1	—	119.4	119.5
$C_5C_6C_1$	—	120.8	120.7	120.8	—	117.9	120.4
$C_6C_1C_2$	—	119.6	119.7	119.6	—	123.2	119.9
$N_7C_1C_2$	—	120.3	119.7	120.2	—	119.5	121.3
$N_7C_1C_6$	—	120.1	120.6	120.1	—	116.8	118.8
$C_1C_2C_8$	—	120.6	120.0	120.6	—	123.2	121.1
$C_3C_2C_8$	—	120.9	121.4	120.9	—	119.8	121.5
$H_{7a}N_7C_1$	—	115.1	114.2	—	—	119.0	123.1
$H_{7b}N_7C_1$	—	114.1	113.2	—	—	117.5	121.2
$H_{7a}N_7H_{7b}$	—	111.0	109.9	110.1	—	116.1	115.7
$C_2C_8H_{8a}$	—	111.8	—	111.3[d]	—	112.4	—
$C_2C_8H_{8b}$	—	111.3	—	111.3[d]	—	113.1	—
$C_2C_8H_{8c}$	—	110.7	—	111.3[d]	—	109.7	—
$H_{8a}C_8H_{8b}$	—	107.5	107.3[d]	107.5[d]	—	107.9	108.0[d]
$H_{8b}C_8H_{8c}$	—	108.0	107.3[d]	107.5[d]	—	106.7	108.0[d]
$H_{8c}C_8H_{8a}$	—	107.3	107.3[d]	107.5[d]	—	106.6	108.0[d]
Dihedral angles/°							
$C_1C_2C_3C_4$	—	−0.5	—	—	—	−6.0	—
$C_2C_3C_4C5$	—	−0.1	—	—	—	1.9	—
$C_3C_4C_5C_6$	—	0.2	—	—	—	−4.4	—
$C_4C_5C_6C_1$	—	0.2	—	—	—	10.4	—
$C_5C_6C_1C_2$	—	−0.7	—	—	—	−13.6	—
$C_6C_1C_2C_3$	—	0.9	—	—	—	11.8	—
$C_5C_6C_1N_7$	—	−177.3	−176.8	—	—	−177.5	0.0
$C_6C_1N_7H_{7a}$	—	−148.5	—	—	—	−165.5	—
$C_6C_1N_7H_{7b}$	—	−18.5	—	—	—	−16.8	—
$C_4C_3C_2C_8$	—	179.2	—	—	—	172.3	—
$C_3C_2C_8H_{8a}$	—	116.0	—	—	—	79.0	—
$C_3C_2C_8H_{8b}$	—	−123.7	—	—	—	−158.5	—
$C_3C_2C_8H_{8c}$	—	−3.6	—	—	—	−39.4	—

[a] This work. [b] MP2/6-31 + G* (S_0) and CIS/6-31 + G* (S_1), Ballesteros and Santos.[23] [c] HF/6-31 + G*, Tzeng *et al.*[22] [d] Average value.

From the geometries of the methyl and amino groups it is deduced that steric hindrance not only affects the benzene ring, but also both substituents themselves. In the ground state it can be seen from the methyl group dihedral angles that it is rotated by about 3.8° with respect to its equilibrium position in toluene, which has the C_8H_{8c} bond in the plane of the benzene ring. For the amino group the combination of steric repulsion and the addition of another electron donating group to the ring causes it to be much more planar than in aniline (where it is out of plane by a 37.5° angle[2]) and tilted away from the methyl rotor, with one hydrogen atom 31.5° below the plane and the other just 18.5°. In the electronically excited state the amino group becomes more planar due to sharing its lone pair electron with the benzene π-electron system, which points to electronic excitation comparable to that in aniline. As a result, the methyl group orientation is now completely different, with the C_8H_{8a} bond in a much more vertical position, not unlike the situation in toluene.[47] Especially for the methyl group the
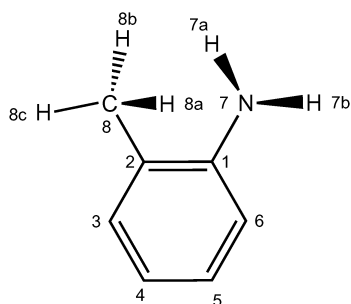
Fig. 3 Atomic numbering of *o*-toluidine used in Table 3.

distortions in the S_1 state are severe, with the three C_2C_8H bond angles differing by as much as 3.4°. Most significantly though, from the $C_4C_3C_2C_8$ dihedral angle the methyl carbon atom is found to move out of the plane of the benzene ring by as much as 7.7°. This supports the explanation that the effective value of 71.6° found for ζ in section 3.2 is due to a precessional motion of the whole methyl group.

4. Conclusions

The $S_1 \leftarrow S_0$ transition in *o*-toluidine has been measured using rotationally resolved electronic spectroscopy. The resulting spectrum consists of two overlapping spectral components which can be assigned to the $0a_1 \leftarrow 0a_1$ and $1e \leftarrow 1e$ transitions between torsional sub-bands that arise from internal rotation of the methyl group. The torsional parameters that can be derived were combined with frequencies of torsional transitions from previous work[11,23] to derive accurate barriers to internal rotation in both electronic states. It was found that the V_3 barrier is lowered from 699 cm^{-1} in the S_0 state to 40.87 cm^{-1} in the S_1 state. This dramatic lowering of the barrier to internal rotation is similar to that observed in other *ortho*-substituted toluenes[9] and can be explained in terms of the difference in π-bond order between both ring carbon bonds geminal to the methyl rotor.[15]

The rotational constants that were determined for both electronic states are close to those resulting from RICC2 calcultions, and an extensive analysis of the predicted molecular geometry was therefore made. As is usual for substituted benzenes, the benzene ring was found to expand on electronic excitation, and the amino group becomes more planar. The excited state geometry has a strongly *ortho*-quinoidal character which shortens both the methyl CC bond and the amino CN bond. *Para*-quinoidal distortion is frequently encountered in *p*-substituted benzenes on electronic excitation[48–50] and given the fact that *o*- and *p*-substituted benzenes are electronically similar this is therefore not unexpected. As a result, the steric interactions between both substituents, which are already visible in the S_0 state, are increased dramatically in the S_1 state: the methyl group makes a 7.7° angle with the local benzene ring orientation and rotates away from the S_0 state geometry. Combined with the fact that an unrealistically large angle between the normal of the benzene plane and the methyl rotor axis resulted from spectral analysis and that the effective rotational constant F was found

to decrease dramatically on electronic excitation, this constitutes a compelling evidence for an S_1 state precessional motion of the whole methyl group.[24]

References

1 N. Mikami, A. Hiraya, I. Fujiwara and M. Ito, *Chem. Phys. Lett.*, 1980, **74**, 531–535.
2 W. E. Sinclair and D. W. Pratt, *J. Chem. Phys.*, 1996, **105**, 7942.
3 N. W. Larsen, E. L. Hansen and F. M. Nicolaisen, *Chem. Phys. Lett.*, 1976, **43**, 584–586.
4 R. A. Kydd and P. J. Krueger, *Chem. Phys. Lett.*, 1977, **49**, 539–543.
5 E. R. T. Kerstel, M. Becucci, G. Pietraperzia and E. Castellucci, *Chem. Phys.*, 1995, **199**, 263–273.
6 E. R. T. Kerstel, M. Becucci, G. Pietraperzia, D. Consalvo and E. Castellucci, *J. Mol. Spectrosc.*, 1996, **177**, 74–78.
7 R. A. Kydd and P. J. Krueger, *J. Chem. Phys.*, 1980, **72**, 280–283.
8 X.-Q. Tan and D. W. Pratt, *J. Chem. Phys.*, 1994, **100**, 7061.
9 Z.-Q. Zhao, C. S. Parmenter, D. B. Moss, A. J. Bradley, A. E. W. Knight and K. G. Owens, *J. Chem. Phys.*, 1992, **96**, 6362–6377.
10 M. Fujii, M. Yamauchi, K. Takazawa and M. Ito, *Spectrochim. Acta, Part A*, 1994, **50**, 1421–1433.
11 K. Okuyama, N. Mikami and M. Ito, *Laser Chem.*, 1987, **7**, 197.
12 H. Ikoma, K. Takazawa, Y. Emura, S. Ikeda, H. Abe, H. Hayashi and M. asaaki Fujii, *J. Chem. Phys.*, 1996, **105**, 10201–10209.
13 J. L. Lin, K. C. Lin and W. B. Tzeng, *J. Phys. Chem. A*, 2002, **106**, 6462–6468.
14 H. Nakai and M. Kawai, *J. Chem. Phys.*, 2000, **113**, 2168–2174.
15 K. T. Lu, F. Weinhold and J. C. Weisshaar, *J. Chem. Phys.*, 1995, **102**, 6787.
16 D. E. Powers, J. B. Hopkins and R. E. Smalley, *J. Chem. Phys.*, 1980, **72**, 5721–5730.
17 R. Tembreull, T. M. Dunn and D. M. Lubman, *Spectrochim. Acta, Part A*, 1986, **42**, 899.
18 W. B. Tzeng and K. Narayanan, *J. Mol. Struct.*, 1998, **446**, 93–102.
19 S. Yan and L. H. Spangler, *J. Chem. Phys.*, 1992, **96**, 4106–4117.
20 L. Santos, E. Martínez, B. Ballesteros and J. Sanchez, *Spectrochim. Acta, Part A*, 2000, **56**, 1905–1915.
21 R. Disselkamp, H. S. Im and E. R. Bernstein, *J. Chem. Phys.*, 1992, **97**, 7889–7901.
22 W. B. Tzeng, K. Narayanan, J. L. Lin and C. C. Tung, *Spectrochim. Acta, Part A*, 1999, **55**, 153.
23 B. Ballesteros and L. Santos, *Spectrochim. Acta, Part A*, 2002, **58**, 1069–1081.
24 P. M. Brodersen and R. D. Gordon, *J. Mol. Struct.*, 2000, **522**, 279–288.
25 M. Schmitt, J. Küpper, D. Spangenberg and A. Westphal, *Chem. Phys.*, 2000, **254**, 349–361.
26 S. Gerstenkorn and P. Luc, *Atlas du spectre d'absorption de la molécule d'iode*, CNRS, Paris, 1982.
27 R. Ahlrichs, M. Bär, M. Häser, H. Horn and C. Kölmel, *Chem. Phys. Lett.*, 1989, **162**, 165–169.
28 A. Schäfer, C. Huber and R. Ahlrichs, *J. Chem. Phys.*, 1994, **100**, 5829–5835.
29 C. Hättig and A. Köhn, *J. Chem. Phys.*, 2002, **113**, 6939.
30 C. Hättig, *J. Chem. Phys.*, 2002, **117**, 7751–7761.

31 H. Horn, H. Weiss, M. Häser, M. Ehrig and R. Ahlrichs, *J. Comput. Chem.*, 1991, **12**, 1058.

32 P. Deglmann, F. Furche and R. Ahlrichs, *Chem. Phys. Lett.*, 2002, **362**, 511–518.

33 S. Grimme and M. Waletzke, *J. Chem. Phys.*, 1999, **111**, 5645–5655.

34 A. D. Becke, *J. Chem. Phys.*, 1993, **98**, 1372.

35 C. Lee, W. Yang and R. Parr, *Phys. Rev. B*, 1988, **37**, 785–789.

36 W. Gordy and R. L. Cook, *Microwave Molecular Spectra*, Wiley, New York, 3 edn, 1984.

37 J. A. Hageman, R. Wehrens, R. de Gelder, W. L. Meerts and L. M. C. Buydens, *J. Chem. Phys.*, 2000, **113**, 7955–7962.

38 W. L. Meerts, M. Schmitt and G. Groenenboom, *Can. J. Chem.*, 2004, **82**, 804–819.

39 W. L. Meerts and M. Schmitt, *Int. Rev. Phys. Chem.*, 2006, **25**, 353–406.

40 I. Kalkman, C. Vu, M. Schmitt and W. L. Meerts, *ChemPhysChem*, 2008, **9**, 1788–1797.

41 C. Jacoby, M. Böhm, C. Vu, C. Ratzer and M. Schmitt, *ChemPhysChem*, 2006, **7**, 448–455.

42 Y. R. Wu and D. H. Levy, *J. Chem. Phys.*, 1989, **91**, 5278–5284.

43 D. F. Plusquellic and D. W. Pratt, *J. Chem. Phys.*, 1992, **97**, 8970.

44 K. Remmers, E. Jalviste, I. Mistrík, G. Berden and W. L. Meerts, *J. Chem. Phys.*, 1998, **108**, 8436–8445.

45 G. Myszkiewicz, W. L. Meerts, C. Ratzer and M. Schmitt, *Phys. Chem. Chem. Phys.*, 2005, **7**, 2142–2150.

46 T. M. Korter, D. R. Borst, C. J. Butler and D. W. Pratt, *J. Am. Chem. Soc.*, 2001, **123**, 96–99.

47 D. R. Borst and D. W. Pratt, *J. Chem. Phys.*, 2000, **113**, 3658–3669.

48 M. Böhm, C. Ratzer and M. Schmitt, *J. Mol. Struct.*, 2005, **800**, 55–61.

49 M. Schmitt, C. Ratzer, C. Jacoby and W. L. Meerts, *J. Mol. Struct.*, 2005, **742**, 123–130.

50 J. W. Ribblett, D. R. Borst and D. W. Pratt, *J. Chem. Phys.*, 1999, **111**, 8454–8461.

5.8   p-Cyanophenol-Wasser-Cluster

CHEMPHYSCHEM

Probing the Acidity of *p*-Substituted Phenols in the Excited State: Electronic Spectroscopy of the *p*-Cyanophenol–Water Cluster

Christoph Jacoby,[a, b] Marcel Böhm,[a] Chau Vu,[a] Christian Ratzer,[a] and Michael Schmitt*[a]

The hydrogen bond structure of the p-cyanophenol–water cluster has been determined in the ground and first excited electronic state by rotationally resolved UV spectroscopy. The water molecule is trans-linearly bound to the hydroxy group of the p-cyanophenol moiety, with hydrogen bond distances considerably shorter in both electronic states than in the similar phenol-water cluster. The structure of the cluster has been elucidated by ab initio calculations at various levels of theory and compared to the experimental findings. The barriers to internal rotation of the water moiety were determined experimentally to be 275 and 183 cm^{-1} for the ground and excited state, respectively. Hydrogen bond distances and the energy barrier to water torsion correlate with the pK$_a$ values of different substituted phenols for both electronic states.

1. Introduction

Hydrogen-bonded clusters of phenol and substituted phenols have found considerable interest as model systems for solvation processes, electronic ground and excited state acidities, and dynamical processes connecting the primary excited state with the electronic ground state. While the phenol-water system has been studied in great detail experimentally and theoretically for both the electronic ground and excited state, little is known about the different substituted phenol-water clusters. Substitution in the *para* position with respect to the hydroxy group allows the study of electronic effects on hydrogen bonding with minimized sterical perturbations. A very interesting system is the *p*-cyanophenol–water cluster, because the cyano group exerts a strong mesomeric effect, which drastically alters properties, like acidities, lifetimes, and excited state structures of both the monomer and the water cluster. Both functional groups in *p*-cyanophenol (*p*-CP), the hydroxy group as well as the cyano group, may bind a water molecule in the binary *p*-CP–water cluster. The geometry of the *p*-CP monomer can be derived from the structures of phenol and benzonitrile. Its water cluster might therefore be *trans*-linearly hydrogen bound via the hydroxy group as in the case of phenol-water,[1–3] or doubly hydrogen bound via the cyano group and the *ortho* hydrogen atom of the aromatic ring.[4, 5]

The complete substitution structure of the phenol in the electronic ground state was determined by Larsen and co-workers[6,7] with microwave spectroscopy. The electronically excited state was examined by Martinez et al.[8] and Berden et al.[1] with laser-induced fluorescence spectroscopy (LIF) and by Helm et al.[9] with resonant two photon ionization (R2PI) spectroscopy. From rotationally resolved spectroscopic studies of isotopmers Ratzer et al.[10] have proposed a partial substitution structure for the electronic excited state of phenol.

The ground state of benzonitrile has also been studied by microwave spectroscopy.[11, 12] The electronic excited state was investigated using high-resolution laser spectroscopy by Helm et al.[13] From the long fluorescence lifetime of benzonitrile they excluded that the charge transfer (CT) state, in which the CN group is nonlinear, is located below the locally excited S$_1$ state. Borst et al.[14] determined the dipole moment of benzonitrile in both electronic states by Stark effect studies of the electronic spectra and found the additivity rule of incremental dipole moments to be valid for the planar S$_1$ state.

Roth et al. determined the vibrational frequencies of *p*-CP in the electronic ground state through laser induced dispersed fluorescence spectra and compared them to ab initio normal mode vibrational frequencies.[15] A rotationally resolved spectrum of the S$_1 \leftarrow$ S$_0$ vibronic origin transition of *p*-CP was reported by Küpper et al.[16] From the changes of the rotational constants upon electronic excitation they postulated a quinoidal distortion of the aromatic ring.

The pK$_a$ value of *p*-CP was determined to be 7.74 in the S$_0$ state and 3.33 in the S$_1$ state,[17] thus *p*-CP is a stronger acid than phenol in both electronic states. Furthermore, the in-

[a] Dr. C. Jacoby, M. Böhm, C. Vu, Dr. C. Ratzer, Dr. M. Schmitt
Heinrich-Heine-Universität, Institut für Physikalische Chemie
40225 Düsseldorf, Germany
Fax: (+49) 211-81-15195
E-mail: mschmitt@uni-duesseldorf.de

[b] Dr. C. Jacoby
Current adress:
Heinrich-Heine-Universität Düsseldorf
Institut für Herz- und Kreislaufphysiologie
40225 Düsseldorf, Germany

crease in acidity upon electronic excitation of *p*-CP is larger than that of phenol.

The binary *p*-CP-(H$_2$O)$_1$ cluster was studied by using fluorescence excitation, resonance enhanced multiphoton ionization (REMPI), hole-burning, and fluorescence detected IR spectroscopy by Biswas et al.[18] They performed ab initio calculations on different isomers of the clusters and found the stabilization energy of the ring-like cyano bound structure to be about 18 kJ mol^{-1} smaller than that of the *trans*-linearly hydroxy bound structure. It was proved by hole-burning spectroscopy, that only one isomer is contributing to the electronic spectrum up to 800 cm^{-1} above the electronic origin. Leutwyler et al.[19] reported the structures of the *p*-CP-(H$_2$O)$_2$ cluster and postulated a cyclic structure with both water moieties bound to the hydroxy group.

Herein, we investigate the influence of the altered acidity in both electronic states on the molecular properties of the *p*-CP binary water cluster.

Experimental Section

The experimental setup for the rotationally resolved LIF is described in detail elsewhere.[20] Briefly, it consists of a ring dye laser (Coherent 899-21) operated with Rhodamine 110, pumped with 6 W from an Ar$^+$-ion laser (514 nm). The light was coupled into an external folded ring cavity (Spectra Physics) for second harmonic generation (SHG). *p*-CP was purchased from Fluka (>97%). The molecular beam was formed by coexpanding *p*-CP (at 190°C and 5 mbar H$_2$O seeded in 600 mbar of argon) through a 100 µm nozzle into the vacuum. The molecular beam machine consists of three differentially pumped vacuum chambers that are linearly connected by skimmers (1 mm and 3 mm) in order to reduce the Doppler width. The molecular beam is crossed at right angles in the third chamber with the laser beam 360 mm downstream of the nozzle. The resulting fluorescence is collected perpendicular to the plane defined by the laser and the molecular beam by an imaging optics setup consisting of a concave mirror and two plano-convex lenses. The resulting Doppler width in this setup is 25 MHz (FWHM). The integrated molecular fluorescence is detected by a photomultiplier tube, whose output is discriminated and digitized by a photon counter and transmitted to a PC for data recording and processing.

The ab initio calculations have been performed using Gaussian 98.[21] The SCF (self-consistent-field) convergence criterion used for our calculations was an energy change below 10^{-8} Hartree, while the convergence criterion for the gradient optimization of the molecular geometry was $\partial E/\partial r < 1.5 \times 10^{-5}$ Hartree/Bohr and $\partial E/\partial \phi < 1.5 \times 10^{-5}$ Hartree/degrees. A normal mode analysis was performed utilizing the analytical second derivatives of the potential energy surface. The basis set superposition error (BSSE), of the binding energy of the cluster, was corrected for using the counterpoise method from Boys and Bernardi.[22] The electronically excited state has been optimized with complete active space, (CAS), SCF using an active space of 12 electrons in 11 orbitals. Additionally, the geometry of the electronically excited state has been optimized using time-dependent density functional theory (TDDFT)[23,24] employing the B3-LYP functional.[25,26] These calculations were performed with the program system TURBOMOLE.[27,28]

2. Results and Discussion

Figure 1 presents the rotationally resolved electronic spectrum of the origin of the binary *p*-CP–water cluster at 35 304.46 cm^{-1}. This origin band is red shifted by 243 cm^{-1} relative to the origin of the *p*-CP monomer. The spectrum of the electronic origin is split into two subbands due to the internal
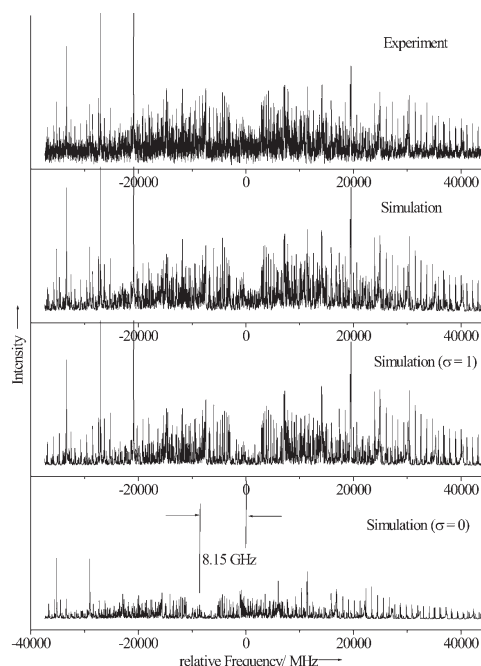

Figure 1. Rotationally resolved electronic spectrum of the origin of the *p*-cyanophenol–water cluster. From top to bottom: experimental spectrum, simulated spectrum using the parameters from Table 1, separate simulations of the torsional subbands.

rotation of the water moiety. The molecular symmetry group, which takes this motion into account, is G_4, isomorphic with the point group C_{2v}. The lowest torsional state (with $\sigma = 0$) is of *A* symmetry, the following energetical state (with $\sigma = 1$) is of *B* symmetry. Both subbands can be fitted using rigid asymmetric rotor selection rules with two sets of rotational constants and with the difference of the vibronic origins as an additional parameter. The theory of coupling of the two-fold internal rotation of the water moiety to the overall rotation of the cluster has been elaborated in detail in refs. [1] and [29] and will not be repeated here. The upper trace of Figure 1 shows the experimental spectrum, the following trace the complete simulation using the parameters from Table 1. The next two traces give the individual simulations for the two torsional subbands caused by the internal rotation of the water moiety. A zoomed in portion of the spectrum is shown in Figure 2.

The spectrum was automatically assigned using the genetic algorithm (GA) based fitting procedure described in refs. [30] and [31]. Since the GA performs a fit of the shape of the com-

Table 1. Molecular parameters of *p*-cyanophenol–water from the GA fit. The doubly primed parameters refer to the electronic ground state. ΔA, ΔB, and ΔC are defined as $A'-A''$, etc. with the singly primed rotational constants describing the electronically excited state. The numbers in parentheses give the standard deviations of the parameters to the number of quoted digits.

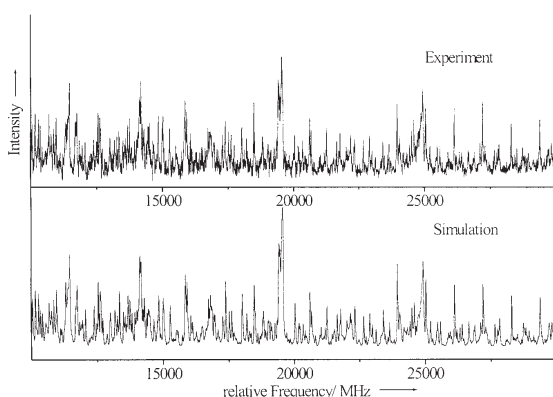| *p*-CP(H$_2$O)$_1$	$\sigma = 0$	$\sigma = 1$
A''[MHz]	3462.16(50)	3459.95(6)
B''[MHz]	587.87(8)	588.00(4)
C''[MHz]	503.62(6)	503.75(2)
ΔA[MHz]	−48.69(24)	−50.39(5)
ΔB[MHz]	−0.11(1)	−0.13(1)
ΔC[MHz]	−1.08(1)	−1.06(1)
θ[°]	69.5(13)	74.48(45)
$\Delta\nu$(Lorentz) [MHz]	15.7(10)	
τ[ns]	10.1(5)	
ν_0[cm^{-1}]	35304.46(2)	35304.70(2)
$\nu_0(A) - \nu_0(B)$ [MHz]	−8149.42(106)	

Figure 2. Magnified 20 GHz portion in the R-branch of the origin of *p*-cyanophenol–water. Upper trace: experimental spectrum, lower trace: simulated spectrum.

plete spectrum, more accurate results on the lineshape parameters are obtained than from a lineshape fitted to a few selected individual lines. The following parameters were used in the GA fit:

(i) the rotational constants *A*, *B*, and *C* of both torsional components for the electronic ground and excited state

(ii) the center frequency ν_0 of the first torsional band

(iii) the difference of the center frequencies of the torsional subbands

(iv) the angle θ of the transition dipole moment with the inertial *a*-axis

(v) the Lorentzian contribution $\Delta\nu$(Lorentz) to the Voigt profile with a fixed Doppler width of 25 MHz. Even for Lorentz contributions well below the Doppler width quite accurate values are obtained because all the lines in the experimental spectrum are included in the lineshape fit.

(vi) two temperatures and a weight factor given by Equation (1):

$$n(T_1, T_2, w) = e^{-\frac{E}{kT_1}} + w e^{-\frac{E}{kT_2}} \qquad (1)$$

where *E* is the energy of the lower state, *k* is the Boltzmann constant, *w* is a weighting factor, and T_1 and T_2 are the temperatures.[32] The resulting temperatures and weights obtained from the individual spectra are not presented in Table 1 as they are strongly correlated and are merely used to facilitate the intensity fit for low and high *J* states simultaneously.

The resulting molecular parameters are given in Table 1. The spectrum is an *ab*-hybrid band with 93 % *b*-type and 7 % *a*-type character and is split into two subbands by the internal rotation of the water moiety, with the low frequency component having 1/3 of the intensity of the high-frequency component. The splitting between the origins of the two subbands amounts to 8149 MHz (0.27 cm^{-1}). The total spectrum contains about 7500 rovibronic lines with a Lorentzian linewidth of 15.7(10) MHz, leading to an excited state lifetime of 10.1(5) ns. (The numbers in parentheses give the standard deviations of the parameters to the number of quoted digits.) This lifetime is within the same accuracy as that of the *p*-CP monomer (10.6 ns).

2.1. Determination of the Intermolecular Structure

The program pKrFit[10] was used to determine the intermolecular structure of *p*-CP–water in the S_0 and S_1 states from the rotational constants given in Table 1. Due to the very limited number of inertial parameters, we performed a fit limited to the partial r_0 structure, which neglects all vibrational contributions.

The change of the *p*-CP monomer geometry upon electronic excitation has been taken from ref. [16]. The mean aromatic C–C bond length in the ground state was determined to be 139.4 pm, increasing to 143.9 upon excitation. Keeping the geometries from ref. [16] fixed together with a fixed water geometry ($R_{OH} = 0.957$ Å, H-O-H $= 104.52°$ from ref. [33]) we fitted the O_7O_{15} distance, the $O_7H_8O_{15}$ angle, and the $H_8O_{15}H_{17}$ angle (cf. Figure 3 for the atomic numbering). The other three intermolecular parameters are kept fixed to the values of a planar *trans*-linear cluster: dihedral $(C_1O_7H_8O_{15}) = 180°$ and dihedral$(O_7H_8O_{15}H_{16}) = -$dihedral$(O_7H_8O_{15}H_{17}) = 60°$. The last two parameters are restricted under the assumption that one of the water lone pairs points towards the hydroxy group. They have opposing signs due to symmetry restrictions. Using this model, we obtained a hydrogen bond length of 282.8(1) pm in the S_0 state and of 269.0(1) pm in the S_1 state. Both values are considerably shorter than the corresponding distances in the phenol-water (293 and 289 pm, respectively). The $O_7H_8O_{15}$ angle was determined to be 177.2(3)° in the S_0 state and 179.0(4)° in the
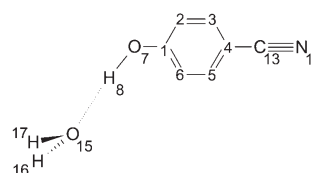

Figure 3. Atomic numbering used in the geometry fit of *p*-CP–water.

S_1 state, and the $H_8O_{15}H_{17}$ angle was determined to be 115(2)°(S_0) and 111(4)°(S_1). The geometry parameters are summarized in Table 2 and compared to the results of ab initio calculations. The change of the hydrogen bond length upon electronic excitation is larger than in the structurally similar phenol-water cluster. These changes reflect both the higher ground state acidity of *p*-CP (pK_a = 7.74) compared to phenol (pK_a = 9.86), and the larger increase of acidity in *p*-CP upon electronic excitation [pK_a(phenol,S_1) = 6 vs pK_a(*p*-CP,S_1) = 3.33].

Table 2. Intermolecular geometry parameters of the *p*-CP–water cluster. The distance (*R*) is given in pm, angles (*A*) and dihedral angles (*D*) in degrees.

	Exp. (S_0)	Exp. (S_1)	MP2 (S_0)	HF (S_0)	CIS (S_1)	DFT (S_0)	TDDFT (S_1)
$R(O_7O_{15})$	282.8	269.0	280.49	287.19	284.90	276.79	270.26
$A(O_7H_8O_{15})$	177.2	178.9	178.734	177.883	178.870	179.628	176.265
$A(H_8O_{15}H_{17})$	115.0	111.4	113.362	118.841	120.033	113.976	113.204
$D(C_1O_7H_8O_{15})$	180[a]	180[a]	179.622	179.992	179.858	178.770	179.887
$D(O_7H_8O_{15}H_{16})$	−60[a]	−60[a]	−59.474	−66.533	−68.106	−61.013	−59.044
$D(O_7H_8O_{15}H_{17})$	60[a]	60[a]	60.230	66.551	68.374	58.681	58.879

[a] Kept fixed at this value.

2.2. Barriers to Internal Rotation of the Water Moiety

The barriers to rotation of the water moiety have been estimated using the program HTorFit. The underlying theory for treating the twofold internal rotation in the frame of the principal axis method (PAM)[34] is given in ref. [29].

Three pieces of information, which can be used for the determination of the torsional barriers, can be extracted from the rovibronic spectrum: (i) the subtorsional splitting arising from transitions belonging to the different torsional components of σ with the selection rule $\Delta\sigma = 0$, (ii) the difference in the rotational constants of the two different components of σ in the ground state, and (iii) this difference in the electronically excited state. The subtorsional splitting between the transitions $(\sigma=0)' \leftarrow (\sigma=0)''$ and $(\sigma=1)' \leftarrow (\sigma=1)''$ was determined to be 8149.42(106) MHz. This splitting, together with the differences in the rotational constants of the $(\sigma=0)$ and $(\sigma=1)$ levels in the electronic ground and excited state, which contain the second-order perturbation coefficients, have been used to fit the barrier to the water torsional motion. Unfortunately, for *p*-CP–water no additional torsional data are available as for the similar phenol-water cluster.[29,35] Thus, we were not able to independently fit the barriers and the torsional constants for both electronic states.

The barriers, which are obtained from this analysis, are effective barriers because the actual motion is more complex than a simple one-dimensional torsion.[2,3] The potential energy in this one-dimensional model is given in Equation (2). It depends only on the torsional coordinate, which is defined by rotation about the symmetry axis of the water molecule:

$$V(\tau) = \frac{1}{2}V_2(1 - \cos 2\alpha). \tag{2}$$

Figure 4 shows why the path, which connects the identical minima that arise from permutation of H1 and H2, cannot be the simple torsion about the water symmetry axis. This motion would break the hydrogen bond between the localized molecular orbital (MO) (1) of the water moiety and the phenolic hydroxy group. The new hydrogen bond would then be formed using the MO (2). The (1,2) permutation of the hydrogen atom can also be achieved in a "smoother" pathway. Rotation about the hydrogen bond would convert the cluster into the *cis* conformer. To bring it back to the most stable *trans* configuration, an inversion[3] or wagging motion[2] would then change the MO involved in the hydrogen bonding. The effective barrier arises from a concerted (coupled) motion along both coordinates, constituting the minimum energy path.

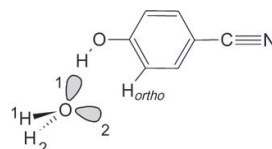With the one-dimensional model we fit the effective barriers using the value for the tor-

Figure 4. Schematic representation of the localized molecular orbitals of the water moiety involved in the hydrogen bonding of the cluster The indices 1 and 2 are used for numbering the atoms to describe the permutation (1,2). For numbering of lone pairs see text.

sional constant *F* of 14.813 cm^{-1} for the electronic ground state and of 13.415 cm^{-1} for the electronically excited state. These torsional constants have been determined from the analysis of several torsional bands in different isotopomers in the phenol-water cluster.[29] Values of $V_2'' = 275(4)$ cm^{-1} and $V_2' = 183(1)$ cm^{-1} for the ground and excited state of the *p*-CP–water cluster, respectively, have been obtained. These barriers are considerably larger than the corresponding values in phenol ($V_2'' = 175.4$ cm^{-1}, $V_2' = 109.1$ cm^{-1}). The reason for the strong increase of the barrier height in the electronic ground state is the formation of an additional hydrogen bond between the *ortho*-CH group in *p*-CP and phenol and the O atom of the water moiety. Feller calculated an OH···O distance of 185.8 pm.[36] for the hydrogen bond in the *trans*-linear phenol-water cluster calculated at the MP2/6-31G(d,p) level. The CH···O distance of the *ortho*-CH group in phenol was calculated to be 270.2 pm. The OH···O distance in *p*-CP is decreased to 182.8 pm, and the CH···O distance to 263.6 pm. Both distances are smaller in *p*-CP compared to phenol due to the higher acidity of *p*-CP. The hydrogen bonds are oriented in the direction of the equivalent oxygen lone pairs of the water moiety and hinder the torsional motion. This effect is larger in *p*-CP ex-

plaining the higher barrier in the ground state. The increase of acidity upon electronic excitation is larger in *p*-CP than in phenol. Thus, also the increase in the barrier height is expected to be larger in *p*-CP as has been found experimentally.

2.3. Comparison to ab initio Calculations

The electronic ground state of the *p*-CP–water cluster has been optimized on the MP2/6-31G(d,p) level of theory. The rotational constants of the optimized structure are given in Table 3 and are compared to the results of the experiment.

Table 3. Experimental and ab initio inertial constants of the *p*-CP–water cluster. TDDFT and DFT calculations were performed with the B3-LYP functional implemented in the TURBOMOLE program system. All calculations have been performed using the 6-31G(d,p) basis set. The rotational constants are given in MHz.

	Exp.	MP2	HF	CIS	CIS-HF	DFT/TDDFT	CAS(12/11)
A''	3461.06	3413	3481	-	-	3422[a]	3439[a]
B''	587.93	586	591	-	-	601[a]	582[a]
C''	503.70	501	506	-	-	512[a]	499[a]
A'	3411.56	-	-	3410	-	3390[b]	3332[b]
B'	587.81	-	-	591	-	599[b]	576[b]
C'	502.63	-	-	505	-	510[b]	492[b]
ΔA	−49.50	-	-	-	−71	−32	−107
ΔB	−0.12	-	-	-	0	−2	−6
ΔC	−1.07	-	-	-	1	−2	7

[a] Geometry optimized to the S_0 state. [b] Geometry optimized to the S_1 state.

The deviations are less than 2% for each of the rotational constants. The MP2 stabilization energy of the cluster, including zero-point energy and BSSE corrections, amounts to 27.43 kJ mol^{-1} (2293.04 cm^{-1}), considerably stronger than the calculated binding energy of 22.93 kJ mol^{-1} for phenol-water using the same method and basis set. Without any symmetry constraints in the calculations, the O_7O_{15} hydrogen bond distance (cf. Figure 3 for atomic numbering) was found to be 280.49 pm on MP2 level. The water oxygen atom is positioned in the aromatic plane [dihedral angle ($C_1O_7H_8O_{15}$) = 179.622°]. The hydrogen bond is linear [angle ($O_7H_8O_{15}$) = 178.734°] and the water molecule is oriented symmetrically about the aromatic plane [dihedral angle ($O_7H_8O_{15}H_{16}$) = −dihedral angle ($O_7H_8O_{15}H_{17}$)], and in an *anti* position with respect to the aromatic ring [angle ($H_8O_{15}H_{17}$) = 113.362°].

The electronically excited state has been optimized using configuration interaction with single excitations [CIS/6-31G-(d,p)]. Due to a favorable cancellation of errors, even the absolute values of the rotational constants nearly match the experimental ones for the CIS calculations. The focus of these calculations is only on the difference of the rotational constants between the CIS and HF values to compute the geometry changes upon electronic excitation. These differences match very closely to the experimental changes of the rotational constants, which is due to the fact of equal approximations in both methods. These differences should merely be viewed as a guidance in the preliminary determination of the parameter limits for the GA fit of the spectrum. More reliable structures

for both electronic states and for the geometry changes can be obtained using density functional theory (DFT) for the ground state and TDDFT for the excited state. Table 3 shows, that using the B3-LYP functional even the absolute values match the experimentally determined rotational constants closely.

Furthermore, the electronic ground and excited states have been optimized with the complete active space SCF method [CASSCF/6-31G(d,p)] with 12 electrons in 11 orbitals. The active space employed in these calculations consists of three orbitals of π symmetry, centered in the aromatic ring: one occupied π orbital is located at the cyano group, one at the hydroxy group, and one at the oxygen atom of the water moiety. The unoccupied orbitals comprise three benzene-like π* orbitals, one antibonding orbital at the cyano group, and one at the water moiety. Under these conditions, only poor agreement with the experimentally determined rotational constants is found.

Inspection of the ab initio geometry parameters in Table 3 shows that the close agreements of the absolute values for the rotational constants of Hartree–Fock (HF) and CIS for ground and excited state with the experimentally determined ones are due to an accidental cancellation of errors. Both HF and CIS O_7O_{15} hydrogen bond lengths are largely overestimated, while the aromatic C−C bonds are underestimated. Also, the decrease of the O−O bond length in the S_1 state is largely underestimated. The comparison of the TDDFT(B3-LYP) calculations with the results of the experiment reveal a very close agreement not only for the rotational constants given in Table 3 but also for the geometry parameters summarized in Table 2.

3. Conclusions

The rotational constants obtained from the rotationally resolved LIF spectrum of the binary *p*-CP–water cluster allowed us to determine the intermolecular geometry parameters. Comparison with the results of ab initio calculations at various levels of theory showed a close agreement for the electronic ground state with the correlated MP2 results. The electronically excited state geometry can be well described using TDDFT with the B3-LYP functional and a moderate size basis set. In contrast, with CASSCF the intermolecular geometry cannot be described appropriately due to a lack of electron correlation and the limited active space employed. Anyhow, an active space of 12 electrons in 11 orbitals [CAS(12/11)] is close to the limit that can be currently calculated. Jansen and Gerhards,[37] have shown a satisfying description of the excited phenol-water geometry which requires the addition of six electrons in

six σ-type orbitals to account for the $\sigma\pi$ and the $\sigma\sigma$ correlations. In the case of *p*-CP–water this would mean a mixed $\sigma\pi$ active space of CAS(18/17), obviously too large for a geometry optimization. Thus, we conclude, that a proper description of excited-state geometries should rely on the TDDFT calculations to describe all the relevant interactions and not on the CASSCF calculations with a too small active space.

Within the uncertainty, the excited state lifetime of the *p*-CP–water cluster is the same as the monomer lifetime. This is very different from the phenol/phenol-water case, where the lifetime increases from 2 to 15 ns upon cluster formation. Sobolewski and Domcke explained the short lifetime of phenol by tunneling through a barrier which separates the $^1\pi\sigma^*$ from the $^1\pi\pi^*$ surface and a subsequent internal conversion to the ground state through a conical intersection with the ground state.[38] Two reasons might be possible for the longer lifetime of *p*-CP: The conical intersection with the ground state might be removed (like in the phenol-water cluster) or the barrier separating the excited states is considerably higher than in phenol. Further calculations are needed to distinguish between the two models.

Furthermore, the barriers to internal rotation of the water moiety about its symmetry axis in both electronic states were estimated. Both barrier heights and hydrogen bond lengths correlate well with the increased acidity of *p*-CP compared to phenol in both electronic states. While in the similar *p*-methyl-phenol-water cluster the hydrogen bond length is close to the values in phenol-water (290 pm in the S_0 state and 285 pm in the S_1 state of *p*-methylphenol-water vs. 293 and 289 pm, respectively, for phenol-water), considerably smaller values of 283 and 269 pm are found in the ground and excited state of *p*-CP–water.

Out of the three phenols compared in Table 4, *p*-methylphenol is the weakest acid in the electronic ground state and has the largest hydrogen bond distance. The O_7O_{15} hydrogen bond distances of the three *p*-substituted phenols scale nearly linearly with the pK_a-values in both electronic states as shown in Table 4 and in Figure 5.

The internal rotation of the water moiety is hindered by two intermolecular interactions: the OH···O hydrogen bond and the (weaker) CH···O hydrogen bond. The lone pairs of the oxygen atom of the water moiety point along both hydrogen bonds. Therefore, the barrier height is a function of the acidity of the hydroxy group as well as of the *ortho*-CH group, and the correlation between the pK_a values and the barrier heights is not so pronounced as in the case of the hydrogen bond length. Nev-
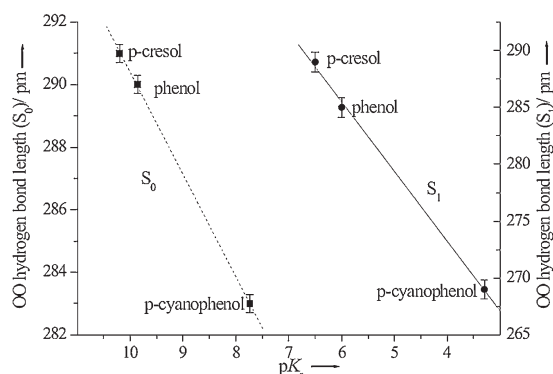

Figure 5. Correlation of the pK_a values of the monomers with the hydrogen bond length O_7O_{15} of the clusters in the electronic ground S_0 (left hand side) and excited S_1 (right hand side) states.

ertheless, it can be inferred from Table 4, that the barrier increases with decreasing pK_a values and with decreasing (calculated) CH···O distances.

[1] G. Berden, W. L. Meerts, M. Schmitt, K. Kleinermanns, *J. Chem. Phys.* **1996**, *104*, 972 – 982.
[2] M. Schütz, T. Bürgi, S. Leutwyler, T. Fischer, *J. Chem. Phys.* **1993**, *98*, 3763 – 3776.
[3] S. Melandri, A. Maris, P. G. Favero, W. Caminati, *Chem. Phys.* **2002**, *283*, 185 – 192.
[4] R. M. Helm, H. P. Vogel, H. J. Neusser, V. Storm, D. Consalvo, H. Dreizler, *Z. Naturforsch. A* **1997**, *52*, 655 – 664.
[5] S. Melandri, D. Consalvo, W. Caminati, P. G. Favero, *J. Chem. Phys.* **1999**, *111*, 3874 – 3879.
[6] T. Pedersen, N. W. Larsen, L. Nygaard, *J. Mol. Struct.* **1969**, *4*, 59 – 77.
[7] N. W. Larsen, *J. Mol. Struct.* **1979**, *51*, 175 – 190.
[8] S. J. Martinez, J. C. Alfano, D. H. Levy, *J. Mol. Spectrosc.* **1992**, *152*, 80 – 88.
[9] R. M. Helm, H. P. Vogel, H. J. Neusser, *J. Chem. Phys.* **1998**, *108*, 4496 – 4504.

Table 4. pK_a values, hydrogen bond lengths O_7O_{15} (in pm), hydrogen bond lengths C_6H···O (in pm), and V_2 barriers (in cm^{-1}) to water internal rotation of phenol,[1] *p*-methylphenol,[39] and *p*-cyanophenol for both electronic states. The twofold barrier V_2 is defined in Equation (2).

	p$K_a(S_0)$	$O_7O_{15}(S_0)$	$V_2(S_0)$	C_6H···O[a]	p$K_a(S_1)$	$O_7O_{15}(S_1)$	$V_2(S_1)$
p-methylphenol	10.2	291	149	272	6.5[b]	289	94
phenol	9.86	290	175	270	6	285	109
p-cyanophenol	7.74	283	275	264	3.33	269	183

[a] Calculated MP2 value. [b] Based on the assumption that the similar red shift of the phenol-water and the cresol-water cluster imply similar changes of acidity upon excitation.[18]

[10] C. Ratzer, J. Küpper, D. Spangenberg, M. Schmitt, *Chem. Phys.* **2002**, *283*, 153–169.

[11] U. Dahmen, W. Stahl, H. Dreizler, *Ber. Bunsen-Ges.* **1994**, *98*, 970–974.

[12] J. Casado, L. Nygaard, G. O. Sørensen, *J. Mol. Struct.* **1971**, *8*, 211–224.

[13] R. M. Helm, H.-P. Vogel, H. J. Neusser, *Chem. Phys. Lett.* **1997**, *270*, 285–291.

[14] D. R. Borst, T. M. Korter, D. W. Pratt, *Chem. Phys. Lett.* **2001**, *350*, 485–490.

[15] W. Roth, P. Imhof, K. Kleinermanns, *Phys. Chem. Chem. Phys.* **2001**, *3*, 1806–1812.

[16] J. Küpper, M. Schmitt, K. Kleinermanns, *Phys. Chem. Chem. Phys.* **2002**, *4*, 4634–4639.

[17] S. Schulman, W. Vincent, W. Underberg, *J. Phys. Chem.* **1981**, *85*, 4068–4071.

[18] N. Biswas, S. Wategaonkar, T. Watanabe, T. Ebata, N. Mikami, *Chem. Phys. Lett.* **2004**, *394*, 61–67.

[19] S. Leutwyler, T. Bürgi, M. Schütz, A. Taylor, *Faraday Discuss.* **1994**, *97*, 285–297.

[20] M. Schmitt, J. Küpper, D. Spangenberg, A. Westphal, *Chem. Phys.* **2000**, *254*, 349–361.

[21] Gaussian 98 (Revision A.7), M. J. Frisch, G. W. Trucks, H. B. Schlegel, G. E. Scuseria, M. A. Robb, J. R. Cheeseman, V. G. Zakrzewski, J. A. Montgomery, R. E. Stratmann, J. C. Burant, S. Dapprich, J. M. Millam, A. D. Daniels, K. N. Kudin, M. C. Strain, O. Farkas, J. Tomasi, V. Barone, M. Cossi, R. Cammi, B. Mennucci, C. Pomelli, C. Adamo, S. Clifford, J. Ochterski, G. A. Petersson, P. Y. Ayala, Q. Cui, K. Morokuma, D. K. Malick, A. D. Rabuck, K. Raghavachari, J. B. Foresman, J. Cioslowski, J. V. Ortiz, B. B. Stefanov, G. Liu, A. Liashenko, P. Piskorz, I. Komaromi, R. Gomperts, R. L. Martin, D. J. Fox, T. Keith, M. A. Al-Laham, C. Y. Peng, A. Nanayakkara, C. Gonzalez, M. Challacombe, P. M. W. Gill, B. G. Johnson, W. Chen, M. W. Wong, J. L. Andres, M. Head-Gordon, E. S. Replogle, J. A. Pople, Gaussian, Inc., Pittsburgh, PA, **1998**.

[22] S. F. Boys, F. Bernardi, *Mol. Phys.* **1970**, *19*, 553–566.

[23] R. Bauernschmitt, R. Ahlrichs, *Chem. Phys. Lett.* **1996**, *256*, 454–464.

[24] R. Bauernschmitt, M. Häser, O. Treutler, R. Ahlrichs, *Chem. Phys. Lett.* **1997**, *264*, 573–578.

[25] C. Lee, W. Yang, R. Parr, *Phys. Rev. B* **1988**, *37*, 785–789.

[26] A. D. Becke, *J. Chem. Phys.* **1993**, *98*, 5648–5652.

[27] R. Ahlrichs, M. Bär, H.-P. Baron, "TURBOMOLE (version 5.6)", Universität Karlsruhe, Germany, **2002**.

[28] R. Ahlrichs, M. Bär, M. Häser, H. Horn, C. Kölmel, *Chem. Phys. Lett.* **1989**, *162*, 165–169.

[29] C. Jacoby, M. Schmitt, *ChemPhysChem* **2004**, *5*, 1686–1694.

[30] J. A. Hageman, R. Wehrens, R. de Gelder, W. L. Meerts, L. M. C. Buydens, *J. Chem. Phys.* **2000**, *113*, 7955–7962.

[31] W. L. Meerts, M. Schmitt, G. Groenenboom, *Can. J. Chem.* **2004**, *82*, 804–819.

[32] Y. R. Wu, D. H. Levy, *J. Chem. Phys.* **1989**, *91*, 5278–5284.

[33] W. S. Benedict, N. Gailar, E. K. Plyler, *J. Chem. Phys.* **1956**, *24*, 1139–1165.

[34] W. Gordy, R. L. Cook, *Microwave Molecular Spectra, 3rd ed.*, Wiley, New York, **1984**.

[35] M. Schmitt, C. Jacoby, K. Kleinermanns, *J. Chem. Phys.* **1998**, *108*, 4486–4495.

[36] D. Feller, M. W. Feyereisen, *J. Comput. Chem.* **1993**, *14*, 1027–1035.

[37] A. Jansen, M. Gerhards, *J. Chem. Phys.* **2001**, *115*, 5445–5453.

[38] A. L. Sobolewski, W. Domcke, *J. Phys. Chem. A* **2001**, *105*, 9275–9283.

[39] G. Myszkiewicz, W. L. Meerts, C. Ratzer, M. Schmitt, *J. Chem. Phys.* **2005**, *123*; 44304-1–44304-7.

Kapitel 6

Zusammenfassung

Die im Rahmen dieser Arbeit durchgeführten Messungen sind im weitesten Sinne als Grundlagenforschung zu bezeichnen. Insbesondere sollen anhand der vorgestellten Moleküle Modellfälle spezifischer Wechselwirkungsmechanismen oder funktioneller Gruppen biologisch relevanter makromolekularer Systeme, wie etwa von Proteinen oder der DNS, untersucht werden. Allen vorgestellten Molekülen ist daher gemein, dass sie spezifische Wechselwirkungen oder funktionelle Gruppen aufweisen, die im diesen Systemen relevant für ihre Struktur sind.

Das Meßprinzip der HRLIF - Apparatur beruht darauf, dass die Probenmoleküle bei Expansion mittels eines Trägergases - im vorliegenden Falle Argon - durch eine Düse ins Vakuum stark abgekühlt werden, sodass sie im resultierenden Molekularstrahl eine sehr niedrige Rotations-und Schwingungstemperatur haben. Die Konformerenumwandlung spielt bei der Expansionsabkühlung hingegen nur eine untergeordnete Rolle, sodass eine Aussage über die stabileren vorkommenden Konformeren möglich ist.

Letztlich ist es so möglich, die Rotationskonstanten sowohl für den Grundzustand als auch für den angeregten Zustand der Moleküle zu bestimmen und hieraus ihre Geometrie in beiden Zuständen zu berechnen. Zur automatisierten Auswertung der Spektren dient dabei die Methode der genetischen Algo-

rithmen, die in Zusammenarbeit mit der Gruppe von Professor Leo Meerts aus Nijmegen entwickelt wurden.

Auf diese Weise ist die Messungen vibrostatischer rotationsaufgelöster elektronischer Anregungsspektren von organischen Molekülen und molekularen Systemen bis zu einer Größe von etwa 15 bis 30 Atomen möglich. Darüber hinaus werden aufgrund der steigenden Masse die Rotationskonstanten der molekularen Kreisel so klein, dass die Spektren nicht mehr sinnvoll ausgewertet werden können. Für die Untersuchungen im Rahmen der vorliegende Arbeit wurden drei Modellsysteme ausgewählt , deren Relevanten für die vorliegende Dissertation im Folgenden kurz erläutert werden.

Zum einen ist dies das 1,4-Benzodioxan, das in drei Konformeren, nämlich Twist, Wanne und planarer Form, auftreten kann. Als biologisches Analogon, bzw. Ausgangspunkt der Fragestellung liegt hier das häufig bei beispielsweise enzymatischen Reaktionen zu beobachtende Schlüssel-Schloß-Prinzip zugrunde, bei dem nur eines der möglichen Konformere eine biologische Funktion aufweist. Im Rahmen dieser Arbeit konnte gezeigt werden, daß 1,4-Benzodioxan sowohl im Grund- als auch im angeregten Zustand in der Twist - Form vorliegt. Allerdings ist die Konfiguration im angeregten Zustand aufgrund des anomeren Effektes weniger planar als im Grundzustand. Dies beweist die Zunahme des Betrages des Inertialsdefekts im angeregten Zustand. Die Erklärung hierfür liefert der anormere Effekt. Diese beschreibt einerseits die Wechselwirkung zwischen dem nichtbindenden p-Typ des Sauerstofforbitals am Ring und dem antibindenden Orbital der axialen CH-Bindung($n_O \rightarrow \sigma^*_{C-H_{ax}}$). Durch diese Wechselwirkung ist die $H_{ax} - C$ Bindung länger als die der $H_{eq} - C$ Bindung (1,0936 $\overset{\circ}{A}$ vs 1,0878 $\overset{\circ}{A}$). Andererseits findet hierbei auch eine Wechselwirkung statt zwischen dem ungebundenen Elektronenpaar am Sauerstoffatom und π-Orbital des Benzol-Rings ($n_O \rightarrow \pi_{C_{arom}}$). Wie im Phenol wird bei der Anregung die Elektronendichte vom ungebundenen Elektronenpaar am Sauerstoff zum aromatischen Ring geschoben, sodass der Dioxan-Ring im angeregten Zustand weniger planar ist als im Grundzustand. Bei 1,4-Benzodioxan dominiert die $n_O \rightarrow \pi_{C_{arom}}$ über die $n_O \rightarrow \sigma^*_{C-H_{ax}}$-Wechselwirkung.

Als weiteres Modellsystem für einen wichtigen, in biologisch relevanten Molekülen häufig auftretenden Effekt wurde die Ausbildung von Wasserstoffbrückenbindungen gewählt, und anhand der Bildung von Wasserclustern von 7-Azaindol untersucht, insbesondere der Cluster $7 - Azaindol - (H2O)_1$ und $7 - Azaindol - (H2O)_2$. Indolderivate haben weitverbreitete biologische Funktionen, sei es als funktionelle Gruppe der natürlich vorkommenden Aminosäure Tryptophan oder beispielsweise als Phytohormon Indol-3-essigsäure. Wasserstoffbrücken insbesondere zwischen Wassermolekülen und Aminosäuren treten in Proteinen nicht nur sporadisch auf. Viele Proteine weisen sogenannte strukturelle Wassermoleküle auf, die innerhalb der Tertiärstruktur des Moleküls fest lokalisiert sind. Sowohl im Grundzustand als auch im angeregten Zustand befindet sich das Wasserstoffatom des 7-Azaindol am Stickstoffatom des Pyrrololrings, obwohl es für den angeregten Zustand der Struktur mit dem Wasserstoff am Pyridinoring stabiler ist. Durch die elektronische Anregung nehmen die Säurestärke der NH-Pyrrolic-Gruppe und die Basenstärke des Pyridino-N-Atoms zu. Dieses bewirkt eine Verkürzung der ersten direkten Verbindung zu den Wassermolekülen. Das Spektrum von 7-Azaindol-$(H_2O)_2$ Cluster zeigt eine Aufspaltung in zwei Teilspektren, die 29 469 MHz voneinander entfernt sind. Diese ergeben sich aus der gegenseitigen Umwandlung zwischen den zwei out-of-plane Wasserstoffatomen der Hydrogen-Verbindungen.

Indoldevivate wie das bereits genannte Tryptophan weisen auch im menschlichen und tierischen Körper zahlreiche biochemische Funktionen auf. Beispielhaft hierfür sei auch das Serotonin genannt, das eine wichtige Neurotransmitter darstellt. In diesem Kontext erscheint es interessant zu untersuchen, welche und wie viele stabile Konformere bei dieser und ähnlichen Substanzen zu beobachten sind. Für das Serotonin ist bereits aus Messungen von Zwier et al. [96] bekannt, das 8 stabile Konformere mit sowohl syn- als auch anti-orientierte Hydroxygruppe existieren. Interessanterweise tritt bei Substitution der Hydroxygruppe durch eine Methoxygruppe eine Redukti-

on auf weniger als die Hälfte ein, nämlich auf 3 beobachtbare Konformere. Diese Konformere weisen alle eine anti-ständige Methoxygruppe auf. Eine Erklärung hierfür könnte in der zu kurzen Lebensdauer mancher Konformere liegen, sodass sie nicht mit der hochauflösenden Spektroskopie erfasst werden können. Durch den Vergleich der experimentellen mit der berechneten Rotationskonstanten können für die drei gemessenen Spektren in Bezug auf die Ethyamino-Gruppe wie folgt zugeordnet werden: Gph(up) zum gemessenen Band B; Gpy(out) zum gemessenen Band A und Gpy(up) zum gemessenen Band C. Die Tatsache einer Bevorzugung der *gauche*-Struktur gegenüber der *anti*-Struktur der Ethyamino-Gruppe liegt an der elektrostatischen Wechselwirkung zwischen der Ethyamino-Gruppe und dem Indolring. Sowohl quantenmechanische Rechnungen als auch der Vergleich der experimentell ermittelten Rotationskonstanten weisen die *Anti*-Rotamers der Methoxygruppe als die stabilere Rotamer im Gegensatz zu der Syn-Form auf. Alle gemessenen Spektren des 5-Methoxytryptamins gehören dem L_b- Zustand nach Platts Nomenklatur (HOMO→LUMO) an.

Während der Messungen zu dieser Dissertation wurden darüber hinaus noch weitere Substanzen untersucht, die jedoch hier nur kurz erwähnt werden, weil sie den Rahmen der Arbeit sprengen würden. Die Mitarbeit bei der Durchführung dieser Messungen war jedoch eine wichtige Hilfe bei der Erlangung experimentelle Fertigkeiten im Umgang mit der komplexen Messapparatur. Die sind bespielsweise folgende Moleküle Tryptamin, Benzoesäure-Dimer, Phenol-Argon-Cluster, o-Toluidine und p-Cyanophenol-Wasser-Cluster.

Bei den hochauflösenden Messungen am Tryptamin wurden nach dem Vergleich der experimentellen mit den berechneten Rotationskonstanten sechs verschiedene Konformeren zugeordnet. Die Anlagerung eines Wassermoleküls am Tryptamin bewirkt ein Kollabieren des Konformerenraums. Nur das Gpy(out) Konformer bildet mit Wasser einen Wasser-Cluster. Das Wassermolekül fungiert hierbei als Protondonator für die Amino-Gruppe der Ethylamin-Gruppe am Tryptamin. Die zusätzliche Wechselwirkung zwischen

dem Wassermolekül mit der aromatischen C-H Verbindung verursacht eine selektive Stabilisierung des Konformers Gpy(out) gegenüber alle anderen Konformeren.

Die Strukturen der fünf verschiedenen Isotopologen von Benzoesäure-Dimer und dessen vibronischen Band, die $57 cm^{-1}$ über dem Ursprung liegt und der out-of-plane Schwingung zugeordnet werden, wurden mit Hilfe der HRLIF-Apparatur untersucht. Aufgrund der lokalen Anregung reduziert sich die Symmetrie vom C_{2h} für den Grundzustand zur C_s in den S_1 angeregten Zustand. Das Tunneln der Protonen bewirkt eine Aufspaltung des Energieniveaus in den Grundzustand und in den angeregten Zustand. Diese beträgt für den Grundzustand $\Delta S_0 = 1385.2 \pm 0.7$ MHz und $\Delta S_1 = 271.2 \pm 0.7$ MHz für den angeregten Zustand.

Die strukturellen Untersuchungen am Phenol-Ar_1- und Phenol-Ar_2-Cluster schlussfolgern eine van der Waals Wechselwirkung zwischen dem Argon Atom und dem Phenol-Ring. Beim Phenol-Ar_2-Cluster befinden sich die Argon-Atome auf unterschiedlichen Seiten des Phenylrings. Die IVR (intramolecular vibrational relaxation) ist stärker im Phenol ausgeprägt und bewirkt eine kürzere Lebensdauer des Phenols als die des Phenol-$Argon_{1,2}$-Clusters.

Der $S_0 \rightarrow S_1$ Übergang von o-Toluidine wurde mit Hilfe der rotationsaufgelösten elektronischen Spektroskopie analysiert. Die strukturelle Veränderung der π-Bindung des Benzolrings bewirkt eine Verlängerung der C-C Bindung zwischen der Methylgruppe und dem Benzolring. Dadurch verringert sich die Barriere der internen Rotation der Methylgruppe im angeregten Zustand im Gegensatz zum Grundzustand. Als Beweis der 'freieren' Bewegung der Methylgruppe im angeregten Zustand zeichnet sich eine Erhöhung des Diederwinkels der Methylgruppe mit dem Benzolring auf 7.7°, der im Grundzustand in der Benzolebene liegt.

Die Struktur der Wasserstoffbindung des p-Cyanophenol-Wasser-Clusters wurde mit Hilfe der HRLIF untersucht. Sowohl für den Grundzustand als auch für den angeregten Zustand wurde eine größere Abnahme des O-O Abstandes gefunden als im Phenol-Wasser-Cluster. Die Barriere der internen Rotation des Wassers beträgt 275 cm^{-1} für den Grundzustand und 183 cm^{-1} für den angeregten Zustand. In beiden elektronischen Zuständen zeigt sich eine Korrelation zwischen dem pKs - Wert und dem O-O Abstand bzw. der Barriere der internen Rotation.

Anhang A

Anhang

A.1 Die quantenmechanische Näherungen des freien Moleküls

Die Gesamtenergie E lässt sich durch die Schrödinger-Gleichung beschreiben als:

$$\widehat{\mathbf{H}}\Psi = E\Psi \qquad (A.1)$$

mit dem Hamiltonoperator $\widehat{\mathbf{H}}$:

$$\widehat{\mathbf{H}} = T + V = -\frac{\hbar^2}{2m}\sum_{i=1}^{N}\Delta_i^2 - \frac{\hbar^2}{2m}\sum_{k=1}^{K}\Delta_k^2 + V_{KK} + V_{Ke} + V_{ee}. \qquad (A.2)$$

Die ersten zwei Summanden beschreiben die kinetische Energie aller Elektronen bzw. aller Kerne. Die potenzielle Energie V setzt sich aus der Summe der Kernabstoßungen V_{KK}, der Elektron-Kern-Anziehungen V_{Ke} und der Elektron-Elektron-Abstoßungen V_{ee} zusammen.

Aufgrund der sehr unterschiedlichen Masse der Elektronen und der Kerne, folgt die Elektronenladung ,*momentan*' der langsamen Kernbewegung. Zu jeder Kernkonfiguration R gehört eine Elektronenverteilung $\Psi_n^{el}(\vec{q}_e\vec{q}_n)$ des elek-

tronischen Zustands n, der nur von der Positionen der Kerne abhängig ist. Ändern sich die Kernpositionen bei der Schwingung, folgt die Elektronenladung dieser *adiabatisch*. Unter dieser Annahme heißt das Modell dementsprechend die *adiabatische* Näherung.

Man addiert die Kernbewegungsenergie (2.Summand der Gleichung A.2) als Störung zu dem ungestörten System des starren Kerngerüstes:

$$\widehat{H} = \widehat{H}_0 + \widehat{H}'. \tag{A.3}$$

$\widehat{H}_0$ stellt den Hamiltonian für die ungestörte Schrödinger Gleichung dar, die die elektrische Energie bei einem starren Kerngerüst wiedergibt:

$$\widehat{H}_0 \psi^{el}(\vec{q}_e \vec{q}_n) = (\widehat{T}_e + V)\psi^{el}(\vec{q}_e \vec{q}_n) = E_{el}(\vec{q}_n)\psi^{el}(\vec{q}_e \vec{q}_n). \tag{A.4}$$

$\psi^{el}(\vec{q}_e \vec{q}_n)$ ist so zu verstehen, dass sie Elektronenwellenfunktionen nur von den Elektronenkoordinaten $\vec{q}_e$ als Variable abhängen. Die $\vec{q}_n$ gehen lediglich als Parameter in die Elektronenfunktion ein.

Die Funktionen ψ^{el} wählen wir so, dass sie ein orthonormales Koordinatensystem bilden. Dadurch lässt sich die Gesamtwellenfunktion durch die lineare Kombination von ψ^{el} ermitteln:

$$\Psi = \sum_m \chi_m(\vec{q}_n)\psi_m^{el}(\vec{q}_e \vec{q}_n). \tag{A.5}$$

χ_m stellen hierbei die Entwicklungskoeffizienten dar, die nur noch von den Kernkoordinaten $\vec{q}_n$ abhängen.

Setzen wir Ψ in die Gleichung A.1 ein, multiplizieren die mit ψ_n^e und integrieren über die Elektronenkoordinaten ergibt sich:

$$\left[\int \psi_n^{*el}(\vec{q}_e \vec{q}_n)(\widehat{H} - E) \sum_m \chi_m \psi_m^{el}(\vec{q}_e \vec{q}_n) \right] dr = 0. \tag{A.6}$$

mit $\widehat{H}_0 + \widehat{H}'$ (Gl.7.3) und der Definition der Kronecker-delta δ_{mn} für orthogonale Systeme:

$$\int \psi_n^* \psi_m dr = \delta_m n \begin{cases} 0 & \text{für} m \neq n \\ 1 & \text{für} m = n \end{cases} \qquad (A.7)$$

wird aus der Gleichung A.6:

$$(E_{el} - E)\chi_n(\vec{q}_n) + \left[\int \psi_n^{*el}(\vec{q}_e\vec{q}_n)H' \sum_m \chi_n(\vec{q}_n)\psi_m^{el}(\vec{q}_e\vec{q}_n)\right] = 0 \qquad (A.8)$$

Der 2.Summand der Gleichung A.8 lässt sich wie folgt umschreiben[35]:

$$\int \psi_n^{*el}(\vec{q}_e\vec{q}_n) \left(H' \sum_m \chi_m(\vec{q}_n) \cdot \psi_m^{el}(\vec{q}_e\vec{q}_n)\right) dr \qquad (A.9)$$

$$= \left[\int \psi_n^{*el}(\vec{q}_e\vec{q}_n) \sum_m (H'\chi_m(\vec{q}_n))\psi_m^{el}(\vec{q}_e\vec{q}_n)\right] dr$$

$$+ \left[\int \psi_n^{*el}(\vec{q}_e\vec{q}_n) \sum_m (H'\psi_m^{el}(\vec{q}_e\vec{q}_n))\chi_m(\vec{q}_n)\right] dr$$

$$-\frac{\hbar^2}{2} \int \psi_n^{*el}(\vec{q}_e\vec{q}_n) \left[\sum_k \frac{1}{M_k} \sum_m \frac{\partial}{\partial R_k}\psi_m^{el}(\vec{q}_e\vec{q}_n)\frac{\partial}{\partial R_k}\chi_m(\vec{q}_n)\right] dr.$$

Da die $\mathbf{H}'$ nur von den Kernkoordinaten $\vec{q}_n$ abhängt, die Integration aber über Elektronenkoordinaten $\vec{q}_e$ geht, kann man unter Berücksichtigung des Kronecker-Delta (Gleichung A.7) den 1. Summand der Gleichung A.10 wie folgt zusammenfassen:

$$\left[\int \psi_n^{*el}(\vec{q}_e\vec{q}_n) \sum_m (H'\chi_n(\vec{q}_n))\psi_m^{el}(\vec{q}_e\vec{q}_n)\right] dr = H'\chi_n(\vec{q}_n). \qquad (A.10)$$

Bei der Einführung eines neuen Parameters c_{nm}:

$$c_{nm} = + \left[\int \psi_n^{*el}(\vec{q}_e\vec{q}_n) H' \psi_m^{el}(\vec{q}_e\vec{q}_n) \right] dr \qquad \text{(A.11)}$$

$$-\frac{\hbar^2}{2} \left[\int \psi_n^{*el}(\vec{q}_e\vec{q}_n) \sum_k \frac{1}{M_k} \frac{\partial}{\partial R_k} \psi_m^{el}(\vec{q}_e\vec{q}_n) dr \right] \frac{\partial}{\partial R_k}.$$

erhalten wir für den 2. und den 3. Summand der Gleichung A.10:

$$\left[\int \psi_n^{*el}(\vec{q}_e\vec{q}_n) \sum_m (H' \psi_m^{el}(\vec{q}_e\vec{q}_n)) \chi_m(\vec{q}_n) \right] dr \qquad \text{(A.12)}$$

$$-\frac{\hbar^2}{2} \int \psi_n^{*el}(\vec{q}_e\vec{q}_n) \left[\sum_k \frac{1}{M_k} \sum_m \frac{\partial}{\partial R_k} \psi_m^{el}(\vec{q}_e\vec{q}_n) \frac{\partial}{\partial R_k} \chi_m(\vec{q}_n) \right] dr.$$

$$= \sum_m c_{nm} \chi_m(\vec{q}_n).$$

Durch das Einsetzen der Gleichung A.10 und der Gleichung A.13 in die Gleichung A.8 ergibt sich die Gleichung A.13:

$$\widehat{H}' \chi_n(\vec{q}_n) + \sum_m c_{nm} \chi_m(\vec{q}_n) = (E - E_{el}) \chi_n(\vec{q}_n). \qquad \text{(A.13)}$$

Ohne den Summenterm stellt die Gleichung A.13 analog zu der Gleichung 7.4 die Schrödingergleichung der Kernwellenfunktion $\chi_n(\vec{q}_n)$ dar. Man erhält somit zwei miteinander gekoppelte Gleichungen:

$$\widehat{H}_0 \psi^{el} = (T_e + V) \psi^{el} = E_{el} \psi^{el} \qquad \text{(A.14)}$$

$$\widehat{H}' \chi_n(\vec{q}_n) + \sum_m c_{nm} \chi_m(\vec{q}_n) = (E_{el} - E) \chi_n(\vec{q}_n). \qquad \text{(A.15)}$$

c_{nm} nennen sich dabei Kopplungsmatrixelemente, die angeben, wie sich die verschiedenen elektronischen Zustände ψ_n^{el}, ψ_m^{el} durch die Kernbewegung miteinander koppeln.

A.1.1 Die Born-Oppenheimer Näherung

Bei der Born-Oppenheimer Näherung werden sämtliche Kopplungsmatrixelemente c_{nm} gleich Null gesetzt. Dadurch entstehen zwei völlig entkoppelte Gleichungen für die Elektronenwellenfunktionen und die Kernwellenfunktionen:

$$\widehat{H}_0 \psi^{el} = (T_e + V)\psi^{el} = E_{el}\psi^{el} \tag{A.16}$$

$$(\widehat{H}' + E_{el})\chi_n(\vec{q}_n) = E\chi_n(\vec{q}_n). \tag{A.17}$$

Als Lösung der beiden Gleichungen A.16 und A.17 erhält man die Elektronenwellenfunktionen ψ_{el} bei einen festen Kernkoordinate und die Kernwellenfunktionen χ_n im n-ten elektronischen Zustand.

A.1.2 Die adiabatische Näherung

Stellt die Elektronenhülle nicht 'momentan' sondern 'zeitverzögert' eine Kernbewegung ein, d.h. die Kerne merken ein Potenzial von der Elektronenkonfiguration, die zur Kernfiguration $\vec{q}_n(t - \Delta t)$ gehören würde, spricht man von der *adiabatischen* Näherung [35]. Hierbei bleibt das Molekül auf derselben Potentialfläche und die einzelnen elektronischen Wellenfunktionen werden nicht durch die Kernbewegungen miteinander gemischt.

Mathematisch bedeutet das eine Betrachtung der Diagonalelemente c_{nn} und eine Vernachlässigung der Nicht-Diagonalelementen c_{nm} der Kopplungsmatrix der Gleichung A.12:

$$c_{nn} = \left[\int \psi_n^{*el} H' \psi_m^{el} \right] dr - \frac{\hbar^2}{2}\left[\int \psi_n^{*el} \sum_k \frac{1}{M_k}\frac{\partial}{\partial R_k}\psi_n^{el} dr \right]\frac{\partial}{\partial R_k}. \tag{A.18}$$

Der 2. Term der Gleichung A.18 kann wie folgt umgeschrieben werden:

$$-\frac{\hbar^2}{2}\left[\int \psi_n^{*el} \sum_k \frac{1}{M_k}\frac{\partial}{\partial R_k}\psi_n^{el} dr \right]\frac{\partial}{\partial R_k} = -\frac{\hbar^2}{2}\left[\int \psi_n^{*el} \hat{A} \psi_n^{el} dr \right]\frac{\partial}{\partial R_k}. \tag{A.19}$$

Wie man aus der Gleichung A.19 erkennen kann, stellt $\int \psi_n^{*el} \hat{A} \psi_n^{el}$ einen Erwartungswert dar, der eine Konstante ist. Da die Ableitung nach einer Konstante Null ergibt, verschwindet der 2. Summand der Gleichung A.18. Nun betrachten wir den ersten Term der Gleichung A.18.

Der Hamilton-Operator der kinetischen Energie der Kernbewegungen definiert sich über das Korrespondenzprinzip als:

$$\widehat{H}' = -\frac{\hbar^2}{2M_k} \sum \frac{\partial^2}{\partial R_K^2}.$$
(A.20)

Das Einsetzen dieser Hamiltonian (Gleichung A.20) unter Eliminierung des 2. Summands ergibt sich für die Gleichung A.18:

$$c_{nn} = \left[\int \psi_n^{*el} \widehat{H}' \psi_m^{el} \right] dr = \sum_K \frac{\hbar^2}{2M_k} \int \left(\frac{\partial \psi_n^{*el}}{\partial R_k} \right)^2 dr.$$
(A.21)

Bei der Veränderung der Kernkoordinaten hängen die Diagonalelemente quadratisch von der Änderung der Elektronenwellenfunktion ψ_n^{*el} ab. Aufgrund der großen Kernmasse M_k ist der Wert für c_{nn} jedoch klein.

Die adiabatische Näherung enthält einen Korrekturterm, der von der Kernmasse abhängig ist. Für unterschiedliche Isotopomeren verschiebt sich die elektronische Energie zu verschiedenen Werten. Dieser Effekt für den elektronischen Zustand ist jedoch klein gegenüber dem Isotopeneffekt bei der Schwingung und bei der Rotation.

A.1.3 Der Abbruch der adiabatischen Näherung

Bei den elektronisch angeregten Zuständen kommt es häufig vor, dass die Potenzialfläche der Zustände $|m\rangle$ und $|n\rangle$ sich nahe kommen oder sogar kreuzen. Hierbei mischen sich die verschiedenen elektronischen Zustände $|m\rangle$ und $|n\rangle$. Die adiabatische Näherung bricht zusammen, was in der Störungsrechnung beschrieben als:

$$H = H_0 + \lambda W,$$
(A.22)

Wobei $\lambda < 1$ ist und das Ausmaß der Störung darstellt. λ ist mit dem Verhältnis der Elektronen-(m) und der Kernmasse (M) wie folgt verbunden: $\left(\lambda = \frac{m}{M}\frac{1}{4}\right)$.

Bis zur 2.Ordung berechnet sich die elektronische Energie:

$$E_n^s = E_n + W_{nn} + \sum_{k \neq n} \frac{W_{kn}W_{nk}}{E_n - E_k}. \tag{A.23}$$

mit $W_{kn} = \int \psi_n^{*el} \widehat{H}' \psi_k^{el}$.

Der 1. Summand der Gleichung A.23 gibt die Energie nach der BO-Näherung wieder.

Die adiabatische Korrektur mit $W_{nn} = c_{nn}$ im zweiten Term der Gleichung A.23 rechnet zu der BO- Energie die zeitliche Verzögerung der Einstellung der Elektronenwellenfunktion auf die Kernbewegung. Der letzter Term der Gleichung A.23 charakterisiert zudem die Korrelation zwischen der Elektronenwellenfunktionen ψ_n^{el} und ψ_k^{el}.

Verwendete mathematische Symbole

A	Fläche
a, b, c	Hauptträgheitsachsen des Molekülkoordinatensystems
A, B, C	Rotationskonstanten bzgl. der Hauptträgheitsachsen
A_{nm}	Einsteinkoeffizient der spontanen Emission beim Übergang von m nach n
b	Druckverbreiterungskonstante
B_e	Rotationskonstante der r_e -Struktur
B_v	Rotationskonstante der r_v -Struktur
B_0	Rotationskonstante der r_0 -Struktur
B_α	Rotationskonstante bezüglich der Achse $\alpha = x, y, z$
$B_\alpha^{(A)}$	Rotationskonstante des A-reduzierten Hamiltonians
$B_\alpha^{(S)}$	Rotationskonstante des S-reduzierten Hamiltonians
c	Lichtgeschwindigkeit
C_{fg}	Kostenfunktion
d	1. Dicke
	2. Durchmesser

$\vec{d_n}$	Vektor zur Beschreibung der Abweichung einer Gleichgewichtsreferenzstruktur
$D_J, D_{JK}, D_K,$	Zentrifugalverzerrungsparameter
$d1, d2, R_5 R_6$	
e	Eulersche Zahl
$e_{i,j,k}$	Permutationssymbol
E	Energie
E^n	Elektrische Feldstärke
f	1. Brennweite
	2. Kraftkonstante
	3. experimentelles Spektrum
F	1. Platzhalter für eine raumfeste Achse F= X,Y,Z
	2. Torsionskonstante
F^*	Finesse
F_{fg}	Fitnessfunktion
g	1. Entartungsgrad
	2. berechnetes Spektrum
G	Gausfunktion
$\vec{g_n}$	Vektor für die Gleichgewichtsreferenzstruktur
h	Plancksches Wirkungsquantum
$\hbar$	$h/2\pi$
$\widehat{H}$	Hamiltonoperator
i	$\sqrt{-1}$
I	1. Intensität
	2. Kernspin

	3. Übergangsintensität
$\mathbf{I}$	Trägheitstensor
I_{tor}	Trägheitsmoment des internen Rotors bezüglich seiner Symmetrieachse
I_{α}	Hauptträgheitsmoment bezüglich der molekülfesten Achse $\alpha = x, y, z$
$I_{\alpha\alpha}$	Trägheitsmoment mit $\alpha = x, y, z$
$I_{\alpha\beta}$	Trägheitsprodukte mit $\alpha = x, y, z$ und $\alpha \neq \beta$
J	Quantenzahl für den Betrag des Drehimpulses
$\hat{J}$	Drehimpulsoperator
$\hat{J}_F$	Drehimpulsoperator bzgl. eines raumfesten Achse $F = X, Y, Z$
$\hat{J}+, \hat{J}_-, \hat{J}^+, \hat{J}^-$	Shiftoperatoren
$\hat{J}_{alpha}$	Drehimpulsoperator bzgl. einer molekülfesten Achse $\alpha = x, y, z$
k_b	Boltzmannkonstante
K	Quantenzahl für die c-Komponente des Drehimpulses
K_a, K_c	Betrag von K für den prolaten und oblaten Grenzfall
L	1. Länge
	3. Lorentzfunktion
m	Masse
M	1. Dipolmoment
	2. Quantenzahl fur die z-Komponente des Drehimpulses
n	Brechungsindex
N	Besetzungszahl
$n_{antisym}$	Anzahl der antisymmetrischen Kernspinfunktionen

N_{JM}	Normierungsfaktor der symmetrischen Rotationswellenfunktion
n_{sym}	Anzahl der symmetrischen Kernspinfunktionen
p	1. Druck
	2. Impuls
P	1. Dielektrische Polarisation
	2. Leistung
q	Ladung
$\vec{q}$	Ortsvektor
r	1. Bindungslänge
	2. Distanz zum Molekülschwerpunkt
R	1. Ein Rotationsparameter
	2. Satz der Rotationsquantenzahlen
$\vec{R}$	Abstandsvektor eines molekülfesten und raumfesten Achsensystems
r_e	Gleichgewichtsbindungslänge
r_s	Substitutions-Bindungslänge nach Kraitchman
r_0	effektive Bindungslänge für den Schwingungsgrundzustand
$\vec{r_{00}}$	Distanz zwischen den Ursprüngen zweier Koordinatensysteme
r_α	Abstand zu einer Trägheitsachse $\alpha = x, y, z$
r_v	effektive Bindungslänge für den Schwingungszustand v
s	Weg
S	Linienstärkefaktor
s_k	Verbreiterungsfunktion

t	Zeit
T_1	1. absolute Temperatur
	2. kinetische Energie
	3. Transmission
$\mathbf{T}$	Transformationsmatrix
$T_{\alpha\alpha}, T_{\alpha\beta}$	effektive Zentrifugalverzerrungsparameter
$\hat{U}$	unitärer Operator
U_J	Wangmatrix
v	Geschwindigkeit
V	1. Potentielle Energie
	2. Voigtfunktion
w	Wichtungsfaktor
x, y, z	Achsen des raumfesten Koordinatensystems
$\Gamma(\ldots)$	irreduzible Darstellung von ...
Δ	Laplace-Operator
ΔE	Energiedifferenz
ΔI	Trägheitsdefekt
Δt	Zeitdifferenz
ϵ_0	elektrische Feldkonstante des Vakuums
θ, φ, χ	Eulersche Winkel
Θ_{JM}, Φ_M, X	Rotationswellenfunktionen
κ	Asymmetrieparameter nach Ray
λ	Wellenlänge
μ	1. Mittelwert
	2. reduzierte Masse

	3. Übergangsdipolmoment
$\mu_{\alpha\beta}$	inverser Trägheitstensor
v	Frequenz
μ_0	Übergangsfrequenz
π	Kreiszahl
τ	Lebensdauer
$\tau_{\alpha\beta\gamma\delta}$	Zentrifugalverzerrungsparameter
σ	Standardabweichung
υ	Schwingungszustand
ϕ	Richtungskosinus
χ	Suszeptibilität
ψ	Wellenfunktion
Ψ	Gesamtwellenfunktion
ω	Winkelgeschwindigkeit bzw. Kreisfrequenz
∇	Nabla-Operator

Abkürzungen

app	AntiPeriPlanen
BBO	BariumBOrat
BM	Bending Mirror
BS	Beam Shifter
BW	Brewster Window
C	Kohlenstoff
CL	Cylindrical Lens
CMA-ES	Covariance Matrix Adaptation Evolution Strategy
DR	Derandomized
ES	Evolutionäre Strategie
FC	Fiber Coupler
FD	Fundamental Detector
FPI	Fabry-Perot-Interferometer
FR	Fresnel Phomb
FSR	Free Spectral Range
FWHM	Full Width at Half Maximum
GA	Genetische Algorithmen

Gph	Aminogruppe ist in Gauche-Stellung bezüglich der Pyrrolo-Gruppe des Indolsrings
Gpy	Aminogruppe ist in Gauche-Stellung bezüglich der Phenyl-Gruppe des Indolsrings
H	Wasserstoff
H_{ax}	Axiales Wasserstoffatom
H_{eq}	Equatoriales Wasserstoffatom
HD	Harmonic Detector
HRLIF	High Resolution Laser Induced Fluorescence
IR	Infrared
KDP	KaliumDihydrogenPhosphat
L	Lense
LiNbO3	Lithiumniobat
N	Stickstoff
Nd-YAG	Neodym-dotierter Yttrium-Aluminium-Granat
NMR	Nuclear Magnetic Resonance
O	Sauerstoff
OF	Optical Fiber
out	Das ungebundene Elektronenpaar der Aminogruppe bildet einem Winkel von 60° mit dem Indolring
P	Prism
PD	Photodiode
PE	Prism Expander
PM	Phase Modulator
PMA	Phase Modulator Assembly
PZT	PieZoelectric Transducer

RB	Resonator Block
RP	Retardation Plate
S	Schwefel
sc	SynClinal
up	Das ungebundene Elektronenpaar der Aminogruppe bildet einem Winkel von 180° mit dem Indolring
UV	UltraViolett

Abbildungsverzeichnis

Tabellenverzeichnis

Literaturverzeichnis

[1] Ahlrichs, R.; Bär, M.; Baron, H.-P.: Turbomole (version 5.7), *Universität Karlsruhe*, Germany, **2002**)

[2] Ahlrichs, R.; Bär, M.; Häser, M.; Horn, H.; Kölmel, C.: *Chem. Phys. Lett.v162* (**1989**), 165-169

[3] Albinsson, B.; Nordén, B.: *J. Phys. Chem. 96* (**1992**), 6204

[4] Allen, H.C.; Cross, P.C.: Molecular Vib-Rotors, *John Wiley & Sons*, New York (**1963**)

[5] Anderson, J. B.: Molecular Beams and Low Density Gasdynamics, *Marcel Decker*, New York (**1974**)

[6] Andersson, K.; Barysz, M.; Bernhardsson, A.; Blomberg, M. R. A.; Cooper, D. L.; Fülscher, M. P.; de Graaf, C.; Hess, B. A.; Karlström, G.; Lindh, R.; Malmqvist, P.-A.; Nakajima, T.; Neogrády, P.; Olsen, J.; Roos, B. O.; Schimmelpfennig, B.; Schütz, M.; Seijo, L.; Serrano-Andrés, L.; Siegbahn, P. E. M.; Stalring, J.; Thorsteinsson, T.; Veryazov, V.; Widmark, P.-O. Molcas Version 5.4, *Lund University*, Sweden (**2002**)

[7] Bayari, S.; Ide S., *Spectrochim. Acta 98* (**2003**), A59, 1255

[8] Becke, A. D.: *J. Chem. Phys. 98* (**1993**), 1372

[9] Becke, A. D.: *J. Chem. Phys. 98* (**1993**), 5648-5652

[10] Berden, G.; Meerts, W. L.; Schmitt, M.; Kleinermanns, K.: *J. Chem. Phys. 104* (**1996**), 972-982

[11] Berden, G.; Meerts, W. Leo: Department of Molecular and Laser Physics, University of Nijmegen, Toernooiveld (**1995**)

[12] Berden, G.; Meerts. W. L.; Jalviste, E.: *J. Chem. Phys. 103* (**1995**), 9596-9606

[13] Bernath, P.F.: Spectra of Atoms and Molecules, *Oxford University Press, New York* (**1995**)

[14] Böhm, M.: Mikrowellen-Ultraviolett-Doppelresonanzspektroskopie an Benzonitril, *Heinrich-Heine-Universität Düsseldorf, Institut für Physikalische Chemie, Diplomarbeit*(**2003**)

[15] Böhm, M.: Rotationsaufgelöste elektronische Spektroskopie an flexiblen Molekülen und Molekülkomplexen, *Heinrich-Heine-Universität Düsseldorf, Institut für Physikalische Chemie, Dissertatio*n (**2010**)

[16] Böhm, M.; Brause, R.; Jacoby, C.; Schmitt, M.: *J. Phys. Chem. A 113* (**2009**), 448-455.

[17] Böhm, M.; Ratzer, C.; Schmitt, M.: *J. Mol. Struc. 800* (**2006**) 55

[18] Böhm, M.; Tatchen, J., Krügler, D.; Kleinermanns, K; Nix, M. G. D.; LeGreve, T. A., Zwier, T. S.; Schmitt, M.: *J. Phys. Chem. A 113* (**2009**) 2456

[19] Brandt, C.: Einfluss der Solvatation auf Lage und Natur der elektronisch angeregten Zustände von Tryptophananalogen, H*einrich-Heine-Universität Düsseldorf, Institut für Physikalische Chemie, Diplomarbeit* (**2008**)

[20] Brause, R.; Krügler, D.; Schmitt, M.; Kleinermanns, K.; Nakajima A.; Miller T. A.: *J. Chem. Phys. 123* (**2005**), 224311

[21] Brause, R.; Schmitt, M.; Spangenberg, D.; Kleinermanns, K.: *Mol. Phys. 102* (**2004**), 1615

[22] Buydens, L C.: M., *J. Chem. Phys. 113* (**2000**), 7955-7962

[23] Caminati, W.: *Phys. Chem. Chem. Phys. 6* (**2004**), 2806-2809

[24] Caminati, W.; Moreschini, P; Rossi, I.; Favero, P.G: *J. Am. Chem.Soc. 120* (**1998**)

[25] Carney, J. R.; Zwier, T. S.: *J. Phys. Chem. A104* (**2000**), 8677

[26] Carney, J. R.; Zwier, T. S.: *J. Phys. Chem. A 103* (**1999**), 9943-9957

[27] Catalán, J.; Paz, J. L. G.; de Paz, J. L. G: *J. Chem. Phys. 122* (**2005**), 244320

[28] Catalán, J.; Pérez, P.; del Valle, J. C.; de Paz, J. L. G.; Kasha M.: *Proc. Natl. Acad. Sci. U.S.A. 99* (**2002**), 5799

[29] Choo, J.; Yoo, S.; Moon, S.; Kwon, Y.; Chung, H.: *Vib. Spect. 17* (**1998**), 173

[30] Clarkson, J. R.; Dian, B. C.; Moriggi, L.; DeFusco, A.; McCarthy, V.; Jordan, K. D.; Zwier, T. S.: *J. Chem. Phys. 122* (**2005**), 214311-1-214311-15

[31] *Coherent Ring-Dye 899-21, User Guide*

[32] Costain, C.C.: Determination of Molecular Structures from Ground State Rotational Constants, *J. Chem. Phys. 29* (**1958**), 864

[33] Darwin, C.: The origin of species, *Oxford University Press*, (**1998**)

[34] Deglmann, P.; Furche, F.; Ahlrichs, R.: *Chem. Phys. Lett. 362* (**2002**), 511-518

[35] Demtröder, W.: Molekülphysik, *Oldenbourg Verlag*, München (**2003**)

[36] Demtröder: Laserspektroskopie, 4.Auflage, korrigierter Nachdruck, *Springer-Verlag*, Berlin Heidelberg New York (**2004**)

[37] Dian, B. C.; Clarkson, J.; Zwier, T. S.: *Science 303* (**2004**), 1169-1173

[38] Dobryakov S. N., Lebedev Y. S., Analysis of spectral lines whose profile is described by a composition of Gaussian and Lorentz profiles, textitSov. Phys. Doklady 13 (**1969**), 873

[39] Drewer, R.; Hall, J.; Kowalski, F.; Hough, J.; Ford, G.; Munley, A.; Ward, H.: Laser phase and frequency stabilization using an optical resonator, *Appl. Phys. B: Laser Opt. 31* (**1983**), 97

[40] Duschinsky F.: *Acta Physicochimica U.R.S.S. 7* (**1937**), 551

[41] Epiotis N. D.; Cherry W. R.; Shaik S.; Yates R. L.; Bernardi F.: Topic in Current Chemistry: Structural Theory of Organic Chemistry; *Springer Verlag*; Berlin, *Vol 70* (**1977**)

[42] Felder, P.; Günthard, H. H.: Conformational interconversions in supersonic jets: matrix IR spectroscopy and model calculations, *Chem. Phys. 71* (**1982**), 9

[43] Fließbach, T.: Elektrodynamik, *Spektrum Akademischer Verlag; Heideberg* (**2008**)

[44] Florio, G. M.; Christie, R. A.; Jordan ,K. D.; Zwier, T. S.: *J. Am. Chem. Soc. 124* (**2002**), 0236-10247

[45] Föllinger, O.: Laplace-, Fourier- und z-Transformation, 8. Aufl., *Hüthig Verlag,* Heidelberg (**2003**)

[46] Folmer, D. E.; Wisniewski, E. S.; Stairs, J. R.; Castleman, J. A. W.: *J. Phys. Chem. A 104* (**2000**), 10545

[47] Freeman, F.; Lee, C.; Hehre, W. J.; Po, H. N.: *J. Comput. Chem. 18* (**1997**), 1392

[48] Frisch, M. J.; Trucks, G. W.; Schlegel, H. B.; Scuseria, G. E.; Robb, M. A.; Cheeseman, J. R.; Zakrzewski, V. G.; Montgomery Jr., J. A.; Stratmann, R. E.; Burant, J. C.; Dapprich, S.; Millam, J. M.; Daniels, A. D.; Kudin, K. N.; Strain, M. C.; Farkas, O.; Tomasi, J.; Barone, V.; Cossi, M.; Cammi, R.; Mennucci, B.; Pomelli, C.; Adamo, C.; Clifford, S.; Ochterski, J.; Petersson, G. A.; Ayala, P. Y.; Cui, Q.; Morokuma,

K.; Salvador, P.; Dannenberg, J. J.; Malick, D. K.; Rabuck, A. D.; Raghavachari, K.; Foresman, J. B.; Cioslowski, J.; Ortiz, J. V.; Baboul, A. G.; Stefanov, B. B.; Liu, G.; Liashenko, A.; Piskorz, P.; Komaromi, I.; Gomperts, R.; Martin, R. L.; Fox, D. J.; Keith, T.; Al-Laham, M. A.; Peng, C. Y.; Nanayakkara, A.; Challacombe, M.; Gill, P. M. W.; Johnson, B.; Chen, W.; Wong, M. W.; Andres, J.; Gonzalez, C.; Head-Gordon, M.; Replogle, E. S.; Pople, J. A.: *GAUSSIAN 98*, revision a.11,

[49] Fuke, K.; Yoshiuchi, H.; Kaya, K.; Achiba, Y.; Sato, K. and Kimura, K.: *J. Phys. Chem. 88* (1984), 584 GAUSSIAN, Inc., Pittsburgh, PA (**2001**)

[50] Gerhards, M.; Schmitt, M.; Kleinermanns, K.; Stahl, W.: *J. Chem. Phys. 104* (**1996**), 967-971

[51] Gerstenkorn, S. ; Luc, P.: Atlas du Spectre d'Absorption de la Molécule d'Iode, *CNRS*, Paris (**1982**)

[52] Gerstenkorn, S.; Luc, P.: Atlas du Spectre d'Absorption de la Molécule d'Iode 14 800-20 000 cm-1, *CNRS*, Paris (**1986**)

[53] Glendening, E. D.; Reed, A. E.; Carpenter, J. E.; Weinhold, F.: *Nbo version 3.1*

[54] Godfrey, P. D.; Brown, R. D.: *J. Am. Chem. Soc.120* (**1998**), 10724

[55] Godfrey, P. D.; Brown, R. D.; Rogers, F. M. The missing conformers of glycine and alanine: relaxation in seeded supersonic jets, *J. Mol. Struct. 376* (**1996**), 65

[56] Goldberg, D. E.: Genetic Algorithms in search, optimisation and machine learning, Addison-Wesley, *Reading MA* (**1989**)

[57] Gordon, R. D.; Hollas, *J. M.: J. Chem. Phys. 99* (**1993**), 3380

[58] Gordon, R. D.; Hollas, *J. M.: J. Mol. Spec. 156* (**1992**), 415

[59] Gordon, R. D.; Hollas, *J. M.: J. Mol. Spec. 163* (**1994**), 159

[60] Gordon, R. D.; Hollas, *J. M.: J. Mol. Struct. 293* (**1993**), 193

[61] Gordy, W.; Cook, R. L.: Microwave Molecular Spectra, 3. ed, *Wiley, New York* (**1984**)

[62] Grimme, S.: *J. Comput. Chem. 25 (2007)*, 1463-1473

[63] Grimme, S.: *J. Comput. Chem. 27* (**2006**), 1787-1799

[64] Grimme, S.; Waletzke M.: *J. Chem. Phys. 111* (**1999**), 5645

[65] Hageman, J. A.; Wehrens, R.; de Gelder, R.; Meerts, W. L.; Buydens, L. M. C.: Direct determination of molecular constants from rovibronic spectra with genetic algorithms, *J. Chem. Phys. 113* (**2000**), 7955-7962

[66] Hansen, N.; Ostermeier, A.: *Evolutionary Computation 9* (*2001*), 159

[67] Hara, A.; Sakota, K.; Nakagaki, M.; Sekiya, H.: *Chem. Phys. Lett. 407* (**2005**), 30

[68] Hättig, C.: *J. Chem. Phys. 118* (**2002**), 7751

[69] Hättig, C.; Köhn, A.: *J. Chem. Phys. 117* (**2002**), 6939

[70] Hättig, C.; Weigend, F.: *J. Chem. Phys. 113* (**2000**), 5154

[71] Heitler, W.: The Quantum Theory of Radiation, *Oxford University Press* (**1954**)

[72] Held, A.; Champagne, B. B.; Pratt, D. W.: Inertial axis reorientation in the $S_1 \leftarrow ? S_0$ electronic transition of 2-pyridone. A rotational Duschinsky effect. Structural and dynamical consequences, *J. Chem. Phys. 95* (**1991**), 8732

[73] Hollas, J. M.: High Resolution Spectroscopy, 2. Aufl., *John Wiley & Sons*, Chichester New York Weinheim Brisbane Singapore Toronto (**1998**)

[74] Horn, H.; Weiss, H.; Häser, M.; Ehrig, M.; Ahlrichs, R.: *J. Comput. Chem. 12* (**1991**), 1058

[75] Hougen, J. T.; Watson, J. K. G.: Anomalous rotational line intensities in electronic transitions of polyatomic molecules:axis-switching, *Can. J. Phys. 43* (**1965**), 298

[76] HP 83711A/12A and 83711B/12B sythesized *CW Generators*, User Guide

[77] *http://www-public.z.uni-duesseldorf.de/mschmitt/Gaussian_logs.html*

[78] Huang, Y.; Arnold, S.; Sulkes, *M.: J. Phys. Chem. 100(**1996**)*, 4734

[79] Imhof, P.; Krügler, D.; Kleinermanns, K. B. R.: Geometry change of simple aromatics upon electronic excitation obtained from Franck-Condon fits of dispersed fluorescence spectra, *J. Chem. Phys. 121* (**1999**), 2598-2610

[80] Jacoby, C.; Roth, W.; Schmitt, M.: *Appl. Phys. B 71* (**2000**), 643

[81] Jacoby, C.; Schmitt, M.: *Chem. Phys. Chem. 5* (**2004**), 1686-1694

[82] Jansen, A.; Gerhards, M.: *J. Chem. Phys. 115* (**2001**), 5445-5453

[83] Jeffrey, G.A.; Pople, J.A.; Radom, L.: *Carbohydr. Res 25* (**1972**),117

[84] Juaristi, E; Cuevas, G: The Anormeric Effect, *CRC Press*, (**1995**)

[85] Kaczor, A.; Reva, I. D.; Proniewicz, L. M.; Fausto, R.: Importance of Entropy in the Conformational Equilibrium of Phenylalanine: A Matrix-Isolation Infrared Spectroscopy and Density Functional Theory Study, *J. Phys. Chem. A 110* (**2006**), 2360

[86] Kang, C.; Yi, J. T.; Pratt, D. W.: *Chem. Phys. Lett. 423* (**2006**), 7

[87] Kang, C.; Yi, J. T.; Pratt, D. W.: *J. Chem. Phys. 123* (**2005**), 094306

[88] Kim, S. K.; Bernstein, E. R.: *J. Phys. Chem. 94* (**1990**), 3531

[89] King,G. W., Hainer, R. M, Cross, P. C., The asymmetric rotor, I. Calculation and symmetry classification of energy levels, *J. Chem. Phys. 11* (**1943**), 27

[90] Kivelson, D.; Wilson Jr, E. B.: Approximate treatment of the effect of centrifugal distortion on the rotational energy levels of asymmetric-rotor molecules, *J. Chem. Phys. 20* (**1952**), 1575

[91] Kraitchman, J.: Determination of molecular structure from microwave spectroscopic data, *Am. J. Phys. 21* (**1953**), 17-24

[92] Kroto, H. W.: Molecular Rotation Spectra, *Dover Publications*, New York (**2003**)

[93] Küpper, J.: Rotationsauflösende Laserspektroskopie - Beziehung zwischen Struktur und interner Dynamik von Molekülen, *Heinrich-Heine-Universität Düsseldorf, Institut für Physikalische Chemie, Dissertation* (**2000**)

[94] Lahmani, F.; Broquier, M.; Zehnacker-Rentien, A.: The o-cyanophenol dimer as studied by laser-induced fluorescence and ir fluorescence dip spectroscopy: a study of a symmetrical double hydrogen bond, *Chem. Phys. Lett. 354* (**2002**), 337-348

[95] Lee, C.; Yang, W.; Parr, R.: *Phys. Rev. B 37* (**1988**), 785-789

[96] LeGreve, T. A.; Baquero, E. E.; Zwier, T. S.: J*J. Am. Chem. Soc. 129* (**2007**), 4028-4038

[97] Lewis, J. D.; Malloy Jr, T. B; Chao, T. H; Laane, J,: *J. Mol. Struct. 12* (**1972**), 427

[98] Martin, R. L.; Fox, D. J.; Keith, T.; Al-Laham, M. A.; Peng, C. Y.; Nanayakkara, A.; Challacombe, M.; Gill, P. M. W.; Johnson, 454 *J. Phys. Chem. A, Vol. 113, No. 2,* (**2009**)

[99] Matos, M. A. R.; Sousa, C. C. S.; Morais, V. M. F.: *J. Phys. Chem. A 112* (2008), 7961

[100] Meerts, W. L.; Schmitt, M.: A new automated assign and analyzing method for high resolution rotaional resolved spectra using Genetic Algorithm, *Phys. Scripta 73* (**2005**), C47-C52

[101] Meerts, W. L.; Schmitt, M.: Application of Genetic Algorithm in automated assignments of high resolution spectra, *Int. Rev. Phys. Chem. 25* (**2006**), 353

[102] Meerts, W. L.; Schmitt, M.: Description and features of the program ga: An automated assign and fit program for high resolution spectra using Genetic Algorithms

[103] Meerts, W. L.; Schmitt, M.; Groenenboom, G.: New applications of the genetic algorithm for the interpretation of high resolution spectra, *Can. J. Chem. 82* (**2004**), 804-819

[104] Meschede, D: Gerthsen Physik, *Springer - Verlag, Berlin Heideberg New York* (**2004**)

[105] Nakajima, A.; Hirano, M.; Hasumi, R.; Kaya, K.; Watanabe, H.; Carter, C. C.; Williamson, J.; Miller, T. A.: *J. Phys. Chem. A 101*(**1999**), 392

[106] Nguyen, T.; Korter, T.; Pratt, D.: *Mol. Phys. 103* (**2005**), 1603-1613

[107] Nguyen, T.; Pratt, D.: *J. Chem. Phys. 124* (**2006**), 054317-1-054317-6

[108] Ostenmeier, A.; Gawelcyk, A.; Hansen, N.: Step-size adatation based on non-local use of selection information, in Parallel Problem Solving from Nature, PPSN III, ed. Davidor Y.; Schwefel H.-P; Männer R.: *Springer - Verlag, Berlin/Heidelberg* (**1994**)

[109] Park, Y. D.; Rizzo, T. R.; Peteanu, L. A.; Levy, D. H.: *J. Chem. Phys. 84* (**1986**), 6539-6549

[110] Pei, L.; Zhang, J.; Wu, C.; Kong, W.: *J. Chem. Phys. 125* (**2006**), 024305-1-024305-8

[111] Peteanu, L. A.; Levy, D. H.: *J. Chem. Phys. 92* (**1988**), 6554-6561

[112] Philips, L. A.; Levy, D. H.: *J. Chem. Phys. 89* (**1988**), 85-90

[113] Platt, J. R.: *J. Chem. Phys. 17* (**1949**)., 484

[114] Quarles, W. G.; Templeton, D. H.; Zalkin, A.: *Acta Crystallogr., Sect. B 30* (**1974**), 95-98.

[115] Radom, L; Hehre, W.J.; Pople, J.A.: *J.Am. Chem.Soc. 94* (**1972**), 2371

[116] Ratzer, C.: Strukturänderung aromatischer Moleküle bei elektronischer Anregung, *Heinrich-Heine-Universität Düsseldorf, Institut für Physikalische Chemie, Dissertation* (**2004**)

[117] Ratzer, C.; Küpper, J.; Spangenberg, D.; Schmitt, M.: The structure of phenol in the S1-state determined by high resolution UV-spectroscopy, *Chem. Phys. 283* (**2002**), 153-169

[118] Ratzer, C.; Nispel, M.; Schmitt, M.: *Phys. Chem. Chem. Phys. 5* (**2002**), 812-819

[119] Ray, B. S.: Über die Eigenwerte des asymmetrischen Kreisels, *Z. Phys. 78* (**1932**), 74

[120] Remmers, K.; Meerts, W. L.; Ozier, I.: Proton tunneling in the benzoic acid dimer studied by high reolution UV spectroscopy, *J. Chem. Phys. 112* (**2000**), S.10890-10894

[121] Romers, C.; Altona, C.; Buys, H.R.; Havinga, E.: *Topics Stereochem. 4* (**1969**), 39

[122] Schäfer, A.; Huber, C.; Ahlrichs, R.: *J. Chem. Phys. 100* (**1994**), 5829-5835

[123] Schmitt, M.: Hochauflösende elektronische Spektroskopie an Molekülen und Clustern, *Heinrich-Heine-Universität Düsseldorf, Math. Nar. Fakultät, Habilitationsschrift* (**2000**)

[124] Schmitt, M.; Brause, R.; Marian, C.; Salzmann, S.; Meerts, W. L.: *J. Chem. Phys. 125* (**2006**), 124309

[125] Schmitt, M.; Feng, K.; Böhm, M.; Kleinermanns, K.: *J. Chem. Phys. 125* (**2006**), 144303

[126] Schmitt, M.; Henrichs, U.; Müller, H.; Kleinermanns, K.: *J. Chem. Phys. 103* (**1995**), 9918-9928

[127] Schmitt, M.; Jacoby, C.; Gerhards, M.; Unterberg, C.; Roth, W.; Kleinermanns, K.: *J. Chem. Phys. 113* (**2000**), 2995-3001

[128] Schmitt, M.; Jacoby, C.; Kleinermanns, K.: *J. Chem. Phys. 108* (**1998**), 4486-4495

[129] Schmitt, M.; Krügler, D.; Böhm, M.; Ratzer, C.; Bednarska, V.; Kalkman, I.; Meerts, W. L.: *Phys. Chem. Chem. Phys. 8* (**2006**), 228-235

[130] Schmitt, M.; Küpper, J.; Spangenberg, D.; Westphal, A.: *Chem. Phys. 254* (**2000**), 349-361

[131] Schmitt, M.; Ratzer, C.; Kleinermanns, K.; Meerts, W. L.: *Mol. Phys. 102* (**2004**), 1605-1614

[132] Schmitt, M.; Ratzer, C.; Meerts, W. L.: *J. Chem. Phys. 120* (**2004**), 2752-2758

[133] Spangenberg, D.: Strukturelle und kinetische Untersuchungen an H-brückengebundenen ionischen Clustern des Phenols, *Heinrich- Heine-Universität, Math. Nat. Fakultät, Düsseldorf, Dissertation* (**2000**)

[134] Spangenberg, D.; Imhof, P.; Kleinermanns, K.: *Phys. Chem. Chem. Phys. 5* (**2003**), 2505-2514

[135] Sturdy, Y. K.; Clary, D. C.: *Phys. Chem. Chem. Phys. 9* (**2007**), 2065-2074

[136] Svartsov, Y. N.; Schmitt, M.: *J. Chem. Phys. 128* (**2008**) 214310

[137] Tausch, M.; Paterkiewicz, D.: "Fluoreszenz und Phosphoreszenz"in Praxis der Naturwissenschaften (Chemie), 36, (**1988**), 14

[138] Thomas, J. A; Alvarez-Valtierra, L.; Pratt, D. W.: *Chem. Phys. Letters 490* (**2010**), 109

[139] Townes, C.H.; Schawlow, A.L.: Microwave Spectroscopy, *Dover Publications, New york*(**1975**)

[140] van Mourik ,T.; Emson, L. E. V.: *Phys. Chem. Chem. Phys. 4* (**2002**), 5863-5871

[141] Van Vleck, J. H.: *Phys. Rev. 33* (**1929**), 467

[142] Varsanyi, G.: Assignments for Vibrational Spectra of 700 Benzene Derivatives, *Wiley, New York,* (**1974**)

[143] Vu, C.: Rotationsauflösende Spektroskopie von Biomolekülen und Biomimetika, Heinrich-Heine-Universität Düsseldorf, *Institut für Physikalische Chemie, Diplomarbeit* (**2006**)

[144] Watson, J. K. G.: Approximations for the inertial defects of planar molecules, *J. Chem. Phys. 98* (**1993**), 5302

[145] Watson, J. K. G.: Aspects of of quartic and sextic centrifugal effects on rotational energy levels, Vibrational Spectra and Structure, Vol. 6, J. R. Durig, ed., *Marcel Dekker, New York* (**1977**)

[146] Watson, J. K. G.: Centrifugal distortion in spherical tops, *J. Mol Spectrosc. 40* (**1971**), 536

[147] Watson, J. K. G.: Determination of centrifugal distortion coefficients of asymmetric top molecules, *J. Chem. Phys. 46* (**1967**), 1935

[148] Watson, J. K. G.: Determination of centrifugal distortion coefficients of asymmetric top molecules, III. Sextic coefficients, *J. Chem. Phys. 48* (**1968**), 4517

[149] Watson, J. K. G.; Roytburg, A.; Ulrich, W.: *J. Mol. Spectrosc. 196* (**1999**), 102-119

[150] *Wavetrain®, User's Manual*

[151] Westphal, A.: Hochaufgelöste Laserfluoreszenzspektroskopie am Phenol(Methanol)1-Cluster, *Heinrich-Heine-Universität Düsseldorf, Institut für Physikalische Chemie, Doktorarbeit* (**2002**)

[152] Westphal, A.; Jacoby, C.; Ratzer, C.; Reichelt, A.; Schmitt, M.: *Phys. Chem. Chem. Phys. 5* (**2003**), 4114-4122

[153] Wiedemann, S.; Metsala, A.; Nolting, D.; Weinkauf, R.: *Phys. Chem. Chem. Phys. 6* (**2004**), 2641-2649.

[154] Winnewisser, G., J.: Millimeter wave rotational spectrum of HSSH and DSSD. II. Anomalous K doubling caused by centrifugal distortion in DSSD, *J.Chem. Phys. 56* (**1972**), 2944

[155] Wolfe, S.: *J. Chem Educ. 56* (**1979**), 438

[156] Wolfe, S.; Rauk, A.; Tel, L. M.; Csizmadia, I.G.: *J. Chem. Soc.(B)* (**1971**), 136

[157] Wu, Y. R.; Levy, D. H.: *J. Chem. Phys. 91* (**1989**), 5278-5284

[158] Yang, J.; Choob, J.; Kwon, O.; Laane, J.: *Spectrochim. Acta A 68*(**2007**), 1170

[159] Yang, J.; Laane, J.:*J. Mol. Struct. 798* (**2006**), 27

[160] Yang, J.; Wagner, M.; Laane, J.: *J. Phys. Chem. A 110* (**2007**), 9805

[161] Yokoyama, H.; Watanbe , H.; Omi, T.; Ishiuchi, S.; Fujii, M.: *J. Phys. Chem. A 105* (**2001**), 9366

Danksagung

Herrn Klaus Kelbert für die Lösung zahlreicher elektronischer Probleme.

Den Mitgliedern der Abteilung Physikalische Chemie I, die mir jederzeit Hilfe aller Art entgegenbrachten, sei es beim Belüften meiner Apparatur oder der Korrektur der Poster und der Vorträge.

Meinen Eltern, die immer für mich da sind und mir bei vielen meinen Entscheidungen geholfen und mich unterstürzt haben.

Meinem Bruder Tien Nguyen Vu und seiner Frau Hang Nguyen, die stets auf meiner Seite stehen und mein Computerwissen um Vieles erweitert haben. Besonders danke ich meinem Bruder für seine Hilfe bei der Erstellung mancher Abbildungen.

Frau Ramona Grahl für die Bereicherung meines Wissens über die medizinischen und politischen Themen.

Herrn Hung Pham für seine stete Hilfsbereitschaft bei meinen diversen Anfrage, seinen Rat und seine Anregungen bezüglich meiner zukünftigen Planung.

Herrn Torsten Berger, Frau Van Thu Ton, Frau Truc Quyen Nguyen, Frau Danielle Kragbe und Herrn Siulweng Gottwald für die menschliche, angenehme Art.